Combined Kinetic and Electrochemical Energy Storage Systems Offering Balancing Services to Electrical Grids

Vom Fachbereich Maschinenbau
an der Technischen Universität Darmstadt
zur Erlangung des Grades eines Doktor-Ingenieurs (Dr.-Ing.)
genehmigte

Dissertation

vorgelegt von

Panagiotis Mouratidis, M.Sc.
aus Kavala, Griechenland

Berichterstatter:	Prof. Dr.-Ing. Stephan Rinderknecht
Mitberichterstatter:	Prof. Dr. Sc. Kari Tammi
Tag der Einreichung:	18.08.2022
Tag der mündlichen Prüfung:	18.10.2022

Darmstadt 2023
D17

Year of publication in tuprints: 2023

Date of thesis defence: 18.10.2022

Please cite this document as:

Panagiotis Mouratidis (2023), Combined Kinetic and Electrochemical Energy Storage Systems Offering Balancing Services to Electrical Grids, Technical University of Darmstadt.

URN: urn:nbn:de:tuda-tuprints-229605

URI: https://tuprints.ulb.tu-darmstadt.de/id/eprint/22960

Kurzfassung

Energiespeichertechnologien weisen ein breites Anwendungsbereich auf. Neben Unterhaltungselektronik und Elektrofahrzeugen werden stationäre Energiespeicher eingesetzt um die Qualität von Stromnetzen durch das Gebot von Regelleistung zu erhöhen. Das untersuchte Energiespeichersystem zur Bereitstellung von Regelleistung in Stromnetzen kombiniert kinetische und elektrochemische Energiespeicher. Der berücksichtigte kinetische Energiespeicher umfasst Hochgeschwindigkeits-Schwungradspeicher nach den Parametern von Prototypen, die an der Technischen Universität Darmstadt entwickelt wurden. Der berücksichtigte Batteriespeicher umfasst Lithium-Ionen-Zellen mit Lithium-Nickel-Mangan-Cobalt-Oxid in der Kathode und Grafit in der Anode.

Um die Betriebskosten des kombinierten Energiespeichersystems einzuschätzen, werden die Leistungsverluste der Lithium-Ionen-Zelle, des Schwungradspeichers sowie der entsprechenden Stromrichter modelliert. Die abgeleitete Verlustfunktion des Schwungradspeichers hängt überwiegend von seiner Drehzahl und vom Strom seiner permanenterregten Synchronmaschine ab. Ebenso hängt die abgeleitete Verlustfunktion der Lithium-Ionen-Zelle großenteils von ihrem Ladezustand und von ihrem Strom ab. Um die Auswirkung der Degradierung der Lithium-Ion-Zellen zu berücksichtigen, wird ein empirisches Degradierungsmodell weiterentwickelt und auf Basis der Herstellerspezifikation für die eingesetzte Lithium-Ionen-Zellen parametrisiert.

Die Frequenzhaltungsreserve entspricht der Hauptanwendung des kombinierten Energiespeichers und bestimmt daher das Lastprofil. Die Wahrscheinlichkeitsverteilung eines abgetasteten Tagesgangs der Netzfrequenz von Kontinentaleuropa wird verwendet, um gemeinschaftlich den kombinierten Energiespeicher zu dimensionieren. Dabei wird die Degradierung der Lithium-Ionen-Zellen berücksichtigt, sodass die Batterie die Anforderungen der Anwendung über die geplante Nutzungsdauer erfüllt.

Das Energiemanagement des kombinierten Energiespeichersystems bezieht nicht nur die Leistungsaufteilung unter den Speichereinheiten ein, sondern auch die Steuerung der Einzelspeicher. Daher wird der Statorstrom, der die Gesamtverlusten der elektrischen Maschine und des Stromrichters des Schwungradspeichers minimiert, abgeleitet. Um die momentanen Energiewandlungsverluste des kombinierten Energiespeichers zu minimieren, wird die optimale Leistungsaufteilung unter den Energiespeichertechnologien anhand vereinfachter Verlustfunktionen analytisch abgeleitet und simulativ bewertet. Anschließend wird das Energiemanagement in einem programmierbaren Steuergerät implementiert und anhand eines kombinierten Energiespeicherprototyps getestet. Trotz der hohen Unsicherheiten, die die experimentelle Untersuchung einbezieht, stimmen deren Ergebnisse qualitativ mit den entsprechenden Simulationen überein.

Die Wirtschaftlichkeit von kombinierten Energiespeichersystemen wird mit der von reinen Batteriesystemen verglichen für die Anwendungen Frequenzhaltungsreserve, Frequenzhaltungsreserve gemeinsam mit der Energierückgewinnung am Wegesrand in Bahnstromnetzen und Frequenzhaltungsreserve gemeinsam mit dem Schnelladen von Elektrofahrzeugen. Um die kombinierten Energiespeichersysteme optimal zu dimensionieren, wird eine Kosten-Nutzen-Analyse durchgeführt. Dabei werden die Gesamtbetriebskosten als Kosten und eine niedrige Degradierung der Lithium-Ionen-Zellen als Nutzen berücksichtigt. Optimal dimensionierte kombinierte Energiespeicher weisen niedrigere Gesamtbetriebskosten als optimal dimensionierte reine Batteriespeicher auf, was deutlicher in Anwendungsfällen mit hoher und häufig wechselnder Last ist.

Abstract

Energy storage technologies have a wide range of applications. Besides consumer electronics and electric vehicles, stationary energy storages are used to improve the power quality of electrical grids by offering balancing services. The investigated energy storage system for the provision of grid balancing services combines kinetic and electrochemical energy storages. The considered kinetic storage comprises high-speed flywheel storages according to the parameters of the prototypes developed at the Technical University of Darmstadt. The considered battery storage is composed of lithium-ion cells with lithium nickel manganese cobalt oxides in the cathode and graphite in the anode.

In order to estimate the operating cost of the combined energy storage system, the power losses of the lithium-ion cell, the flywheel storage and the corresponding power converters are modelled. The derived loss function of the flywheel storage predominantly depends on its speed and the current of its permanent magnet synchronous machine. Similarly, the derived loss function of the lithium-ion cell mainly depends on its state of charge and its current. To consider the effects of the lithium-ion cell degradation, an empirical degradation model is further developed and parametrized based on the manufacturer specification for the lithium-ion cells used.

The frequency containment reserve constitutes the main application of the combined energy storage and therefore determines the load profile. The probability distribution of a sampled 24-hour profile of the grid frequency of continental Europe is used to collectively size the combined energy storage. The degradation of the lithium-ion cells is thereby considered, so that the battery fulfils the requirements of the application throughout the target service life.

The energy management of the combined storage system involves not only the power split among the storage units, but also the control of the individual storages. Therefore, the stator current that minimizes the total losses of both the electric machine and the power converter of the flywheel storage is derived. To minimize the instantaneous energy conversion losses of the combined energy storage, the optimal power share of the storage technologies is analytically derived using simplified loss functions and evaluated through simulations. Subsequently, the energy management is implemented in a programmable controller and tested on a prototype combined energy storage system. Despite the high uncertainties involved in the experimental investigation, its results are in qualitative congruence with the corresponding simulations.

The cost-efficiency of combined energy storage systems is compared with that of battery-only systems for the applications of frequency containment reserve, frequency containment reserve along with wayside energy recovery in railway networks and frequency containment reserve along with electric vehicle fast charging. To optimally size the combined energy storage systems, a cost-benefit analysis is conducted, in which the total cost of ownership serves as cost and a low degradation of the lithium-ion cells serves as benefit. Optimally sized combined energy storages result in a lower total cost of ownership than optimally sized battery-only storages, which is more pronounced in use cases that involve high and frequent alternating load.

Contents

Nomenclature

The main variables and indices used in the present work are listed below. Generally, variables are explained when first appear in text.

Variables in Latin

Variable	Typical unit	Description
b	-	battery degradation factor
C	F	capacitance
C	J/K	heat capacity
C	cu	cost (cu stands for cost unit, hence currency independent)
E	Wh	energy
f	Hz	frequency
G	....	uncertainty
g	-	relative error
I	A	electric current
k	-	constant, factor
L	Vs/A	inductance
m	kg	mass
M	Nm	torque
n	rpm	rotational speed
N	-	non-negative integer number
p	-	number of pole pairs
P	W	power
q	-	relative charge, relative charge capacity, state of charge
Q	As	electric charge
Q	W	heat
r	-	relative resistance
R	Ω	electrical resistance
R	K/W	thermal resistance
S	VA	apparent power
s	-	share
t	s	time
T	s	time, duration, period
U	V	voltage
v	m/s	velocity
w	-	energy state
Z	Ω	impedance

Variables in Greek

Variable	Typical unit	Description
α	m/s^2	acceleration
α	1/K	temperature coefficient
α	-	exponent of battery degradation function
η	-	efficiency
ϑ	°C	temperature
Θ	kg m^2	moment of inertia
Ψ	Vs	flux linkage
ω	rad/s	angular frequency

Special characters and notation

j	imaginary unit
$\underline{(\,)}$	complex number, space vector
$(\,)^*$	complex conjugate
Re{ }	real part of a complex number
Im{ }	imaginary part of a complex number
$\overline{(\,)}$	mean as defined in text
$\widehat{(\,)}$	amplitude, peak value

Indices

acq	acquisition
b	battery
br	braking
bs	battery storage system (comprising several batteries)
c	lithium-ion cell
c	capacity
c	cutoff
cal	calendrical
cs	combined storage system
Cu	copper
cyc	cyclic
d	direct component
e	electrical
e	expected
ed	eddy current
EFC	equivalent full cycles
EoL	End of Life
eq	equivalent
Fe	iron
fw	flywheel
h	main
hy	hysteresis
i	counter
i	increase
i	internal
inv	investment
ks	kinetic storage system (comprising several flywheels)
L	losses
lo	lower
m	mechanical
max	maximum
min	minimum
N	nominal
oc	open circuit
pc	power converter
PQ	prequalified

q	quadrature component
s	series
s	state
s	stator
t	total
up	upper

Abbreviations

AC	Alternating Current
AMB	Active Magnetic Bearing
BS	Battery Storage
CAN	Controller Area Network
CS	Combined Storage
DC	Direct Current
EFC	Equivalent Full Cycles
EoL	End of Life
EVFC	Electric Vehicle Fast Charging
FCR	Frequency Containment Reserve
hs	hybrid storage
IEC	International Electrotechnical Commission
KS	Kinetic Storage
Li-ion	Lithium-ion
NMC	Nickel Manganese Cobalt oxides
PLC	Programmable Logic Controller
PMSM	Permanent Magnet Synchronous Machine
PQ	Prequalification
OPS	Optimal Power Share
O&M	Operation and Maintenance
rms	root mean square
SO GL	System Operation Guideline
SoC	State of Charge
TCO	Total Cost of Ownership
TSO	Transmission System Operator
WERS	Wayside Energy Recovery System
3xAC	three-phase Alternating Current

1. Introduction

Since the beginning of history there is a perpetual need for energy sources. Energy sources that have both high volumetric and high gravimetric energy density such as fossil fuels can easily be stored, so that the use of fossil fuels along with the invention of the steam engine were among the key drivers of the first industrial revolution. The combustion of fossil fuels is considered to be an irreversible process as processes that convert chemical components to synthetic fuels are still not efficient enough. The carbon dioxide that has been emitted by the combustion of fossil fuels over the past two centuries is considered as the main reason for the temperature rise that has globally been observed in the last decades. Unfortunately, the temperature rise leads to a climate change with adverse consequences.

To limit the use of fossil fuels, renewable energy sources, such as wind and solar energy, have increasingly been used to generate electricity over the past two decades. Electrical grids constitute a clean and efficient way to distribute the energy generated by producers to consumers. In all kinds of electrical grids, power supply and demand should be in equilibrium to achieve a reliable operation. Power grid operators have several measures at their disposal to compensate for imbalances between generation and consumption. In simplified terms, grid operators can switch on loads that sink power at times of overproduction or activate generators that supply power at times of underproduction. In this respect energy storages that operate bidirectionally can play both the role of consumer and producer.

1.1 Motivation

Over the course of time, alternatives to fossil fuels have evolved. Rechargeable electrochemical storages or rechargeable batteries are able to store electric charge in their chemical bonds as well as to release the charge stored, hence converting electrical to chemical energy and vice versa. Although the first rechargeable batteries were invented in the beginning of the 19th century, their advantages became more evident when electrical grids evolved. Over the last three decades, small batteries have increasingly been integrated into consumer electronics. During the last decade, lithium-ion batteries have been the major driver of the electrification of the vehicle fleet. Furthermore, the installation of large-scale battery systems in electrical grids to compensate for imbalances between production and generation has evolved into a typical practice over the past few years.

The kinetic energy stored in flywheels that rotate at relatively high speed is a technology much older than batteries. The kinetic energy stored in large generators in synchronous power grids is the first line of defence against power imbalances. Conventional synchronous generators convert mechanical to electrical energy without semiconductors, so that their moment of inertia directly contributes to the *grid inertia* which is defined as the ability of the power grid, as a whole, to resist to changes in its frequency. The penetration of wind and solar energy in electrical grids have increased the uncertainties in the power generation without increasing the grid inertia because photovoltaic and wind turbines operate in a different way than conventional generators. Although high grid inertia is generally desirable, an additional measure in order to enhance the reliability of power grids is to quickly compensate for imbalances by activating units that reserve power for this purpose. In this respect flywheel storages integrated through power converters into electrical grids constitute an alternative to electrochemical batteries to provide balancing reserve power.

Although the specific energy of flywheel storages is significantly lower than that of batteries, they degrade much slower over usage compared to batteries.

Renewable power generation is not the only issue that concerns the operators of electrical grids. The market share of electric vehicles has constantly been increasing in the past few years and it is reasonably expected to further increase, not only due to climate change policies, but also due to technological advancements. Although in many places around the world the development of charging infrastructure for electric vehicles evolves slower than the electric vehicle market itself, fast charging of electric vehicles is already a mature technology. On the one hand, fast charging of electric vehicles results in an enhanced experience for the vehicle users, on the other hand, it causes power peaks with adverse effects on electrical grids. Peak power in the order of a few hundred kW challenges the network infrastructure, so that often additional investments are required. Energy storages integrated next to electric vehicle charging stations aim to limit the power rating of the network infrastructure by sharing part of the load as wells as to mitigate the effect of power peaks on the grid side. The mitigation of power peaks due to electric vehicle charging contributes to a reliable operation of power grids by reducing the need for balancing services. In other words, the mitigation of power peaks can be seen as a balancing service itself.

Stationary energy storages can also be used in railway networks to recover the braking energy of rail vehicles and feed it back to the network when rail vehicles accelerate. In this regard energy storages contribute to the mitigation of power peaks and voltage fluctuations in railway networks. As power peaks in railway networks do have an impact on the interconnected power grid, energy storages that mitigate power peaks in railway networks can be seen as a balancing service for the interconnected power grid.

1.2 Research Questions

As both generation and consumption of electricity become less predictable, the demand for balancing power in electrical grids is expected to increase. Although flywheel and battery storages have quite different characteristics, they can both provide grid balancing services. When planning a project for a new balancing reserve facility or a new fast charging station for electric vehicles with storage units, the question of which storage technology should be used is raised. The discussion can develop further into whether the storage system should include only flywheels, only batteries or a combination of both. If the combination of both seems worthwhile, the question of how many batteries should be combined with how many flywheels is raised. Furthermore, the question of how to split the load between the flywheels and the batteries also looks for an answer. The requirements and the load profiles of balancing services vary depending on the specific application, for instance, grid frequency regulation corresponds to different requirements and load profiles than the mitigation of power peaks. Thus, a question is raised whether certain applications and load profiles are advantageous for combined storages. Although the initial question concerns a single project in a certain location, similar questions are relevant for utilities that manage a portfolio of grid connected facilities in different locations and plan to expand their balancing service portfolio.

1.3 Objectives

The combination of flywheels and batteries usually aims to reduce the cyclic degradation of the batteries by splitting the load between the storage technologies. Alternatively, additional batteries can be connected in parallel instead of flywheels, which also reduces the battery load and therefore its cyclic degradation. Flywheel-only systems are not further considered due to their high energy capacity cost in relation to the relatively high energy capacity needed in balancing reserve applications. To facilitate the decision between battery-flywheel variants and battery-only variants, the cost of acquiring and operating both variants should be evaluated. Furthermore, the battery degradation should be estimated, so that it is ensured that the battery system is operational throughout the target service life.

The present work aims to find the optimal combination of flywheels and batteries in balancing reserve applications that minimizes the total cost of ownership, provided that the state of the battery degradation remains below a certain threshold. The optimal system size should be determined by evaluating several system variants. In this respect a sizing algorithm that determines the initial variant is needed. To examine the effect of the load profile on the economic performance of the combined storage, load profiles of several use cases should be considered. The characteristics of load profiles that are favourable for combined storage systems should also be explored.

The acquisition cost of storage units constitutes an important cost factor that affects the economic assessment of all system variants. Since the estimation of the acquisition cost involves uncertainties, a variable acquisition cost should be considered through sensitivity analyses. Sensitivity analyses should reveal which cost drivers significantly affect the decision between combined and single-technology systems. The operating cost of flywheels and batteries predominantly depends on their energy conversion losses. To estimate the losses in the flywheel storage, an elaborate model of its electric machine should be developed. Additionally, a loss model for the lithium-ion cells is also needed.

To estimate the energy losses and therefore the operating cost of the storage units, their power share should be first determined. In order to exploit the flywheels so that the battery degradation is minimized, the maximum power share of the kinetic storage should be considered. However, the power split that minimizes the total energy losses of the combined system should also be investigated for use cases in which the minimization of the battery degradation has only secondary importance. Furthermore, to facilitate the implementation of the power split algorithm in the controller of a combined storage prototype, the optimization problem should be formulated so that it can be analytically solved.

1.4 Contributions

The main contribution of this work is the development of a methodology to optimally size energy storage systems that comprise lithium-ion batteries and high-speed flywheels for balancing services in electrical grids. The combined storages are optimally sized according to the lowest total cost ownership, provided that the battery degradation remains below a certain threshold. The optimal sizing of battery-only systems is performed under the same conditions applied for the sizing of combined systems. In addition to load profiles for grid frequency regulation, load profiles resulting from energy recovery in railway networks and fast charging of electric vehicles are considered. It is shown that for all load profiles considered in this work, the total cost of ownership of the optimal combined system is lower than that of the optimal battery-only system.

The present work contributes to the optimal operation of high-speed flywheels with permanent magnet synchronous machines. The copper and iron losses of the electric machine are modelled with the aid of an equivalent circuit. The resulting loss function is used to determine the stator current that minimizes the losses of the electric machine including its power converter. In this respect the advantages of operating the machine in field weakening are explained. Moreover, with the aid of the equivalent circuit, analytic expressions for the braking torque due to eddy currents and the corresponding stator current required to keep the flywheel rotating at constant speed are derived.

A contribution towards the estimation of the cyclic degradation of lithium-ion cells is made in this work. Although numerous models for the cyclic degradation of lithium-ion cells have been suggested in the literature, they claim validity only for the specific cell under test. The present work suggests a method in which an existing cyclic degradation model that is based on experimental results is parametrized using the manufacturer specification for the cyclic degradation of the lithium-ion cells actually used.

In the field of energy management, the present work contributes towards a computational efficient optimal power split strategy between flywheel and battery storages. Various optimization-based strategies for energy storage systems have been suggested in the literature, however, their implementation in real controllers is often difficult or unfeasible due to high demands on computational resources. In the present work, simplified loss functions of the storage units are derived in order to obtain a closed-form expression of the optimal policy. The energy management including the optimal policy is successfully implemented in a real controller and tested on a prototype combined storage system.

1.5 Outline

The present chapter, **Chapter 1,** introduces the motivation, the research questions, the objectives and the contributions of this work preceding the review of the state of the art in **Chapter 2**. The state-of-the-art review discusses the market developments in stationary energy storage systems, explores battery-flywheel storage projects and addresses energy storage projects at Technical University of Darmstadt. Furthermore, the state-of-the-art review explores recent scientific articles related to the energy management, the sizing and the cost assessment of battery-flywheel storages in order to stress the contributions of this work. The modelling, which is addressed in **Chapter 3,** focuses on the power losses in energy storages by describing the equivalent circuit of the electric machine of the flywheel as well as the equivalent circuit of the lithium-ion cells that make up the battery. Furthermore, a simplified loss model for the power converters is described. **Chapter 4** deals with the sizing of a reference battery-flywheel storage system for the application of frequency containment reserve. Moreover, the rated power of energy storages, the characteristics of the power grid frequency and specific requirements of grid balancing services related to energy storage are discussed. **Chapter 5** addresses the energy management, which includes both the low-level control of the individual storage units and the high-level control that focuses on the power split between the storage units. The approach to derive the optimal policy that minimizes the energy conversion losses of the combined storage system is described. Subsequently, the performance of the optimal policy is investigated through simulations. Moreover, the implementation of the energy management in a real controller and the corresponding tests on a prototype combined storage system are presented. **Chapter 6** introduces the methodology for the estimation of the total cost of ownership and compares the cost-efficiency of combined storage systems with that of battery-only systems. Besides frequency containment reserve, the application of wayside energy recovery in railway networks and the fast charging of electric vehicles are also investigated. Finally, in **Chapter 7**, the key findings related to the research questions of this work are summarized and implications for future research and practice are discussed.

2. State of the Art

Modern energy storage systems can be integrated via power converters into electrical grids and therefore facilitate applications, such as Uninterruptible Power Supply (UPS), power quality and frequency regulation. The frequency regulation includes services such as the Frequency Containment Reserve (FCR) in the power grid of continental Europe. Energy storages are also widely used in vehicular systems, which are, however, beyond the scope of the present investigation. Nevertheless, battery storages installed in electric vehicles can be potentially used as stationary systems in the so-called *vehicle-to-grid* applications.

2.1 Stationary Battery and Flywheel Storage Systems

The number of grid-connected electrochemical storages has constantly been growing over the past decade, which signifies that electrochemical storages, especially lithium-ion batteries, are widely seen as the mainstream solution in a series of applications. According to a report of the International Renewable Energy Agency (IRENA) based on information retrieved within 2017 from the online Global Energy Storage Database maintained by the United States Department of Energy (DOE), the worldwide installed power capacity of stationary electrochemical energy storage systems was estimated at 1.9 GW compared to 0.9 GW of installed power capacity of stationary flywheel storages (IRENA, 2017). However, a forecast for a significant increase in the integration of electrochemical energy storages was made in the same report. The installed power capacity of electrochemical storages in Germany as of 2021, including behind-the-meter storages such as household batteries combined with photovoltaics, is estimated at 2.64 GW (Figgener, et al., 2022), which already exceeds the worldwide estimation of installed electrochemical storages made five years earlier (IRENA, 2017). Thus, the increase of the grid-connected electrochemical energy storages in Germany over the past five years has been tremendous.

An effort to register and classify and the development of battery storage projects in Germany using both public and private databases was pursued by research institutes throughout the last decade and the corresponding figures as of 2021 are presented by Figgener et al. (2022). According to Figgener et al. (2022), the large-scale stationary battery storage systems in Germany, which have an energy capacity that equals or exceeds 1 MWh, added up to 750 MWh of installed energy and 620 MW of installed power, from which about 550 MW correspond to lithium-ion batteries and only 50 MW to lead acid batteries. Within the years 2020 and 2021 a decrease in the installation of new large-scale battery storage systems that target at the FCR market was observed. According to Figgener et al. (2022), the FCR market in Germany is saturated as the market demand for FCR approaches 555 MW in 2022 and the prequalified power of stationary battery storage systems for balancing services approximates 480 MW.

Less information is available for the development of stationary flywheel storage systems, which implies that flywheels have a substantially lower market share than batteries. Some stationary flywheel storage projects are discussed by Amiryar & Pullen (2017) and some are listed in the work of Perez-Diaz et al. (2020). Both articles refer to two flywheel storage facilities with an installed power capacity of 20 MW in the United States, the first in Stephentown, New York, and the second in Hazle Township, Pennsylvania. Each facility comprises 200 flywheel storage units, each with a nominal power of 100 kW and a nominal energy capacity of 25 kWh, hence an installed energy capacity of 5 MWh. Furthermore, both facilities were raised by the flywheel manufacturer Beacon Power LLC, which also currently manages the facilities with the purpose of providing balancing services to the electricity grid.

According to a press release of 2015, the utility Stadtwerke München in Germany made a kinetic storage system that is connected to the grid at the site of its manufacturer Stornetic GmbH in Jülich available for trading in a virtual factory. The kinetic storage system can be remotely controlled through a dedicated network interface. The system is intended to compensate for discrepancies between the forecast and the actual generation of renewable energies and therefore contribute to the avoidance of mismatch penalties. The kinetic storage system is named DuraStor and comprises 28 flywheels with a maximum speed of 45 000 rpm, which add up to a total power capacity of 600 kVA and an energy capacity of 100 kWh.

2.2 Stationary Battery-Flywheel Storage Systems

Although many stationary energy storage systems that are composed of batteries and a few systems that are composed of flywheels has been implemented around the world, there is little information avaialable about implemented combined battery-flywheel energy storage systems. On the one hand the combination of batteries and flywheels in stationary systems is a relative new approach that has not found a lot of examples yet. On the other hand, even when combined storage projects are implemented, there are presumably not classified as combined or hybrid, which makes them hard traceable in annual market reports. Therefore, an effort to find a handful of representative examples of battery-flywheel storage systems is pursued.

The energy storage integrator Schwungrad Energie demonstrated a battery-flywheel storage system in Rhode, Ireland (Meng, et al., 2020; Leon, et al., 2021). The project confirmed the ability of energy storage systems to contribute to the reliable operation of the Irish electrical grid, which is challenged by the growing wind power penetration. The system combined two high-speed flywheel storages manufactured by Beacon Power rated at 160 kW and 30 kWh each and a valve regulated lead acid battery system with a rated power of 160 kW and an energy capacity of 576 kWh (Schwungrad Energie, 2017). The project confirmed that the hybrid energy storage system can regulate the power flow at its terminals with respect to the deviation of the grid frequency from its reference value.

According to a common press release of S4 Energy B.V., which is based in the Netherlands, and Leclanche SA, which is headquartered in Switzerland, a hybrid energy storage system is completed in Almelo, the Netherlands, as from August 2020 and handed over to Almelo Ancillary Services B.V., a local provider of energy services. The hybrid storage is composed of lithium-ion batteries with a power capacity of 8.8 MW and an energy capacity of 7.12 MWh as well as a kinetic storage with a power capacity of 3 MW. Although the rated energy capacity of the kinetic storage was not specified in the press release, presumably, six flywheels of the type KINEXT manufactured by S4 Energy were installed. According the data sheet of KINEXT, it has a rated energy capacity of 30 kWh, hence an estimated energy capacity of 180 kWh for the kinetic storage. The facility aims to serve in the energy reserve market by providing 9 MW of prequalified balancing reserve power. Moreover, the combination of flywheel and batteries is intended to reduce the cyclic degradation of the battery system and therefore extend its service life to at least 15 years.

A series of flywheel storage prototypes were developed by the Institute of Mechatronic Systems at the Technical University of Darmstadt. The first prototype is described by Schaede (2015), the second prototype named ETA290, whose technical data can be found in Table A.9, is described by Quurck et al. (2017) and the third prototype named SWIVT290, with its main technical parameters summarized in Table A.10, is discussed by Schneider & Rinderknecht (2019). The developed flywheel storages are equipped with an innovative highly integrated outer rotor, which levitates in vacuum suspended by Active Magnetic Bearings (AMBs). Thus, bearing friction losses vanish and air friction losses are substantially decreased depending on the pressure range. The electromechanical energy conversion is realized by a Permanent Magnet Synchronous Machine (PMSM), which is driven by a power converter that modulates the voltage of the stator windings in order to fulfil the set acceleration profile.

The ETA290 flywheel prototype is combined with four lithium-ion batteries, each with a nominal energy capacity of 30.6 kWh with the technical parameters listed in Table A.5, in order to form the hybrid storage hsETA as described by Mouratidis, Schüßler and Rinderknecht (2019). The hybrid storage hsETA presented in Figure 2.1 is installed in the model factory *ETA-Fabrik* (Abele, et al., 2016) located in the campus Lichtwiese of the Technical University of Darmstadt. The aim of hsETA is not only to improve the power quality of the ETA-Fabrik, but also to contribute to the stability of the electricity grid by offering balancing services (Plößer, et al., 2017). The flywheel storage protype SWIVT290 is also combined with a lithium-ion battery system of 49 kWh to form the hybrid storage hsSWIVT as presented by Mouratidis, Schneider et al. (2019). The main objective of the prototype hsSWIVT, which is presented in Figure 2.2, is the experimental investigation of peak shifting in residential microgrids (Conci & Schneider, 2017). However, additional applications such as grid balancing services are also investigated through the hsSWIVT.

The described battery-flywheel systems are summarized in Table 2.1. Clearly, the kinetic storage systems developed at the Technical University of Darmstadt have a lower power capacity compared to that of the commercial and the pilot project; first because they employ a single flywheel storage unit, second because the technology of outer rotor is relatively new and still has not reached its full potential. Furthermore, the university premises can rarely host large scale systems, which are usually built in remote locations. Although the system of Schwungrad Energie employed lead acid batteries as of 2017, recent projects integrated lithium-ion batteries. Interestingly, the pilot and the commercial project are intended only for grid balancing services, whereas the research projects also consider additional applications.

Table 2.1 Examples of implemented battery-flywheel projects

Project, location	Electrochemical storage			Kinetic storage		Type	Applications	First reported
	Power capacity (kW)	Energy capacity (kWh)	Type	Power capacity (kW)	Energy capacity (kWh)			
S4 Energy, Almelo, the Netherlands	8800	7120	Li-ion	3000	180	Commercial	FCR	2020
hsSWIVT, TU Darmstadt, Germany	30	49	Li-ion	50	1.8	Research	FCR, peak shifting	2019
hsETA, TU Darmstadt, Germany	120	122	Li-ion	60	1.4	Research	FCR, UPS, peak shifting, power quality	2019
Schwungrad Energie, Rhode, Ireland	160	576	Lead acid	320	60	Pilot project	Grid balancing services	2017

Figure 2.1 Prototype hybrid storage hsETA, **1**: flywheel storage **2**: battery storage

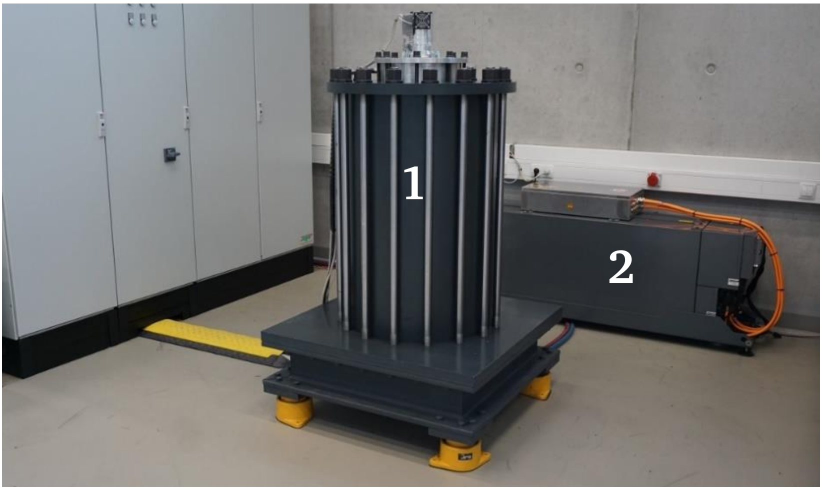

Figure 2.2 Prototype hybrid storage hsSWIVT, **1**: flywheel storage **2**: battery storage

2.3 Energy management

A considerable stream of research has focused on the management of energy storage systems over the past decade. A comprehensive literature review conducted by Weitzel & Glock (2018) concentrated on a sample of 202 articles which was derived from systematically screening the results of a database search in scientific journals when keywords such as “energy storage”, “optimal management” and “grid” were given. The study reveals a significant growth in the number of publications under the given keywords after 2012. Weitzel & Glock (2018) classify the publications into a conceptual framework, discuss the identified research streams and suggest future research opportunities. Two of the propositions suggested by Weitzel & Glock (2018) are highlighted as they influence the current investigation. First most of the articles concern single storage technologies and only 16 out of the 202 sampled articles investigated the benefits of the combination of different storage technologies. Second, although most publications employ numerical optimization techniques because of the complex structure of the problem, there is little work done to derive closed-form representations of the optimal policy.

Bocklisch (2016) discusses the range of methods to split the load among the units of hybrid storage systems and suggests a differentiation between rule-based and optimization-based energy management strategies. From the terminology perspective, the objective function of an optimization algorithm also constitutes a rule which delivers the same output for the same input and initial states. It is therefore preferred to distinguish between energy management approaches in which a model of the storage units is necessary and energy management approaches that do not require any model. Even a simplified consideration of the characteristics of the storage units in the energy management strategy such as a constant efficiency factor is considered as a storage model. Energy management strategies that do not employ any storage model, may apply models for other processes, such as cost models for generators and market models.

Optimization strategies can be formulated independent of storage models, which implies that the objective function does not include any parameters related to the characteristics of the storage units. On the other hand, if a storage model is available, it can be considered in the objective function in order to minimize, for instance, the power losses in the energy storage. In this respect the performance of optimization strategies substantially depends on the accuracy of the model. The optimization strategy usually involves the part of the energy management that concerns the operating cost, but several additional practical functions, such as the control of a cooling circuit or the activation of a safety mode, also concern the energy management independent of the optimization goals.

In the *frequency decoupling* approach, the load of the combined storage is divided into a high dynamic part that the flywheels should share and a low dynamic part that the batteries should share. The frequency decoupling is usually realised through a low pass filter, which can be tuned without considering any storage model. Nevertheless, if the low pass filter is tuned with the aid of storage models, frequency decoupling can be classified into the model-based energy management strategies. Similarly, if the filter parameters are adjusted based on an optimization algorithm, frequency decoupling can be classified as an optimization-based strategy.

Although the current investigation concerns the energy management of stationary systems, energy management approaches suggested in vehicular systems are also screened for its potential in stationary applications. Briat, et al. (2007) investigate the integration of a battery-flywheel storage into a heavy-duty electric vehicle using simulations as well as a test bench. The power split between the battery and the flywheel is dealt with a state machine that determines the current of the electric machine driving the flywheel using only the reference traction current and the actual flywheel speed. Therefore, the energy management can be implemented in the test bench without the need of a storage model.

To reduce fuel consumption and CO_2 emissions, the hybridization of a diesel locomotive through the integration of a battery-flywheel energy storage system is investigated by Jaafar et al. (2009). In order to split the power between the battery and the flywheel, a pure frequency decoupling approach with a low pass filter as well as a state machine that adjusts the output of the low pass filter according to certain criteria are suggested. The combination of frequency decoupling with a state machine apparently improves several performance indicators.

The frequency decoupling approach is also applied in a battery-flywheel storage system which is intended to provide frequency regulation services to the electricity grid (Dambone Sessa, et al., 2018). The frequency decoupling is realised through a low pass filter tuned at a certain cutoff frequency. The study concludes that the combination of batteries and flywheels under the frequency decoupling strategy extends the useful life of the lithium-ion cells by more than 20 % compared to battery-only systems.

A frequency decoupling approach with two major improvements was demonstrated in a prototype microgrid built in Baoding, Hebei Province, China (Zhao, et al., 2018). The microgrid combines a lithium-ion battery with an energy capacity of 200 kWh, a flywheel storage with an energy capacity of 1.5 kWh and a nominal power of 100 kW, a diesel generator with a nominal power of 100 kW and photovoltaic modules with an installed power of 200 kW. The first improvement is a state machine which ensures that no power exchange between the flywheel and the battery storage occurs. The second improvement is that the cutoff frequency of the low pass filter, which is responsible for the power split, is adjusted according to the state of charge of the battery. The improved algorithm is tested in the microgrid justifying that no energy exchange between the flywheel and the battery occurs. Furthermore, it is reasonably claimed that the elimination of the power exchange between flywheel and battery leads to an extended battery service life, since the battery charge throughput is reduced.

Ding et al. (2019) simulated a battery-flywheel storage system which compensates for the deviation of the photovoltaic generation from the actual consumption in a DC microgrid. The resulting load of the combined storage is divided into a flywheel share and a battery share using a low pass filter. Subsequently, fuzzy logic controllers are used to correct the power reference of the storage units according to their actual state of charge. Finally, state machines are developed for both the flywheel and the battery to address cases that are not covered by the fuzzy logic controllers. According to the control structure suggested in Ding et al. (2019), no storage model is required to implement the energy management.

Dhand & Pullen (2015) simulated an electric vehicle which combines a battery with a flywheel storage. The flywheel is not electrically coupled in the vehicle powertrain but mechanically with a continuously variable transmission. In this respect the flywheel gains the bulk of its energy through regenerative braking. The power split between the battery and the flywheel is addressed though dynamic programming, where the optimization goal is to minimize the charge flow through the battery. Thus, not only the battery load throughout a driving cycle is reduced but also the cyclic degradation of the battery is decreased. To implement the dynamic programming algorithm, the battery state of charge and the flywheel state of energy should be predicted, therefore, storage models are required. The study concludes that, under intense driving cycles, the combination of the flywheel and the battery leads to a significant reduction in the peak battery current and an increase in the overall vehicle efficiency compared to battery-only vehicles.

Rigo-Mariani et al. (2016) address the power split between lithium-ion batteries and high-speed flywheels in a microgrid powered by photovoltaics using optimization algorithms that solve the day-ahead scheduling problem. Two separate formulation of the optimization problem were investigated through simulations; the first minimizes the energy conversion losses in the storage units, whereas the second additionally minimizes the battery degradation, hence resulting in a multicriteria optimization problem. In both cases a storage model is required. A drawback of the optimization algorithms applied to solve the day-ahead problem is the long computation time, which lies in the range of hours.

Böhm et al. (2019) discuss a power distribution algorithm that maximizes the efficiency of a hybrid storage which is composed of a high-speed flywheel rated at 60 kW and 3.6 kWh and a redox flow battery rated at 40 kW and 15 kWh. The hybrid system is intended for ancillary services in electrical grids, such as the compensation of reactive power. In order to determine the power split that maximises the efficiency of the combined storage system, the power losses of the individual storage units are modelled and used to derive the efficiency map of the combined system.

Hou et al. (2021) simulated a battery-flywheel storage system which is intended to mitigate load fluctuations in shipboard microgrids, since the load fluctuations caused by the propulsion system in conjunction with the encountered waves set challenges to shipboard microgrids. For the power split between the battery and the flywheel, a model predictive control that minimizes the total losses of the combined storage system while compensating for the load fluctuations is suggested. Therefore, both the flywheel and the battery losses are modelled as a function of load and state of charge.

The attempt to review and classify energy management approaches for battery-flywheel storages according to the use of storage models concludes with the overview presented in Table 2.2. Energy management strategies that do not require any storage model are further divided into those using a state machine, those using frequency decoupling and those using fuzzy logic. Similarly, the energy management strategies that require a storage model are divided into those minimizing the total energy conversion losses of the hybrid system and those that additionally consider the battery degradation in the objective function. Obviously, the works are not strictly classified because some research articles investigated a combination of energy management approaches. For instance, Jaafar et al. (2009) evaluated the performance of frequency decoupling with and without a state machine. Further, Rigo-Mariani et al. (2016) investigated several formulations of the optimization problem. However, it is observed that when a storage model is available, the researchers tend to investigate energy management strategies that aim to minimize the energy conversion losses of the storage system. The publications summarized in Table 2.2 are only representative; there several other publications that could be classified into the categories of Table 2.2 as well as several other energy management approaches.

Table 2.2 Classification of energy management strategies for battery-flywheel storage systems according to the need of storage model

No storage model needed			**Storage model needed**	
State machine	**Frequency decoupling**	**Fuzzy logic**	**Loss minimization**	**Loss and battery degradation minimization**
Briat et al. (2007)	Jaafar et al. (2009)	Ding et al. (2019)	Rigo-Mariani et al. (2016)	Dhand & Pullen (2015)
Jaafar et al. (2009)	Dambone Sessa et al. (2018)		Böhm et al. (2019)	Rigo-Mariani et al. (2016)
Zhao et al. (2018)	Zhao et al. (2018)		Hou et al. (2021)	
Ding et al. (2019)	Ding et al. (2019)			

2.4 Related Work

A large number of scientific works have investigated the energy management of microgrids with energy storages over the past decade (Weitzel & Glock, 2018). According to the works reviewed in the present investigation, the first works dealing with the energy management of battery-flywheel storages appeared in the field of vehicular systems. However, the growing penetration of renewable energies in electrical grids, made stationary storages that are able to compensate for the intermittencies of renewable power generation an interesting approach. Elaborate energy management strategies for combined storage systems are reasonable due to the additional degrees of freedom compared to systems with a single storage technology. However, the current investigation does not focus only on the energy management but also on the sizing and the economic assessment of combined storage systems. Therefore, a brief review of scientific articles that consider economic aspects of stationary battery-flywheel storage systems beyond the energy management is worthwhile.

Prodromidis & Coutelieris (2012) investigated a battery-flywheel energy storage that is able to support the autonomous power system of a typical household with a yearly consumption of nearly 7.8 GWh in the island of Naxos, Greece. A flywheel of 10 kW is combined with several variants of lead acid batteries to buffer the excess energy generated by the photovoltaics and the small wind turbines integrated into the autonomous power grid of the household. The simulations conducted for six variants of battery-flywheel and battery-only systems show that although the capital cost of the combined systems is higher than that of the battery-only systems, the resulting net present cost is comparable. Furthermore, some of the combined system variants led to a lower levelized cost of energy than the battery-only systems.

An envisaged hybrid photovoltaic-diesel system with a power capacity of 2.2 GW able to cover the power demand of the city of Makkah, Saudi Arabia, is equipped with a hybrid battery-flywheel storage which is intended to store the excess energy (Ramli, et al., 2015). The investigation considers a flywheel of the type PowerStore-500 together with flooded deep cycle lead-acid batteries. Several variants of the envisaged power system are sized through a software program for the given load and operating conditions with the aim of optimizing the net present cost. The results show that the variants with the hybrid storage reduce the CO_2 emissions, the levelized cost of energy and the net present cost compared to a pure photovoltaic-diesel system.

Wandelt et al. (2015) compare pure flywheel and pure battery storage systems which are intended to provide FCR in the power grid of continental Europe. Assuming that the storage system cannot participate in the energy market of its own, in order to keep the storage size low, a combination with a flexible load such as an industrial plant is suggested. The industrial plant should therefore be able to regulate its power consumption when the storage system reaches its energy state limits. The article claims that the business case of FCR leads to positive net present values either with batteries or flywheels. Moreover, it is claimed that the flywheel system has a lower net present value than the battery system when a service life over twelve years is considered, as the battery should be in the meantime replaced due to its advanced degradation.

Weitzel et al. (2018, REMOO) simulated a hybrid flyhweel-battery storage for a residential microgrid. The hybrid storage should be able to compensate for the difference betweeen generation and consumption in the microgrid and at the same time provide the service of FCR. The power split between the battery and the flywheel is dealt with a low pass filter which is tuned at a certain frequency. Additionaly, a dedicated controller for the energy state of the flywheel storage is used. The study explores the sizing of the hybrid storage system through a genetic algorithm as well as a lion optimization algorithm with the goal to minimize the yearly cost. The cyclic degradation of the battery is also considered in the yearly cost by using the estimated acquistion cost of lithium-ion batteries. Both algorithms converge to hybrid systems with comparable yearly costs, however, with a big discipancy in the size of the flywheel storage. The article concludes that an optimally sized hybrid system can achieve a service life of eight years at a lower yearly cost than an optimally sized battery-only system.

Ayodele et al. (2020) investigate the combination of lead acid batteries with a flywheel in a photovoltaic powered fishery and poultry farm. The flywheel is intended to limit the high starting currents of the induction machines that pump the required water in the facility, which would otherwise lead to high currents drawn from the lead acid batteries accelerating their degradation. The study describes an iterative sizing algorithm that determines the optimal number of lead acid batteries and photovoltaic panels. It is claimed that the limitation of the starting current for the pumps due to the flywheel integration leads to a reduction in the required number of batteries and photovoltaic panels compared to systems that have only batteries. Furthermore, the flywheel integration leads to an extension of the battery lifetime by 2 years and a reduction in the total cost of ownership by 36 % for a time span of 10 years.

Barelli et al. (2021) simulated a wind farm coupled with a battery-flywheel storage which is intended to mitigate the inherent intermittences of wind power generation. The study concludes that the levelized cost of energy of a wind farm that includes a hybrid storage with cells that have lithium nickel manganese cobalt oxides in the cathode is lower than that of a wind farm without energy storage units, provided that the hybrid storage additionally offers the so-called fast reserve service to the Italian power grid.

2.5 Differentiation from Related Work

Although the present work is influenced by related works in the field of energy storage systems, it addresses aspects that have not been investigated in the works reviewed as far. Therefore, it is worthwhile to highlight the contributions of this work compared to related works and briefly explain the reasons for the methodology used.

Schneider (2019) modelled the power losses of the flywheel prototype SWIVT290, however, the power losses were not expressed as a function of the stator current and stator frequency of the electric machine. Although Schneider (2019) presents an analytical loss model of the electric machine and validates it with measurements, the measurements are not used to identify the parameters of an equivalent circuit of the electric machine. An equivalent circuit is worthwhile as it leads to a relatively simple loss function, which facilitates a closed-form solution of the minimization problem concerning the total losses of the battery-flywheel system.

Sizing of battery storage systems for grid balancing services has been discussed in the literature, for instance in Oudalov et al. (2007) and Zeh et al. (2016). The sizing of hybrid storage systems aimed for power smoothing in wind farms was addressed by Zhao et al. (2015), where a spectral decomposition of the imbalance power is suggested in order to determine the energy and power capacity of the storage units. Moreover, the sizing of hybrid storages for peak shaving in industrial context using a generic energy storage model and applying a linear optimization algorithm was investigated by Emde et al. (2020).

Karrari (2021) discusses the collective sizing of high power and high energy density storages, which are intended for power smoothing in low voltage distribution grids. The approach followed in Karrari (2021) includes the derivation of a representative load profile by identifying reoccurring patterns and the subsequent split of the load between the storages using a low pass filter.

Using frequency decoupling to size the combined storage system as suggested by Zhao et al. (2015) and Karrari (2021), implies that frequency decoupling is also used to split the power in operation, which results in the inflexibility that sizing and energy management cannot be dealt independently. Furthermore, despite the fact that the cyclic degradation of lithium-ion batteries is considered in the sizing algorithm proposed by Karrari (2021), the service life of the combined system in conjunction with the calendrical degradation of lithium-ion cells was not addressed. It can be concluded that although some scientific works discuss the sizing of battery-flywheel storage systems, there is little work done in particular for the sizing of flywheels combined with lithium-ion batteries for grid balancing services, which should be anyway addressed in order to pursue the goals of the current investigation.

Although a great deal of energy management strategies has already been suggested for energy storage systems in general, energy management strategies specific for battery-flywheel storage systems are less often investigated. A disadvantage of the frequency decoupling strategy, which is suggested in four of the works listed in Table 2.2, is that if the direction of the load changes, the delay of the low dynamic power profile leads to a mutual energy exchange between the storage units, unless additional measures are taken such as those suggested in Zhao et al. (2018). In other words, power is exchanged between the storage units without contributing to cover the load. Mutual energy exchange between the storages is inexpedient as it causes energy conversion losses without any obvious benefit and should therefore be avoided.

The suggested energy management strategies for battery-flywheel storage systems summarized in Table 2.2 are limited in simulations, with the exception of Briat et al. (2007) and Zhao et al. (2018). The current investigation aims not only to simulate the energy management but also to implement it in a real controller and test it with the aid of a prototype combined storage. Four of the works listed in Table 2.2 apply optimization algorithms to minimize the energy losses, from which three employ computationally intensive algorithms, such as model predictive control, dynamic programming and mixed integer linear programming. However, optimization algorithms with low computational cost that facilitate the implementation in controllers with moderate resources are rarely investigated. A similar observation is also made by Weitzel & Glock (2018) who conclude that it is worthwhile to investigate the properties of optimal policies by deriving closed-form solutions of the optimization problem.

Concerning the formulation of the optimization problem; although Hou et al. (2021) use elaborate models for the energy losses of the storage units in the objective function of the model predictive control, they neglect the losses in the power converters required to integrate the storage units into the shipboard microgrid. The present investigation, in contrast, considers the power converter losses in the objective function.

Battery degradation as a cost in the optimization problem was addressed by Rigo-Mariani et al. (2016) for a battery-flywheel storage as well as by Weitzel et al. (2018, pp. 638-654) for a battery-only system. Weitzel et al. (2018, pp. 638-654) also include a literature review in the consideration of battery degradation costs in the energy management. The motivation behind considering battery degradation as a cost in the objective function is to extend the battery service life in applications where the battery load is flexible.

Although the consideration of the battery degradation in the energy management can extend the battery service life, it has a low importance when the battery load is less flexible or the battery is sized so that it can withstand the expected load throughout its calendrical lifetime. The current investigation aims to size the battery such that it is operational throughout the target service life under the given load profile. In this respect the target service life for the combined storage system roughly corresponds to the typical calendrical lifetime (15 years) of a battery. Extending the service life of the battery through dedicated energy management over its nominal calendrical lifetime has low practical importance, as it comes at the cost of high failure rates. In contrast, the usual practice is to replace critical electrical equipment when it approaches the end of its lifespan in order to keep the failure rates low. Furthermore, the consideration of the battery degradation in the objective function does not facilitate the validation of the optimization algorithm in the real system. Although the energy losses can be estimated by measurements on a single operating cycle, the estimation of the battery degradation requires measurements over repetitive operating cycles that are outside the scope of the current investigation. For an unpredictable load such that resulting from FCR, a simple strategy to minimize the battery degradation is to operate the flywheel at the maximum feasible power share.

Zakeri & Syri (2015) assess the life cycle cost of various energy storage technologies. A similar more recent study conducted by Mongird et al. (2020) evaluates the cost of various storage technologies with special focus in electrochemical storages. The results of both studies can be used as a reference in order to obtain a quick overview of the cost linked to the acquisition and operation of different energy storage technologies. Whereas Zakeri & Syri (2015) estimate the operation and maintenance cost for the applications of bulk energy storage, transmission and distribution services and frequency regulation, Mongird et al. (2020) use a certain annual energy output in order to estimate the operation and maintenance cost. Both studies neither refer to energy storage models nor to a strictly specified load profile in order to calculate the energy conversion losses that are necessary to estimate the operation and maintenance cost.

Weitzel et al. (2018, REMOO) investigate the optimal sizing of a battery-flywheel storage for a residential microgrid, which, among other things, is intended to provide FCR. The article claims that an optimally sized hybrid system achieves a lower yearly cost than an optimally sized battery-only system. However, only the investment cost of the storage units was considered in the objective function and not the operating cost, although flywheel storages have relatively high no-load losses that result in a considerable operating cost. Furthermore, fixed cost factors were assumed for the investment cost of the storage units and no sensitivity analyses were performed.

Only one of the reviewed articles investigates battery-flywheel storages for the provision of grid balancing services in particular (Dambone Sessa, et al., 2018). Although Dambone Sessa et al. (2018) highlight the benefits of extended battery service life through the integration of flywheels, the cost of the combined storage system compared to the battery-only system is not discussed. In this respect the option to oversize the battery storage in order to achieve a lower cyclic degradation than that achieved with the flywheel is also not investigated. However, in order to evaluate the value proposition of combined storage systems, their cost should be compared with that of single-technology systems. Ayodele et al. (2020) address the sizing of a battery-flywheel system by an iterative algorithm that finds the optimal number of lead acid batteries that minimizes a set of performance indicators including the total cost of ownership. However, compared to Ayodele et al. (2020), the current investigation concerns lithium-ion cells that have substantially different degradation characteristics. Furthermore, the load resulting from FCR is much different than that of the power peaks in the combined poultry and fishery plant considered in Ayodele et al. (2020).

Although some of the reviewed works address the sizing, the energy management as well as the cost of battery-flywheel systems for various use cases, the problem of how to economically size and operate a battery-flywheel system for grid balancing services in particular has inadequately been investigated. Furthermore, the question of whether a battery-flywheel combination leads to a lower total cost of ownership compared to a battery-only system has rarely been addressed. Therefore, among other things, the present work focuses on the investigation of the economical sizing and operation of battery-flywheel storages compared to battery-only systems

3. Modelling

The aspects and the corresponding level of detail to be modelled depend on the investigation goals. In other words, the investigation goals should be clear before deciding on the physical phenomena that should be modelled. The operating cost has a decisive role in the assessment of the cost-effectiveness of energy storage systems. As the operating cost substantially depends on the energy conversion efficiency, the modelling focuses on the energy losses in the storage units. On the other hand, aspects such as, mechanical dynamics of flywheels and chemical reactions in lithium-ion cells, are out of scope, since they only have a minor effect on the operating cost.

3.1 Kinetic Energy Storage

The kinetic energy storage ,or equivalently, flywheel storage to be modelled concerns the prototypes ETA290 (Quurck, et al., 2017) and SWIVT290 (Schneider & Rinderknecht, 2019) developed at the Technical University of Darmstadt, the main technical data of which are summarized in Table A.9 and Table A.8 respectively. The modelling focuses on the operating cost and consequently on the energy conversion losses. Since the electric machine that drives the flywheel dominates the energy conversion losses, the investigation focuses on the modelling of the electric machine. The losses in the AMBs and the vacuum pumps are also considered, however not modelled.

Useful energy and energy state

The kinetic energy E_{fw} stored in a flywheel that has a moment of inertia Θ with respect to its axis of rotation and rotates with an angular (mechanical) frequency ω_{m} is

$$E_{\mathrm{fw}} = \frac{1}{2}\Theta\omega_{\mathrm{m}}^2.$$

Flywheels are designed for a maximum operating angular frequency (speed) $\omega_{\mathrm{m,max}}$, among others things, due to the limited material strength at high centrifugal stresses. As the stored energy increases quadratically with speed, the available energy in the low speed range is often insignificant and therefore a minimum operating speed $\omega_{\mathrm{m,min}}$ is set. Consequently, the useful energy of flywheel storages corresponds to

$$E_{\mathrm{fw,u}} = \frac{1}{2}\Theta\left(\omega_{\mathrm{m,max}}^2 - \omega_{\mathrm{m,min}}^2\right).$$

In order to obtain a dimensionless quantity for the energy stored with respect to the useful energy of flywheel storages, the flywheel *energy state* is defined as

$$w_{\mathrm{fw}}(\omega_{\mathrm{m}}) = \frac{\omega_{\mathrm{m}}^2 - \omega_{\mathrm{m,min}}^2}{\omega_{\mathrm{m,max}}^2 - \omega_{\mathrm{m,min}}^2}, \qquad \omega_{\mathrm{m,min}} \leq \omega_{\mathrm{m}} \leq \omega_{\mathrm{m,max}}.$$

At minimum speed the flywheel energy state is zero, whereas at maximum speed the energy state corresponds to unity. The energy state is undefined outside of the operating speed range. If the energy state is given, the operating speed can be calculated using the inverse function

$$\omega_{\mathrm{m}}(w_{\mathrm{fw}}) = \sqrt{\omega_{\mathrm{m,min}}^2 + w_{\mathrm{fw}}\left(\omega_{\mathrm{m,max}}^2 - \omega_{\mathrm{m,min}}^2\right)}. \tag{3.1}$$

According to Eq. (3.1), the speed corresponding to the middle of the energy state range is the quadratic mean of the minimum and the maximum speed

$$\omega_{\mathrm{m,m}} = \sqrt{\frac{\omega_{\mathrm{m,max}}^2 + \omega_{\mathrm{m,min}}^2}{2}}.$$

Figure 3.1 qualitatively depicts the energy stored in a flywheel storage over the flywheel speed. The useful energy resulting from the minimum and the maximum operating speed and the speed corresponding to the middle of the energy state range are also annotated.

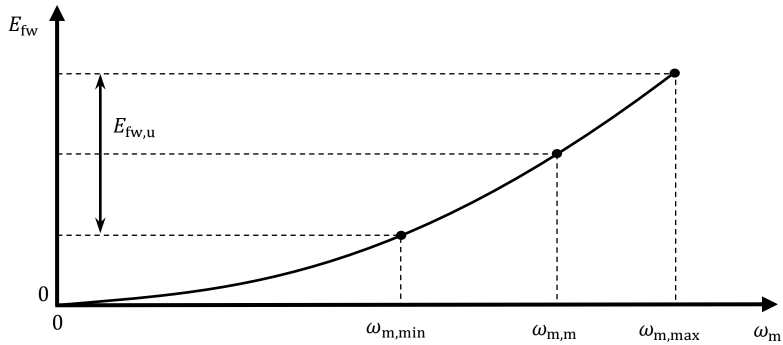

Figure 3.1 Energy stored in a flywheel as a function of the flywheel's angular frequency. The useful energy depends on the minimum and the maximum operating speed. The quadratic mean of the minimum and the maximum speed $\omega_{\mathrm{m,m}}$ corresponds to the middle of the useful energy range.

Permanent Magnet Synchronous Machine

Power losses in electric machines can be divided into electrical and mechanical losses. Mechanical losses include friction and windage losses. Electrical losses are typically divided into copper and iron losses. Since bearing friction losses are eliminated through magnetic suspension and windage losses are significantly reduced due to vacuum, the ratio of electrical to mechanical losses is high enough to neglect the mechanical losses in the investigated flywheel prototypes. Therefore, the investigation focuses on the modelling of the iron and copper losses of the electric machine.

Equivalent Circuit

The equivalent circuit of the Permanent Magnet Synchronous Machine (PMSM) driving the flywheel protypes is illustrated in Figure 3.2. The stator windings, which are connected to a common star point (wye connection), are modelled through the resistance R_{s}, the stray inductance $L_{\sigma\mathrm{s}}$ and the main inductance L_{h}. A cylindrical rotor with a negligible saliency is considered, so that the main inductance remains constant independent of the rotor orientation with respect to the stator. The underlined notation for current and voltage denotes a three-phase space vector such that

$$\underline{x} = x_{\mathrm{L1}}(t) + \underline{a}x_{\mathrm{L2}}(t) + \underline{a}^2 x_{\mathrm{L3}}(t),$$

where

$$\underline{a} = e^{\mathrm{j}2\pi/3} = -\frac{1}{2} + \mathrm{j}\frac{\sqrt{3}}{2},$$

and the variables x_{L1}, x_{L2}, x_{L3} represent time-varying quantities related to the phases L1, L2 and L3 (Binder, 2017, pp. 1013-1021). The space vector of the three-phase voltage across the star-connected stator windings of the electric machine is $\underline{U}_s$, whereas the space vector of the three-phase current in the stator windings is $\underline{I}_s$.

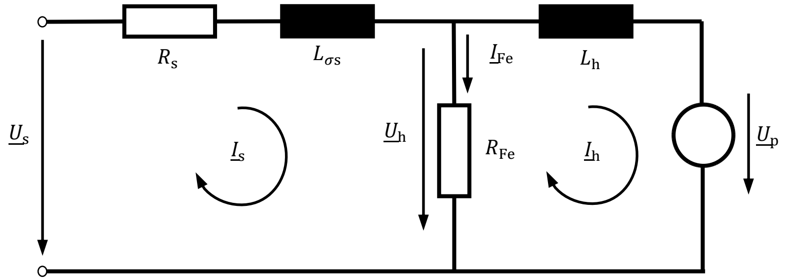

Figure 3.2 Equivalent circuit of the permanent magnet synchronous machine driving the flywheel prototypes. The iron resistance branch is intended for the estimation of the iron losses.

The operation of the PMSM is preferably described in a rotor-fixed reference frame. The direct axis (d-axis) of the rotor-fixed reference frame aligns with the direction of the maximum magnetic flux density of the rotor's magnetic field, whereas the quadrature axis (q-axis) aligns with the direction of the minimum flux density of the rotor's magnetic field. Stator currents and voltages can be expressed with respect to the dq reference frame and can therefore be decomposed into a direct and quadrature component such that

$$\underline{U} = U_d + jU_q,$$

$$\underline{I} = I_d + jI_q.$$

The electrical angular frequency ω_e of the stator voltage is linked to the mechanical angular frequency ω_m of the rotor. For a single rotor revolution, the stator voltage changes direction as many times as the number of pole pairs p of the electric machine, hence

$$\omega_e = p\,\omega_m. \tag{3.2}$$

The voltage induced in the stator windings by the rotating magnetic field generated by the permanent magnets is

$$\underline{U}_p = j\omega_e \Psi_p, \tag{3.3}$$

where Ψ_p is the flux linkage of the stator windings per pole and phase due to the field of the permanent magnets. The main voltage $\underline{U}_h$ of the stator windings at steady state results from the superposition of the voltages induced by the magnetic fields generated by the stator current and the permanent magnets, that is

$$\underline{U}_h = j\omega_e L_h \underline{I}_h + \underline{U}_p. \tag{3.4}$$

Due to the magnetic coupling between the stator phases, the main inductance L_h is higher than the measured self-inductance per phase L_{ph}, that is L_h=3/2·L_{ph} (Binder, 2017, pp. 182-184). The self-inductance L_{ph} should be measured between the terminals of a single phase (access to the star point is required) under exclusive AC excitation of this phase.

The magnetic flux density and therefore the flux linkage Ψ_p caused by the permanent magnets depend on the temperature. Equation (3.5) quantifies the effect of the permanent magnet temperature ϑ_{PM} on the flux linkage using the temperature coefficient of remanence α_{PM} and the flux linkage at 20 °C, that is $\Psi_{p,20}$. The permanent magnets have a negative temperature coefficient, which means that the magnetic flux density decreases with increasing temperature.

$$\Psi_\mathrm{p} = \Psi_\mathrm{p,20}[1 + \alpha_\mathrm{PM}(\vartheta_\mathrm{PM} - 20°\mathrm{C})] \tag{3.5}$$

The mesh analysis of the equivalent circuit of the PMSM depicted in Figure 3.2 results in the system of equations

$$\begin{aligned} &\underline{U}_s - R_s\underline{I}_s - \mathrm{j}\omega_\mathrm{e}L_{\sigma\mathrm{h}}\underline{I}_s - R_\mathrm{Fe}\left(\underline{I}_s - \underline{I}_\mathrm{h}\right) = 0, \\ &-\mathrm{j}\omega_\mathrm{e}L_\mathrm{h}\underline{I}_\mathrm{h} - \mathrm{j}\omega_\mathrm{e}\Psi_\mathrm{p} + R_\mathrm{Fe}\left(\underline{I}_s - \underline{I}_\mathrm{h}\right) = 0. \end{aligned}$$

Neglecting the stray inductance $L_{\sigma s}$, the system of equations is solved for; the main current $\underline{I}_h$ as a function of the stator current $\underline{I}_s$

$$\underline{I}_\mathrm{h} = \frac{R_\mathrm{Fe}\underline{I}_s - \mathrm{j}\omega_\mathrm{e}\Psi_\mathrm{p}}{\mathrm{j}\omega_\mathrm{e}L_\mathrm{h} + R_\mathrm{Fe}}, \tag{3.6}$$

the stator current $\underline{I}_s$ as function of the stator voltage $\underline{U}_s$

$$\underline{I}_s = \frac{(\mathrm{j}\omega_\mathrm{e}L_\mathrm{h} + R_\mathrm{Fe})\underline{U}_s - \mathrm{j}\omega_\mathrm{e}\Psi_\mathrm{p}R_\mathrm{Fe}}{\mathrm{j}\omega_\mathrm{e}L_\mathrm{h}(R_\mathrm{s} + R_\mathrm{Fe}) + R_\mathrm{Fe}R_\mathrm{s}}, \tag{3.7}$$

and the iron branch current as a function of the stator current

$$\underline{I}_\mathrm{Fe} = \underline{I}_s - \underline{I}_\mathrm{h} = \frac{\mathrm{j}\omega_\mathrm{e}\left(L_\mathrm{h}\underline{I}_s + \Psi_\mathrm{p}\right)}{\mathrm{j}\omega_\mathrm{e}L_\mathrm{h} + R_\mathrm{Fe}}. \tag{3.8}$$

Rearranging Eq.(3.7), the stator voltage is expressed as a function of the stator current

$$\underline{U}_s = \left(R_\mathrm{s} + \frac{\mathrm{j}\omega_\mathrm{e}L_\mathrm{h}R_\mathrm{Fe}}{\mathrm{j}\omega_\mathrm{e}L_\mathrm{h} + R_\mathrm{Fe}}\right)\underline{I}_s + \frac{\mathrm{j}\omega_\mathrm{e}\Psi_\mathrm{p}R_\mathrm{Fe}}{\mathrm{j}\omega_\mathrm{e}L_\mathrm{h} + R_\mathrm{Fe}}. \tag{3.9}$$

Copper losses

Windings in electric machines are usually made of copper due to its good conducting properties. Thus, conduction losses in the windings of electric machines are often referred to as copper losses. Copper losses are proportional to the conductor resistance as well as to the square of the conductor current. The copper losses in three-phase windings with the phase resistance R_s and the space vector current $\underline{I}_s$ are

$$P_\mathrm{Cu} = \frac{3}{2}R_\mathrm{s}\left|\underline{I}_s\right|^2. \tag{3.10}$$

Manufacturers of electric machines typically specify the DC resistance of the stator windings at room temperature, although the winding resistance may be considerable higher at operating temperature. Equation (3.11) expresses the phase resistance R_s as a linear function of the winding temperature ϑ_{cu}, where α_{Cu} is the temperature coefficient of copper and $R_{s,20}$ is the phase DC resistance at 20 °C. The so-called skin effect that leads to increased conductor resistance at high electrical frequencies is neglected due to the relatively small radius of the windings.

$$R_\mathrm{s} = R_\mathrm{s,20}[1 + \alpha_\mathrm{Cu}(\vartheta_\mathrm{Cu} - 20°\mathrm{C})] \tag{3.11}$$

The temperature dependence of the winding resistance is significant for the thermal stability of electric machines. For instance, for the typical temperature coefficient of copper α_{Cu}=0.004 K^{-1}, an increase in the winding temperature from 20 °C to 80 °C leads to an increase of 24 % in the phase resistance and therefore to the copper losses for the same current.

Iron losses

A time-varying magnetic field in an iron core induces an electric field. The induced electric field causes the so-called *eddy currents*, the magnetic field of which opposes the initial magnetic field. Eddy currents are proportional to the rate of change of the magnetic field. In addition to eddy currents, a time-varying magnetic field in an iron core causes hysteresis losses. Hysteresis losses highly depend on the medium and signify that only a part of the energy stored in the medium's magnetic field can be recovered. Furthermore, hysteresis losses depend on the magnitude and the frequency of the time-varying magnetic field. As both eddy current and hysteresis losses, which make up iron losses, increase with electrical frequency, a high number of pole pairs is usually avoided in high-speed electric machines.

Since the magnetic field distribution and the material properties of an iron volume can significantly vary, numerical methods are often applied to calculate the iron losses in electric machines. The iron resistance R_{Fe} in the equivalent circuit presented in Figure 3.2 constitutes a simplification in order to model the iron losses. There is no galvanic connection between the stator windings and the iron resistance, although it is counterintuitive to the equivalent circuit presented in Figure 3.2.

The main voltage $\underline{U}_{\mathrm{h}}$ across the stator windings is induced by the magnetic field resulting from the superposition of the stator and the rotor magnetic fields in the air gap. The magnitude of the main voltage is therefore proportional to the rate of change and the intensity of the air gap magnetic field. Since eddy current losses are proportional to both the square of the rate of change and the square of the intensity of the magnetic field, the iron losses approximate

$$P_{\mathrm{Fe}} = \frac{3}{2}\frac{\left|\underline{U}_{\mathrm{h}}\right|^2}{R_{\mathrm{Fe}}}. \tag{3.12}$$

To develop the model of iron losses further, it is distinguished between eddy current and hysteresis losses. Therefore, the equivalent iron resistance R_{Fe} is divided into a constant part R_{ed} that corresponds to the eddy current losses and a frequency-dependent part $R_{\mathrm{hy}}\, f_{\mathrm{e}}/f_{\mathrm{e,N}}$ that corresponds to the hysteresis losses

$$\frac{1}{R_{\mathrm{Fe}}} = \frac{1}{R_{\mathrm{ed}}} + \frac{1}{R_{\mathrm{hy}}\, f_{\mathrm{e}}/f_{\mathrm{e,N}}}, \quad f_{\mathrm{e}} > 0, \tag{3.13}$$

(Schröder & Kennel, 2021, pp. 583-587). The frequency-dependent term is normalized by the nominal electrical frequency $f_{\mathrm{e,N}}$ of the electric machine. Consequently, the ratio of R_{ed} to R_{hy} corresponds to the ratio of hysteresis to eddy current losses at nominal frequency. Both R_{ed} and R_{hy} can be identified by experimentally estimating the electromagnetic torque at approximate no-load (Fernández-Bernal, et al., 2001). Alternatively, R_{ed} and R_{hy} can be experimentally estimated through the variation of the direct current component of the stator current, provided that the torque remains constant (Urasaki, et al., 2003).

Substituting $\underline{U}_{\mathrm{h}}$ and R_{Fe} from Eq. (3.4) and Eq. (3.13) respectively into Eq. (3.12), the iron losses are expressed as a quadratic function of the electrical frequency, in which the hysteresis losses correspond to the linear term and the eddy current losses to the quadratic term. The ratio of eddy current to hysteresis losses substantially depends on the lamination of the stator iron stack in such a way that the thinner the lamination is, the lower the eddy current losses are. At low frequencies the frequency-dependent term $R_{hy} f_e/f_{e,N}$ is comparatively low, so that R_{Fe} is approximately proportional to the electrical frequency. Although the term $R_{hy} f_e/f_{e,N}$ and therefore R_{Fe} decrease with decreasing frequency, the current divider between the branch of the iron resistance and the branch of the main inductance in the equivalent circuit presented in Figure 3.2 is not significantly affected, as the main reactance $\omega_e L_h$ also decreases with decreasing frequency. In other words, the comparatively low iron resistance at low frequencies does not lead to a significant increase in the proportion of iron losses to total losses. At zero electrical frequency, the iron resistance is undefined because iron losses are the result of time-varying magnetic fields. At high frequencies the term $(R_{hy} f_e/f_{e,N})^{-1}$ vanishes, so that the iron resistance approaches the constant value R_{ed}. Nevertheless, it is unlikely that the electric machine is able to operate at such high speeds. In conclusion, the iron losses comprise both hysteresis and eddy current losses in the typical operating speed range, in which the ratio of eddy current to hysteresis losses increases with speed.

Electromagnetic Torque and Eddy Current Braking

Neglecting windage and friction losses due to the operation in vacuum and the magnetic levitation implies that only the electromagnetic field exerts forces on the rotor. The torque exerted by the electromagnetic field on the rotor of the PMSM is proportional to the flux linkage of the stator windings with the permanent magnet field and the quadrature component of the main current

$$M_e = \frac{3}{2}\, p\, \Psi_p \operatorname{Im}\{\underline{I}_h\}, \tag{3.14}$$

(Binder, 2017, pp. 651-655). An increase in the flux linkage of the stator windings with the permanent magnet field increases the torque at constant current. Since high currents lead to high power losses and therefore thermal stresses, it is expedient to design the machine for a high flux linkage of the stator windings with the rotor field, which leads to an increased electromagnetic utilisation (Binder, 2017, pp. 215-220).

The varying magnetic field, which results from the relative motion of the rotor's permanent magnets with respect to the stator, induces eddy currents in the stator iron. The eddy currents in turn generate a magnetic field that counters the change of the original field. Since the cause of the varying magnetic field is the relative motion between rotor and stator, as a direct consequence of Lenz's law, the field generated by the induced eddy currents exerts a force opposing the motion (Meschede, 2015). In other words, the magnetic field generated by the rotor-induced eddy currents in the stator exerts a braking torque on the rotor. The resulting braking torque opposes the rotation regardless of whether the machine accelerates in motor mode or decelerates in generator mode. Replacing the main current in Eq. (3.14) with the difference between the stator current and the iron branch current leads to the expression of the electromagnetic torque as the difference between the torque M_s due to the quadrature component of the stator current and the braking torque M_{br}, that is

$$M_e = \frac{3}{2}\, p\, \Psi_p \operatorname{Im}\{\underline{I}_s - \underline{I}_{Fe}\} = \frac{3}{2}\, p\, \Psi_p \operatorname{Im}\{\underline{I}_s\} - \frac{3}{2}\, p\, \Psi_p \operatorname{Im}\{\underline{I}_{Fe}\} = M_s - M_{br}. \tag{3.15}$$

In the case of open circuit at the stator terminals, for instance, if the power supply is interrupted while the rotor spins, as depicted in Figure 3.3, the braking torque due to eddy currents is the only torque exerted on the rotor.

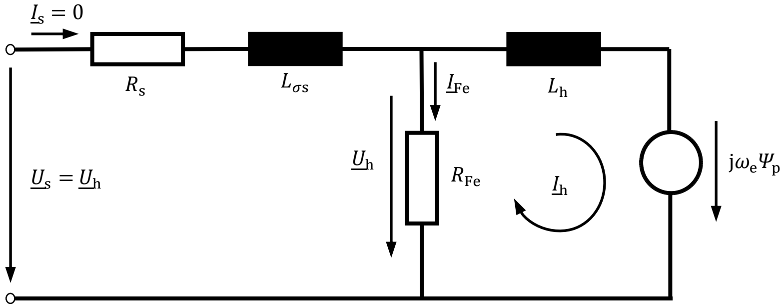

Figure 3.3 Power flow in the case of open circuit ($\underline{I}_s$=0) and spinning rotor ω_e>0. The rotor brakes by inducing eddy currents in the stator. The kinetic energy stored in the flywheel dissipates into the iron resistance R_{Fe}.

The loop that comprises the induced voltage, the main inductance and the iron resistance in Figure 3.3 models the eddy current braking and therefore the dissipation of kinetic energy. The open circuit at the machine terminals implies that the stator windings are irrelevant for the braking, since they cannot generate any magnetic field. However, the magnetic field generated by the eddy currents not only counters the permanent magnet field but also induces the voltage $j\omega_e L_h \underline{I}_h$ in the stator windings. Therefore, the open circuit voltage across the stator windings is

$$\underline{U}_{s,oc} = \frac{R_{Fe}}{j\omega_e L_h + R_{Fe}} j\omega_e \Psi_p$$

and the iron branch current is

$$\underline{I}_{Fe,oc} = \frac{j\omega_e \Psi_p}{j\omega_e L_h + R_{Fe}}.$$

The imaginary part of the iron branch current at open circuit

$$\mathrm{Im}\{\underline{I}_{Fe,oc}\} = \frac{R_{Fe}\omega_e\Psi_p}{(\omega_e L_h)^2 + R_{Fe}^2}$$

causes the braking torque

$$M_{br,oc} = \frac{3}{2}\, p\, \Psi_p \mathrm{Im}\{\underline{I}_{Fe,oc}\} = \frac{3}{2}\, p \frac{R_{Fe}\omega_e\Psi_p^2}{(\omega_e L_h)^2 + R_{Fe}^2}$$

that results in the braking power

$$P_{br,oc} = M_{br,oc}\omega_m = \frac{3}{2} \frac{R_{Fe}\omega_e^2\Psi_p^2}{(\omega_e L_h)^2 + R_{Fe}^2}. \tag{3.16}$$

The same result as the braking power calculated in Eq. (3.16) can be derived by evaluating the power losses in the iron branch

$$P_{Fe,oc} = \frac{3}{2} R_{Fe} \left|\underline{I}_{Fe,oc}\right|^2 = \frac{3}{2} R_{Fe} \frac{(\omega_e\Psi_p)^2}{(\omega_e L_h)^2 + R_{Fe}^2}. \tag{3.17}$$

Equations (3.16) and (3.17) signify that the braking energy dissipates entirely into heat in the stator iron. The eddy current braking is the main reason for no-load losses in flywheels that are driven by PMSMs, when friction and windage losses are negligible due to magnetic levitation and vacuum.

In order to keep the flywheel rotating at constant speed, the braking torque term in Eq. (3.15) should be compensated by such a stator current that the electromagnetic torque M_e equals zero. Therefore, according to Eq. (3.14) the imaginary part of the main current should vanish, that is $\mathrm{Im}\{\underline{I}_h\} = 0$. Substituting the main current defined in Eq. (3.6) into the equation $\mathrm{Im}\{\underline{I}_h\} = 0$ and neglecting the direct current component, the quadrature current component that keeps the flywheel rotating at the electrical speed ω_e is

$$I_{s,q,0} = \frac{\omega_e \Psi_p}{R_{Fe}}. \tag{3.18}$$

Electromechanical power conversion

The apparent power at the terminals of the PMSM with respect to the dq reference frame is

$$S_s = \frac{3}{2} \underline{U}_s \underline{I}_s^*. \tag{3.19}$$

The stator voltage calculated in Eq. (3.9) can be rearranged to

$$\underline{U}_s = \left[R_s + \frac{(\omega_e L_h)^2 R_{Fe} + j\omega_e L_h R_{Fe}^2}{R_{Fe}^2 + (\omega_e L_h)^2}\right] \underline{I}_s + \frac{\omega_e^2 L_h \Psi_p R_{Fe} + j\omega_e \Psi_p R_{Fe}^2}{R_{Fe}^2 + (\omega_e L_h)^2}. \tag{3.20}$$

Substituting the stator voltage defined in Eq. (3.20) into Eq. (3.19) results in

$$\underline{S}_s = \frac{3}{2}\left[R_s + \frac{R_{Fe}(\omega_e L_h)^2 + j\omega_e L_h R_{Fe}^2}{R_{Fe}^2 + (\omega_e L_h)^2}\right] \left|\underline{I}_s\right|^2 + \frac{3}{2} \frac{R_{Fe}\omega_e^2 L_h \Psi_p + j\omega_e \Psi_p R_{Fe}^2}{R_{Fe}^2 + (\omega_e L_h)^2} \underline{I}_s^*.$$

Decomposing the stator current into the quadrature component $I_{s,q}$ and the direct component $I_{s,d}$ yields the real power at the machine terminals

$$P_s = \frac{3}{2}\left[R_s + \frac{R_{Fe}(\omega_e L_h)^2}{R_{Fe}^2 + (\omega_e L_h)^2}\right] \left|\underline{I}_s\right|^2 + \frac{3}{2} \frac{R_{Fe}\omega_e^2 L_h \Psi_p}{R_{Fe}^2 + (\omega_e L_h)^2} I_{s,d} + \frac{3}{2} \frac{\omega_e \Psi_p R_{Fe}^2}{R_{Fe}^2 + (\omega_e L_h)^2} I_{s,q}. \tag{3.21}$$

Although Eq. (3.21) expresses the terminal power as a function of the stator current, an insight into the losses due to the braking torque is missing.

The power losses of the PMSM correspond to the power consumption in the resistances of the equivalent circuit

$$P_L = \frac{3}{2}\left(R_s \left|\underline{I}_s\right|^2 + R_{Fe} \left|\underline{I}_{Fe}\right|^2\right). \tag{3.22}$$

According to Eq. (3.8), the square of the iron branch current magnitude is

$$\left|\underline{I}_{Fe}\right|^2 = \frac{\omega_{el}^2 \left|L_h \underline{I}_s + \Psi_p\right|^2}{R_{Fe}^2 + (\omega_{el} L_h)^2},$$

which can be rearranged into

$$\left|\underline{I}_{Fe}\right|^2 = \omega_e^2 \frac{L_h^2 \left|\underline{I}_s\right|^2 + 2 L_h \Psi_p \mathrm{Re}\{\underline{I}_s\} + \Psi_p^2}{R_{Fe}^2 + (\omega_e L_h)^2},$$

and further into

$$\left|\underline{I}_{\mathrm{Fe}}\right|^2=\frac{(\omega_\mathrm{e}L_\mathrm{h})^2}{R_\mathrm{Fe}^2+(\omega_\mathrm{e}L_\mathrm{h})^2}\left|\underline{I}_\mathrm{s}\right|^2+\frac{2\omega_\mathrm{e}^2L_\mathrm{h}\Psi_\mathrm{p}}{R_\mathrm{Fe}^2+(\omega_\mathrm{e}L_\mathrm{h})^2}I_\mathrm{s,d}+\frac{\left(\omega_\mathrm{e}\Psi_\mathrm{p}\right)^2}{R_\mathrm{Fe}^2+(\omega_\mathrm{e}L_\mathrm{h})^2},\tag{3.23}$$

which when substituted into Eq. (3.22) results in

$$P_\mathrm{L}=\frac{3}{2}R_\mathrm{s}\left|\underline{I}_\mathrm{s}\right|^2+\frac{3}{2}\frac{R_\mathrm{Fe}(\omega_\mathrm{e}L_\mathrm{h})^2}{R_\mathrm{Fe}^2+(\omega_\mathrm{e}L_\mathrm{h})^2}\left|\underline{I}_\mathrm{s}\right|^2+\frac{3}{2}\frac{2R_\mathrm{Fe}\omega_\mathrm{e}^2L_\mathrm{h}\Psi_\mathrm{p}}{R_\mathrm{Fe}^2+(\omega_\mathrm{e}L_\mathrm{h})^2}I_\mathrm{s,d}+\frac{3}{2}\frac{R_\mathrm{Fe}\left(\omega_\mathrm{e}\Psi_\mathrm{p}\right)^2}{R_\mathrm{Fe}^2+(\omega_\mathrm{e}L_\mathrm{h})^2}.\tag{3.24}$$

The first term on the right-hand side of Eq. (3.24) corresponds to the resistive losses in the stator windings, whereas the second term corresponds to the iron losses due to the magnetic field generated by the stator current. The third term corresponds to the iron losses due to the combined effect of the magnetic field generated by the direct current component of the stator windings and the field of the permanent magnets. The fourth term corresponds to the iron losses due to the permanent magnet field. Interestingly, a negative direct current component leads to a negative term in Eq. (3.24) that reduces the power losses. A negative direct current component generates a magnetic field that counters the permanent magnet excitation, so that the superimposed magnetic field in the air gap weakens. Therefore, the operation of PMSMs under negative direct current corresponds to *field weakening*.

The electromechanical power conversion corresponds to the power exchange across the induced voltage $\underline{U}_\mathrm{p}$, that is

$$P_\mathrm{m}=\frac{3}{2}\underline{U}_\mathrm{p}\underline{I}_\mathrm{h}^*=\frac{3}{2}\mathrm{j}\omega_\mathrm{e}\Psi_\mathrm{p}\underline{I}_\mathrm{h}^*=\frac{3}{2}\omega_\mathrm{e}\Psi_\mathrm{p}I_\mathrm{h,q}.\tag{3.25}$$

According to the convention used, electrical power is converted into mechanical power when the machine accelerates though a positive quadrature component of the main current $I_\mathrm{h,q}$, whereas mechanical power is converted into electrical power when the machine decelerates through a negative quadrature component of the main current $I_\mathrm{h,q}$. In the equivalent circuit presented in Figure 3.2, real power can be exchanged only across $\underline{U}_\mathrm{p}$ as well as across the resistances R_s and R_Fe. Thus, considering Eq. (3.22) and Eq. (3.25), an alternative expression for the power at the machine terminals is

$$P_\mathrm{s}=P_\mathrm{m}+P_\mathrm{L}.\tag{3.26}$$

To countercheck that Eq. (3.26) is equivalent to Eq. (3.21), P_m should be expressed as a function of the stator current $\underline{I}_\mathrm{s}$. Rearranging Eq. (3.6) to express the main current as a function of $\underline{I}_\mathrm{s}$ yields

$$\underline{I}_\mathrm{h}=\frac{-\mathrm{j}\omega_\mathrm{e}L_\mathrm{h}R_\mathrm{Fe}\underline{I}_\mathrm{s}+\omega_\mathrm{e}^2L_\mathrm{h}\Psi_\mathrm{p}+R_\mathrm{Fe}^2\underline{I}_\mathrm{s}-\mathrm{j}\omega_\mathrm{e}\Psi_\mathrm{p}R_\mathrm{Fe}}{R_\mathrm{Fe}^2+(\omega_\mathrm{e}L_\mathrm{h})^2},$$

thus, the quadrature component of the main current is

$$I_\mathrm{h,q}=\mathrm{Im}\{\underline{I}_\mathrm{h}\}=\frac{R_\mathrm{Fe}^2I_\mathrm{s,q}-\omega_\mathrm{e}L_\mathrm{h}R_\mathrm{Fe}I_\mathrm{s,d}-\omega_\mathrm{e}\Psi_\mathrm{p}R_\mathrm{Fe}}{R_\mathrm{Fe}^2+(\omega_\mathrm{e}L_\mathrm{h})^2}.\tag{3.27}$$

Replacing $I_\mathrm{h,q}$ defined in Eq. (3.27) into Eq. (3.25) results in

$$P_\mathrm{m}=\frac{3}{2}\omega_\mathrm{e}\Psi_\mathrm{p}I_\mathrm{h,q}=\frac{3}{2}\frac{\omega_\mathrm{e}\Psi_\mathrm{p}R_\mathrm{Fe}^2}{R_\mathrm{Fe}^2+(\omega_\mathrm{e}L_\mathrm{h})^2}I_\mathrm{s,q}-\frac{3}{2}\frac{R_\mathrm{Fe}\omega_\mathrm{e}^2L_\mathrm{h}\Psi_\mathrm{p}}{R_\mathrm{Fe}^2+(\omega_\mathrm{e}L_\mathrm{h})^2}I_\mathrm{s,d}-\frac{3}{2}\frac{R_\mathrm{Fe}\left(\omega_\mathrm{e}\Psi_\mathrm{p}\right)^2}{R_\mathrm{Fe}^2+(\omega_\mathrm{e}L_\mathrm{h})^2}.\tag{3.28}$$

Equation (3.28) along with Eq. (3.24) confirm that Eq. (3.21) and Eq. (3.26) are equivalent. The first term on the right-hand side of Eq. (3.28) corresponds to power resulting from the quadrature component of the stator current, which in contrast to P_{m} includes dissipative terms. The second term implies that a positive direct current component partly contributes to a braking power and therefore to dissipation. The third term corresponds to the braking power due to eddy currents. As the third term corresponds to power dissipated inside the machine independent of the stator current, it does not appear in Eq. (3.21) that describes the power balance at the terminals of the machine.

Loss and efficiency maps

The equivalent circuit enables the calculation of the internal voltages and currents at each operating point of the electric machine. Moreover, the total power losses of the electric machine can be calculated as the sum of the iron and copper losses defined in Eq. (3.22), since friction and windage losses are neglected due to vacuum and magnetic levitation. The experimentally estimated power losses of the SWIVT290 flywheel prototype in Schneider & Rinderknecht (2019) led to the identification of R_{ed}=265 Ω and R_{hy}=260 Ω, which are needed to calculate the iron resistance according to Eq. (3.13), considering as nominal electrical frequency $f_{\mathrm{e,N}}$=1 kHz. Consequently, using the electric machine parameters summarized in Table 3.1, the loss and efficiency maps of the electric machine can be calculated. Additional technical data for the PMSM of the flywheel prototype SWIVT290 can be found in Table A.1. Figure 3.4 presents the calculated power losses of the PMSM over rotor torque and speed. The calculated losses correspond to motor operation under zero direct current component (I_{d}=0), a winding temperature of 60 °C and a permanent magnet temperature of 60 °C. Furthermore, Figure 3.5 presents the efficiency map of the electric machine, where the efficiency is defined as the ratio of the mechanical power of the rotor to the electrical power supplied at the PMSM terminals.

The copper losses depend on the amplitude of the stator current according to Eq. (3.10) and therefore increase with torque, as torque increases with current according to Eq. (3.14). The iron losses depend both on the stator current and the electrical frequency according to Equations (3.12) and (3.13), thus, they increase both with torque and speed. In Figure 3.4, it can be observed that the total power losses increase both with torque and speed, however, at the low torque range, that is M<20 Nm, the power losses increase mainly with speed. According to the efficiency characteristic map presented in Figure 3.5, operating the electric machine within the area bounded by 15 Nm, 50 Nm, 2000 rpm and 14000 rpm corresponds to an efficiency over 95 %. As expected, low mechanical power, which corresponds to either low torque or low speed, leads to a relative low efficiency.

Table 3.1 Main parameters of the Permanent Magnet Synchronous Machine of the flywheel prototype SWIVT290, which has a maximum electric power of 100 kW.

Parameter	Value	Description
p	5	Number of pole pairs
$I_{\mathrm{s,max}}$	119 A	Maximum continuous phase current
L_{h}	220 µH	Main inductance
Ψ_p	43 mVs	Flux linkage
R_{s}	6.5 mΩ	phase DC resistance
R_{ed}	265 Ω	Eddy current term of iron resistance
R_{hy}	260 Ω	Hysteresis term of iron resistance at $f_{\mathrm{e,N}}$=1 kHz

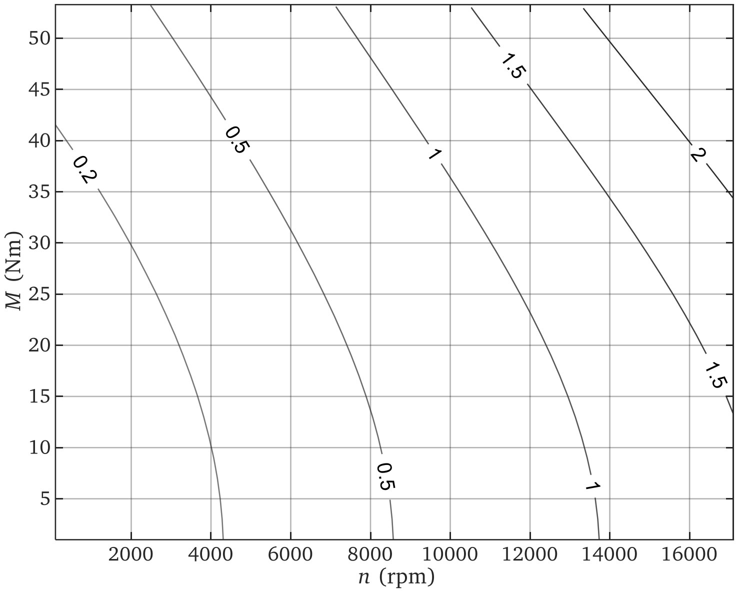

Figure 3.4 Calculated copper and iron losses of the PMSM of the flywheel prototype SWIVT290 in kW under motor operation with zero direct current component (I_d=0), where M denotes to the rotor torque and n denotes to the rotor speed.

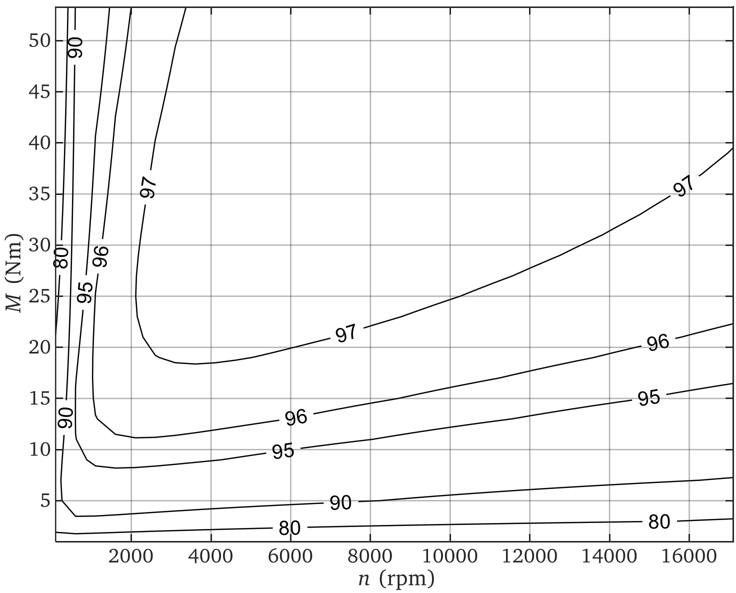

Figure 3.5 Calculated efficiency map of the PMSM of the flywheel prototype SWIVT290 under motor operation with zero direct current component (I_d=0), where M denotes to the rotor torque and n denotes to the rotor speed. The efficiency is expressed as a percentage.

Idle power consumption

Although the no-load losses account only for a fraction of the nominal power of the flywheel, they are always present, which is a clear disadvantage when the flywheel storage idles for a significant amount of time. Idling of the flywheel storage does not correspond to standstill, but to rotation at a speed high enough to enable both acceleration and deceleration, that is, to enable the flywheel to both sink and supply power. The AMBs and the vacuum system have an approximately constant power consumption that adds to the no-load losses and thus to the operating cost. The power consumption of idling outer-rotor flywheel storages is therefore estimated with the aid of the flywheel prototype SWIVT290 (Schneider & Rinderknecht, 2019).

The windage losses of rotors with large circumference that rotate at high speed are considerably higher than the power required to maintain vacuum and therefore the operation in vacuum is justified. The vacuum system consists of a backing pump and a turbomolecular pump connected in series. The backing pump is able to establish medium vacuum in the containment of the kinetic energy storage in the range of $10^2 \ldots 10^3$ Pa. By the time medium vacuum is established, the turbomolecular pump is switched on to establish high vacuum in the range of $10^{-2} \ldots 10^{-3}$ Pa. Although the evacuation of the containment usually loads the vacuum pumps at nominal power, it is only a transient process. By the time the desired vacuum is established, the consumption of the vacuum pumps decreases and remains almost constant. The continuous power consumption of the backing pump for the containment of SWIVT290 is estimated in the range of 150…250 W, whereas the power consumption of the turbomolecular pump is estimated in the range of 50…70 W. It would be interesting to investigate whether several flywheels that operate in parallel can share the same backing pump or even the same turbomolecular pump to reduce the investment as well as the operating cost. Since no such investigations are yet accomplished, it is considered that each flywheel requires its own backing and turbomolecular pump.

The AMBs comprise a bias coil, the power consumption of which is constant and thus determines the no-load losses, and a control coil, the power consumption of which depends on the rotor speed. Although different AMB configurations for outer rotors are available and improvements are anticipated, according to recent developments described in Franz, Richter et al. (2019), the power consumption of both the bias and the control coil of a single AMB ranges between 100 W and 125 W. Since two AMBs are required to effectively suspend the rotor, the total consumption for the magnetic suspension doubles.

Eddy currents induced in the stator of electric machines with permanent magnets in the rotor cause a braking torque as long as the rotor spins. The flywheel should preferably rotate in the middle of its energy state range when idling, as depicted in Figure 3.1. The idle speed of the SWIVT290 prototype ranges between 12 000 rpm and 14 000 rpm, thus, according to Eq. (3.16) and the parameters listed in Table 3.1, the idle losses of the PMSM range between 800 W and 1100 W. The power converter should compensate for the braking torque by feeding a current in the stator windings that is high enough to keep the flywheel rotating at idle speed, otherwise the flywheel decelerates. According to Eq. (3.18), the quadrature component of the stator current required to keep the flywheel rotating between 12 000 rpm and 14 000 rpm ranges from 1.7 A to 2 A. Since the required current is significantly lower than the nominal current of the power converter, which corresponds to the maximum continuous current of the PMSM, the power converter losses are neglected.

Although basic equipment, such as electronic control units, communication gateways and cooling systems, also consumes power, in storage systems that comprise several storage units, the units usually share the same basic equipment, the power consumption of which is therefore considered at storage system level. The estimated range of idle power consumption and the corresponding share of the main flywheel components are summarized in Table 3.2. It is obvious that the spinning PMSM dominates the idle power consumption. Technically, the consumer is the power converter that drives the PMSM and not the PMSM itself, though the PMSM is listed as the consumer of its own power losses. Considering that the nominal power of the prototype SWIVT290 is 50 kW, the idle power consumption accounts for 2…3 % of the nominal power.

Since flywheels with higher nominal power and higher energy capacity than the SWIVT290 prototype are favourable for several applications, it is worth investigating the change in the idle power consumption when increasing the power and the energy rating. Changes in the axial or radial dimensions of the flywheel within a reasonable range only slightly increase the load of the vacuum system and therefore its consumption. Elongation of the rotor to increase the energy capacity for the same nominal power should not significantly change the design of the PMSM and the AMBs, thus, their idle power consumption remains almost unchanged. An increase in the bore diameter in order to increase the power or the energy capacity, expands the dimensions of the AMBs, which in turn increases the dimensions of its bias coils and therefore its power losses for the same bias current. Moreover, if additional pole pairs are introduced in the PMSM to exploit the increased bore diameter when the flux linkage per pole and phase remains unchanged, the idle losses of the PMSM increase according to Eq. (3.17), because the required electrical frequency for the same mechanical speed increases. Nevertheless, a larger bore diameter could be used to increase the current rating instead of increasing the number of pole pairs. Generally, the effect of the bore diameter on the power losses should be investigated with an elaborate model of the electric machine.

Table 3.2 Estimated idle power consumption per component of the flywheel protype SWIVT290, which has a nominal power of 50 kW and an energy capacity of 1.8 kWh.

Component	**Range of idle power consumption (W)**	**Range of idle power consumption share (%)**
PMSM at idle speed	800...1100	59…73
Active Magnetic Bearings	200...250	13…20
Vacuum System	200...300	13…23
Total	**1200…1650**	-

3.2 Electrochemical Energy Storage

Several battery technologies have been developed since the early 19^{th} century when Alessandro Volta invented the voltaic pile. Lithium-ion batteries were introduced in the late 20^{th} century and had their first applications in the segment of consumer electronics, where a single cell typically comprises the whole battery. Constantly improving properties and decreasing prices led to lithium-ion battery systems of several hundred of cells for electric vehicles. Recently, lithium-ion batteries were introduced in stationary applications such as uninterruptible power supplies replacing well established battery technologies. Lithium-ion battery systems consist of several lithium-ion cells connected in series and in parallel in order to achieve high voltage and divide the load respectively. Since the estimation of the energy losses of the battery system is the main objective, modelling on the basis of an equivalent circuit is considered sufficient. The cell degradation is also considered through dedicated models that estimate the capacity fade and the internal resistance increase over time and usage.

Charge and energy capacity of lithium-ion cells

The nominal charge capacity Q_{N} of a lithium-ion cell is specified by its manufacturer, typically in Ah, so that it corresponds to the maximum charge that can be retrieved when the cell is fully charged or, equivalently, the maximum charge than can be stored when the cell is empty, under ideal conditions. The tests conducted by manufacturers to determine the nominal charge capacity of lithium-ion cells involve quite low currents and controlled temperature usually at 25 °C (Plett, 2015). Temperatures below 0 °C significantly reduce the available charge capacity. Therefore, the nominal charge capacity of lithium-ion cells can fully be exploited only at ideal conditions. To approach the nominal charge capacity, a cell operating temperature close to room temperature and reduced current when approaching the voltage limits of the cell should be ensured. The decrease in the available charge capacity is not linked to energy losses, but to the fact that the cell can exchange less charge at high currents and low temperatures than under ideal conditions as it reaches its voltage limits.

Manufacturers often use the term *C-rate* to refer to the charge or discharge rate of lithium-ion cells. A C-rate of 1C corresponds to the discharge rate in order to discharge a fully charged battery within one hour, whereas 2C corresponds to twice the discharge rate of 1C, so that the battery is completely discharged within half an hour. Thus, the term C-rate has the unit h^{-1}. The nominal lithium-ion cell current I_{N} usually corresponds to the current required to discharge the cell at 1C.

The open circuit voltage U_{oc} is the voltage that can be measured at the terminals of lithium-ion cells when ideally no charge exchange occurs and sufficient time elapsed since the last charge exchange between the cell and the environment. The open circuit voltage increases with the charge stored in the cell. Measurements to obtain the characteristic of open circuit voltage over charge are therefore conducted at low current in order to approach a quasi-static process. The characteristic curve of open circuit voltage over charge for a certain temperature is qualitatively depicted in Figure 3.6. The point of minimum voltage U_{min} and minimum charge Q_{min} signifies that no charge should be further removed from the cell, whereas the point of maximum voltage U_{max} and maximum charge Q_{max} signifies that no additional charge should be stored in the cell. Because the cell temperature influences the U_{oc}-Q characteristic, measurements are usually repeated in climate rooms under controlled temperature, in order to obtain different U_{oc}-Q characteristics for different temperatures.

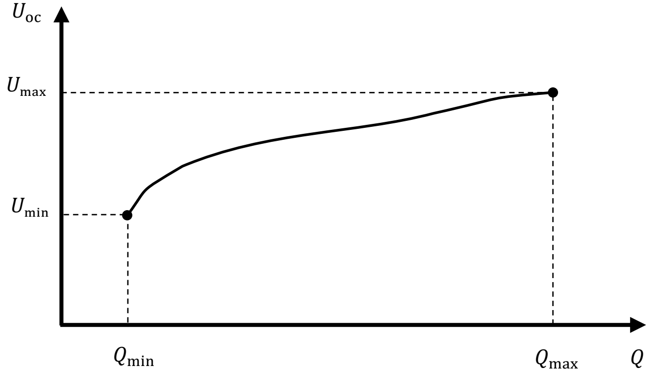

Figure 3.6 Qualitative characteristic curve of the open circuit voltage U_{oc} over the charge Q stored in a lithium-ion cell at a certain temperature.

In accordance with Figure 3.6, the usable energy as a function of the charge Q stored in the lithium-ion cell is

$$E(Q) = \int_{Q_{min}}^{Q} U_{oc}(q)\mathrm{d}q, \tag{3.29}$$

where dq is the infinitesimal change of charge in the cell. Therefore, the energy stored in the cell at maximum charge is

$$E(Q_{max}) = \int_{Q_{min}}^{Q_{max}} U_{oc}(q)\mathrm{d}q. \tag{3.30}$$

The average open circuit voltage over charge stored in the cell is

$$\overline{U}_{oc} = \frac{1}{Q_{max} - Q_{min}} \int_{Q_{min}}^{Q_{max}} U_{oc}(q)\mathrm{d}q. \tag{3.31}$$

It is reasonable to define the nominal charge capacity of the cell as the maximum available charge, that is $Q_N = Q_{max} - Q_{min}$, and the nominal energy capacity as the energy stored at maximum charge, that is $E_N = E(Q_{max})$. Although the voltage of lithium-ion cells varies with charge, a rated voltage should be typically specified. Defining the average open circuit voltage over stored charge as the nominal voltage, that is $U_N = \overline{U}_{oc}$, shows the advantage that, according to Equations (3.30) and (3.31), the nominal energy capacity of the cell equals the product of the nominal voltage and the nominal charge capacity, that is

$$E_N = E(Q_{max}) = \overline{U}_{oc}(Q_{max} - Q_{min}) = U_N Q_N. \tag{3.32}$$

Thus, manufacturers typically define the average open circuit voltage over stored charge as the nominal cell voltage. Furthermore, manufacturers determine the nominal charge capacity Q_N through tests, so that the nominal energy capacity E_N can be defined using Eq. (3.32). However, only a lower energy than E_N can be recovered when discharging the cell, because the voltage drop across the internal resistance leads to a lower terminal voltage than the open circuit voltage. An energy that approaches E_N can be recovered when the cell is discharged at a quite low C-rate, for instance 0.02C. The deficit between stored energy and recovered energy corresponds to the energy conversion losses that are inherent in any energy storage technology.

State of charge

The State of Charge (SoC) is defined as the deviation of the charge Q stored in a lithium-ion cell from the minimum permissible charge Q_{min} over the charge capacity, which corresponds to the difference between maximum and minimum permissible charge, that is

$$q_{\text{s}} = \frac{Q - Q_{\text{min}}}{Q_{\text{max}} - Q_{\text{min}}}, \qquad Q_{\text{min}} \leq Q \leq Q_{\text{max}}. \tag{3.33}$$

According to Eq. (3.33), the SoC is a unitless quantity that ranges between 0 and 1. The minimum and maximum permissible charge are not constant but change over time due to the inherent cell degradation. Therefore, the charge capacity varies with time, so that the denominator on the right-hand side of Eq. (3.33) is time-dependent such that $Q_{\text{c}}(t)=Q_{\text{max}}(t)\text{-}Q_{\text{min}}(t)$. The initial charge capacity or a fresh cell typically equals the nominal charge capacity specified by the manufacturer, that is $Q_{\text{c}}(0)=Q_{\text{N}}$.

The SoC can also be defined with respect to a time-varying current $I(t)$ through the cell, as in Eq. (3.34) which is often used for the estimation of the SoC in batteries (Plett, 2015). The first term on the right-hand side of Eq. (3.34) corresponds to the initial SoC at $t=t_0$. The term $\eta(t)$ denotes the time dependent coulombic efficiency of the cell. In this respect the coulombic efficiency of lithium-ion cells is usually considered unity, that is $\eta(t)=1$. Furthermore, a time-varying charge capacity $Q_{\text{c}}(t)$ is considered. Although the SoC defined in Eq. (3.34) is unconstrained, estimation algorithms should limit the SoC between 0 and 1.

$$q_{\text{s}}(t) = q_{\text{s}}(t_0) + \frac{1}{Q_{\text{c}}(t)} \int_{t_0}^{t} \eta(\tau) I(\tau) \, \text{d}\tau \tag{3.34}$$

Energy state

The SoC provides information about the charge stored with respect to the charge capacity of a lithium-ion cell. However, the energy with respect to the energy capacity that can be retrieved from a lithium-ion cell does not directly correspond to the SoC. Retrieving the same amount of charge at constant current leads to a higher energy yield at high cell voltage than at low cell voltage. Using the energy stored in the lithium-ion cell defined in Eq. (3.29), the energy state can be defined as a function of the charge stored in the cell such that

$$w(Q) = \frac{E(Q)}{E(Q_{\text{max}})}.$$

The energy state is thus a metric ranging from 0 to 1 that corresponds to the energy stored with respect to the energy capacity of a lithium-ion cell.

The SoC is tracked by measuring the current when a coulombic efficiency close to unity is assumed. On the other hand, measuring the power flow to estimate the energy state leads to a relatively high error, since the energy conversion efficiency is always lower than unity. Therefore, the SoC is preferably tracked and then used to estimate the energy state. As both the state of charge and the energy state can be expressed as a function of the charge stored in a lithium-ion cell, a function $w= f(q_{\text{s}})$ that links the energy state to the SoC can be derived.

Equivalent circuit

Equivalent circuits are usually applied to model lithium-ion cells when the effect of chemical reactions is only secondary to the goals of the investigation. To consider diffusion voltages, an equivalent circuit with two independent RC loops, as that presented in Figure 3.7 is used (Plett, 2015). The equivalent circuit is parametrized for a cell made of lithium Nickel Manganese Cobalt oxides (NMC) in the cathode and graphite in the anode, the main technical data of which are summarized in Table A.3. Since the technical data provided by the cell manufacturer are not sufficient to parametrize an equivalent circuit with two RC loops, a parameter identification study conducted for the same cell is used (Rahmoun & Biechl, 2012).

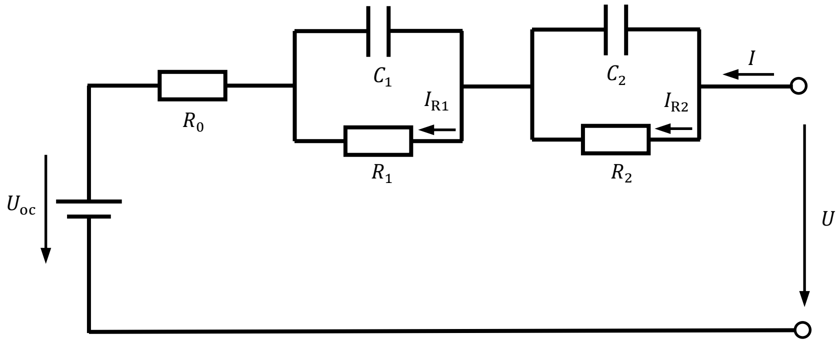

Figure 3.7 Equivalent circuit of a lithium-ion cell with two independent RC loops

The dynamic response of the equivalent circuit can be explained with the aid of a single RC loop. Let R be the resistance and C be the capacitance of a single RC loop of the equivalent circuit depicted in Figure 3.7, the cell current I splits into the current of the capacitive branch I_C and the current I_R in the resistive branch such that

$$I(t) = I_c(t) + I_R(t). \tag{3.35}$$

The capacitance C and the resistance R share the same voltage U. The capacitive current corresponds to the rate of change of the charge stored in the capacitance, which in turn can be expressed as the product of the capacitance and its voltage, hence

$$I_c(t) = C\frac{\mathrm{d}U(t)}{\mathrm{d}t}. \tag{3.36}$$

The resistive current is proportional to the voltage of the resistive branch such that

$$U(t) = RI_R(t).$$

Substituting the capacitive current derived in Eq. (3.36) into Eq. (3.35) and eliminating the common voltage, results in a differential equation that links the cell current I with the resistive current I_R

$$\frac{\mathrm{d}I_R(t)}{\mathrm{d}t} = \frac{1}{RC}[I(t) - I_R(t)],$$

which when solved for $I_R(t)$ considering the initial condition $I_R(0) = I_{R0}$ yields

$$I_R(t) = I(t) + e^{-t/(RC)}[I_{R0} - I(t)].$$

The product of the capacitance and the resistance RC has the unit of time and is called the *time constant* of the RC loop. The solution of the differential equation signifies that the resistive current I_{R} of the RC loop converges exponentially with the time constant RC to the cell current I. In other words, as the dynamic response of the cell to a current input approaches steady state, the current in the resistive branch approaches the cell current. For a high capacitance and therefore a long time constant, steady state can only be reached at low C-rates. Whereas the cell current I corresponds to a real current that can be measured, the branch currents I_{R1} and I_{R2} are fictive currents that model the electrochemical dynamics.

Experimental results for lithium-ion cells show a significant dependence of the equivalent circuit parameters on the state of charge. Furthermore, the equivalent circuit parameters depend on the direction of charge flow. The parameters of the equivalent circuit with two independent RC loops for an NMC lithium-ion cell under charging at an SoC of 50 % and a cell temperature of 25 °C according to Rahmoun & Biechl (2012) are listed in Table A.6.

Power Flow and Power Losses

A battery can operate both as load and generator. Passive sign convention or, equivalently, load convention is used at the terminals of the equivalent circuit presented in Figure 3.7. Therefore, positive power or positive current means that energy flows into the cell, that is, the cell is charged, which corresponds to the annotated (with arrow) current direction in Figure 3.7. On the other hand, negative power or current means that energy flows out of the cell, that is, the cell is discharged. Since charge moves from high to low potential, when charging the cell, the terminal voltage is higher than U_{oc}, whereas when discharging the cell, U_{oc} is higher than the terminal voltage. Consequently, according to the applied load convention and the equivalent circuit presented in Figure 3.7 the voltage at the cell terminals is

$$U = R_0 I + R_1 I_1 + R_2 I_2 + U_{oc}. \tag{3.37}$$

The total power losses of the cell comprise the sum of the power losses in each resistance of the equivalent circuit, that is

$$P_{L} = R_0 I^2 + R_1 I_{R1}^2 + R_2 I_{R2}^2. \tag{3.38}$$

Multiplying both sides of Eq. (3.37) with the cell current and replacing the cell losses with the expression defined in Eq. (3.38) leads to the power at the cell terminals

$$P = UI = U_{oc} I + P_{L}. \tag{3.39}$$

According to Eq. (3.38), in order to determine the total cell losses, the currents in the resistive branches should be known. To determine the currents in the resistive branches, in turn, the initial states of the currents should be known. Alternatively, to estimate the cell power losses without the need to know the initial states of the currents in the resistive branches, the RC loops can be replaced with an equivalent impedance at a frequency that approaches the load frequency. The cell losses can thus be expressed as a univariate function of the cell current at a given frequency. Let a sinusoidal current source with the frequency ω excite the equivalent circuit of the cell such that the equivalent impedance Z of a single RC loop is

$$\underline{Z}_{RC}(\omega) = \frac{1}{\frac{1}{R} + j\omega C} = \frac{R}{1 + j\omega RC}.$$

Therefore, the real part of the impedance that corresponds to the resistive losses is

$$\mathrm{Re}\{\underline{Z}_{\mathrm{RC}}(\omega)\} = \frac{R}{1+(\omega RC)^2}. \tag{3.40}$$

Substituting the cutoff frequency $\omega_\mathrm{c} = 1/(RC)$ in Eq. (3.40) yields

$$\mathrm{Re}\{\underline{Z}_{\mathrm{RC}}(\omega)\} = R\frac{1}{1+\left(\frac{\omega}{\omega_\mathrm{c}}\right)^2}. \tag{3.41}$$

According to Eq. (3.41), for frequencies well below the cutoff frequency ω_c, the real part of the impedance approaches the resistance R, whereas for frequencies well above the cutoff frequency ω_c, the real part of the impedance vanishes. Consequently, at high frequencies the series resistance R_0 dominates.

Using Eq. (3.40) to determine the real part of the impedance for the expected frequency ω_e of the load applied at the terminals of the lithium-ion cell, leads to the estimation of the equivalent cell resistance R_eq as the sum of the series resistance R_0 and the real part of the impedances of the two RC loops, that is

$$R_\mathrm{eq} = R_0 + \mathrm{Re}\{\underline{Z}_{\mathrm{RC1}}(\omega_\mathrm{e})\} + \mathrm{Re}\{\underline{Z}_{\mathrm{RC2}}(\omega_\mathrm{e})\}. \tag{3.42}$$

The equivalent resistance is not intended to replace the RC loops, but to estimate the power losses and therefore the efficiency of lithium-ion cells. Generally, when the dynamic response of lithium-ion cells is secondary to the goals of the investigation, the equivalent circuit can be simplified with the aid of the equivalent resistance.

According to Eq. (3.39), the efficiency of a lithium-ion cell corresponds to $(U_\mathrm{oc}I)/P$ when charging and to $P/(U_\mathrm{oc}I)$ when discharging. Considering a load with a frequency of 1 mHz at the terminals of the lithium-ion cell with the equivalent circuit parameters identified in Rahmoun & Biechl (2012), using the equivalent resistance defined in Eq. (3.42), the loss and efficiency map over terminal voltage and current for both charging and discharging are depicted in Figure 3.8 and Figure 3.9 respectively. The equivalent circuit parameters correspond to a cell temperature of 25 °C. The current varies from -80 A to 80 A, where the highest value corresponds to a C-rate of 1.5C with respect to the cell charge capacity of 53 Ah. The terminal voltage lies within the permissible range of 3.2 V to 4.2 V.

The area under the contours in Figure 3.8 and Figure 3.9 correspond to feasible operating points. Charging at high current and low terminal voltage is unfeasible, since the voltage across the internal resistance increases the terminal voltage. Similarly, discharging at high current and high terminal voltage is unfeasible due to the voltage drop across the internal resistance. As expected from Eq. (3.38), the higher the current is, the higher the power losses are. As a result of the characteristic of the equivalent circuit parameters over SoC, the lower the voltage for the same current is, the higher the power losses are and thus the lower the efficiency is. The power losses are roughly symmetrical with respect to current, with the exception of charging at low voltage, which leads to higher losses than discharging at low voltage. Terminal voltages over 3.4 V under constant current have almost no effect on the power losses when discharging. Similarly, terminal voltages over 3.8 V under constant current have almost no effect on the power losses when charging. For currents below 7 A, which corresponds to a C-rate of 0.13C, the efficiency of the lithium-ion cell is higher than 98 % for both charging and discharging within the complete voltage range.

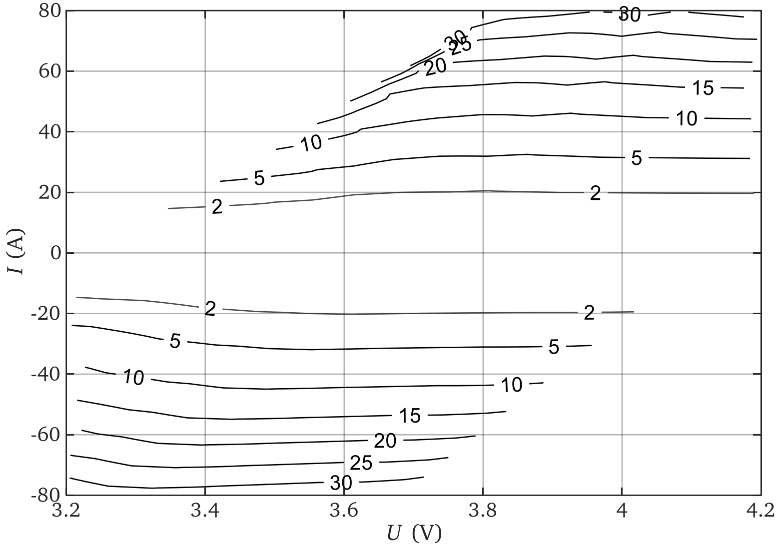

Figure 3.8 Power losses in W of a 53 Ah NMC lithium-ion cell with the equivalent circuit parameters identified in Rahmoun & Biechl (2012) over the terminal voltage U and the current I under a load frequency of 1 mHz. Positive current corresponds to charging and negative current to discharging. According to the manufacturer, the average cell voltage is 3.7 V.

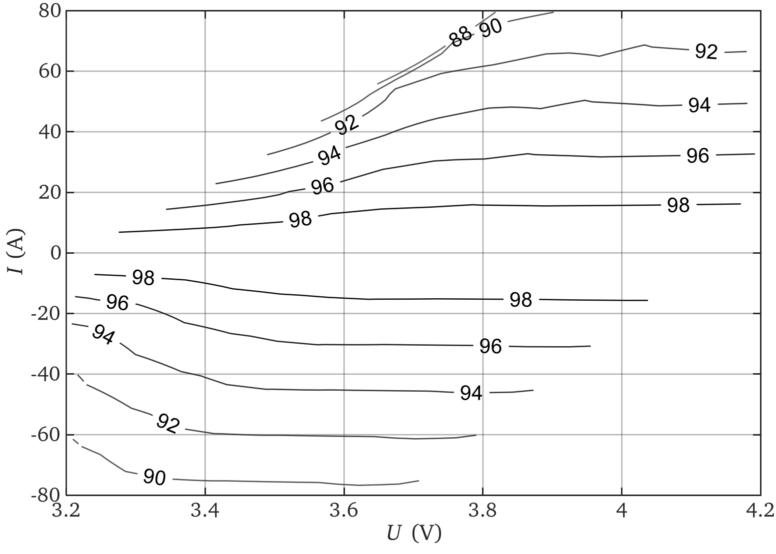

Figure 3.9 Efficiency of a 53 Ah NMC lithium-ion cell with the equivalent circuit parameters identified in Rahmoun & Biechl (2012) over the terminal voltage U and the current I under a load frequency of 1 mHz. Positive current corresponds to charging and negative current to discharging. The efficiency is expressed as a percentage. According to the manufacturer, the average cell voltage is 3.7 V.

Thermal behaviour

Power losses in lithium-ion cells lead to a temperature increase that affects their operating characteristics and accelerates their degradation. The operating temperature of the cell should be known in order to estimate temperature-dependent parameters and the cell degradation. Since no thermal parameters are specified by the cell manufacturer, the overall heat transfer coefficient a_c=5 W/(Km^2) and the volumetric heat capacity s_c=2.04 MJ/(Km^3) are assumed, as identified for a similar cell of the same manufacturer (Huria, et al., 2012). As the cell dimensions are known, the cell volume V_c and the cell outer surface S_c can be determined. Since the thickness of pouch cells is considerably smaller than their side length, only the side surface is considered in the outer surface. Therefore, the thermal resistance of the cell to its boundaries is $R_{th}=1/(a_c S_c)$ in K/W and the cell heat capacity is $C_{th}=s_c V_c$ in J/K. The response of the cell temperature ϑ_c to the heat Q caused by power losses can therefore be estimated with the aid of the one-dimensional heat diffusion equation

$$C_{\mathrm{th}} \frac{\mathrm{d}\vartheta_{\mathrm{c}}}{\mathrm{d}t} + \frac{\vartheta_{\mathrm{c}} - \vartheta_{\mathrm{amb}}}{R_{\mathrm{th}}} = Q,$$

where ϑ_{amb} is the ambient temperature at the cell boundaries. The cells are stacked and enclosed in a housing that forms a battery, thus, the cell ambient temperature can be considerably higher than the battery ambient temperature. However, a constant cell ambient temperature ϑ_{amb} can be assumed, if forced convection with air or water as coolant is applied inside the battery.

Degradation

As many materials and components lithium-ion cells also degrade with time and usage. In addition to the term degradation, the term ageing is interchangeably used in the literature. The degradation of an unused battery over time is called calendrical, whereas the degradation due to usage is called cyclic. Degradation leads to a decrease in the charge capacity and an increase in the internal resistance of lithium-ion cells.

The calendrical degradation is temperature-dependent with high temperature negatively affecting the lifetime of lithium-ion cells. Additionally, it has been observed that high state of charge accelerates the calendrical degradation of lithium-ion cells (Ecker, et al., 2014; Schmalstieg, et al., 2014). Lithium-ion cells degrade by charge flow, which corresponds to cyclic degradation. The operating temperature, the cycle depth and the C-rate are all factors that influence the cyclic degradation. To quantify the effect of several factors on the cyclic degradation, various experimental approaches and corresponding models have been suggested (Schmalstieg, et al., 2014; Sarasketa-Zabala, et al., 2015; Schuster, et al., 2015; Smith, et al., 2021). A comparison of the empirical models that result from experimental investigations is often a difficult task, since the technology of the lithium-ion cells tested vary significantly. In other words, it is difficult to converge on a degradation model for a wide range of lithium-ion cell technologies. However, cell manufacturers usually provide information about the cyclic degradation, which can be used to parametrize empirical degradation models for similar lithium-ion cell technologies.

The time-varying normalized charge capacity q_c(t) of a lithium-ion cell is defined as the charge capacity Q_c(t) at the present time over the nominal charge capacity Q_N, that is

$$q_{\mathrm{c}}(t) = \frac{Q_{\mathrm{c}}(t)}{Q_{\mathrm{N}}}. \tag{3.43}$$

In addition to the charge capacity fade, the internal resistance of lithium-ion cells increases due to degradation. The normalized series resistance r_s is defined as the present equivalent series resistance R_s over the nominal series resistance $R_{s,N}$ specified by the manufacturer for a certain frequency, hence

$$r_s(t) = \frac{R_s(t)}{R_{s,N}}. \tag{3.44}$$

Cell manufacturers often specify the cycle life as the number of cycles that the cell should be able to perform under normal conditions. In this respect the nominal numbers of cycles N_N is defined as the number of cycles that the cell undergoes under the nominal cycle depth $\Delta q_{s,N}$ and a constant C-rate until the normalized charge capacity falls below the threshold $q_{c,Eol}$ which corresponds to the *End of Life* (EoL) of the cell. As indicative values; the applied C-rate is typically 1C, the nominal cycle depth ranges between 70 % and 90 %, and the threshold of the normalized charge capacity that corresponds to the EoL ranges from 70 % to 80 %.

The cycle life can also be expressed as the charge or energy throughput that lithium-ion cells undergo under normal operating conditions until the EoL. Although the charge throughput depends only on the charge exchanged through the cell electrodes, the energy throughput additionally depends on the cell voltage that varies with SoC and C-rate. Therefore, the charge throughput is usually preferred to track the degradation of lithium-ion cells. The charge throughput Q_{th} is defined as the absolute charge exchanged through a battery cell over time

$$Q_{th}(t) = \int_0^t |I(\tau)| \, d\tau. \tag{3.45}$$

A full cycle is defined as the complete discharge of a fully charged fresh cell and the subsequent complete charge under ideal conditions, so that the absolute charge $2Q_N$ is exchanged through the cell electrodes. Therefore, the number of Equivalent Full Cycles (EFC) that a cell undergoes is defined as the charge throughput over twice the nominal charge capacity of the cell, that is

$$n_{EFC}(t) = \frac{Q_{th}(t)}{2Q_N}. \tag{3.46}$$

The quantity n_{EFC} is unitless and belongs to the real numbers. In contrast to the charge throughput, the undergone equivalent full cycles n_{EFC} facilitate a direct comparison with the nominal cycles N_N.

Degradation function

The effect of calendrical and cyclic degradation on the internal resistance and charge capacity is described by Eq. (3.47), which corresponds to the empirical observations for a commercial lithium-ion cell that is made of lithium Nickel Manganese Cobalt oxides (NMC) in the cathode and graphite in the anode (Schmalstieg, et al., 2014). The variable y denotes the degradation state of a physical quantity, for example the charge capacity loss. The variable x denotes the accumulated physical quantity that causes the degradation, for instance the charge throughput. The degradation factor b is a variable that depends on the operating conditions, such as temperature and cycle depth, whereas the exponent a is assumed constant during the degradation process.

$$y = f(x) = bx^a \tag{3.47}$$

The experimental results in Schmalstieg et al. (2014) show that lithium-ion cells degrade faster at the early stages of cyclic or calendrical degradation tests. Therefore, the exponent a assumes values below unity ($a<1$). On the contrary, if a linear degradation over stress is observed, the exponent a should equal unity ($a=1$). Moreover, it is experimentally observed that stressing a commercial NMC cell with graphite in the anode at a high degradation state leads to a steep increase in charge capacity loss over stress (Schuster, et al., 2015). A steep increase in charge capacity loss over stress corresponds to an exponent that is greater than unity (a>1). Therefore, the assumption of a constant exponent a is invalid at a high degradation state.

Defining the degradation factor as

$$b = \frac{y_{\mathrm{EoL}}}{x_{\mathrm{EoL}}^{a}},$$

so that the point (x_{Eol}, y_{EoL}) corresponds to the EoL of the lithium-ion cell, the degradation function defined in Eq. (3.47) is qualitatively drawn in Figure 3.10 for $a<1$, $a=1$ and $a>1$.

If the degradation state is known and the physical quantity that caused the degradation under a certain degradation factor b should be found, the inverse function f^{-1} can be used to determine the physical quantity, that is

$$x = f^{-1}(y) = \left(\frac{y}{b}\right)^{1/a}.$$

Although the degradation function defined in (3.47) is continuous, in practice the degradation estimation is discrete because a monitored physical quantity x such as the accumulated charge throughput is updated at certain intervals. Since the degradation function is nonlinear, to calculate the degradation increment after a stress process requires knowledge of the initial degradation state. Therefore, a recurrence relation is used. As calendrical and cyclic degradation occur in parallel, the calendrical and cyclic degradation increments are separately calculated by recurrence relations. The degradation state is then updated for the next iteration.

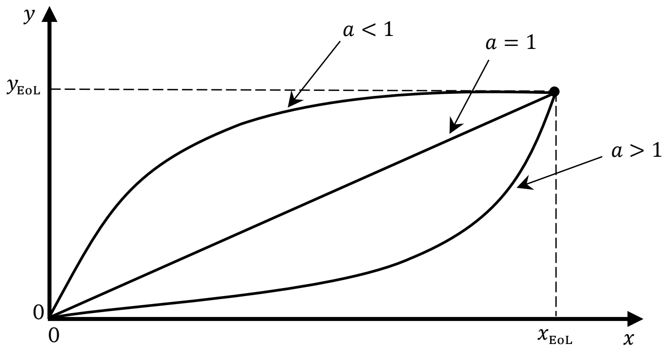

Figure 3.10 Effect of the exponent a on the degradation state, where y denotes the degradation state and x denotes the accumulated physical quantity that causes the degradation such that $y=bx^a$. All curves end at the same EoL point (x_{EoL}, y_{EoL}) according to the definition of the degradation factor b.

Let the degradation state be the charge capacity loss q_L with respect to the initial charge capacity. In other words, q_L corresponds to the normalized charge capacity loss. According to Eq. (3.43), the normalized charge capacity of a fresh lithium-ion cell is unity. Therefore, the degradation state and the normalized charge capacity are complementary quantities such that

$$q_\mathrm{L} = 1 - q_\mathrm{c}. \tag{3.48}$$

Similarly, let the degradation state of the internal resistance, which corresponds to the normalized internal resistance increase, be r_i. According to Eq. (3.44), the normalized series resistance of a fresh cell equals unity, therefore the relationship between the normalized resistance increase and the normalized series resistance is

$$r_\mathrm{i} = r_\mathrm{s} - 1. \tag{3.49}$$

Let $a_\mathrm{cyc,q}$ be the exponent and $b_\mathrm{cyc,q}$ be the degradation factor for the cyclic charge capacity loss. Similarly let $a_\mathrm{cyc,r}$ be the exponent and $b_\mathrm{cyc,r}$ be the degradation factor for the cyclic internal resistance increase. Similar parameters are defined for the calendrical degradation; $a_\mathrm{cal,q}$ and $b_\mathrm{cal,q}$ for the charge capacity loss, $a_\mathrm{cal,r}$ and $b_\mathrm{cal,r}$ for the internal resistance increase. The degradation factor b depends on the conditions during the degradation process. Considering that the conditions vary during the degradation process, which implies that the degradation factor varies, the incremental cyclic capacity loss is determined with the aid of the recurrence relation defined in Eq. (3.50), where q_L corresponds to the degradation state and n_EFC to the quantity that causes the degradation. Given the charge capacity loss at the end of the $(k\text{-}1)^\mathrm{th}$ interval $q_\mathrm{L}[k\text{-}1]$ and the undergone equivalent cycles during the k^th interval $n_\mathrm{EFC}[k]$ under the conditions of the degradation factor $b_\mathrm{cyc,q}[k]$, the incremental charge capacity loss due to cyclic degradation during the k^th interval $\Delta q_\mathrm{L,cyc}[k]$ is determined. The basis of the power with the exponent $1/a_\mathrm{cyc,q}$ on the right-hand side of Eq. (3.50) corresponds to the fictive equivalent full cycles that would have been undergone to cause the charge capacity loss $q_\mathrm{L}[k\text{-}1]$ under the conditions of the degradation factor $b_\mathrm{cyc,q}[k]$. Using the dimensionless equivalent full cycles instead of the charge throughput used in Schmalstieg et al. (2014), the degradation factor and consequently the recurrence relation defined in Eq. (3.50) are independent of the nominal charge capacity of the cell.

Similarly, the recurrence relation defined in Eq. (3.51) determines the incremental charge capacity loss due to calendrical degradation during the k^th interval $\Delta q_\mathrm{L,cal}[k]$, for the time elapsed during the k^th interval $t[\mathrm{k}]$ under the conditions of the degradation factor $b_\mathrm{cal,q}[k]$ when the charge capacity loss at the end of the $(k\text{-}1)^\mathrm{th}$ interval is $q_\mathrm{L}[k\text{-}1]$. Similar recurrence relations are defined in Eq. (3.52) and Eq. (3.53) for the internal resistance increase.

$$\Delta q_\mathrm{L,cyc}[k] = b_\mathrm{cyc,q}[k]\left[\left(\frac{q_\mathrm{L}[k-1]}{b_\mathrm{cyc,q}[k]}\right)^{1/a_\mathrm{cyc,q}} + n_\mathrm{EFC}[k]\right]^{a_\mathrm{cyc,q}} - q_\mathrm{L}[k-1] \tag{3.50}$$

$$\Delta q_\mathrm{L,cal}[k] = b_\mathrm{cal,q}[k]\left[\left(\frac{q_\mathrm{L}[k-1]}{b_\mathrm{cal,q}[k]}\right)^{1/a_\mathrm{cal,q}} + t[k]\right]^{a_\mathrm{cal,q}} - q_\mathrm{L}[k-1] \tag{3.51}$$

$$\Delta r_{\mathrm{i,cyc}}[k] = b_{\mathrm{cyc,r}}[k]\left[\left(\frac{r_{\mathrm{i}}[k-1]}{b_{\mathrm{cyc,r}}[k]}\right)^{1/a_{\mathrm{cyc,r}}} + n_{\mathrm{EFC}}[k]\right]^{a_{\mathrm{cyc,r}}} - r_{\mathrm{i}}[k-1] \tag{3.52}$$

$$\Delta r_{\mathrm{i,cal}}[k] = b_{\mathrm{cal,r}}[k]\left[\left(\frac{r_{i}[k-1]}{b_{\mathrm{cal,r}}[k]}\right)^{1/a_{\mathrm{cal,r}}} + t[k]\right]^{a_{\mathrm{cal,r}}} - r_{\mathrm{i}}[k-1] \tag{3.53}$$

The charge capacity loss at the end of the k^{th} interval $q_{\mathrm{L}}[k]$ is determined by adding the incremental changes $\Delta q_{\mathrm{L,cal}}[k]$ and $\Delta q_{\mathrm{L,cyc}}[k]$ to the charge capacity loss at the end of the $(k\text{-}1)^{\mathrm{th}}$ interval $q_{\mathrm{L}}[k\text{-}1]$, as defined in Eq. (3.54). Similarly, the resistance increase at the end of the k^{th} interval $r_{\mathrm{i}}[k]$ is determined by adding the incremental changes $\Delta r_{\mathrm{i,cal}}[k]$ and $\Delta r_{\mathrm{i,cyc}}[k]$ to the resistance increase at the end of the $(k\text{-}1)^{\mathrm{th}}$ interval $r_{\mathrm{i}}[k\text{-}1]$, as defined in Eq. (3.55).

$$q_{\mathrm{L}}[k] = q_{\mathrm{L}}[k-1] + \Delta q_{\mathrm{L,cyc}}[k] + \Delta q_{\mathrm{L,cal}}[k] \tag{3.54}$$

$$r_{\mathrm{i}}[k] = r_{\mathrm{i}}[k-1] + \Delta r_{\mathrm{i,cyc}}[k] + \Delta r_{\mathrm{i,cal}}[k] \tag{3.55}$$

The degradation factors are based on the relations identified in Schmalstieg et al. (2014). Calendrical degradation factors depend on the voltage across the cell electrodes and the cell temperature. The relationship between degradation factors and terminal voltage is linear, whereas the relationship between degradation factors and temperature is exponential following the Arrhenius equation. In order to obtain a degradation model that is independent of the characteristic of open circuit voltage over SoC, the dependence on voltage is replaced with a dependence on SoC. Therefore, the calendrical degradation factors can be expressed as a function of temperature and SoC. Equation (3.56) defines the calendrical degradation factor of charge capacity $b_{\mathrm{cal,q}}$, whereas Eq. (3.57) defines the calendrical degradation factor of internal resistance $b_{\mathrm{cal,r}}$, where ϑ_{c} denotes the cell temperature in Kelvin. The values of the parameters $k_{cal,q1}$, $k_{cal,q2}$, $k_{cal,r1}$ and $k_{cal,r2}$ correspond to those identified in Schmalstieg et al. (2014) and can be found in Table A.7.

$$b_{\mathrm{cal,q}} = k_{\mathrm{cal,q1}}\left(k_{\mathrm{cal,q2}} + q_{\mathrm{s}}\right)e^{-k_{\mathrm{cal,q3}}/\vartheta_{\mathrm{c}}} \tag{3.56}$$

$$b_{\mathrm{cal,r}} = k_{\mathrm{cal,r1}}\left(k_{\mathrm{cal,r2}} + q_{\mathrm{s}}\right)e^{-k_{\mathrm{cal,r3}}/\vartheta_{\mathrm{c}}} \tag{3.57}$$

Cell manufacturers usually provide little information about the calendrical degradation, but they typically specify the cell cycle life under normal conditions. Therefore, the degradation model of Schmalstieg et al. (2014) is only qualitatively used to be parametrized with the manufacturer specification for the degradation of the lithium-ion cells used in the investigation. A linear relationship between cycle depth and cyclic degradation and a quadratic relationship between SoC and cyclic degradation was observed in Schmalstieg et al. (2014). Since manufacturer information is usually scarce to quantify the effect of SoC on cyclic degradation, the cycle depth Δq_{s} is the only variable used to determine the cyclic degradation factors in this work. The cyclic degradation factor of charge capacity is defined in Eq. (3.58) and the cyclic degradation factor of internal resistance is defined in Eq. (3.59). The values of the parameters $k_{\mathrm{cyc,q1}}$, $k_{\mathrm{cyc,q2}}$, $k_{\mathrm{cyc,r1}}$ and $k_{\mathrm{cyc,r2}}$ are listed in Table A.7.

$$b_{\mathrm{cyc,q}} = k_{\mathrm{cyc,q1}} + k_{\mathrm{cyc,q2}}\Delta q_{\mathrm{s}} \tag{3.58}$$

$$b_{\mathrm{cyc,r}} = k_{\mathrm{cyc,r1}} + k_{\mathrm{cyc,r2}}\Delta q_{\mathrm{s}} \tag{3.59}$$

Nominal Equivalent Full Cycles

The nominal number of cycles N_N specified by the cell manufacturer does not correspond to the number of equivalent full cycles until EoL. The equivalent full cycles until EoL are lower than the nominal cycles N_N for two reasons. First the cell manufacturers specify the nominal cycles only for a fraction of the maximum cycle depth. Second the equivalent full cycles correspond to the charge exchanged through the cell, whereas the nominal cycles refer to the cycles within a certain voltage range at the cell terminals. Since the charge capacity of the cell decreases with degradation, less charge can be exchanged per cycle within the same voltage range. A relationship between the equivalent full cycles until EoL and the nominal cycles specified by the manufacturer should thus be derived, considering that the equivalent full cycles until EoL correspond to the charge throughput throughout the degradation test that the manufacturer conducted to determine the nominal cycles.

Let x be a real variable that represents the number of undergone cycles during a cyclic degradation test. Further, according to the manufacturer specification for the test conditions; $\Delta q_{s,N}$ corresponds to the cycle depth and N_N to the number of cycles until the charge capacity reaches $q_{c,EoL}$ that corresponds to the EoL of the cell. The equivalent full cycles until EoL or, equivalently, the nominal equivalent full cycles $n_{EFC,N}$ correspond to the nominal cycle depth times the integral of the decreasing charge capacity q_c over the undergone cycles up to N_N

$$n_{\mathrm{EFC,N}} = \Delta q_{\mathrm{s,N}} \int_0^{N_\mathrm{N}} q_\mathrm{c}(x)\,\mathrm{d}x. \tag{3.60}$$

Replacing the charge capacity q_c in Eq. (3.60) with the relationship that connects it to the complementary degradation state q_L defined in Eq. (3.48) results in

$$n_{\mathrm{EFC,N}} = \Delta q_{\mathrm{s,N}} \int_0^{N_\mathrm{N}} [1 - q_\mathrm{L}(x)]\,\mathrm{d}x\,. \tag{3.61}$$

Considering that the number of test cycles is the quantity that causes the degradation of the lithium-ion cells, the relationship between the degradation state $q_L(x)$ and the number of test cycles x corresponds to the nonlinear degradation function defined in (3.47), hence

$$n_{\mathrm{EFC,N}} = \Delta q_{\mathrm{s,N}} \int_0^{N_\mathrm{N}} (1 - bx^a)\,\mathrm{d}x, \tag{3.62}$$

which results in

$$n_{\mathrm{EFC,N}} = \Delta q_{\mathrm{s,N}} \left(N_\mathrm{N} - \frac{b {N_\mathrm{N}}^{a+1}}{a+1} \right). \tag{3.63}$$

By the time the undergone cycles in the degradation test reach the nominal cycles N_N, the charge capacity equals $q_{c,EoL}$. Therefore, according to Eq. (3.47), assuming a constant degradation factor throughout the degradation process, the degradation factor should be

$$b = \frac{1 - q_{\mathrm{c,EoL}}}{N_\mathrm{N}^a}. \tag{3.64}$$

Replacing the degradation factor derived in Eq. (3.64) into Eq. (3.63) leads to

$$n_{\mathrm{EFC,N}} = \Delta q_{\mathrm{s,N}}\, N_\mathrm{N} \left(1 - \frac{1 - q_{\mathrm{c,EoL}}}{a+1}\right) = \Delta q_{\mathrm{s,N}}\, N_\mathrm{N} \frac{a + q_{\mathrm{c,EoL}}}{a+1}. \tag{3.65}$$

Thus, a relationship between the nominal equivalent cycles $n_{EFC,N}$ and the nominal cycles N_N defined by the manufacturer is derived. For example, for the linear degradation case that corresponds to the exponent $a=1$, according to Eq. (3.65), the equivalent full cycles are $\frac{1}{2}\Delta q_{\mathrm{s,N}} N_{\mathrm{N}}\left(1+q_{\mathrm{c,EoL}}\right)$.

The derived relationship between $n_{\mathrm{EFC,N}}$ and N_{N} can therefore be used to estimate the charge capacity over the equivalent full cycles. Defining the degradation factor

$$b=\frac{1-q_{\mathrm{c,EoL}}}{n_{\mathrm{EFC,N}}^{a}},$$

so that, according to the degradation function defined in Eq. (3.47), the point ($q_{\mathrm{c,Eol}}$, $n_{\mathrm{EFC,N}}$) corresponds to the EoL of the lithium-ion cell, the qualitative characteristic of the normalized charge capacity q_{c} over the equivalent full cycles n_{EFC} for the exponents $a<1$, $a=1$ and $a>1$ is drawn in Figure 3.11.

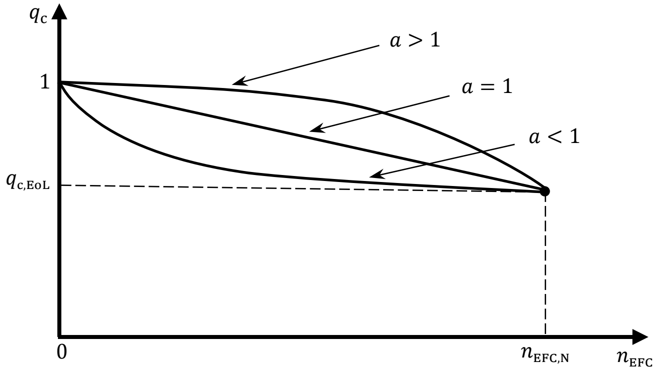

Figure 3.11 Qualitative characteristic of the normalized charge capacity q_{c} over the number of equivalent full cycles n_{EFC}. All curves end to the same EoL point ($q_{\mathrm{c,EoL}}$, $n_{\mathrm{EFC,N}}$).

Cyclic Degradation Coefficients

The coefficients for the cyclic degradation are determined using the technical data specified by the manufacturer and the nonlinear degradation function defined in Eq. (3.47). For the nonlinear degradation model used, degradation states from at least two separate degradation tests with different cycle depths are required. However, cell manufacturers usually declare the results of a single degradation test with a relatively high cycle depth. Therefore, a maximum number of equivalent full cycles $n_{\mathrm{EFC,max}}$ regardless of the cycle depth is assumed in this work, which is defined as the product of the nominal equivalent full cycles and the factor $k_{\mathrm{EFC,max}}$, that is $n_{\mathrm{EFC,max}}=k_{\mathrm{EFC,max}} n_{\mathrm{EFC,N}}$. The maximum number of equivalent full cycles corresponds to the number of equivalent full cycles under infinitesimal cycle depth Δq_{s} that result in the same degradation as the nominal equivalent full cycles under the nominal cycle depth. In other words, as the cycle depth approaches zero, the maximum equivalent full cycles that can be achieved approach $n_{\mathrm{EFC,max}}$. Consequently, substituting $\Delta q_{\mathrm{s}}=0$ into Eq. (3.58) and then substituting the resulting relationship for the degradation factor into Eq. (3.47) with $x=n_{\mathrm{EFC,max}}$ and $y=q_{\mathrm{c,EoL}}$, determines the first cyclic degradation coefficient for the charge capacity

$$k_{\mathrm{cyc,q1}}=\frac{1-q_{\mathrm{c,EoL}}}{n_{\mathrm{EFC,max}}^{a_{\mathrm{cyc,q}}}}. \tag{3.66}$$

The nominal equivalent cycles $n_{\mathrm{EFC,N}}$ are determined according to Eq. (3.65) using the manufacturer specification about the nominal cycles N_{N} under the nominal cycle depth $\Delta q_{\mathrm{s,N}}$. Thus, the degradation coefficient $k_{\mathrm{cyc,q2}}$ can be determined by substituting the relationship for the degradation factor according to Eq. (3.58) using the known values of $\Delta q_{\mathrm{s,N}}$ and $k_{\mathrm{cyc,q1}}$ into Eq. (3.47) with $x = n_{\mathrm{EFC,N}}$ and $y = q_{\mathrm{c,EoL}}$, which results in

$$k_{\mathrm{cyc,q2}} = \frac{1}{\Delta q_{\mathrm{s,N}}}\left(\frac{1 - q_{\mathrm{c,EoL}}}{n_{\mathrm{EFC,N}}^{a_{\mathrm{cyc,q}}}} - k_{\mathrm{cyc,q1}}\right).$$

Cell manufacturers usually provide no information about the internal resistance increase due to degradation. Therefore, a value should be assumed for the normalized internal resistance at EoL $r_{\mathrm{s,EoL}}$. Considering that $r_{\mathrm{s,EoL}}$ is reached either when the cycles $n_{\mathrm{EFC,max}}$ are undergone at infinitesimal cycle depth or the cycles $n_{\mathrm{EFC,N}}$ are undergone at nominal cycle depth, the cyclic degradation coefficients for the internal resistance are determined as those for the charge capacity using Eq. (3.59) and Eq. (3.47), which yields

$$k_{\mathrm{cyc,r1}} = \frac{r_{\mathrm{s,EoL}} - 1}{n_{\mathrm{EFC,max}}^{a_{\mathrm{cyc,r}}}},$$

and

$$k_{\mathrm{cyc,r2}} = \frac{1}{\Delta q_{\mathrm{s,N}}}\left(\frac{r_{\mathrm{s,EoL}} - 1}{n_{\mathrm{EFC,N}}^{a_{\mathrm{cyc,r}}}} - k_{\mathrm{cyc,r1}}\right).$$

The coefficients for the cyclic degradation of the lithium-ion cells are determined with the aid of the manufacturer degradation data listed in Table A.3. The coefficients for both cyclic and calendrical degradation are summarized in Table A.7.

3.3 Power Converters

Power converters are required in order to integrate flywheels and batteries into power grids that impose voltage and frequency, including DC grids. Since the losses of power converters add to the total losses of an energy storage, they are estimated in order to increase the accuracy of the loss model. As power converters are systems that comprise several electronic components, such as semiconductors, capacitors and inductors, several locations of power dissipation exist. However, the load losses of power converters mainly occur in their semiconductors. Although power converters have also no-load losses, for instance due to leakage currents in capacitors and semiconductors, they account for a small proportion of the total losses at nominal load. Nevertheless, when power converters include transformers or chokes with iron core, the no-load losses may account for a considerable proportion of the total losses. The control unit of power converters is often powered by auxiliary power supplies at low voltage and therefore its consumption can be considered as basic equipment losses instead of power converter losses.

Power losses in semiconductors are divided into conduction, reverse and switching losses (Michel, 2011). At high load, the conduction losses mainly depend on the *root mean square* (rms) current through the semiconductors. The reverse losses depend on the profiles of reverse current and voltage, whereas the switching losses depend on the switching frequency as well as the profiles of current and voltage during the switching process. If the switching frequency is constant, the switching losses depend only on the voltage and current profiles during switching with higher switching currents leading to higher losses. Therefore, for constant switching frequency, the power converter losses can approximately be expressed as a univariate function of the current through the semiconductors.

Since the investigation does not focus on a specific power converter or semiconductor type, modelling the power converter losses in detail is of minor importance. The power load of power converters is rather inappropriate to estimate their power losses, as due to variable voltage it is not directly linked to the current through the semiconductors. It is therefore assumed that the power converter losses are roughly proportional to the square of the root mean square (rms) current through the semiconductors. For DC-3xAC converters, the rms phase current on the AC side is considered, whereas for DC-DC converters the current on the side that is actively switching is relevant.

The per unit system is widely used in power system analysis, especially in power flow calculations that involves several voltage levels (Kundur, 1994). Using the per unit system, the per unit power converter losses p_L are defined as the power converter losses P_L over the nominal apparent power S_N of the power converter, that is

$$p_{\mathrm{L}} = \frac{P_{\mathrm{L}}}{S_{\mathrm{N}}}. \tag{3.67}$$

A quadratic relationship between the power converter losses P_L and the power converter current I is assumed, that is $P_L=R_{pc}I^2$, where R_{pc} is the equivalent resistance of the power converter. Since the per unit current is $i=I/I_N$ and the base impedance is $Z_b = S_N/I_N^2$, using Eq. (3.67) the per unit power converter losses can be expressed as

$$p_{\mathrm{L}} = \frac{R_{\mathrm{pc}}I^2}{S_{\mathrm{N}}} = \frac{R_{\mathrm{pc}}I^2}{Z_b I_{\mathrm{N}}^2} = \frac{R_{\mathrm{pc}}}{Z_b}\left(\frac{I}{I_{\mathrm{N}}}\right)^2 = r_{\mathrm{pc}}i^2, \tag{3.68}$$

where r_{pc} is the per unit equivalent resistance of the power converter. Considering that the nominal power converter losses $P_{L,N}$ correspond to the power losses for the nominal power converter current I_N, according to Eq. (3.68) the per unit nominal power converter losses $p_{L,N}$ equal the per unit equivalent resistance r_{pc}.

The technical data of the power converters used in the combined storage prototypes hsSWIVT and hsETA are listed in Table A.10. The per unit nominal (maximum) power losses of the four power converters range from 0.02 pu to 0.03 pu and average at 0.025 pu. For power converters that operate at constant switching frequency and their power losses at nominal current are known, Eq. (3.68) can be used to estimate their power losses at any current. Furthermore, the equivalent resistance r_{pc}=0.025 pu can be assumed for power converters that have a similar power rating as those listed in Table A.10

3.4 Cycle Efficiency

Flywheels and batteries are modelled as closed systems which can exchange heat and work with their surroundings but no matter. Although flywheels and batteries exchange electric charge with their surroundings, it is assumed that exchange of electric charge corresponds to pure work exchange. According to the first law of thermodynamics, the change in the internal energy of a closed system equals the heat transferred to the system minus the work done by the system on its surroundings. The internal energy change ΔE_i of a closed system such as an energy storage system equals the total energy exchange E_{ex} with its surroundings, that is

$$\Delta E_{\mathrm{i}} = E_{\mathrm{ex}}. \tag{3.69}$$

Positive sign corresponds by definition to energy transferred to the system, whereas negative sign corresponds to energy withdrawn from the system. To distinguish between heat and work, the work exchange is denoted by E_w, whereas the heat exchange is denoted by E_Q, so that the total energy exchange is expressed as

$$E_{ex} = E_w + E_Q. \tag{3.70}$$

The work exchange equals the work $E_{w,in}$ supplied to the storage minus the work $E_{w,out}$ withdrawn from the storage, that is

$$E_w = E_{w,in} - E_{w,out}, \tag{3.71}$$

where $E_{w,in}$ and $E_{w,out}$ can only assume nonnegative values. It is assumed that the energy storage only dissipates heat to its surroundings and therefore E_Q can only assume negative values. Therefore, the heat exchange equals the negative heat E_L dissipated by the storage to its surroundings due to energy conversion losses, that is

$$E_Q = -E_L. \tag{3.72}$$

Consequently, combining Equations (3.69), (3.70), (3.71) and (3.72) the internal energy change of the storage system can be expressed as

$$\Delta E_i = E_{w,in} - E_{w,out} - E_L. \tag{3.73}$$

Equation (3.73) is useful in order to experimentally estimate the energy losses in a storage by measuring the work exchange E_w between the storage and its surroundings and estimating the internal energy change ΔE_i in the same storage. Considering Eq. (3.73), the cycle efficiency of an energy storage system is defined as

$$\eta = \begin{cases} \dfrac{E_{w,out}}{E_{w,in} - \Delta E_i}, & \Delta E_i < 0 \\ \\ \dfrac{E_{w,out} + \Delta E_i}{E_{w,in}}, & \Delta E_i \geq 0. \end{cases} \tag{3.74}$$

According to the definition of the cycle efficiency, the internal energy change is considered as a cost when negative but as benefit when positive, which is reasonable from the storage system perspective as it is preferred to store than withdraw energy. The cycle efficiency as a function of the internal energy change ΔE_i is continuous at $\Delta E_i=0$ provided that $E_{w,in}>0$. An advantage of the cycle efficiency described by Eq. (3.74) is that the η is defined also for cases of unidirectional power flow. If $\Delta E_i<0$ and $E_{w,in}=0$, η corresponds to a pure generator efficiency, whereas if $\Delta E_i>0$ and $E_{w,out}=0$, η corresponds to a pure storage efficiency. Including the internal energy change in the definition of the cycle efficiency enables the efficiency estimation for cycles in which the storage system does not return to the initial energy state, that is, $\Delta E_i \neq 0$. If a cyclic load profile is repeated several times so that the internal energy change is considerably lower than both the energy $E_{w,in}$ supplied to the storage and the energy $E_{w,out}$ withdrawn from the storage, the cycle efficiency approximates

$$\eta \approx \frac{E_{w,out}}{E_{w,in}}.$$

4. Sizing

The size of storage systems depends on the application requirements such as the requirements for the provision of balancing services to the electricity grid. Flexibilities in the application requirements and different storage technologies can be exploited to pursue optimization goals, such as the minimization of investment and operating cost. Although the sizing of combined storage systems goes beyond the sizing of the individual storage units, the individual storage units that make up a combined storage should also be sized. Moreover, the power converters that integrate the individual storage units into the combined storage should also be sized.

4.1 Power Rating of Energy Storages

Electrical equipment is usually rated at the maximum terminal power under which it should be able to operate continuously, which applies both for loads and generators. The requirement to continuously operate the equipment at rated power relates to the power losses and the corresponding heat dissipation under which the equipment remains thermally stable. The heat dissipation depends on the equipment design as well as on external conditions, such as the ambient and eventually the cooling temperature. Consequently, the equipment manufacturer should specify the power rating, along with the permissible range of external conditions. Furthermore, derating curves as a function of varying external conditions are also often provided.

The nominal voltage of electrical equipment usually corresponds to the expected operating voltage and is lower than the maximum permissible voltage. On the contrary, the nominal current usually corresponds to the maximum continuous current. Therefore, currents above the nominal current are unacceptable, except for a short time overload. The power losses of electrical equipment mainly depend on the current magnitude and frequency. Thus, the rated power of electrical equipment usually corresponds to the product of nominal voltage and nominal current within a permissible frequency range.

Energy storages both sink and source power. Reversing the power flow at the equipment terminals implies a reverse current of the same magnitude provided that the voltage remains unchanged. Consequently, the power losses and the corresponding thermal behaviour of energy storages should be unaffected when reversing the power flow. If energy storages have considerable asymmetries under reverse power flow, separate power ratings for load and generator operation should be specified. For small asymmetries, the manufacturer can specify the lowest between the maximum load and the maximum generator power as the rated power.

The available power increases with speed for flywheels and with voltage for batteries. However, energy storages such as batteries and flywheels usually need to reduce their terminal power when approaching their energy state limits. Therefore, the power constraints of energy storages over their energy state have a characteristic like that illustrated in Figure 4.1, in which a nearly symmetrical operation is assumed. The energy state w_{up} and the power P_{up} correspond to the point at which the power flow into the storage should be decreased, whereas the energy state w_{lo} and the power $-P_{lo}$ correspond to the point at which the power flow out of the storage should be decreased. If $P_{lo} \leq P_{up}$, the manufacturer may specify P_{lo} as the rated power for the energy state range between w_{lo} and w_{up}, since the storage can operate bidirectionally and continuously between w_{lo} and

w_{up} for a power magnitude as high as P_{lo}. Specifying a power higher than P_{lo} as the rated power should be aligned with the specification of a narrower energy state range, which implies that the rated energy capacity is reduced. Setting w_{lo} and w_{up} at the energy state extrema, that is w_{lo}=0 and w_{up}=1, constitutes another option which implies that P_{lo} cannot be applied in the complete energy state range.

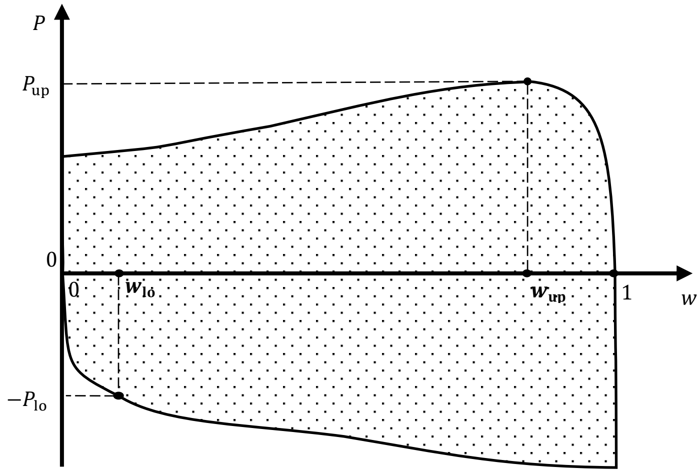

Figure 4.1 Characteristic of power constraints over energy state for energy storages

Considering Figure 4.1, the following quantities can be specified by the manufacturer, for instance, in the rating plate of an energy storage:

- the nominal power P_N=P_{lo} that corresponds to the maximum continuous power in the energy state range of w_{lo} to w_{up}
- the nominal current I_N=I_{max} that corresponds to the maximum continuous current in the energy state range of w_{lo} t w_{up}
- the maximum permissible voltage U_{max} across the terminals of the energy storage
- the nominal voltage U_N that corresponds to the middle of the energy state range, that is,
  - the average open circuit voltage of a lithium-ion cell times the number of cells connected in series for a battery,
  - the stator voltage corresponding to the angular frequency $\omega_{m,m}$ as shown in Figure 3.1 for a flywheel
- the nominal rotational speed n_N in revolutions per minute corresponding to $\omega_{m,m}$ for a flywheel
- the minimum permissible voltage U_{min} across the terminals of a battery

4.2 Power Converter Rating

Due to variable voltage at the terminals of energy storages, power converters are usually necessary in order to form a system that combines several storages. Electric machines are characterized by a maximum permissible continuous current in the stator windings, whereas flywheels by a maximum permissible angular speed. The power converter should be able to supply the maximum continuous current of the electric machine to fully exploit its rating. Neglecting the ohmic voltage drop in the stator windings and considering that the machine operates at motor mode with a current that comprises only a quadrature component, the maximum amplitude of the fundamental line-to-line voltage at the machine terminals is

$$\hat{U}_{\mathrm{s,LL,max}} = \sqrt{3}p\omega_{\mathrm{m,max}}\sqrt{\Psi_{\mathrm{p}}^2 + 2\left(L_{\mathrm{h}}I_{\mathrm{s,max}}\right)^2}, \tag{4.1}$$

where $\omega_{\mathrm{m,max}}$ is the maximum permissible speed of the flywheel and $I_{\mathrm{s,max}}$ is the maximum continuous phase current of the electric machine (Binder, 2017, pp. 670-674). The fundamental line-to-line voltage across the terminals of the electric machine should be lower than the voltage on the DC side of the power converter at motor operation. Therefore, an AC-DC converter capable to drive the flywheel up to its maximum speed, without employing field weakening, should be able to apply a voltage as high as $\hat{U}_{\mathrm{s,LL,max}}$ on its DC side. According to Eq. (4.1), the voltage drop across the main inductance increases the line-to-line voltage and causes reactive power flow, which reduces the power factor of the electric machine. Therefore, the rating of AC-DC power converters is specified in kVA, as they often supply capacitive or inductive loads such as electric machines. Defining the nominal current of the power converter of the flywheel storage as high as the maximum continuous phase current of the electric machine

$$I_{\mathrm{fw,pc,N}} = I_{\mathrm{s,max}}, \tag{4.2}$$

the nominal apparent power of the power converter should be

$$S_{\mathrm{fw,pc,N}} = \sqrt{3}/\sqrt{2}\,\hat{U}_{\mathrm{s,LL,max}}\,I_{\mathrm{s,max}}. \tag{4.3}$$

A nominal current of the power converter that is lower than the maximum continuous current of the electric machine limits the power of the storage over the complete energy state range presented in Figure 4.1. On the other hand, a voltage on the DC side of the power converter that is lower than $\hat{U}_{\mathrm{s,LL,max}}$ limits the storage power only at the high energy state range. However, due to standardization, the typical voltage levels for power converters are only a few. Furthermore, if an energy storage should be integrated into a DC grid, the voltage on the DC side of the power converter is determined by the grid voltage, unless an additional conversion stage is implemented.

The switching frequency of power converters can be a limiting factor for high-speed machines. For block commutation, the switching frequency equals the electrical frequency of the machine, whereas for pulse width modulation the switching frequency should be considerably higher than the electrical frequency of the machine.

The power converter of the battery storage should be able to carry the maximum continuous battery current and operate the battery up to its maximum voltage $U_{\mathrm{b,max}}$. The maximum voltage of the battery depends on the number and the maximum voltage of the lithium-ion cells used. The maximum continuous current of the battery $I_{\mathrm{b,max}}$ can be only applied above w_{lo} when discharging and below w_{up} when charging as shown in Figure 4.1, otherwise the current should be limited to keep the voltage of the lithium-ion cells within the permissible range. If the battery is connected into a DC grid, a DC-DC converter can be used. Independent of the selection of AC-DC or DC-DC conversion, the power converter should be able to carry the maximum continuous battery current

$$I_{\mathrm{b,pc,N}} = I_{\mathrm{b,max}}, \tag{4.4}$$

when the maximum battery voltage applies on the battery side.

Therefore, the apparent power of the power converter should be

$$S_{\mathrm{b,pc,N}} = U_{\mathrm{b,max}} I_{\mathrm{b,max}}. \tag{4.5}$$

The maximum continuous current of lithium-ion cells is less significant for applications that require energy capacity rather than power capacity. In high energy capacity applications, the current rating of the power converter may be lower than the maximum continuous current of the battery. From the power electronics perspective, it is advantageous that the variable battery voltage is always either above or below the voltage on the other side of the power converter. In other words, the power converter has no overlapping voltage, which can reduce the number of required semiconductors.

4.3 Energy to Power Ratio

The ratio of nominal energy capacity E_{N} to nominal power capacity P_{N} of energy storages

$$T_{\mathrm{N}} = \frac{E_{\mathrm{N}}}{P_{\mathrm{N}}},$$

has the unit of time and is named *energy to power ratio*. For example, if the energy capacity is expressed in kWh and the power capacity in kW, the energy to power ratio corresponds to the time in hours that an energy storage can operate unidirectionally at nominal power. However, due to the power constraints over energy state illustrated in Figure 4.1, the energy to power ratio only approximates the time required to operate from the minimum to the maximum energy state and vice versa, provided that the power P_{lo} annotated in Figure 4.1 corresponds to the nominal power of the energy storage.

Considering an energy storage system that comprises several storage units connected in parallel through power converters, the energy to power ratio provides an estimation of the time that the system can operate unidirectionally, but it does not provide any reliable information about the energy to power ratio of its storage units. The power converters may limit the power of the individual storage units. Furthermore, the storage units may correspond to different storage technologies with different energy to power ratios.

Generally, the energy to power ratio of storage technologies should be evaluated at unit level and not at system level, that is, a single cell for battery storages and a single flywheel for kinetic storages. From the energy technology perspective, the energy to power ratio corresponds to the ratio of specific energy to specific power. The specific energy is the available energy per unit of mass, whereas the specific power is the available power per unit of mass. The amount of useful energy is typically used to determine the specific energy, whereas the maximum power at which the storage can operate continuously over a large proportion of the available energy is typically used to determine the specific power. If a single storage technology is used to form a storage system and the available power and energy of the individual storage units are unconstrained, the energy to power ratio of the system corresponds to the ratio of specific energy to specific power of the energy storage technology applied.

The energy to power ratio of energy storage technologies can be illustrated in the so-called *Ragone* plots, which not only aim to compare different storage technologies but also different implementations within the same storage technology. Ragone plots provide system designers with an overview of the available options in order to select an energy storage technology that matches the energy to power ratio required by the application.

The energy to power ratio of a storage unit of a certain storage technology can be designed within a feasible range. The energy to power ratio of flywheels can be increased by increasing the rotor inertia, all else unchanged, or decreased by increasing the power rating of the electric machine, all else unchanged. The maximum C-rate of lithium-ion cells can be increased by increasing their outer surface and therefore improving their heat dissipation. However, an increase in the outer surface may increase the mass of the lithium-ion cell, which in turn leads to a reduction in the specific energy. The power of lithium-ion cells is usually rated so that it corresponds to C-rate of 1C, therefore, the energy to power ratio of lithium-ion cells is typically 1 h. The assumption of an energy to power ratio of 1 h for lithium-ion cells is reasonable, since C-rates higher than 1C limit their available energy. At normal conditions, lithium-ion cells can exploit a large proportion of their energy capacity when operated at 1C. Energy to power ratios in the range of several hours are unfeasible either with the flywheel or with the lithium-ion cell technologies considered in the present study. To obtain a system with an energy to power ratio in the range of hours, several storage units should be combined.

According to the technical data of the flywheel prototypes SWIVT290 and ETA290 (Table A.8 and Table A.9) as well as that of the lithium-ion cells KOKAM 46 and KOKAM 53 (Table A.4 and Table A.3), the energy density, the specific power and the energy to power ratio of each storage unit are summarized in Table 4.1 and illustrated in a Ragone plot in Figure 4.2 with logarithmic scale in both the vertical and the horizontal axes. The nominal power of the flywheel storages corresponds to the maximum power at the lower speed limit, whereas the nominal power of the lithium-ion cells corresponds to 1C at nominal voltage. The specific energy of either flywheel prototype approaches 10 Wh/kg, whereas the lowest specific energy of the lithium-ion cells approximates 150 Wh/kg, hence about 15 times higher than that of either flywheel prototype. On the other hand, the specific power of the SWIVT290 prototype is almost double the specific power of KOKAM 46. The energy to power ratio of the flywheel prototypes is in the range of a few minutes, whereas the energy to power ratio of the lithium-ion cells is 1 h, hence about 30 times higher than that of the flywheel prototypes.

Table 4.1 Specific energy, specific power and energy to power ratio according to the technical data of the flywheel prototypes SWIVT290 and ETA290 and the lithium-ion cells KOKAM 46 and KOKAM 53

Storage Technology	**Storage Unit**	**Nominal energy capacity (Wh)**	**Nominal power capacity (W)**	**Mass of storage medium (kg)**	**Specific energy (Wh/kg)**	**Specific power (W/kg)**	**Energy to power ratio**
Flywheel	ETA290	1400	60 000	153	9.2	392	84 s
	SWIVT290	1800	50 000	170.6	10.5	293	130 s
Lithium-ion cell	KOKAM 46	170.2	170.2	1.145	149	149	1 h
	KOKAM 53	196.1	196.1	1.095	179	179	1 h

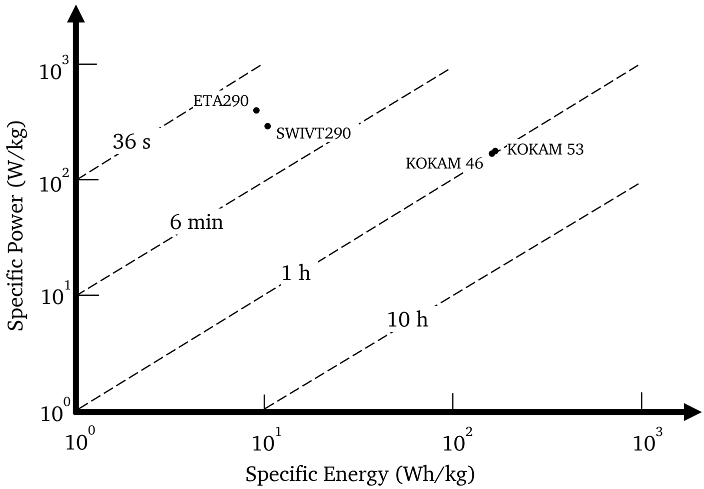

Figure 4.2 Log-log Ragone plot depicting the flywheel prototypes ETA290 and SWIVT290, and the lithium-ion cells KOKAM 46 and KOKAM 53. The energy to power ratio of both flywheels is in the range of a few minutes, whereas the energy to power ratio of both lithium-ion cells equals by definition one hour. The specific energy of the lithium-ion cells is about 15 times higher than that of the flywheels, whereas the specific power of the flywheels is about double the specific power of the lithium-ion cells.

4.4 Sizing for Grid Balancing Services

Grid balancing services are aimed at compensating for power imbalances and thus correcting the frequency of synchronous electrical grids towards the reference frequency. In the past, grid balancing services were predominantly provided by conventional power plants that regulated their output power according to the grid frequency. The liberalisation of the electricity market gave the chance to small electric utilities to participate in the tendering of balancing reserve power. Furthermore, technological improvements in electrochemical storages followed by decreasing prices due to the growing electrification of the vehicle fleet made electrochemical storages an economical alternative for grid balancing services. The main drawback of electrochemical storages compared to conventional technologies for grid balancing services is their pronounced degradation. On the other hand, flywheel storages show a much less remarkable degradation than electrochemical storages, both cyclic and calendrical. Therefore, flywheel storages can effectively complement electrochemical storages to provide balancing services by reducing the load share of electrochemical storages and consequently their degradation.

Characteristics of the Electrical Grid Frequency

Although the course of the grid frequency is a stochastic process, it includes the effects of deterministic processes, such as the hourly and quarter-hourly trading intervals and the *dispatch* of power plants. The disturbances caused by a new dispatch of power plants result in surges or sags in the grid frequency that follow an exponential decay, the time constant of which depends on the inertia and the damping of the power grid (Schäfer, et al., 2018). According to Schäfer et al. (2018), deterministic processes in power grids such as the quarter-hourly trading intervals lead to a probability density function of the grid frequency with heavy tails that significantly deviates from that of a normal distribution.

The histogram in Figure 4.3 presents the probability distribution of the grid frequency of continental Europe sampled each second for 24 hours on 01 October 2021 starting at 00:00:01 made available by TransnetBW GmbH. The width of each bin is 10 mHz. The height of each bin corresponds to the probability that the grid frequency would lie within the corresponding frequency interval. It is observed that the mean frequency approaches 50 Hz as expected for the power grid of continental Europe. In particular, the mean frequency is only 0.07 mHz over 50 Hz and the standard deviation is 2.12 mHz. Moreover, grid frequency deviations from 50 Hz higher than 5 mHz have a probability below 2.5 %. Although the probability distribution presented in Figure 4.3 seems to be normal, in the general case, the probability distribution of the grid frequency of continental Europe deviates from the normal distribution (Schäfer, et al., 2018).

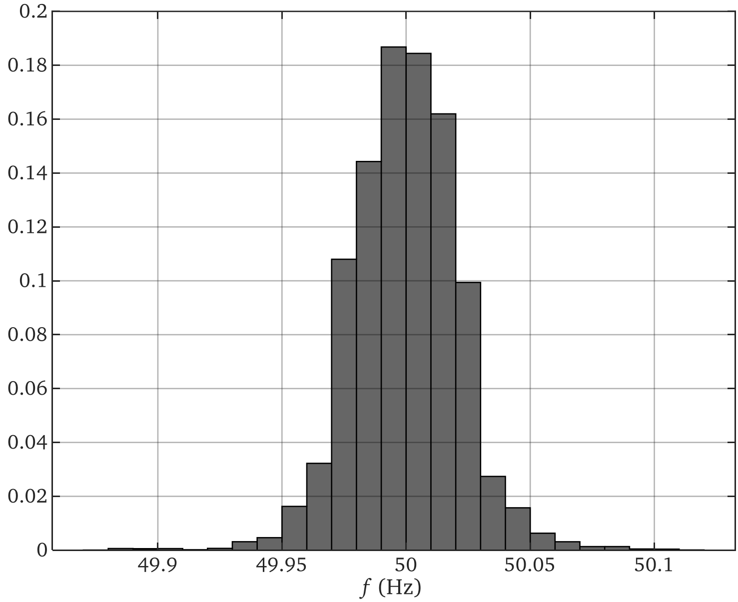

Figure 4.3 Probability distribution of the grid frequency of continental Europe measured for 24 hours with a sampling period of 1 s on 01.10.2021 starting at 00:00:01. The width of each bin is 10 mHz.

Frequency Containment Reserve

To exploit the fast dynamics of electrochemical energy storages for grid balancing services, a combination with conventional power plants is expedient. Forming a group of several *reserve providing units* to provide balancing services is a practice described both in Regulation 2017/1485-Establishing a guideline on electricity transmission system operation issued by the European Commission, hereafter SO GL, as well as in the Prequalification Process for Balancing Service Providers issued by the German Transmission System Operators (TSOs), hereafter PQ Conditions. According to the PQ conditions, it is possible to connect several *technical units* at different grid locations to form a *reserve providing group* or a *pool*, as long as the power of each technical unit is independently measured.

The development of the balancing reserve market in Germany led to a minimum bid of 1 MW and to a minimum bid increment of 1 MW for balancing reserve products. Leading role to the definition of the bid volume has the German Federal Network Agency (Bundesnetzagentur). The reserve providing units neither need to be physically in the same place nor to have a power capacity over 1 MW as they can be combined to form a balancing reserve group according to SO GL. Several products are traded in the balancing reserve market of continental Europe, from which the Frequency Containment Reserve (FCR) is favourable for energy storages as it concerns a symmetrical power profile. Before July 2019 the tendering of FCR took place on a weekly basis and the tender winners committed to provide FCR continuously for one week. The decision with reference number BK6-18-006 of the German Federal Network Agency changed the rules so that since July 2020 the tendering closes in the day ahead and involves six individual four-hour time slots of the next day. The first time slot is from 0 h to 4 h and the last from 20 h to 24 h. The new rules have advantages for balancing service providers that operate small energy storage units, as they can exploit the reduced commitment time for FCR to find time slots in which they correct the energy state of their storage units.

According to the PQ conditions, energy storages should be able to regulate their energy *reservoir* or equivalently their energy state. Scheduled electric power flow which is exchanged either market-based or over the counter is the usual way to regulate the energy reservoir of storage systems. In this respect the intraday market and the spot market are typical examples of electricity markets. Scheduled power flow involves a certain amount of power at a certain time slot which is superimposed to the balancing reserve power. In order to save an additional grid connection or measuring point for the energy storage system, the grid connection used for balancing services can also carry the power corresponding to scheduled power flow. Although the operating point of the storage system shifts away from the required balancing reserve power, the shift corresponds to scheduled power flow, which is traceable by the TSO that controls whether the provided power at the measuring point matches the required power. Consequently, no additional connection or measuring point than that for balancing reserve is necessary, as long as only scheduled and communicated to the TSO power flow is involved. Although energy markets provide a convenient way to correct the energy state of storage units, a minimum bid increment of 100 kW applies currently in Germany. However, if technical units belong to a balancing reserve group or a pool, a scheduled power flow that is lower than the minimum bid is also feasible.

According to the PQ conditions, the marketable power P_{MP} is the power that a balancing service provider should be able to provide for four hours, whereas the prequalified power P_{PQ} is the total power that the technical units of a balancing service provider demonstrably provided for a certain amount of time during a test. Therefore, at technical unit level, only the prequalified power is meaningful as the technical units are tested for the prequalified power and not the marketable power. A TSO should confirm the fulfilment of the prequalification conditions and award a prequalified power to a technical unit.

According to the PQ Conditions, for technical units with limited energy capacity such as energy storages, additional conditions apply; the ratio of the usable energy for FCR E_{FCR} to the prequalified power P_{PQ}, which is defined as the time T_{FCR} in Eq. (4.6), should be higher than a certain threshold which is defined by the TSOs.

$$T_{\mathrm{FCR}} = \frac{E_{\mathrm{FCR}}}{P_{\mathrm{PQ}}} \tag{4.6}$$

The TSOs, in accordance with the SO GL, require a unidirectional provision of the prequalified power for at least 15 min for the contingency in which the transmission system is in the alert state. The SO GL defines the conditions that should be met to set the transmission system to the alert state, for instance, one of the criteria is that the grid frequency continuously deviates from its reference for a certain threshold and a certain time. Consequently, according to the PQ conditions, the energy state of a storage system with respect to E_{FCR} should lie within the limits

$$
\begin{aligned}
w_{\mathrm{FCR,lo}} &= \frac{1/4\ \mathrm{h} \cdot P_{\mathrm{PQ}}}{E_{\mathrm{FCR}}} = \frac{1\ \mathrm{h}}{4T_{\mathrm{FCR}}}, \\
w_{\mathrm{FCR,up}} &= \frac{E_{\mathrm{FCR}} - 1/4\ \mathrm{h} \cdot P_{\mathrm{PQ}}}{E_{\mathrm{FCR}}} = 1 - \frac{1\ \mathrm{h}}{4T_{\mathrm{FCR}}},
\end{aligned}
\tag{4.7}
$$

when the transmission system is not in the alert state. Figure 4.4 illustrates the upper and lower energy state limits according to limits (4.7) and consequently their effect on the permissible energy state range.

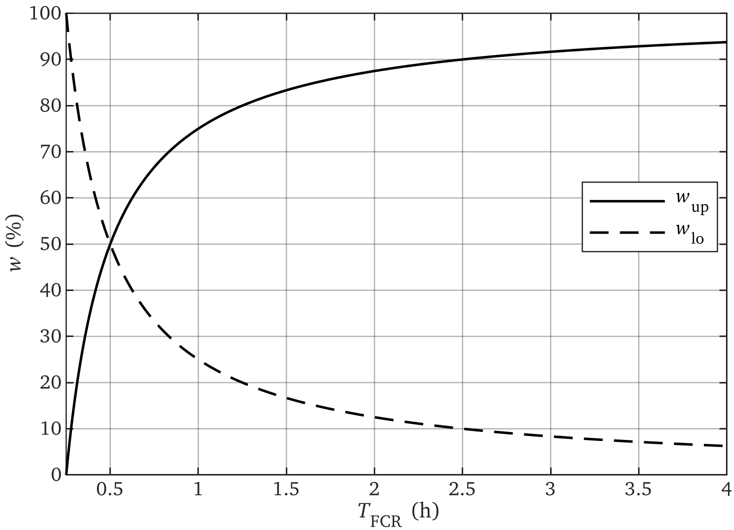

Figure 4.4 Upper w_{up} and lower w_{lo} energy state limits with respect to usable energy for FCR over the ratio of usable energy for FCR to prequalified power (T_{FCR}), so that the energy storage system can provide its prequalified power for the contingency of an alert state of 15 min in the transmission system.

It is obvious that for a T_{FCR} below 0.5 h, the permissible energy state range vanishes, whereas a T_{FCR} of 1 h results in a realisable energy state range, from $w_{FCR,lo}$=25 % to $w_{FCR,up}$=75 %, which is also reasonable for batteries as operation close to the extrema of SoC should be avoided. Although it seems that T_{FCR}=0.5 h is the theoretical minimum, the German TSOs based on the SO GL require a T_{FCR}>0.5 h for storage systems due to the effect of a previous alert activation as well as the effect of a delayed activation of the energy management. According to the interpretation of the SO GL by the German TSOs, depending on the delay of the energy management activation, there is a minimum permissible ratio of usable energy for FCR to prequalified power $T_{FCR,min}$ that ranges between 0.675 h and 0.75 h. Specifying a $T_{\mathrm{FCR,min}}$ according to the PQ conditions, the minimum energy capacity that an energy storage should have in order to provide the prequalified power P_{PQ} is

$$E_{\mathrm{FCR,min}} = T_{\mathrm{FCR,min}} P_{\mathrm{PQ}}. \tag{4.8}$$

According to the energy state limits presented in Figure 4.4, sizing the energy storage so that $T_{\mathrm{FCR,min}}$=0.675 h results in a permissible energy state range of only 26 %. Therefore, it is often reasonable to size the storage well above $E_{\mathrm{FCR,min}}$ in order to increase its availability and reduce the need of corrective measures towards the middle of its energy state.

According to the PQ conditions, power capacity requirements also apply for technical units with limited reservoir. Energy storages should be able to sink or supply a power that is 25 % higher than the prequalified power, so that when the prequalified power is fully required, corrective measures that correspond to an additional power of $0.25P_{\mathrm{PQ}}$ are available. Therefore, the minimum power capacity of energy storages with the prequalified power P_{PQ} should be

$$P_{\mathrm{FCR,min}} = 1.25 P_{\mathrm{PQ}}. \tag{4.9}$$

The *frequency deviation* Δf is defined as the deviation of the actual grid frequency f from the reference grid frequency f_{ref}, that is

$$\Delta f = f - f_{\mathrm{ref}}.$$

The reference frequency of the synchronous grid of continental Europe is 50 Hz. According to current regulations applicable to the synchronous grid of continental Europe, the prequalified power of a technical unit for FCR should be provided when the absolute frequency deviation $|\Delta f|$ is greater than or equal to 200 mHz. For small frequency deviations in the range of -10 mHz to 10 mHz, which is often referred to as deadband, special arrangements between the TSOs and the balancing service providers may apply, which dictate whether and how balancing reserve power should be provided. However, the balancing reserve provider is not allowed to supply or sink power in the opposite direction implied by the sign of the frequency deviation within the deadband. In other words, corrective measures regarding the energy state of the storage units within the deadband are permissible only when the power flow direction conforms with the sign of the frequency deviation. Assuming that either due to TSO requirements or based on a decision of the balancing reserve provider, the balancing reserve power should follow the frequency deviation also inside the deadband, the balancing reserve power for FCR is expressed as

$$P_{\mathrm{FCR}}(\Delta f) = \begin{cases} \dfrac{\Delta f}{\Delta f_{\mathrm{max}}} P_{\mathrm{PQ}}, & |\Delta f| < \Delta f_{\mathrm{max}} \\ \mathrm{sgn}(\Delta f) P_{\mathrm{PQ}}, & |\Delta f| \geq \Delta f_{\mathrm{max}}, \end{cases} \tag{4.10}$$

where Δf_{max} equals 200 mHz in the power grid of continental Europe. In other words, the balancing reserve power P_{FCR} is proportional to the frequency deviation Δf until the absolute frequency deviation reaches the maximum frequency deviation Δf_{max}, where P_{FCR} peaks at the prequalified power.

The PQ conditions allow discrepancies from the exact balancing reserve power defined in Eq. (4.10), which are based on a deadband at low frequency deviations, a minimum power ramp rate and an overfulfilment of the balancing reserve power. The permissible discrepancies can be interpreted as flexibilities by the balancing service providers. In this respect balancing service providers can program their energy management so that it exploits the available flexibilities to operate the storage units towards the middle of their energy state range.

Configuration of the Combined Storage System

There are various configuration options for energy storage systems which comprise a single storage technology. Even more configuration options arise for combined energy storage systems. Specifying the application of the energy storage system helps to narrow down the configuration options. For instance, the different requirements between autonomous and grid-connected storage systems considerably affect the set of feasible configurations because grid-connected systems should meet the conditions imposed by the grid.

The intended energy storage system should provide at least 1 MW of balancing reserve power for FCR, which makes a connection to the low-voltage network inefficient due to the resulting high current. Instead, a connection to the medium-voltage network by using a three-phase power transformer on the side of the balancing service provider as an integral part of the storage system is considered. The grid connection corresponds to the point where the energy metering instrumentation is installed.

The connection of flywheel storages to AC grids requires a two-stage conversion, that is, from variable frequency AC to DC and then to constant frequency AC. A disadvantage of the two-stage conversion is the additional investment and operating cost of the second power converter. On the contrary, connecting the flywheel storage to a DC grid results in a single-stage conversion and therefore to reduced costs. However, AC grids rather than DC grids are usually available. Generally, if several flywheel storages should be connected in parallel a DC grid turns to be an expedient investment.

For combined energy storage systems that are intended for grid balancing services, two configurations are further considered. In the first configuration presented in Figure 4.5, the batteries are connected directly to the AC grid through AC-DC power converters, hence a single-stage conversion, whereas the flywheel storages are first connected to a DC bus and then through AC-DC power converters to the AC grid. The second configuration presented in Figure 4.6 involves a common DC bus to which both flywheel and battery storages are connected by DC-DC power converters. The common DC bus is then coupled to the power grid by an AC-DC converter that carries the total power of the installation.

The configuration with single-stage conversion for the batteries has the advantage that the power rating of the AC-DC converter that integrates the flywheels into the AC grid is lower than that of the grid-side AC-DC converter in the configuration with a common DC bus. Since the grid-side power converter should bear the total load of the installation, its power losses are higher than that of the power converter required only for the flywheel storages.

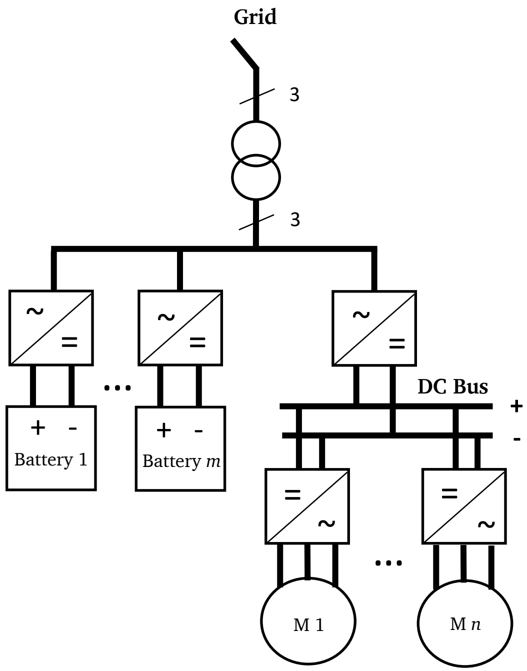

Figure 4.5 Combined storage configuration with single-stage conversion for batteries

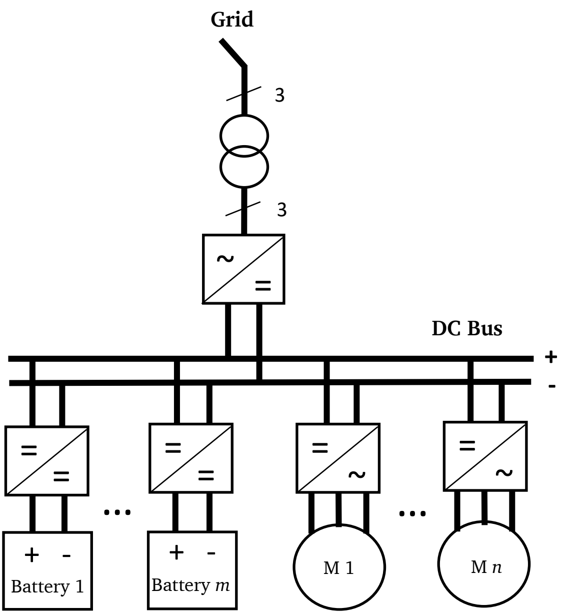

Figure 4.6 Combined storage configuration with a common DC-bus for both batteries and flywheels

A simulation study for a grid-connected battery storage for balancing services confirms the reasonable expectation that single-stage power conversion leads to lower power losses at system level (Schimpe, et al., 2018). However, the configuration presented in Figure 4.6 is used in the combined storage prototypes hsSWIVT and hsETA with the only modification that the batteries share a common DC-DC power converter. The background of the common DC bus configuration is that the grid-side converter can be rated lower than the cumulative power rating of the storage units, if the storage units are not simultaneously loaded at rated power. Furthermore, if an existing DC grid is available, for instance, in an industrial network, the grid-side converter and the power transformer are usually already available.

Several batteries can be connected in parallel using a common power converter, whereas flywheel storages always need an individual AC-DC converter to drive their electric machine. A common power converter for batteries can be implemented with either DC-AC conversion or DC-DC conversion. Although a common power converter that is shared by identical batteries is an option that can save cost, connecting batteries in parallel increases the effort required to balance their voltage.

In conclusion, although it seems that the configuration with single-stage power conversion for the batteries is more cost-efficient than the common DC-bus configuration, depending on the ratio of flywheels to batteries and eventually additional requirements, for instance, a fast charging station for electric vehicles connected to the DC bus, the common DC bus configuration can be a competitive alternative.

Sizing of the Kinetic Storage

The main objective of the kinetic storage, which may comprise several flywheels, is to contain the battery degradation by sharing part of the load. A reduced power share for the battery storage corresponds to reduced cycling degradation, which in turn may reduce the battery size required for the target service life. Generally, it is expedient to size the energy capacity of the battery as low as the minimum capacity required by the application. In other words, flywheel storages can be used instead of oversized batteries which are intended for a prolonged lifetime.

The required balancing reserve power for FCR depends on the deviation of the grid frequency from its reference as defined in Eq. (4.10). According to the probability distribution of the 24-hour grid frequency presented in Figure 4.3, the higher the deviation from the reference frequency is, the lower is its probability. Sizing the flywheel to handle high frequency deviations is rather inefficient, since the available flywheel power is not adequately exploited. However, according to the PQ conditions for FCR, energy storages should be able to provide the balancing reserve power that corresponds to the maximum frequency deviation for at least 15 min. Flywheels have significantly lower specific energy as well as energy to power ratio than lithium-ion batteries. Even if the kinetic storage is sized with a power capacity as high as the prequalified power, the requirement to provide the prequalified power for at least 15 min, makes additional flywheels necessary because the energy to power ratio of flywheels is typically below 15 min. Consequently, the battery should take the role of the long-term storage that should be able to cover long periods of unidirectional power flow, as batteries have substantially higher energy to power ratio than flywheels. On the other hand, the kinetic storage should cover the bidirectional power flow in order to reduce the battery load.

In order to maximize the power share of the kinetic storage without disproportionately increasing its size, its load should correspond to the smallest possible range of frequency deviation with a sufficiently high probability, which can be selected with the aid of the probability distribution of the grid frequency presented in Figure 4.3. Considering a frequency deviation range that is symmetrical with respect to zero, only the upper bound Δf_{ks} should be selected to determine the range of frequency deviation that the kinetic storage should handle, that is

$$|\Delta f| \leq \Delta f_{\mathrm{ks}},$$

and therefore

$$-\Delta f_{\mathrm{ks}} \leq \Delta f \leq \Delta f_{\mathrm{ks}}.$$

The expected value of the absolute frequency deviation $|\Delta f|$ below Δf_{ks} with respect to the complete set of Δf for the 24-hour course of the grid frequency is defined as $\mathrm{E}[|\Delta f| \leq \Delta f_{\mathrm{ks}}]$. Thus, considering Eq. (4.10), the expected power of the kinetic storage is defined as

$$P_{\mathrm{ks,e}} = \frac{\mathrm{E}[|\Delta f| \leq \Delta f_{\mathrm{ks}}\,]}{\Delta f_{\mathrm{max}}} P_{\mathrm{PQ}}. \tag{4.11}$$

The upper bound of the absolute frequency deviation that the kinetic storage should cover can be used to determine the maximum continuous power of the kinetic storage according to Eq. (4.10), or equivalently, the nominal power of the kinetic storage, that is

$$P_{\mathrm{ks,N}} = \frac{\Delta f_{\mathrm{ks}}}{\Delta f_{\mathrm{max}}} P_{\mathrm{PQ}}. \tag{4.12}$$

Apart from the nominal power capacity of the kinetic storage, its energy capacity should also be sized. To size the energy capacity of the kinetic storage, the typical time it operates unidirectionally should be estimated. The course of the grid frequency is a stochastic process with superimposed deterministic processes that introduce oscillations. However, the characteristics of the superimposed oscillations vary significantly. Therefore, to estimate the time that the kinetic storage operates unidirectionally, the number of *zero crossings* of the 24-hour course of the frequency deviation is counted. In other words, the points where the frequency deviation changes sign are counted. To avoid counting zero crossings that lead to a relatively short time of unidirectional power flow, a band with a width of a few mHz is introduced, so that only zero crossings that exceed the limits of the band are counted. The number of zero crossings over the duration of the frequency profile correspond to the mean time between two consecutive zero crossings $\bar{T}_{\mathrm{zc}}$. Considering that the kinetic storage should be able to operate unidirectionally providing the nominal power $P_{\mathrm{ks,N}}$ between two consecutive zero-crossings, its nominal energy capacity should be

$$E_{\mathrm{ks,N}} = P_{\mathrm{ks,N}} \bar{T}_{\mathrm{zc}}. \tag{4.13}$$

Obviously, $\bar{T}_{\mathrm{zc}}$ corresponds to the energy to power ratio of the kinetic storage. However, the energy to power ratio of the available flywheel storages is not necessarily designed to equal $\bar{T}_{\mathrm{zc}}$. If the energy to power ratio of the available flywheels lies above $\bar{T}_{\mathrm{zc}}$, the nominal power capacity $P_{\mathrm{ks,N}}$ is decisive for the number of flywheels required, whereas if the energy to power ratio of the flywheels lies below $\bar{T}_{\mathrm{zc}}$, the nominal energy capacity $E_{\mathrm{ks,N}}$ is decisive for the number of flywheels required. In this respect the number of flywheels can be minimized when their energy to power ratio approaches $\bar{T}_{\mathrm{zc}}$.

Sizing of the Battery Storage

Sizing of battery systems for grid balancing services has been addressed in several works, for instance, Zeh et al. (2016) investigated the sizing of battery systems for FCR according to the conditions of the German TSOs. However, the combination of batteries and flywheels extends the available options and flexibilities.

The energy capacity of the battery system should be at least as high as the minimum energy capacity $E_{FCR,min}$ defined in Eq. (4.8) according to the PQ conditions. Adding the energy capacity of the kinetic storage to that of the battery storage in order to reach the minimum required energy capacity has low practical importance, as the ratio of kinetic to battery energy capacity is usually insignificant. Moreover, disregarding the energy capacity of the kinetic storage in order to determine the minimum energy capacity, which is reserved for the alert state of the transmission system, simplifies the energy state management of the kinetic storage as limits (4.7) apply only for the battery storage.

Sizing the energy capacity of the battery system close to $E_{FCR,min}$ can set the installation unable to provide the prequalified power over the course of time due to the fading charge capacity of the lithium-ion cells. Therefore, the degradation of the lithium-ion cells is considered in the sizing of the battery storage. In order to estimate the battery degradation, the target service life T_{SL} of the combined storage and the forecast for the charge throughput of the lithium-ion cells should be known. The service life corresponds to the calendrical time that the combined storage should be operational, but not necessarily operating. In other words, the service life may also include idle time. The service life belongs to the parameters that are required to investigate the feasibility of a potential investment and therefore is known in advance, whereas the charge throughput can be estimated with the aid of historical data for the application load.

Assuming that the average voltage of the battery system remains unchanged throughout its service life, it is considered that the energy capacity of the battery system is proportional to its charge capacity. Therefore, the required charge capacity of the battery system is $Q_{bs,req}=E_{FCR,min}/U_{b,N}$, where $U_{b,N}$ denotes the nominal voltage of the battery system. In order to fulfil the application requirements, the charge capacity of the battery system at the end of the service life should be greater than or equal to the charge capacity required by the application, that is

$$q_{c,SL} Q_{bs,0} \geq Q_{bs,req}, \tag{4.14}$$

where $Q_{bs,0}$ is the initial charge capacity of the battery system and $q_{c,SL}$ is the forecast of the normalized charge capacity of the lithium-ion cells at the end of the service life.

To forecast the degradation state of the batteries at the end of the service life, both their calendrical and their cyclic degradation should be estimated. To estimate the cyclic degradation, the load profile of the lithium-ion cells should be known. Since the kinetic storage shares a significant amount of the application load, only the rest load is considered for the battery system. The kinetic storage should handle the absolute frequency deviations that are lower than or equal to Δf_{ks}, therefore, the battery should handle the absolute frequency deviations that are greater than Δf_{ks}. Consequently, similar to the expected power share of the flywheel storage, the expected power share of the battery storage is defined as

$$P_{bs,e} = \frac{\mathrm{E}[|\Delta f| > \Delta f_{ks}]}{\Delta f_{max}} P_{PQ}. \tag{4.15}$$

According to the definition of the expected value of the absolute grid frequency deviation with respect to the complete set of Δf, it holds $\mathrm{E}[|\Delta f|] = \mathrm{E}[|\Delta f| \leq \Delta f_{\mathrm{ks}}] + \mathrm{E}[|\Delta f| > \Delta f_{\mathrm{ks}}]$, which means that the battery storage and the kinetic storage share the total load resulting from the grid frequency profile.

For a battery system configuration with N_b batteries connected in parallel that is loaded with the expected power $P_{bs,e}$, where each battery has N_p cells connected in parallel and N_s cells connected in series with the nominal cell voltage $U_{c,N}$, the expected cell current is

$$I_{\mathrm{c,e}} = \frac{P_{\mathrm{bs,e}}}{N_{\mathrm{b}} N_{\mathrm{p}} N_{\mathrm{s}} U_{\mathrm{c,N}}}. \tag{4.16}$$

According to Eq. (4.15), the expected battery power is positive and hence the expected battery current $I_{c,e}$ is also positive. The expected current times the duration of the application profile corresponds to the expected charge throughput in a single lithium-ion cell. Consequently, the equivalent full cycles for a lithium-ion cell with a certain charge capacity can also be determined using Eq. (3.46).

The cyclic degradation of the lithium-ion cells is estimated by iteratively applying the degradation model throughout the service life using a time step that equals the duration of the load profile. In order to apply the cyclic degradation model of the charge capacity described by Equations (3.50) and (3.58), the equivalent full cycles should be substituted in the base of the exponential function and a degradation factor $b_{cyc,q}$ should be assumed. For the initial battery system with the minimum energy capacity $E_{FCR,min}$, the SoC range corresponds to the available energy state range according to limits (4.7), whereas for batteries with an energy capacity higher than $E_{FCR,min}$, the SoC range is decreased with respect to the initial battery system. Therefore, the cyclic degradation factor can be determined using Eq. (3.58) and consequently the incremental charge capacity loss due to cyclic degradation $\Delta q_{L,cyc}$ can be calculated. However, in order to calculate the total charge capacity loss according to Eq. (3.54), the incremental charge capacity loss due to calendrical degradation should also be calculated in the same interval.

The incremental charge capacity loss $\Delta q_{L,cal}$ due to calendrical degradation can be iteratively calculated using Eq. (3.51) and specifying the SoC and the temperature throughout the service life. An average SoC of 50 % is a reasonable assumption for the stochastically symmetrical power profile of FCR. The FCR application implies battery operation at predominantly low load and therefore an assumption of a low cell temperature close to the ambient temperature of the battery system is also reasonable. An average cell temperature a bit higher than the room temperature can be assumed for indoor systems. For outdoor systems, the average cell temperature can be assumed a bit higher than the reference temperature of the container. If additional information for the designated location of the outdoor system are available, the algorithm can involve a season-dependent temperature. Consequently, the overall degradation state at the end of the service life can be calculated via Eq. (3.54), which leads to the forecast of the charge capacity at the end of the service life, that is $q_{c,SL}$=1- $q_{L,SL}$.

In order to estimate the cyclic degradation, it was assumed that the configuration of the battery system is known, so that the current flow per lithium-ion cell can be determined using Eq. (4.16). However, the number of batteries N_b that should be connected in parallel is unknow and should be determined by the sizing algorithm. To simplify the sizing algorithm, the configuration of a single battery is considered as given. Substituting the forecast of charge capacity $q_{c,SL}Q_{BS,0}$ at the end of the service life and the required capacity

$Q_{bs,req}$ as a function of N_b in inequality (4.14), leads to an inequality that should be solved for N_b. Depending on the cyclic degradation function, the inequality may be solved for an analytical solution. However, for elaborate degradation models, it is unlikely that the inequality can be solved analytically. Moreover, an analytical solution should be rounded up, since N_b accepts only integer values. Therefore, the minimum number of parallel connected batteries N_b that fulfils inequality (4.14) is calculated by iteratively increasing N_b with a unity step. Although the lowest number of parallel connected batteries that satisfies the condition (4.14) can therefore be determined, it should be additionally ensured that the cell charge capacity does not fall below the threshold considered as EoL. In this respect a margin for error can also be considered, which means that the charge capacity considered as EoL should not necessarily correspond to the manufacturer specification. Moreover, to increase the reliability of the degradation estimation, the charge capacity should lie within the range that the degradation model is valid for.

The energy capacity of the battery system corresponds to a certain nominal power, since the energy to power ratio of lithium-ion cells is considered fixed at 1 h. If the sizing algorithm results in a nominal battery power that is lower than the minimum power capacity for FCR defined in Eq. (4.9), the overload capabilities of the battery can cover the difference. Oversizing the battery to achieve higher power capacity is inefficient because the maximum balancing reserve power is rarely required. Operation in C-rates as high as 2C within a reasonable SoC and temperature range is typical for contemporary lithium-ion technologies. A battery system with overload capabilities up to 2C and an energy capacity such that $T_{FCR}>0.75$ h should be able to provide a power higher than $P_{FCR,min}$. Although the nominal power of the battery system may lie below $P_{FCR,min}$, its power converters should be rated so that they are able to continuously provide a power greater than or equal to $P_{FCR,min}$ because the overload capabilities of power electronics are usually limited in the range of a few seconds. Consequently, a typical lithium-ion battery system fulfilling the energy capacity requirements of FCR, in most cases also fulfils the FCR power capacity requirements.

Counting the power capacity of the kinetic storage together with the power capacity of the battery system to reach a higher power capacity of the combined system, could be reasonable for short-term energy storage applications. However, due the 15 min provision requirement in the case of FCR, the low energy to power ratio of the kinetic storage only slightly increases the prequalified power.

Sizing of Refence Energy Storage Systems

The energy storage system should be sized so that it is able to provide 1 MW of balancing reserve power which currently corresponds to the minimum bid in the balancing market. An energy storage system that is able to provide a balancing reserve power as high as the minimum bid makes its operator able to individually participate in the balancing market. However, a system sized for a lower balancing reserve power can still offer balancing services by participating in a pool. Storage systems that aim to provide a balancing reserve power in the range of a few MW, can be considered by scaling a reference system of 1 MW.

The battery storage should be preferably designed for a high terminal voltage in order to reduce the power losses that predominantly depend on the current. The maximum battery voltage is selected at 1000 V as it is a widely used threshold between low and high voltage. It is anticipated that the requirements of electrical components with nominal voltage up to 1000 V do not drive up the cost as it may be for components with a nominal voltage over 1000 V. Considering that the voltage of a fully charged NMC lithium-ion cell ranges between 4.1 V and 4.2 V, the number of cells connected in series to reach 1000 V should be between 238 and 244. Considering 238 cells in series and a minimum cell voltage of 3.0 V, the lowest battery voltage is roughly 714 V. Therefore, in addition to the typical three-phase line-to-line voltage of 400 V, a voltage level of 690 V on the 3xAC side of the battery power converter presented in Figure 4.5 can be achieved without overlapping with the voltage on the battery side. Due to the high battery voltage, a voltage level of 690 V on the 3xAC side of the grid-side power converter is also achievable in the configuration presented in Figure 4.6. Therefore, a three-phase voltage of 690 V on the low-voltage side of the power transformer is considered.

The power capacity of a battery depends on the nominal current of its lithium-ion cells, whereas the energy capacity of a battery depends on the nominal charge capacity of its lithium-ion cells. The nominal current of a lithium-ion cell is linked to its rated charge capacity because it is usually defined as the current required to discharge the cell in 1 h. Therefore, a fixed energy to power ratio of 1 h is considered for the battery. The energy capacity of lithium-ion cells depends on their cathode technology, such as Lithium Nickel Mangan Cobalt oxide (NMC), Lithium Iron Phosphate (LFP) and Lithium Titanium Oxide (LTO). Furthermore, the energy capacity of lithium-ion cells depends on their design such as round, pouch, and prismatic. For a certain cell technology and design the energy capacity depends mainly on the dimensions of the cells, with greater dimensions leading to higher charge capacities. Furthermore, greater cell dimensions may lead to a reduction in the internal resistance and an increase in the outer surface, which in turn results in enhanced thermal behaviour. The pouch NMC lithium-ion cells KOKAM 53 are used in the current investigation because adequate data to parametrize their equivalent circuit and their degradation model are available (Table A.3 and Table A.6). Moreover, pouch cells have good thermal properties compared to other cell designs, which is an important property when a relatively long service life is required. Considering 240 cell connected in series where each individual cell has a rated capacity of 53 Ah and a nominal voltage of 3.7 V, the energy capacity of the battery results in $240 \cdot 3.7\ \text{V} \cdot 53\ \text{Ah} = 47\ \text{kWh}$. The power converter of the battery is sized for the maximum battery voltage and the maximum battery current as described in Equations (4.4) and (4.5). The maximum battery voltage is selected at 1000 V and the maximum cell current is limited at 53 A, which corresponds to 1C. Therefore, the apparent power of the power converter should be 53 kVA.

The flywheel prototype SWIVT290, whose parameters are summarised in Table A.9, is considered for the FCR application. The inverter of the flywheel is sized according to Equations (4.2) and (4.3), which results in the apparent power of 130 kVA. Since the maximum electric power of the PMSM driving the flywheel (Table A.1) is about 100 kW, there is an evident difference between the machine and the converter power rating due to the reactive power which is required by the electric machine. On the contrary, the battery neither supplies nor sinks reactive power and therefore there is no difference between its power capacity and the power rating of its power converter, which is a certain economical advantage compared to flywheels.

The combined storage should be sized so that it provides 1 MW of balancing reserve power, that is, a prequalified power of 1 MW is required. The minimum energy to power ratio $T_{\mathrm{FCR.min}}=1$ h is selected for the application of FCR, so that the battery system can use a wide energy state range, which according to limits (4.7) ranges from $w_{\mathrm{FCR,lo}}=0.25$ to $w_{\mathrm{FCR,up}}=0.75$. Consequently, substituting $T_{\mathrm{FCR.min}}=1$ h and $P_{\mathrm{PQ}}=1$ MW in Eq. (4.8), the minimum energy capacity results in $E_{\mathrm{FCR.min}}=1$ MWh. Therefore, the lowest number of batteries that cover the minimum energy capacity is 1 MWh/47 kWh ≈ 22.

Sizing of a reference battery-only storage system

To estimate the cell degradation which results from the FCR application, the 24-hour grid frequency profile of continental Europe recorded on 01 October 2021 is used. According to Eq. (4.10), the grid frequency profile results in an average absolute balancing reserve power of roughly 83 kW. Considering first a battery-only system, depending on the number of parallel connected batteries, the average absolute balancing reserve power leads to an average charge throughput for each lithium-ion cell, which is used to estimate its cyclic degradation. To estimate the calendrical degradation, an average SoC of 50 % and an average cell temperature of 22 °C are considered. The charge capacity should lie over 75 % at the end of the service life in order to leave a margin for error considering the charge capacity of 70 % as the end of life. For a target service life of 15 years, or 15 a using “a” as the unit of time for a year, which is derived from the Latin word *annus*, the iterative calculation of the battery capacity in order to satisfy inequality (4.14) results in 42 batteries instead of the 22 calculated without considering the battery degradation, which signifies an increase of roughly 91 %.

The configuration with a common DC bus presented in Figure 4.6 is considered for the energy storage system. According to the minimum power capacity for FCR which is defined in Eq. (4.9), the grid-side equipment should be rated at $1.25P_{PQ}$, which results in the power rating of 1.25 MVA for both the AC-DC power converter and the three-phase power transformer. An undersized grid-side AC-DC power converter is an unfeasible option, since power electronics have overload capabilities in the range of a few seconds. An undersized transformer is a feasible option, as depending on the transformer technology and the cooling system, an overload in the range of a few hours is permissible. Since the provision of maximum balancing reserve power is a rare occasion, the potential degradation of the transformer due to overload is insignificant. However, it is a usual practice to oversize rather than undersize grid-side transformers, in order to keep reserve for future expansions that involve additional loads. Depending on the transformer size and technology, a dedicated installation area for the transformers should be allocated. Allocating a small area for undersized transformers is unfavourable for future expansions. Furthermore, redundant transformers that enable operation in case a single transformer fails are often installed in critical installations. Therefore, in most cases, it is less expedient to save cost through an undersized grid-side transformer. Consequently, both the grid-side power converter and the power transformer are sized for the maximum power required by the FCR application. The electrical equipment sized for the reference battery-only system and the application of FCR is summarised in Table 4.2.

Table 4.2 Electrical equipment of a reference battery-only storage system for a balancing reserve power of 1 MW and a target service life of 15 a that is intended for FCR

Level	**Property**	**Value**
Battery Unit	Number of lithium-ion cells	240
	Energy capacity	47 kWh
	Nominal power	47 kW
	Power converter rating	53 kVA
Battery Storage	Number of batteries	42
	Power capacity	1974 kW
	Energy capacity	1974 kWh
Grid	Power converter rating	1250 kVA
	Transformer rating	1250 kVA

Sizing of a reference combined storage system

In order to size the combined storage, the power split between the battery and the kinetic storage should be estimated by selecting an upper bound Δf_{ks} for the frequency deviation that the kinetic storage should handle. Figure 4.7 presents the probability distribution and the corresponding cumulative probability distribution of the absolute deviation of the grid frequency of continental Europe on 01.10.2021 from 50 Hz. Selecting Δf_{ks}=20 mHz covers about 70 % of the frequency deviations, Δf_{ks}=30 mHz covers 87 % and Δf_{ks}=40 mHz covers 95 %. However, an upper bound of 30 mHz or 40 mHz come at the cost of 1.5-times or 2-times higher power capacity for the kinetic storage respectively. Therefore, the upper bound of 20 mHz is selected to keep the power rating of the kinetic storage low. Consequently, according to Eq. (4.12), the power capacity of the kinetic storage should be (20 mHz)/(200 mHz)·1 MW=100 kW, which corresponds to two SWIVT290 flywheel prototypes. Considering a band of 5 mHz, in which zero crossings are not counted, the average time between two consecutive zero crossings for the 24-hour course of the grid frequency is about 114 s. Therefore, according to Eq. (4.13), the required energy capacity for the kinetic storage is 100 kW·114 s=11.4 MJ=3.17 kWh, which can also be covered by two SWIVT290 flywheel prototypes. Consequently, both the required energy capacity and the required power capacity can be covered by two SWIVT290 flywheel prototypes.

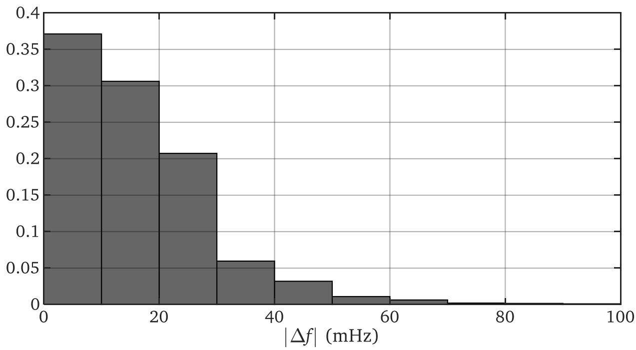

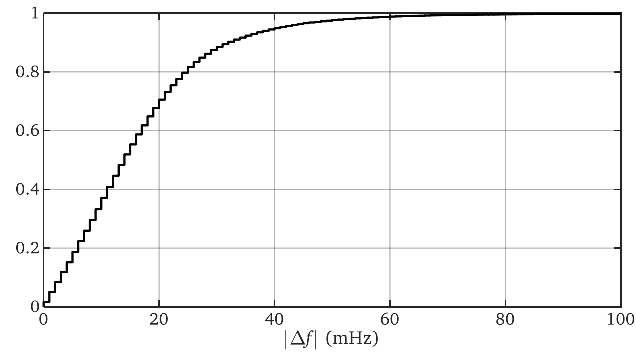

Figure 4.7 **Top:** probability distribution of the absolute frequency deviation from 50 Hz, **bottom:** cumulative probability distribution of the absolute frequency deviation from 50 Hz, both for the 24-hour course of the grid frequency of continental Europe measured on 01.10.2021 with a sampling period of 1 s.

The energy capacity of the battery system that fulfils the FCR requirements is already determined at 22 batteries, each with an energy capacity of 47 kWh. According to Equations (4.11) and (4.15), for the upper bound Δf_{ks}=20 mHz, the battery is expected to share a load of 50 kW, whereas the flywheel is expected to share a load of 33 kW. Compared to the total average power of 83 kW resulting from the FCR load profile, the expected battery load is reduced by almost 40 %. The battery degradation is estimated using the same input parameters as for the battery-only system. Consequently, due to the reduced battery load, only 30 batteries are required in the combined storage system for a target service life of 15 a, compared to the 42 batteries of the battery-only system, which signifies a decrease of roughly 29 %. The twelve fewer batteries of the combined storage than the battery-only storage is the outcome of the integration of flywheel storages. In other words, two flywheel storages with an energy capacity of 2·1.8 kWh=3.6 kWh apparently replace twelve batteries with an energy capacity of 12·47 kWh=564 kWh. Thus, it can be claimed that under the considered conditions and a target service life of 15 a, 1 kWh of flywheel energy capacity is able to replace about 150 kWh of lithium-ion battery energy capacity.

The requirements for the grid-side equipment of the battery-only system that arise from the provision of 1 MW of FCR apply equivalently to the combined system. Therefore, the grid-side equipment of the combined system is sized equally to that of the battery-only system. The electrical equipment considered for the reference combined storage system is summarized in Table 4.3. Furthermore, the parameters that are relevant to the electricity consumption of the basic equipment are summarized in Table A.14.

Table 4.3 Electrical equipment of a reference combined storage system for a balancing reserve power of 1 MW and a target service life of 15 a that is intended for FCR

Level	Property	Value
Battery Unit	Number of lithium-ion cells	240
	Energy capacity	47 kWh
	Nominal power	47 kW
	Power converter rating	53 kVA
Battery Storage	Number of batteries	30
	Power capacity	1410 kW
	Energy capacity	1410 kWh
Flywheel Unit	Energy capacity	1.8 kWh
	Nominal power	50 kW
	Power converter rating	130 kVA
Kinetic Storage	Number of flywheels	2
	Power capacity	100 kW
	Energy capacity	3.6 kWh
Grid	Power converter rating	1250 kVA
	Transformer rating	1250 kVA

The sizing algorithm of the combined storage system is illustrated with the aid of the flow chart presented in Figure 4.8 in order to provide a better overview. The prequalified balancing reserve power and the target service life constitute the main inputs of the sizing algorithm. Furthermore, a feasible energy to power ratio for the FCR application should be selected. Additionally, the properties of the individual storage units such as the lithium-ion cells, the battery configuration and the flywheel type should be defined. The selection of the frequency deviation range that the kinetic storage should handle, leads to the estimation of the power split between the kinetic and the battery storage, so that the size of the kinetic storage can be determined. The minimum number of batteries that are needed to fulfil the energy capacity requirements of FCR is determined and then increased iteratively until the charge capacity of the battery system at the end of the target service life exceeds both the charge capacity required by FCR as well as the desired minimum charge capacity. Finally, the algorithm outputs the number of flywheels and batteries required to fulfil the requirements of FCR throughout the target service life.

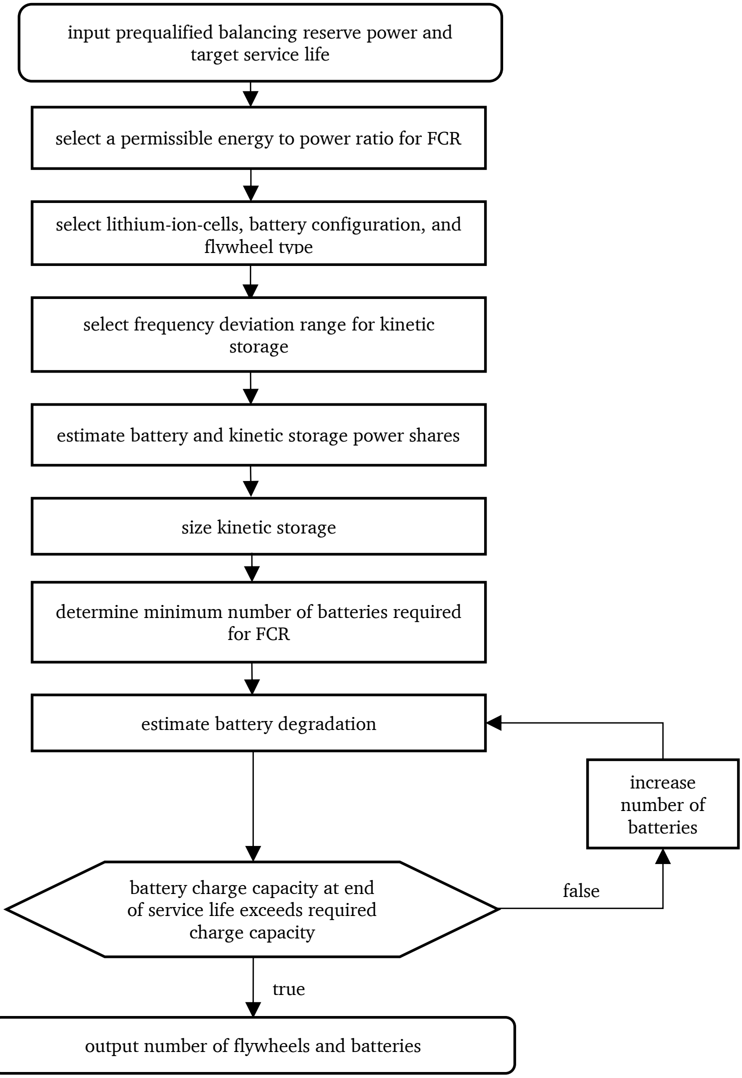

Figure 4.8 Flow chart of the sizing algorithm of the combined energy storage system intended for FCR

The frequency deviation bound Δf_{ks}=20 mHz was determined with the aid of the cumulative probability distribution of the absolute frequency deviation presented in Figure 4.7. However, the selection of the frequency deviation bound can also be confirmed by iterating the sizing algorithm with an increment of 1 mHz for Δf_{ks} as presented in Figure 4.9. If Δf_{ks}=0 mHz, the battery-only system is sized with 42 batteries. Increasing Δf_{ks} up to 10 mHz leads to one extra flywheel and four fewer batteries. Increasing Δf_{ks} from 11 mHz to 20 mHz reduces the number of batteries further to 30 without increasing the number of flywheels. The highest rate of decrease of the number of batteries is observed when Δf_{ks} shifts from 12 mHz to 21 mHz. Exactly at Δf_{ks}=20 mHz the reference combined storage system with 30 batteries and 2 flywheels is observed, which corresponds to twelve fewer batteries than the battery-only system at Δf_{ks}=0 mHz. Increasing the Δf_{ks} over 20 mHz leads to an approximate rate of one fewer battery for one more flywheel, which is less attractive than the battery reduction achieved with lower frequency deviation bounds. However, the decision of whether a higher frequency deviation bound is expedient also depends on the flywheel cost with respect to the battery cost.

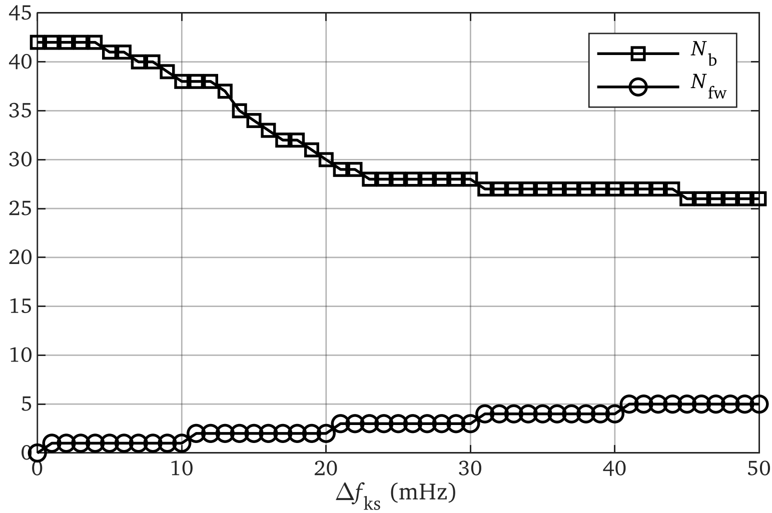

Figure 4.9 Resulting number of flywheels N_{fw} and number of batteries N_b when iterating the sizing algorithm with 1 mHz increment for the frequency deviation bound Δf_{ks} of the kinetic storage. Increasing the Δf_{ks} from 12 mHz to 21 mHz leads to a high rate of decrease for the number of batteries. Selecting Δf_{ks}=20 mHz only 30 batteries are required compared to the 42 batteries required in the battery-only system.

Discussion

Additional battery units are needed, not for their energy or power capacity, but to split the load among the lithium-ion cells and therefore limit their cyclic degradation, so that the requirements of FCR are fulfilled throughout the target service life of 15 years. Due to uncertainties in both the load forecast and the degradation model of the lithium-ion cells, an even higher number of batteries may be installed to leave a margin for error between the charge capacity forecast at the end of the service life and the charge capacity that is considered as the end of life. Flywheel storages, which have a substantially longer cycle life than lithium-on cells, can be installed instead of batteries to share the load and therefore mitigate the cyclic degradation of the batteries.

The sizing algorithm assumes a constant power split between the storages. However, the power split between the storages depends on the energy management strategy and the ability of storages, especially of short-term storages such as flywheels, to operate in the middle of their energy state range. When storage units tend to operate close to their energy state limits, other storages should share part of their load.

The sizing algorithm leads to feasible energy storage systems that respect the requirements of FCR throughout the target service life. The reference combined storage system can be used as an initial system to pursue further goals such as optimization objectives. Possible optimization objectives are the minimization of the energy conversion losses, the containment of the battery degradation, as well as the minimization of the total cost of ownership. A simulation of the storage system for the application of FCR, including the energy management, can reveal whether the initially sized system is also optimal for the performance goals set or other system variants perform better.

5. Energy Management

The energy management of combined storage systems, usually focuses on the power split among storage units of different technologies. The flexibility to split the load among storage units of different technologies can be exploited to attain certain optimization objectives. The present work aims to develop an energy management strategy that minimizes the total energy losses of the combined storage system. Additional optimization goals that are not directly connected to the energy losses such as the limitation of the battery degradation would result in a multicriteria optimization problem. However, in order to verify the effect of the energy management on battery degradation, degradation tests of long duration are required.

The power split between the battery and the kinetic storage concerns the central energy management that runs at high-level with respect to the complete control structure. The low-level control includes the control loops of the batteries and the flywheels. The present work investigates the operation of the electric machine of the flywheels in field weakening in order to minimize the total power losses of the kinetic storage system. Therefore, an additional optimization algorithm runs at low-level in congruence with the central optimization goal to minimize the energy losses of the combined storage system.

Generally, energy management algorithms of low computation effort are favourable for implementations in real controllers. The combined storage prototype hsETA facilitates the verification of the energy management algorithm developed in this work. Additionally, the prototype hsETA facilitates the comparison between experimental and simulated response in order to verify the models of the storage units.

5.1 Low-level Control

Controllers at a lower level than the central energy management execute tasks that are related to the operation of the individual energy storage units. Although the development of low-level controllers is not in focus, the interaction of the energy management with the low-level controllers is essential to simulate the combined storage system. The central energy management requires the actual states and limitations of the storage units to update the reference values for the storage units. Furthermore, the reference values cannot directly be transformed into control action without involving the low-level controllers. Therefore, the low-level controllers are simulated, along with the central energy management.

The control of the battery power flow is simulated as current control either on the DC bus side or on the battery side of the power converter. The Battery Management System (BMS) is also simulated, as it has a key role in the reliable operation of the battery by providing essential information, such as the actual current limitations and the cell temperature, to the high-level energy management. The control of the kinetic storage corresponds to the control of the individual flywheel storages, which in turn corresponds to the control of their PMSMs. As the high-level energy management minimizes the total energy conversion losses, a low-level control strategy that minimizes the power losses in the electric machine and the power converter of the flywheels is additionally developed and simulated. Moreover, current limitations which aim to constrain the flywheel operation within the set speed limits are developed.

Battery Control Loop

The batteries are integrated into the common DC bus of the combined storage with bidirectional power converters as shown in Figure 4.6. The energy management delivers a power refence with respect to the DC bus, which is relevant for the total battery system. The power reference is then equally divided among the individual batteries. Regulation of power flow implies that the battery power converter operates in current control mode. Two options concerning the current control of the battery power converter are usually available. The first option is to apply current control on the side of the DC bus which has an approximately constant voltage. Therefore, the current reference of the power converter corresponds to the power reference of the battery storage over the DC bus voltage. The second option is to apply current control on the battery side, which means that the current reference of the power converter corresponds to the power reference on the DC bus side over the varying battery voltage plus a current component for the compensation of the power converter losses. Although the varying battery voltage is usually monitored, it is difficult to estimate the power converter losses accurately, so that an additional feedback control loop that measures the battery power on the DC bus side should be used to improve steady state accuracy. Thus, the first option is usually preferred as it is easier to implement.

Battery Management System

A battery management system is composed of electronic control units, sensors and protection equipment which should ensure safe operation by activating protective functions whenever the battery voltage, current or temperature exceed the permissible range. For instance, if the battery current exceeds the set limits, the BMS should break the circuit according to a time-current characteristic to protect the battery. Although the permissible range of voltage and temperature are usually fixed for a given lithium-ion cell, the current limits depend on the cell temperature and the state of charge. The BMS should determine the current limitations and communicate them to other devices such as the central energy management.

The maximum permissible charging current I_{ch} and the maximum permissible discharging current I_{dis} of lithium-ion cells at nominal temperature are specified by the manufacturer, such as the limits listed in Table A.3 and Table A.4. Consequently, at nominal temperature the permissible range of the cell current I is defined by

$$-I_{\mathrm{dis}} \leq I \leq I_{\mathrm{ch}}. \tag{5.1}$$

Additionally, the manufacturer usually specifies the temperature independent voltage limits U_{min} and U_{max} for the cell terminal voltage U, hence

$$U_{\mathrm{min}} \leq U \leq U_{\mathrm{max}}. \tag{5.2}$$

A voltage outside the permissible range can irreversible deteriorate the cell characteristics and should therefore be avoided (Dorn, et al., 2018). The constrained operating area of a lithium-ion cell as a function of current and voltage at nominal temperature is illustrated in Figure 5.1.

The voltage limits determine the minimum and maximum open circuit voltage and therefore the minimum and maximum charge that can be stored in the cell. Operating the lithium-ion cells at a higher temperature than the nominal temperature may result in storing or retrieving more charge than the nominal charge within the permissible voltage range. At temperatures lower than the nominal temperature, the reverse effect is observed;

the nominal charge cannot fully be retrieved or stored within the permissible voltage range. The cell should be first warmed up to the nominal temperature to be able to retrieve or store the nominal charge. In other words, the nominal charge capacity is valid only for the nominal temperature. If the nominal charge is already retrieved or stored, the BMS may limit the current to zero in order to prevent operating the cell beyond the rated charge capacity.

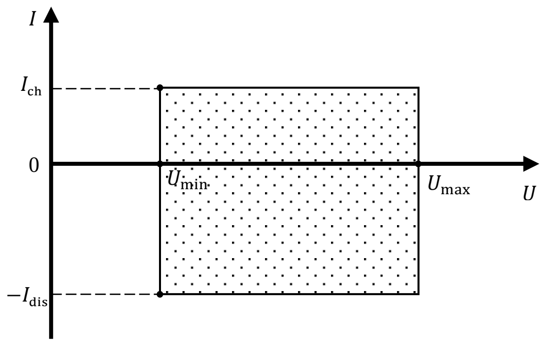

Figure 5.1 Operating area of a lithium-ion cell as a function of current and voltage at nominal temperature

Interrupting the charge flow when reaching the voltage limits does not necessarily mean that the cell is charged up to the maximum open circuit voltage or discharged down to the minimum open circuit voltage. The cell current I causes a voltage drop across the equivalent internal resistance R_{eq}. Substituting the terminal voltage of the cell in inequality (5.2) results in

$$U_{min} \leq U_{oc} + IR_{eq} \leq U_{max}. \tag{5.3}$$

If the current is interrupted, the voltage drop at the equivalent internal resistance instantly vanishes, which leads to an abrupt voltage change at cell terminals. Considering that the terminal voltage lies within the permissible voltage range after the current interruption, the current can be retriggered by control action, which leads to oscillations. Therefore, it is worthwhile to smoothly limit the current when the lithium-ion cell approaches the voltage limits. Assuming knowledge of the equivalent resistance and the open circuit voltage for a given temperature and state of charge, the current limits are derived from inequality (5.3) such that

$$\frac{U_{min}-U_{oc}}{R_{eq}} \leq I \leq \frac{U_{max}-U_{oc}}{R_{eq}}. \tag{5.4}$$

Considering that the open circuit voltage U_{oc} corresponds to a certain SoC and temperature, according to inequality (5.4), the magnitude of the current limitation decreases as the SoC shifts towards its extrema. Furthermore, the slope of the current limitation over terminal voltage depends on the internal resistance; the higher the equivalent resistance, the lower is the slope of the current limitation over terminal voltage. The current limits of inequality (5.4) are relevant when the cell voltage approaches the voltage limits, whereas the current limits of inequality (5.1) are always valid.

Due to the inherent inaccuracies in the estimation of the SoC and consequently in the estimation of the open circuit voltage and the internal resistance, the current limits of inequality (5.4) can be additionally tuned, for instance by introducing an uncertainty factor for the internal resistance. If the voltage of the lithium-ion cells exceeds the permissible voltage range despite the current limits communicated to the central energy management by the BMS, the BMS should break the circuit.

The described limitations apply for a single cell. A stack of lithium-ion cells is prone to imbalances which result in discrepancies in voltage and temperature among the cells. The BMS should therefore monitor the voltage and temperature of each single cell and determine the current limitations according to the highest cell temperature and the SoC of the cell that lies closest to its SoC extrema. In the current investigation, a perfect balance among the lithium-ion cells is assumed, which means that all lithium-ion cells are stressed by the same current, voltage and temperature.

Flywheel Control Loop

The flywheel control loop manipulates the current of the electric machine in order to meet the power required at the DC terminals of the power converter that integrates the flywheel storage into the DC bus. Since the parameters of the electric machine are known, model-based control is feasible. Furthermore, closed loop control to improve the steady state accuracy can additionally be implemented, if the power at the connection between flywheel storage and DC bus is measured.

Provided that the power converter driving the electric machine supports field-oriented control, the direct and quadrature components of the stator current should be determined by the control algorithm and delivered as reference to the current control loop of the power converter. Although the control approach of zero direct current component ($I_d=0$) typically leads to the maximum torque per stator current magnitude in PMSMs, it does not lead to the minimum power losses for an operating point that is defined by a certain torque and a certain speed. According to Eq. (3.24), a negative direct current component, which corresponds to operation in field weakening, reduces the power losses.

The optimal operating point of surface mounted PMSMs was both theoretically and experimentally investigated by Colby & Novotny (1987). A loss minimization method that exploits field weakening in surface mounted PMSMs was experimentally verified by Mademlis et al. (2000). Furthermore, theoretical investigations and test results that confirm the reduction of power losses in interior PMSMs under field weakening compared to the zero direct current strategy ($I_d=0$) were presented by Morimoto et al. (1994) and Mademlis et al. (2004). However, the cited investigations neglected the losses in the power converter driving the electric machine, although they increase with the direct current component.

Optimization problem (5.5) describes the search for a pair of quadrature and direct current components that minimize the loss function $f(x, y)$, which corresponds to the power losses in both the electric machine and the power converter of the flywheel storage, subject to the constraints of reference power and maximum stator current. The part of the loss function $f(x, y)$ that relates to the losses of the electric machine results from Eq. (3.24). The feasible set of the quadrature and direct current components is subject to the power balance equation $g(x, y)=p$ at the DC terminals of the power converter which is partly derived from Eq. (3.21) and the inequality $h(x, y) \leq G$ which corresponds to the maximum continuous stator current. The power P_{ref} denotes the reference power at the DC terminals of the power converter. It is assumed that the magnetic field caused by the maximum continuous stator current can be aligned along the direct axis opposing the magnetic field of the permanent magnets without demagnetizing them. The parameters a, b, c and q are positive and depend only on the electrical frequency and the properties of the electric machine. Noticeably, the parameter a includes the equivalent resistance $R_{\mathrm{fw,pc}}$ of the power converter in order to consider its power losses in the objective function. Since the power converter losses are also considered in the power balance equation, the direct and quadrature current component that result from the solution of the optimization problem comprise the stator current required to obtain the reference power P_{ref} at the DC terminals of the power converter.

$$
\begin{aligned}
\min_{x,y} \quad & f(x,y) = ax^2 + ay^2 + 2bx + c \\
\text{subject to} \quad & g(x,y) = ax^2 + ay^2 + bx + qy = p \\
& h(x,y) = x^2 + y^2 \leq G,
\end{aligned}
\tag{5.5}
$$

where

$$x = I_{\mathrm{s,d}}, \qquad y = I_{\mathrm{s,q}}, \qquad G = I_{\mathrm{s,max}}^2,$$

$$a = \frac{3}{2}\left[\frac{R_{\mathrm{fw,pc}}}{3} + R_{\mathrm{s}} + \frac{R_{\mathrm{Fe}}(\omega_{\mathrm{e}}L_{\mathrm{h}})^2}{R_{\mathrm{Fe}}^2 + (\omega_{\mathrm{e}}L_{\mathrm{h}})^2}\right], \qquad b = \frac{3}{2}\frac{R_{\mathrm{Fe}}\omega_{\mathrm{e}}^2 L_{\mathrm{h}}\Psi_{\mathrm{p}}}{R_{\mathrm{Fe}}^2 + (\omega_{\mathrm{e}}L_{\mathrm{h}})^2}, \qquad c = \frac{3}{2}\frac{R_{\mathrm{Fe}}\left(\omega_{\mathrm{el}}\Psi_{\mathrm{p}}\right)^2}{R_{\mathrm{Fe}}^2 + (\omega_{\mathrm{el}}L_{\mathrm{h}})^2},$$

$$q = \frac{3}{2}\frac{\omega_{\mathrm{e}}\Psi_{\mathrm{p}}R_{\mathrm{Fe}}^2}{R_{\mathrm{Fe}}^2 + (\omega_{\mathrm{e}}L_{\mathrm{h}})^2}, \qquad p = P_{\mathrm{ref}}.$$

For reasonable electric machine parameters, the parameter q is considerably higher than the parameter b, since R_{Fe} is significantly higher than $\omega_{\mathrm{e}}L_{\mathrm{h}}$. Furthermore, considering that the power losses are low compared to the useful power, for a given P_{ref} the quadrature current that fulfils the constraints remains approximately constant when the direct current variates. Consequently, the feasible set has a considerable wider range of x values than of y values. Thus, the range of the objective function f for the feasible set is significantly wider for the variation of x than the variation of y. In other words, the term ay^2 in the objective function f can be assumed constant. Therefore, the critical points of the objective function f should lie near the curve that results from the condition

$$\frac{\partial f}{\partial x} = 2ax + 2b = 0,$$

that is, the line $x_{\mathrm{c}}=-b/a$. The critical points are then determined by substituting x_{c} to the equality constraint $g(x, y)=p$, which yields

$$y_{\mathrm{c1,c2}} = \frac{-q \pm \sqrt{q^2 + 4ap}}{2a},$$

where $y_{\mathrm{c1}}<y_{\mathrm{c2}}$. The critical points $(x_{\mathrm{c}}, y_{\mathrm{c1}})$ and $(x_{\mathrm{c}}, y_{\mathrm{c2}})$ exist as long as $p>-q^2/4a$, which means that a terminal power below $-q^2/4a$ is unfeasible.

Substituting $(x_{\mathrm{c}}, y_{\mathrm{c1}})$ and $(x_{\mathrm{c}}, y_{\mathrm{c2}})$ into the objective function becomes apparent that $(x_{\mathrm{c}}, y_{\mathrm{c1}})$ is a local maximum, whereas $(x_{\mathrm{c}}, y_{\mathrm{c2}})$ is a local minimum. As a demonstration of the local minimum properties; the point with zero direct current component $(0, y_{\mathrm{c2}})$ and the local minimum $(x_{\mathrm{c}}, y_{\mathrm{c2}})$ both belong to the feasible set, but the local minimum $(x_{\mathrm{c}}, y_{\mathrm{c2}})$ results in lower losses compared to the point $(0, y_{\mathrm{c2}})$, that is

$$f(0, y_{\mathrm{c2}}) = ay_{\mathrm{c2}}^2 + c \; > \; f(x_{\mathrm{c}}, y_{\mathrm{c2}}) = ay_{\mathrm{c2}}^2 - 2\frac{b^2}{a} + c.$$

In other words, the negative direct current component $I_{s,d}$=$-b/a$ leads to lower power losses than the zero direct current component $I_{s,d}$=0. Consequently, using the electric machine parameters and the equivalent resistance of the power converter, the optimal direct current component for a given angular frequency ω_e is expressed as

$$I_{\mathrm{s,d,opt}} = -\frac{R_{\mathrm{Fe}}\omega_{\mathrm{e}}^2 L_{\mathrm{h}} \Psi_{\mathrm{p}}}{\left(R_{\mathrm{s}} + \frac{R_{\mathrm{fw,pc}}}{3}\right) R_{\mathrm{Fe}}^2 + \left(R_{\mathrm{s}} + \frac{R_{\mathrm{fw,pc}}}{3} + R_{\mathrm{Fe}}\right)(\omega_{\mathrm{e}} L_{\mathrm{h}})^2}. \tag{5.6}$$

Equation (5.6) expresses the optimal $I_{s,d}$ regardless of the constraint of maximum stator current. It should thus additionally be checked whether the local minimum (x_c, y_{c2}) lies within the area bounded by the circle $x^2+y^2=G$. If $f(x, y)$ subject to $g(x, y)=p$ has a local minimum outside the circle $x^2+y^2=G$, a local minimum that fulfils the constraints of problem (5.5) should lie at the intersection of the curve $g(x, y)=p$ and the circle $x^2+y^2=G$. Solving the system of equations that consists of $g(x, y)=p$ and $x^2+y^2=G$, leads to two individual roots at most, from which the one that results in the lowest level of the objective function corresponds to the local minimum.

If the equality constraint $g(x, y)=p$ and the circle $x^2+y^2=G$ do not intersect, it means that all points that satisfy $g(x, y)=p$ lie outside the circle $x^2+y^2=G$, as at least one point, which is the local minimum (x_c, y_{c2}), lies outside the circle. Therefore, problem (5.5) is unfeasible, which means that the reference power cannot be delivered because the maximum continuous stator current is not high enough. However, in order to fulfil the power reference to the technical feasible extent, the maximum available power should be provided. The maximum available power in either direction corresponds to the extrema of the terminal power that are the extrema of the function $g(x, y)$ at maximum stator current, which lies in the circumference of the circle $x^2+y^2=G$.

In conclusion, a method to minimize the power losses of both the PMSM and the power converter of the flywheel storage is developed. The method implies that the electric machine operates in field weakening by applying a negative direct current component. In field weakening, the magnetic field caused by the current in the stator windings counters the field generated by the permanent magnets, which reduces the magnetic flux density in the stator iron and therefore the iron losses.

Flywheel Speed Limits

Flywheels usually operate between a lower and an upper speed limit. A lower speed limit aims to avoid operation at low speed, under which the power rating of the electric machine is unexploited. An upper speed limit is required for several reasons, such as voltage or switching frequency limitations in the power converter, limitations in the bandwidth of the AMBs and limited stability of the flywheel materials at high circumferential speed. In order to constrain the flywheel within the speed limits, the stator current should be limited accordingly, which implies that power reference towards the violation of the speed limits remains unfulfilled.

Interrupting the current when reaching the speed limits results in power peaks with a negative impact on the performance of the storage system, since power peaks cause voltage transients and electromagnetic interferences. Furthermore, current oscillations due to control action when the flywheel approaches the speed limits should also be avoided. On the contrary, a smooth current decay as the flywheel approaches the speed limits is worthwhile. To smooth the current near the speed limits, the lower and the upper current limits are defined as a function of the deviation of the actual speed from the lower and the upper speed limit respectively, offset by the current required to keep the flywheel rotating at constant speed

$$I_{\mathrm{lim,up}} = k_{\mathrm{l,up}} \left(\omega_{\mathrm{m,max}} - \omega_{\mathrm{m}}\right) + \frac{p\omega_{\mathrm{m,max}}\Psi_{\mathrm{p}}}{R_{\mathrm{Fe}}}, \tag{5.7}$$

$$I_{\mathrm{lim,lo}} = k_{\mathrm{l,lo}} \left(\omega_{\mathrm{m,min}} - \omega_{\mathrm{m}}\right) + \frac{p\omega_{\mathrm{m,min}}\Psi_{\mathrm{p}}}{R_{\mathrm{Fe}}}, \tag{5.8}$$

where $k_{\mathrm{l,lo}}$, $k_{\mathrm{l,up}}$ are tuneable gains. The current limits $I_{\mathrm{lim,up}}$ and $I_{\mathrm{lim,lo}}$ correspond to the quadrature component of the three-phase current space vector. The optimum direct current component defined in (5.6) can still be applied, although the quadrature current component is limited.

The current limits $I_{\mathrm{lim,up}}$ and $I_{\mathrm{lim,lo}}$ become relevant when the flywheel approaches the speed limits. In this respect the maximum continuous current of the electric machine is always considered. The higher the gains $k_{\mathrm{l,lo}}$ and $k_{\mathrm{l,up}}$ are, the faster is the decay of the current limits when the flywheel approaches the speed limits. The current limitations resemble a control law in which the speed limit corresponds to the reference variable, the actual speed corresponds to the controlled variable and the current corresponds to the manipulated variable, which is, however, not directly manipulated but serves as a limit. In order to effectively implement the current limitations, the sampling period of the flywheel speed as well as the update rate of the current limits should be low enough.

The second term on the right-hand side of Equations (5.7) and (5.8) is the quadrature component of the stator current that compensates the braking torque according to Eq. (3.18). Consequently, due to the current limits, the flywheel approaches a constant speed as it approaches the speed limits. In other words, the current magnitude is reduced towards the minimum current required to keep the flywheel rotating close to the speed limits by compensating the no-load losses, hence preventing deceleration. If the flywheel exceeds either speed limit, the speed deviation from the speed limit changes sign and the current limit is adjusted so that the flywheel is forced to return to the permissible speed range. Since the equivalent circuit only approximately describes the system behaviour, the current required to compensate the braking torque is also inexact. Consequently, depending on the gains $k_{\mathrm{l,lo}}$, $k_{\mathrm{l,up}}$ and the equivalent circuit parameters, the flywheel rotates at a speed that is close but not exactly that of the speed limits. However, the error can effectively be reduced by increasing the gains $k_{\mathrm{l,lo}}$ and $k_{\mathrm{l,up}}$.

5.2 High-level Control

Energy management algorithms for storage systems are usually implemented in a central electronic control unit. The algorithms follow certain objectives in order to deliver refence values to subordinate storage units as well as control signals to auxiliary devices. The low-level controllers of the storage units strive then to follow the reference values. Among the functions of the high-level control, three are distinguished as significant for the operation of the storage system and are further described; first the constraints imposed by the storage units, second the energy state management using the flexibilities of the application and third the compensation of the self-consumption. Regarding the energy management strategy, the strategy of optimal power share which splits the load between the battery and the kinetic storage by minimizing the total energy conversion losses is further described.

Storage Unit Constraints

Unfeasible reference power can distort operation as the control units of the individual storages may switch in error mode. Information about the constraints and the actual energy states of the storage units is usually available to the central energy management. Therefore, the energy management should use the available information, consider the storage constraints and output feasible power reference values.

Two options to consider the constraints of the individual energy storage units in the energy management algorithm are distinguished; first each storage unit communicates its constraints to the central controller, second the central controller employs a model of the storage units to estimate their constraints. In other words, the constraints can be determined decentralized at storage unit level or centralized at energy management level. Either option implemented, the actual energy state of the storage units is required to determine the constraints. Since the present investigation aims to simulate the energy storage system, the second option is further investigated, under which the central controller estimates the power constraints of the storage units using only their actual energy state.

The power constraints and the energy state have a nonlinear characteristic in the general case as that presented in Figure 4.1. Although the available battery power increases with energy state, as higher energy state corresponds to higher SoC and therefore higher voltage, the power converter is rated significantly lower than the maximum available battery power, since the battery operates at low C-rates. Therefore, the maximum available battery power corresponds to the rating of its power converter. When batteries approach their SoC extrema, the current limits should be adjusted so that the battery voltage lies within the permissible voltage range. The current limits over SoC depend on the internal resistance of the battery which also varies over SoC, with the highest rate of change being usually near the SOC extrema. As battery operation near the SoC extrema should generally be avoided, the limitation of battery power can be initiated at a lower battery energy state threshold $w_{\mathrm{b,lo}}$ and an upper battery energy state threshold $w_{\mathrm{b,up}}$, which are selected considering the internal resistance of the battery including a safety margin. For a linear decrease of the power limits over energy state, the upper and lower power limits of the battery storage are defined as

$$P_{\mathrm{b,lim,lo}} = \begin{cases} -\dfrac{w_{\mathrm{b}}}{w_{\mathrm{b,lo}}} P_{\mathrm{b,N}}, & w_{\mathrm{b}} < w_{\mathrm{b,lo}} \\ -P_{\mathrm{b,N}}, & w_{\mathrm{b}} \geq w_{\mathrm{b,lo}} \end{cases} \tag{5.9}$$

$$P_{\mathrm{b,lim,up}} = \begin{cases} P_{\mathrm{b,N}}, & w_{\mathrm{b}} < w_{\mathrm{b,up}} \\ \dfrac{1 - w_{\mathrm{b}}}{1 - w_{\mathrm{b,up}}} P_{\mathrm{b,N}}, & w_{\mathrm{b}} \geq w_{\mathrm{b,up},} \end{cases} \tag{5.10}$$

where $P_{\mathrm{b,N}}$ is the nominal power of the battery storage unit and w_{b} is the actual battery energy state ranging from 0 to 1. The limits $P_{\mathrm{b,lim,lo}}$ and $P_{\mathrm{b,lim,up}}$ are relevant for a single battery storage with its power converter. The power limits of the complete battery system can be derived by adding up the power limits of the individual battery storage units.

The available power of flywheel storages increases with energy state because their energy state increases with speed and the available power of electric machines is proportional to the speed. Unlike batteries, the power converter of flywheels is sized for the maximum power of their electric machine, which in turn corresponds to maximum flywheel speed. Considering that the nominal power of the flywheel storage $P_{\mathrm{fw,n}}$ corresponds to the available power at minimum operating speed, the upper and lower power limits of the flywheel storage are defined as

$$P_{\mathrm{fw,lim,lo}} = -\frac{n}{n_{\mathrm{min}}} P_{\mathrm{fw,N}},$$

$$P_{\mathrm{fw,lim,up}} = \frac{n}{n_{\mathrm{min}}} P_{\mathrm{fw,N}},$$

where n is the actual flywheel speed ranging from n_{min} to n_{max}. Using Eq. (3.1) which links flywheel speed and energy state, the speed ratio is expressed as a function of the flywheel energy state

$$\frac{n}{n_{\mathrm{min}}} = \frac{\sqrt{n_{\mathrm{min}}^2 + w_{\mathrm{fw}}(n_{\mathrm{max}}^2 - n_{\mathrm{min}}^2)}}{n_{\mathrm{min}}} = \sqrt{1 + w_{\mathrm{fw}}\left[\left(\frac{n_{\mathrm{max}}}{n_{\mathrm{min}}}\right)^2 - 1\right]}.$$

For example, $n_{\mathrm{max}}/n_{\mathrm{min}}=2$ and $w_{\mathrm{fw}}=0.5$ result in $n/n_{\mathrm{min}}=1.58$ and therefore to the upper power limit $P_{\mathrm{fw.lim,up}}=1.58P_{\mathrm{N}}$.

If the flywheel current is limited by low-level control as defined in Eq. (5.7) and Eq. (5.8), the high-level energy management should also limit the power reference of the flywheel. The power limits near the energy state extrema of the flywheel can be implemented through a linear decrease in the available power similar to the limitations defined in Equations (5.9) and (5.10) for the battery. Thus, a lower flywheel energy state threshold $w_{\mathrm{fw,lo}}$ and an upper flywheel energy state threshold $w_{\mathrm{fw,up}}$ should be defined. Unlike the battery storage, an offset should be added to the lower power limit of the flywheel storage to compensate for the no-load losses, so that the flywheel does not decelerate below the minimum speed.

Energy state management

Unless energy state correction measures are taken, storage units which are loaded by symmetrical power profiles such as that resulting from FCR gradually empty out due to energy conversion losses. The favourable energy state for storages used for FCR lies in the middle of their energy state range, so that they are able to react without restrictions to bidirectional power profiles. According to the PQ Conditions, corrections to the energy state of storages can be realized by exchanging a set amount of energy with the power grid at a scheduled time. Although energy exchange between the kinetic and the battery storage to correct their energy state is also a feasible option, it leads to energy conversion losses without contributing to the load. Since the energy management strategy aims to minimize the energy conversion losses, the option of energy exchange between storage units is not further considered.

In addition to scheduled energy exchange with the power grid, the PQ conditions refer to flexibilities that can be used to correct the energy state of storage systems. A useful flexibility according to the PQ Conditions, is the overfulfilment of the balancing reserve power by up to 20 %. Another flexibility is the deadband of ±10 mHz from the reference frequency of 50 Hz, which corresponds to the inherent frequency response insensitivity according to the SO GL. The TSO may exempt balancing service providers from providing balancing reserve power within the deadband. However, the balancing service provider is not permitted to impose a power flow that opposes the correct balancing direction within the deadband. Instead, the balancing reserve provider can freely decide whether he provides balancing reserve power towards the correct balancing direction within the deadband, considering whether this is expedient for the energy state of his storage system.

The energy management algorithm developed in the present work actively uses the overfulfilment of balancing reserve power and the deadband to correct the energy state of the battery storage. The energy state of the kinetic storage is irrelevant for the corrective measures, as it constitutes a short-term storage with a volatile energy state. The corrective measures are activated according to the energy state of the battery storage with respect to an inner and an outer energy state band. If the energy state of the battery lies inside the inner energy state band, no corrective measures apply. As soon as the energy state exceeds the inner energy state band corrective measures apply. The intensity of the corrective measures increases as the energy state moves towards the limits of the outer energy state band, peaks when the energy state reaches either limit of the outer band and remains at maximum as long as the energy state lies outside the outer band. The limits of the inner and outer bands should be defined considering the application requirements.

The intensity of the corrective measures depends on the difference between the maximum and the minimum balancing reserve power that the storage system should provide when the deadband and the overfulfilment flexibilities are considered. Since low battery load corresponds to both low losses and low cyclic degradation, the lowest balancing reserve power is always preferred when no energy state correction is needed. In contrast, when energy state correction is needed, the difference between the maximum and the minimum required balancing reserve power is exploited to correct the energy state. Consequently, using the flexibilities of the FCR application, there is no fixed balancing reserve power but a permissible range, in which the operator of the energy storage system can flexible determine the balancing reserve power he provides.

Self-consumption compensation

Considering the flexibilities of FCR, the balancing reserve power that the combined storage system should provide at the grid connection is determined. However, the battery and the kinetic storage are not the only equipment; the combined storage includes basic electrical equipment, the consumption of which adds to the power flow at the grid connection point. The basic electrical equipment comprises the three-phase power transformer and the central power converter which are depicted in Figure 4.6 as well as auxiliary equipment, such as pumps for the cooling circuit, ventilators and electronic control units. In order to deliver the reference power on the grid side, the power that the energy storage units supply at the DC bus should be as high as the reference power on the grid side plus the consumption of the basic equipment. In other words, the self-consumption of the storage system should be compensated.

The consumption of equipment, such as pumps, ventilators and electronic control units is assumed load-independent and therefore time-invariant, whereas the self-consumption of the central power converter and the power transformer are considered load-dependent such that they can be estimated with the aid of their equivalent resistances. The load of the power transformer and the central power converter correspond roughly to the reference power at the grid connection point plus the load-independent consumption of the basic equipment. Therefore, the total power consumption of the basic equipment can be estimated and added to the reference balancing reserve power, which results in the power reference for the storage units. Although FCR results in a perpetually changing power reference, for which steady state accuracy is usually less important, the accuracy of the power delivered on the grid side can be improved through closed loop control, which uses the power measured on the grid side as the controlled variable and the power output of the storage units as the manipulated variable.

Optimal Power Share

The minimization of energy losses is a common objective in a wide variety of applications. In vehicular systems, for instance, reduced energy losses save energy in the reservoir and therefore extend the vehicle range. Low energy losses correspond to low heat generation and therefore low temperature increase in electrochemical storages, which has a positive effect on their service life. For the application of FCR in particular, reduced energy losses correspond to reduced operating cost because less energy should be acquired from the market to compensate for the energy deficit in the storage units.

The energy losses depend on the energy state of the storage units. For the same power flow and the same internal resistance, the battery losses decrease with increasing energy state because the voltage across the battery increases and therefore its current decreases. The no-load losses of the flywheel storage increase with energy state because an increase in the flywheel speed corresponds to an increase in the electrical frequency, which in turn increases the iron losses in the electric machine. Considering the no-load losses of the flywheels in the objective function of the optimization algorithm may decrease the total losses of the combined system but also tends to decelerate the flywheels to their minimum speed which corresponds to the lowest no-load losses. However, at the minimum speed, the flywheels can operate only unidirectionally, which means they can sink but they cannot supply power. As the grid frequency is unpredictable in the use case of FCR, the future energy states of the storage units are also unpredictable. Thus, the present work aims to minimize the instantaneous load losses of the combined storage disregarding no-load losses and future power losses.

Since the energy management algorithm should run in a real controller, the optimization problem should be ideally formulated such that it can be solved analytically. Expressing the power losses of both the kinetic and the battery storage as a function of their terminal power and their energy state simplifies the loss function of the combined system, which facilitates an analytical solution of the optimization problem.

Simplified Loss Function of the Battery System

To distinguish between cell, battery and battery system level, separate subscripts are used; *c* refers to cell level, *b* refers to battery level and *bs* refers to battery system level. A single battery is composed of N_s cells connected in series and N_p cells connected in parallel, so that the battery load is balanced among the cells. Therefore, the number of cells of a single battery is $N_p N_s$. A battery system comprises N_b batteries connected in parallel. Therefore, the total number of cells in a battery system is $N_b N_p N_s$.

According to the equivalent circuit of the lithium-ion cell presented in Figure 3.7, the power losses depend not only on the cell current, but also on the currents I_{R1} and I_{R2} in the resistive branches. However, to simplify the loss function of the battery system, only the cell current is considered using an equivalent resistance instead of the RC loops. If a load of a given frequency is applied on the lithium-ion cell, the equivalent cell resistance can be estimated with the aid of Eq. (3.42). It is assumed that the load resulting from a generic FCR profile has an expected period of 15 min, which corresponds to the dispatch of power plants and the trading interval of the electricity market. Consequently, the expected frequency is $f_e \approx 1.1$ mHz which corresponds to the angular frequency $\omega_e \approx 0.007$ rad/s.

It is assumed that the same voltage applies across the electrodes of each lithium-ion cell, in other words, imbalances among the lithium-ion cells are neglected. Additionally, the same current I_c is assumed through each cell. Furthermore, the cells share the same properties, such as open circuit voltage and internal resistance, which may change due to degradation effects, however, to the same extent for all cells. Given the equivalent cell resistance $R_{c,eq}$ and the open circuit voltage U_{oc}, the voltage across the cell terminals is

$$U_{\mathrm{c}} = R_{\mathrm{c,eq}} I_{\mathrm{c}} + U_{\mathrm{oc}}. \tag{5.11}$$

Multiplying both sides of Eq. (5.11) by the cell current I_c leads to the power flow at the cell terminals

$$P_{\mathrm{c}} = R_{\mathrm{c,eq}} I_{\mathrm{c}}^2 + U_{\mathrm{oc}} I_{\mathrm{c}},$$

which can be rearranged to the quadratic equation

$$R_{\mathrm{c,eq}} I_{\mathrm{c}}^2 + U_{\mathrm{oc}} I_{\mathrm{c}} - P_{\mathrm{c}} = 0, \tag{5.12}$$

with the cell current I_c as an unknown. The discriminant of the quadratic polynomial of Eq. (5.12) reveals that Eq. (5.12) has no real roots if P_c is lower than

$$P_{\mathrm{c,min}} = -\frac{U_{\mathrm{oc}}^2}{4R_{\mathrm{c,eq}}}. \tag{5.13}$$

In other words, the cell cannot be discharged for a terminal power lower than $P_{c,min}$ because the losses in the internal resistance, which increase quadratically with current, become more significant than the power $U_{oc}I_c$. Provided that $P_c \geq P_{c,min}$, the current required to obtain the power P_c at the cell terminals is

$$I_{\mathrm{c}} = \frac{-U_{\mathrm{oc}} + \sqrt{U_{\mathrm{oc}}^2 + 4R_{\mathrm{c,eq}} P_{\mathrm{c}}}}{2R_{\mathrm{c,eq}}}, \tag{5.14}$$

where the second root of Eq. (5.12) is omitted as it results in higher power losses in the internal resistance than the terminal power. Although Eq. (5.14) gives the exact current to obtain the power P_c at the cell terminals, to simplify the battery loss function, it is assumed that the power losses in the internal resistance are considerably lower than the power $U_{oc}I_c$. Therefore, according to Eq. (5.12), the cell current approximates

$$I_{\mathrm{c}} \approx \frac{P_{\mathrm{c}}}{U_{\mathrm{oc}}}. \tag{5.15}$$

The power losses of a lithium-ion battery with N_pN_s cells are

$$P_{\mathrm{b,L}} = N_{\mathrm{p}} N_{\mathrm{s}} P_{\mathrm{c,L}}, \tag{5.16}$$

where $P_{c,L}$ corresponds to the power losses of a single cell

$$P_{\mathrm{c,L}} = R_{\mathrm{c,eq}} I_{\mathrm{c}}^2.$$

Thus, using the cell current defined in Eq. (5.15), the battery losses can be expressed as

$$P_{\mathrm{b,L}} \approx N_{\mathrm{p}} N_s R_{\mathrm{c,eq}} \left(\frac{P_{\mathrm{c}}}{U_{\mathrm{oc}}}\right)^2. \tag{5.17}$$

The power flow at the battery terminals corresponds to the cumulative power flow at the terminals of each cell, that is

$$P_{\mathrm{b}} = N_{\mathrm{p}} N_s P_{\mathrm{c}}.$$

Consequently, the battery losses defined in Eq. (5.17) can be expressed as a function of the battery power P_{b}, that is

$$P_{\mathrm{b,L}} \approx N_{\mathrm{p}} N_s R_{\mathrm{c,eq}} \left(\frac{P_{\mathrm{b}}}{N_{\mathrm{p}} N_s U_{\mathrm{oc}}} \right)^2,$$

hence

$$P_{\mathrm{b,L}} \approx \frac{R_{\mathrm{c,eq}}}{N_{\mathrm{p}} N_s U_{\mathrm{oc}}^2} P_{\mathrm{b}}^2. \tag{5.18}$$

The same result can be derived by expressing the battery power losses as a function of the total battery current I_{b} and the equivalent resistance of the battery, that is

$$P_{\mathrm{b,L}} = R_{\mathrm{b,eq}} I_{\mathrm{b}}^2, \tag{5.19}$$

where

$$R_{\mathrm{b,eq}} = \frac{N_{\mathrm{s}}}{N_{\mathrm{p}}} R_{\mathrm{c,eq}}.$$

Similar to the approximation of the cell current, the battery current approximates

$$I_{\mathrm{b}} \approx \frac{P_{\mathrm{b}}}{N_{\mathrm{s}} U_{\mathrm{oc}}}. \tag{5.20}$$

Consequently, substituting the battery current defined in Eq. (5.20) into Eq. (5.19) yields the battery power losses

$$P_{\mathrm{b,L}} \approx \frac{R_{\mathrm{b,eq}}}{(N_{\mathrm{s}} U_{\mathrm{oc}})^2} P_{\mathrm{b}}^2. \tag{5.21}$$

Equations (5.18) and (5.21) equivalently express the battery losses as a function of the power at the battery terminals, where the open circuit voltage and the internal resistance correspond to a certain SoC and temperature. Neglecting the temperature dependence in order to further simplify the loss function, the battery losses can be expressed as a function of battery power and SoC, that is, $P_{\mathrm{b,L}} = f(P_{\mathrm{b}}, q_{\mathrm{s}})$. Using the relationship between SoC and energy state, the battery losses can be expressed as a function of battery power and energy state, that is, $P_{\mathrm{b,L}} = f(P_{\mathrm{b}}, w_{\mathrm{b}})$.

According to the configuration presented in Figure 4.6, the losses of the power converter of each battery should also be considered in order to estimate the losses of each battery storage up to the DC bus terminals. The power converter losses correspond to the losses in its equivalent resistance $R_{\mathrm{b,pc}}$ caused by the battery side current I_{b} defined in Eq. (5.20). Consequently, the power losses of the battery along with the losses of its power converter approximate

$$P_{\mathrm{b\&pc,L}} \approx \frac{R_{\mathrm{b,pc}} + R_{\mathrm{b,eq}}}{(N_{\mathrm{s}} U_{\mathrm{oc}})^2} P_{\mathrm{b}}^2. \tag{5.22}$$

Since the battery system comprises N_b batteries connected in parallel that equally share the total power P_{bs} assigned to the battery system, the power losses of the battery system approximate

$$P_{\mathrm{bs,L}} \approx N_{\mathrm{b}} \frac{R_{\mathrm{b,pc}} + R_{\mathrm{b,eq}}}{(N_{\mathrm{s}} U_{\mathrm{oc}})^2} \left(\frac{P_{\mathrm{bs}}}{N_{\mathrm{b}}} \right)^2 = \frac{R_{\mathrm{b,pc}} + R_{\mathrm{b,eq}}}{N_{\mathrm{b}} (N_{\mathrm{s}} U_{\mathrm{oc}})^2} P_{\mathrm{bs}}^2. \tag{5.23}$$

Obviously, according to Eq. (5.23), connecting additional batteries in parallel reduces the power losses of the battery system because the load is divided among more batteries. In other words, the equivalent resistance of the battery system decreases when connecting more batteries in parallel. Equivalent to the power losses of individual batteries, the power losses of the battery system can be expressed as a function of battery system power and energy state, that is, $P_{\mathrm{bs,L}} = f(P_{\mathrm{bs}}, w_{\mathrm{bs}})$.

Simplified Loss Function of the Kinetic Storage System

The flywheel power P_{fw} equals the power P_{s} at the terminals of the PMSM defined in Eq. (3.21), which in turn depends on the electrical frequency ω_{e} and the stator current $\underline{I}_{\mathrm{s}}$. Neglecting the loss terms that depend on the square of the stator current and the direct current component in Eq. (3.21), the quadrature current component is expressed as a linear function of the flywheel power

$$I_{\mathrm{s,q}} \approx \frac{2}{3}\left[1 + \left(\frac{\omega_{\mathrm{e}} L_{\mathrm{h}}}{R_{\mathrm{Fe}}}\right)^2\right] \frac{P_{\mathrm{fw}}}{\omega_{\mathrm{e}} \Psi_{\mathrm{p}}}. \tag{5.24}$$

Substituting the quadrature current component defined in Eq. (5.24) into Eq. (3.24), the flywheel power losses due to the operation of the PMSM approximate

$$P_{\mathrm{fw,L}} \approx \frac{2}{3}\left[R_{\mathrm{s}} + R_{\mathrm{Fe}} \frac{(\omega_{\mathrm{e}} L_{\mathrm{h}})^2}{R_{\mathrm{Fe}}^2 + (\omega_{\mathrm{e}} L_{\mathrm{h}})^2}\right] \frac{\left[\left(\frac{\omega_{\mathrm{e}} L_{\mathrm{h}}}{R_{\mathrm{Fe}}}\right)^2 + 1\right]^2}{\left(\omega_{\mathrm{e}} \Psi_{\mathrm{p}}\right)^2} P_{\mathrm{fw}}^2 + \frac{3}{2} \frac{R_{\mathrm{Fe}} \left(\omega_{\mathrm{e}} \Psi_{\mathrm{p}}\right)^2}{R_{\mathrm{Fe}}^2 + (\omega_{\mathrm{e}} L_{\mathrm{h}})^2}. \tag{5.25}$$

The flywheel power losses $P_{\mathrm{fw,L}}$ comprise a term that depends on the square of the flywheel power and a load-independent term that depends on the electrical frequency ω_{e}. Although the load-independent term accounts for a significant part of the PMSM losses, it is disregarded in the objective function, as it remains unchanged within the interval used in the optimization algorithm. The power-dependent term is rearranged so that the load losses of the flywheel can be expressed as

$$P_{\mathrm{fw,ld,L}} \approx \frac{2}{3} \frac{(\zeta + 1)^2 R_{\mathrm{s}} + \zeta(\zeta + 1) R_{\mathrm{Fe}}}{\left(\omega_{\mathrm{e}} \Psi_{\mathrm{p}}\right)^2} P_{\mathrm{fw}}^2,$$

where

$$\zeta = \left(\frac{\omega_{\mathrm{e}} L_{\mathrm{h}}}{R_{\mathrm{Fe}}}\right)^2.$$

To estimate the power losses of the flywheel storage up to the DC bus terminals, as shown in Figure 4.6, the losses in the AC-DC converter driving the PMSM should additionally be considered. The power converter losses correspond to the losses in its equivalent resistance $R_{\mathrm{fw,pc}}$ caused by the current defined in Eq. (5.24). However, the quadrature current component should be divided by $\sqrt{2}$ so that it equals the rms phase current at the AC side of the power converter. Therefore, the power converter losses approximate

$$P_{\mathrm{fw,pc,L}} \approx R_{\mathrm{fw,pc}} \left(\frac{I_{\mathrm{s,q}}}{\sqrt{2}}\right)^2 = \frac{2}{3} \frac{R_{\mathrm{fw,pc}}}{3} \frac{(\zeta + 1)^2}{\left(\omega_{\mathrm{e}} \Psi_{\mathrm{p}}\right)^2} P_{\mathrm{fw}}^2.$$

Consequently, the combined losses of the flywheel and the power converter approximate

$$P_{\mathrm{fw\&pc,L}} \approx \frac{2}{3} \frac{(\zeta + 1)^2 \left(R_{\mathrm{s}} + \frac{R_{\mathrm{fw,pc}}}{3}\right) + \zeta(\zeta + 1) R_{\mathrm{Fe}}}{\left(\omega_{\mathrm{e}} \Psi_{\mathrm{p}}\right)^2} P_{\mathrm{fw}}^2.$$

The kinetic storage system consists of N_{fw} flywheels connected in parallel that equally share the power P_{ks} assigned to the kinetic storage system. Therefore, assuming that all flywheels rotate at the same speed, the power losses of the kinetic storage system approximate

$$P_{ks,L} \approx \frac{2}{3} \frac{(\zeta+1)^2\left(R_s + \frac{R_{fw,pc}}{3}\right) + \zeta(\zeta+1)R_{Fe}}{N_{fw}\left(\omega_e \Psi_p\right)^2} P_{ks}^2. \tag{5.26}$$

According to Eq. (5.26), the losses of the kinetic storage system depend on the kinetic storage power and the electrical frequency of the flywheels. According to Eq. (3.1) and Eq. (3.2), the electrical frequency can be expressed as a function of the energy state of the flywheel. Consequently, as for the battery system, the power losses of the kinetic storage system can be expressed as a function of power and energy state, that is, $P_{ks,L} = f(P_{ks}, w_{ks})$, where the energy state w_{ks} of the kinetic storage system equals the energy state w_{fw} of each flywheel storage, assuming that all flywheels rotate at the same speed.

Objective function

The optimization objective is to minimize the energy losses of the combined storage when the power P_{cs} of the combined storage splits into the power P_{ks} of the kinetic storage and the power P_{bs} of the battery storage, all with respect to the DC bus for the configuration presented in Figure 4.6, that is

$$P_{cs} = P_{ks} + P_{bs}.$$

The objective function considers only the load losses of the kinetic and the battery storage. The batteries have insignificant no-load losses. The variable part of the no-load losses of the kinetic storage depends on the energy state of the flywheels which remains unchanged in the interval considered in the optimization problem. The load losses of the basic equipment depend on the total power of the combined storage system which is independent of the power split among the individual storage units. Therefore, the no-load losses of the kinetic storage and the losses of the basic equipment are omitted from the objective function as they have no effect on the optimal policy. According to Equations (5.23) and (5.26), for a given energy state, the load losses of each storage system depend only on its power. Consequently, the load losses of the battery and the kinetic storage system can be expressed as

$$f(P_{ks}, P_{bs}) = P_{ks,L}(P_{ks}) + P_{bs,L}(P_{bs}).$$

Since both functions $P_{ks,L}(P_{ks})$ and $P_{bs,L}(P_{bs})$ are quadratic, the optimization problem is formulated as

$$\begin{aligned} \min_{x_1, x_2} \quad & f(x_1, x_2) = c_1 x_1^2 + c_2 x_2^2, \\ \text{subject to} \quad & x_1 + x_2 = a, \\ & b_{1,lo} \le x_1 \le b_{1,up}, \\ & b_{2,lo} \le x_2 \le b_{2,up}, \end{aligned} \tag{5.27}$$

where

- f is the objective function to be minimized corresponding to the load losses of the kinetic and the battery storage
- x_1 and x_2 are the optimization variables corresponding to the power of the kinetic storage and the battery storage respectively

- c_1 and c_2 are strictly positive coefficients resulting from the loss function of the kinetic storage given in Eq. (5.26) and that of the battery storage given in Eq. (5.23) for certain energy states
- a in the equality constraint represents the combined storage power P_{cs} that the kinetic and the battery storage should share
- $b_{1,lo}$, $b_{1,up}$, $b_{2,lo}$, $b_{2,up}$ in the inequality constraints correspond to the lower and the upper bounds of the power of the kinetic and the battery storage respectively

Since x_1 and x_2 are linearly constrained according to equation $x_1+x_2=a$, the objective function can be reformulated as a univariate quadratic function

$$f(x_1) = c_1 x_1^2 + c_2(a - x_1)^2,$$

and therefore

$$f(x_1) = (c_1 + c_2)x_1^2 - 2c_2 a x_1 + c_2 a^2.$$

The parameters c_1 and c_2 are both strictly positive, therefore, the univariate quadratic function f is minimized at the root of its first-order derivative

$$\frac{\partial f}{\partial x_1} = 2(c_1 + c_2)x_1 - 2c_2 a = 0.$$

Thus, the optimum of x_1, that is $x_{1,opt}$, is determined. Substituting $x_{1,opt}$ in the equality constraint leads to the determination of $x_{2,opt}$. Consequently, the optimization problem is solved, resulting in a global minimum at

$$\begin{aligned} x_{1,\mathrm{opt}} &= \frac{c_2}{c_1 + c_2} a, \\ x_{2,\mathrm{opt}} &= \frac{c_1}{c_1 + c_2} a. \end{aligned} \tag{5.28}$$

The result signifies that the optimal power share of each storage relative to the reference power a depends only on the quadratic coefficients c_1 and c_2. The storage with the lowest quadratic coefficient should share a higher load than the storage with the highest quadratic coefficient. In other words, the load ratio $x_{1,opt}/x_{2,opt}$ is the inverse of the quadratic coefficient ratio c_1/c_2. The result is reasonable as the power losses increase with the quadratic coefficients according to Eq. (5.23) and Eq. (5.26). Therefore, according to the optimal policy, the storage with the lowest quadratic coefficient should share the highest load.

If the optimal power shares $x_{1,opt}$ and $x_{2,opt}$ lie inside the inequality constraints, no further action is needed, that is, the optimal power split corresponds to the point ($x_{1,opt}$, $x_{2,opt}$) derived in (5.28). Since the objective function has a global minimum, if either $x_{1,opt}$ or $x_{2,opt}$ does not satisfy the inequality constraints, the optimal power split corresponds to the point that results by substituting the bound of the inequality that could not be satisfied into the equality constraint. For instance, if $x_{1,opt}$ exceeds $b_{1,up}$, the optimal power split results in ($b_{1,up}$, a-$b_{1,up}$). If both $x_{1,opt}$ and $x_{2,opt}$ do not satisfy the inequality constraints, problem (5.27) is unfeasible. In other words, the power reference is higher than the available power of the storages. Although the system cannot provide the reference power at full extent, both storages should provide their maximum available power to the direction of the reference power. Since the solution of the optimization problem determines the optimal power that each storage should share, the optimization algorithm is referred to as Optimal Power Share (OPS).

Simulation

The OPS minimizes the load losses of the combined storage system. Energy management strategies in real systems are usually evaluated with the aid of the total power losses which can be easier measured than the losses at equipment level. Therefore, the total losses of the combined storage are used as a performance indicator because compared to the load losses of the individual storage units, they additionally include the no-load losses of the storage units and the losses of the basic equipment, such as the central power converter and the power transformer. Since the no-load losses of the kinetic storage account for a significant part of the combined storage losses, to demonstrate the performance of the OPS, a power reference that is high enough to cause battery losses that outweigh the flywheel no-load losses should be applied.

The simulations concern the reference combined storage system summarized in Table 4.3, which comprises 2 flywheels and 30 batteries. The initial speed of the flywheels is always 12 000 rpm that corresponds to an energy state of 28 % and the initial voltage of the battery is always 866 V that corresponds to an energy state of 48 %. Unless otherwise specified, the power reference of the combined storage system corresponds to a square profile with an amplitude of 400 kW and a period of 180 s which includes 10 s of idle time at the beginning and at the end, hereafter square power reference.

Figure 5.2 presents the response of the Combined Storage (CS) under OPS to the square power reference. It is observed that the power shares of the Kinetic Storage (KS) and the Battery Storage (BS) vary over time. As the speed of the flywheels and therefore their energy state increase, the stator current required for the same terminal power decreases, which corresponds to a higher energy conversion efficiency. Consequently, the OPS algorithm increases the power share of the KS in order to decrease the load losses of the CS. On the other hand, the no-load losses of the KS increase with speed. Generally, the losses of the CS are higher than the sum of the BS and KS losses because they include the losses of the basic equipment.

To illustrate the performance of the OPS, the response of the CS to the same square power reference applied under OPS is applied under the fixed KS power share s_{ks}=25 % and the fixed BS power share s_{bs}=75 % as presented in Figure 5.3. In comparison with the response to the OPS presented in Figure 5.2, in Figure 5.3 the power shares of the KS and the BS are independent of the energy state and remain unchanged as long as the reference power remains unchanged. Furthermore, the KS power under fixed power share is higher than that under OPS, which results in higher KS losses than BS losses throughout the square power reference. It is observed that the power losses of the CS under fixed power share are increased compared to that under OPS. The increased power losses of the KS under fixed power share are more remarkable at low energy state, as it can be observed comparing the KS and the CS power losses in Figure 5.2 and Figure 5.3 between 180 s and 190 s. The OPS algorithm reduces the power share of the KS at low energy state, as according to the KS loss function, the KS is less efficient at low energy state.

The energy losses of the CS throughout the square power reference and a fixed power split with a share of 25 % for the KS and a share of 75 % for the battery result in 1046 Wh. The CS energy losses for the same square power reference, however, under OPS are 1017 Wh. Therefore, a loss reduction of 2.8 % is achieved through the OPS compared to the fixed power split.

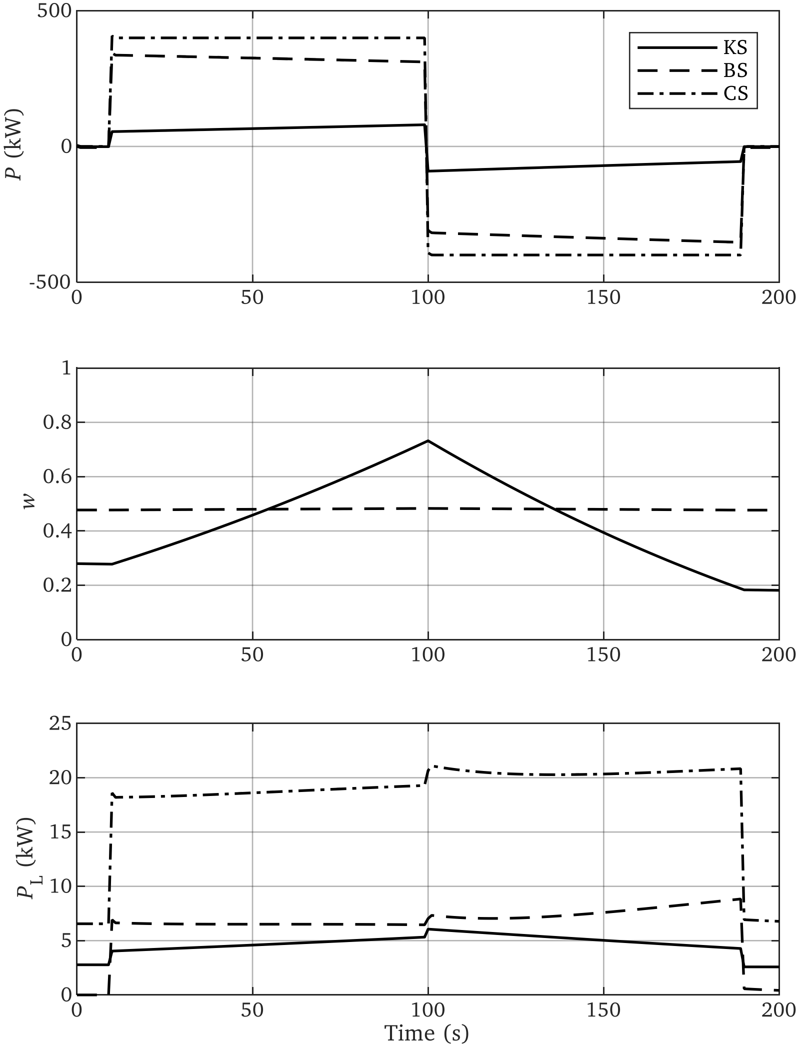

Figure 5.2 Response of the reference Combined Storage (CS) that comprises a Kinetic Storage (KS) with 2 flywheels and a Battery Storage (BS) with 30 batteries to a square power reference using the Optimal Power Share (OPS) algorithm. **Up**: power at the terminals of the KS, the BS and the CS, **middle**: energy state of the KS and the BS, **down**: power losses in the CS, the KS and the BS. Obviously, the power share of the KS increases as its energy state increases.

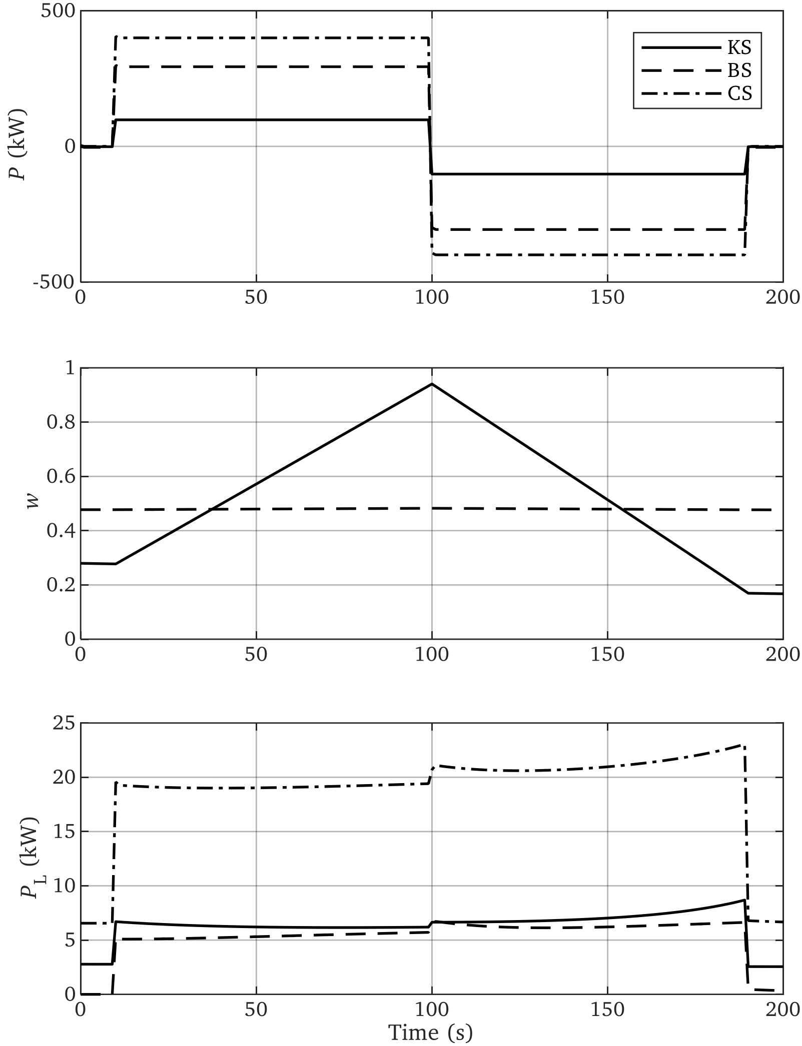

Figure 5.3 Response of the reference CS to a square power reference under the fixed KS power share s_{ks}=25 % and the fixed BS power share s_{bs}=75 %. Under fixed power share the KS is unfavourably loaded at low energy state where it is less efficient, as it can be observed in the relatively high losses of both the KS and the CS between 180 s and 190 s.

To investigate further the energy savings through OPS, the response of the CS to the square power reference is simulated by increasing the fixed power share of the KS in increments of 5 % from 0 % to 100 % and the resulting energy losses of the CS throughout the power profile are shown in Figure 5.4. The power share of the battery storage is complementary to that of the kinetic storage, that is, $s_{bs}=1\text{-}s_{ks}$. For KS power shares that exceed 40 %, the KS peaks at its maximum available power. Consequently, the energy losses of the CS are almost constant for $s_{ks}>40$ %. The energy losses under OPS for the same square power reference are also depicted as a level in Figure 5.4. The CS energy losses under OPS are 1017 Wh, whereas the CS energy losses for $s_{ks}>40$ % are 1136 Wh. Consequently, the OPS reduces the energy losses of the CS by 10.5 % compared to fixed KS power shares that are higher than 40 %. Obviously, the energy losses under OPS are lower than that under fixed power shares with the exception of $s_{ks}=15$ %.

The existence of fixed power shares that lead to lower energy losses of the CS than the OPS is clarified by decreasing the increment of fixed KS shares to 1 % in the 10-20 % range as shown in Figure 5.5. Although the difference in the energy losses is small, it is clearly observed that under a fixed KS power share between 13 % and 16 % the CS losses are lower than that under OPS. Simplified loss functions of the KS and the BS are used in the OPS algorithm, whereas more elaborate models are used to simulate the storage units. Consequently, it is reasonable that the energy losses under OPS approach but not exactly correspond to the minimum energy losses.

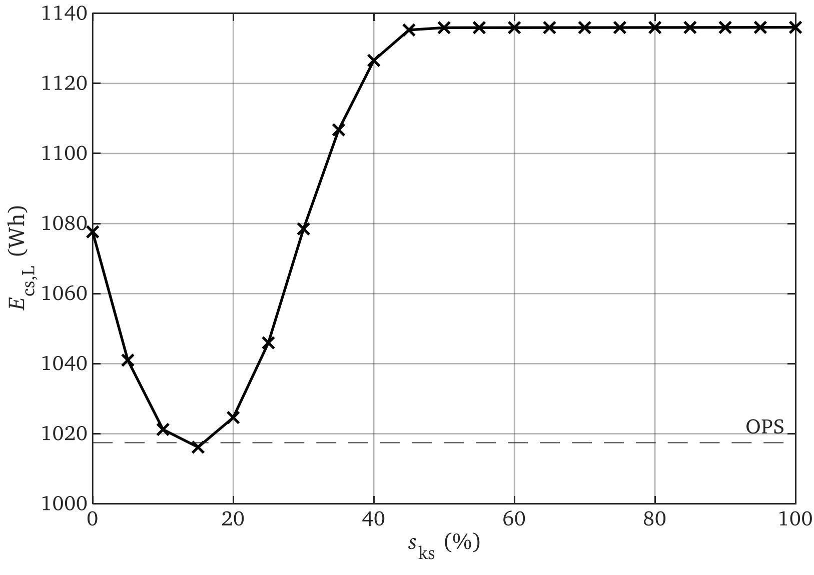

Figure 5.4 Energy losses of the reference combined storage system under the square power reference over fixed power shares of the kinetic storage in increments of 5 %. The energy losses under OPS for the same combined system and power reference are also annotated. The minimum losses under fixed power share approach the losses under OPS.

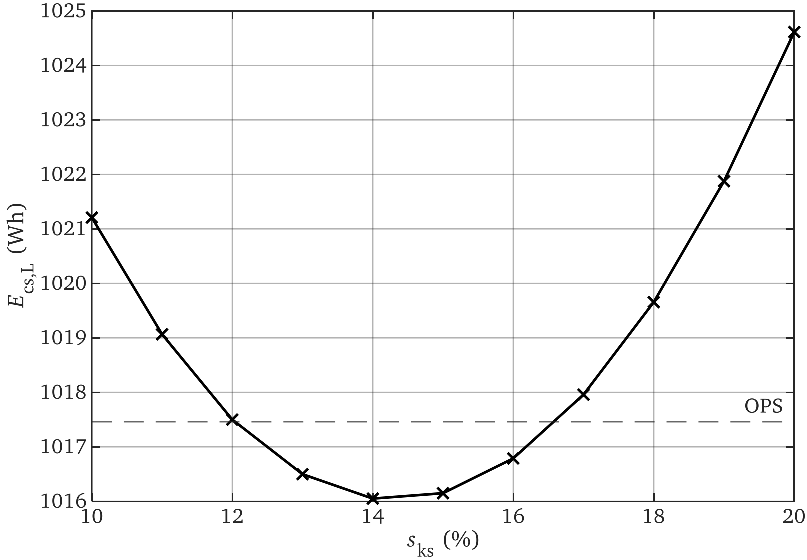

Figure 5.5 Energy losses of the reference combined storage system under the square power reference over fixed power shares of the kinetic storage in increments of 1 %. The losses of the combined storage under OPS are slightly higher than that under a fixed s_{KS} between 13 % and 16 %.

The objective function of OPS ignores the no-load losses of the kinetic storage which account for a significant part of the total losses at low load. To investigate the effect of low load, the amplitude of the square power reference is decreased from 400 kW to 50 kW and the energy losses of the CS over fixed KS power shares are shown in Figure 5.6. Due to the relatively high no-load losses of the KS, the lowest CS losses correspond to s_{ks}=0 %. The energy losses of the CS under fixed power shares below 10 % are lower than that under OPS. Since the objective function does not consider the no-load losses, it is reasonable that the OPS results in higher losses than some of the fixed power shares.

The effect of the flywheel no-load losses is further investigated by increasing the load of the CS and therefore reducing the share of no-load losses with respect to the total CS losses. Figure 5.7 presents the energy losses of the CS over fixed KS power shares under the square power refence, however, with its amplitude increased from 400 kW to 600 kW. In contrast to the energy losses under the square power reference with an amplitude of 400 kW in Figure 5.4 and an amplitude of 50 kW in Figure 5.6, it is observed that for an amplitude of 600 kW the highest energy losses correspond to the lowest power share of the KS. Precisely, in Figure 5.7, fixed KS power shares in the 0-5 % range correspond to the highest CS losses.

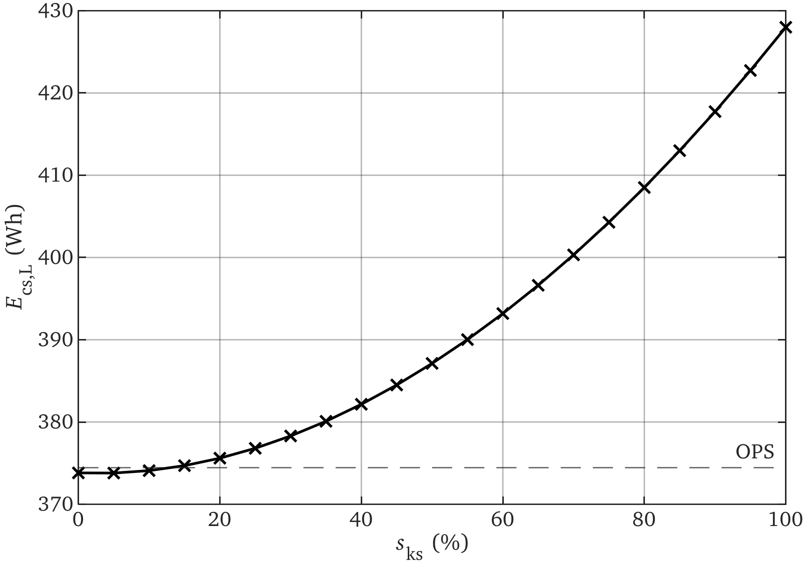

Figure 5.6 Energy losses of the reference combined storage system under a square power reference with an amplitude of 50 kW and a period of 180 s over fixed power shares of the kinetic storage. The energy losses under OPS are higher than that under KS fixed power shares below 10 %.

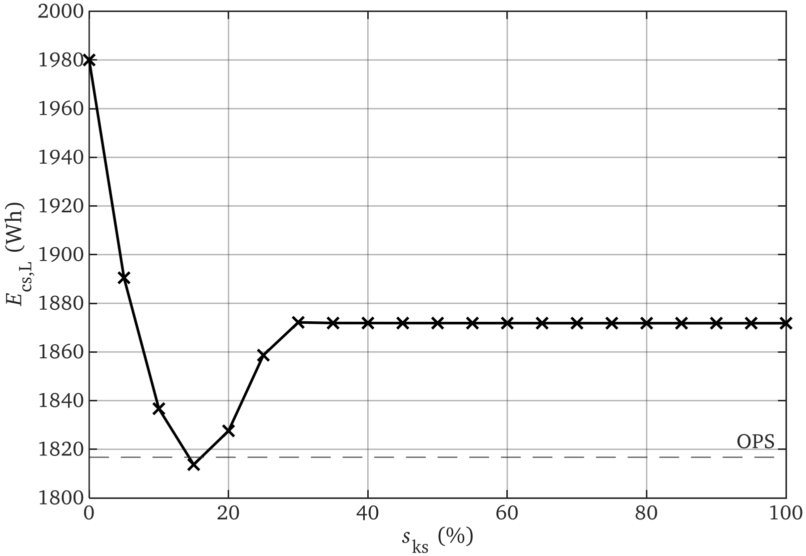

Figure 5.7 Energy losses of the combined storage system under a square power reference with an amplitude of 600 kW and a period of 180 s over fixed power shares of the kinetic storage. The highest energy losses correspond to the 0-5 % s_{ks} range.

Discussion

The power split between battery and kinetic storage is optimized for minimum instantaneous load losses. The results of the simulations show that for a square power reference with a high enough amplitude, most of the fixed power shares lead to higher combined storage losses than the OPS. However, fixed power shares that lead to lower total losses compared to OPS also exist, since the no-load losses of the kinetic storage are not considered in the objective function of the OPS. Considering the no-load losses of the kinetic storage in the objective function implies that the flywheels tend to operate at low speed, which is, however, in conflict with the operating principle of high-speed flywheels. Under a sufficient high load, the battery losses outweigh the no-load losses of the flywheels and therefore the OPS strategy leads to minimum total losses. Nevertheless, as a general recommendation for use cases that involve long intervals at low load; it is more efficient with respect to the energy losses to keep the flywheels rotating at minimum speed or bring them to standstill and operate only the batteries. Generally, selecting a higher flywheel power share than that resulting from OPS, reduces the load and therefore the cyclic degradation of the battery at the cost of increased combined system losses.

The OPS algorithm adjusts the power split between the storage units using information about their actual energy states and the actual power reference in order to minimize the power losses of the combined storage, whereas fixed power shares correspond to a constant power split. Therefore, for a high enough load and a precise loss model, the energy losses of the combined storage system under OPS should be lower than that under fixed power splits. In other words, fixed power splits lead to lower combined storage efficiency than OPS because the flexibility to adjust the power share of the storage units according to their loss function is unexploited.

5.3 Experimental Investigation

The implementation of the energy management algorithm in a real controller of a combined storage prototype pursues three main goals. First to assess the performance of the energy management in a real controller and a real system. Second to assess the performance of the optimal power share against fixed power shares. Third to evaluate the congruence between measured and simulated system response, since part of the model parameters were identified for similar systems but not for the system under test.

Measurement Configuration of the hsETA Prototype

The prototype combined storage system hsETA depicted in Figure 2.1 consists of the flywheel prototype ETA290, the technical data of which are summarized in Table A.9, and a battery storage that includes four batteries connected in parallel, the technical data of which are summarized in Table A.5. The flywheel and the battery are integrated into a common DC bus as depicted in Figure 5.8. The electric machine driving the flywheel is connected to a 3xAC-DC converter through a line filter. The technical data of the 3xAC-DC converter and the DC-DC converter that integrate the flywheel and the battery respectively into the DC-bus can be found in Table A.10. An additional DC-3xAC converter transmits the power between the DC bus and the power grid. Furthermore, a sinus filter is placed between the DC-3xAC converter and the grid. The sinus filter serves several goals, such as the suppression of harmonic distortion caused by the switching of semiconductors and the reduction of electromagnetic emissions. Moreover, the sinus filter serves as a short-term energy storage that enables the power converter to operate at boost mode.

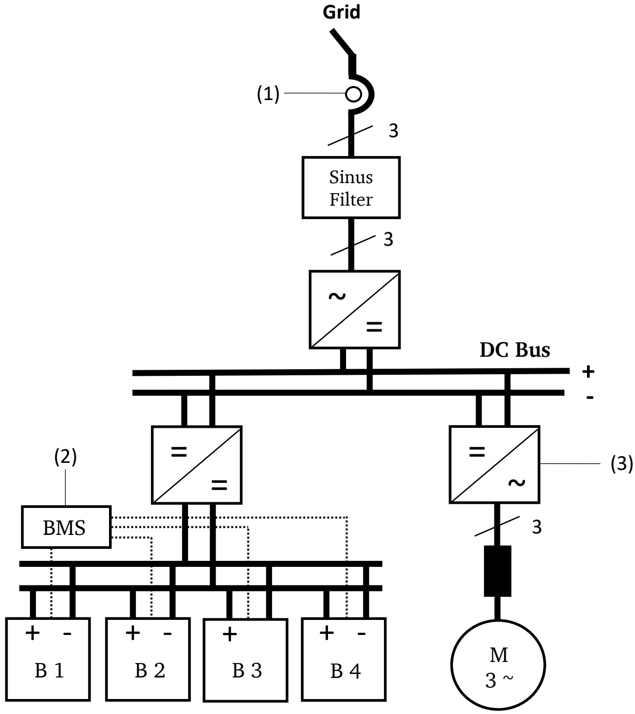

Figure 5.8 Overview of the combined energy storage system hsETA, with the measuring points: (1) grid connection, (2) Battery Management System, (3) power converter of the electric machine

The three measuring points annotated in Figure 5.8 are further explained:

(1) Measurement of the three-phase real power on the grid side using a power analyser. The power analyser employs external current transformers for the current measurement, whereas the voltage is measured internally.

(2) The BMS transmits measurements to the central controller via Controller Area Network (CAN). The BMS measures the voltage across the terminals of each of the four batteries connected in parallel and communicates the average voltage of the battery system. Furthermore, the BMS measures the current of each battery and communicates the cumulative current of the battery system.

(3) The control unit of the power converter driving the electric machine measures the three-phase current and calculates the quadrature component of its space vector times $1/\sqrt{2}$. Moreover, the control unit of the power converter estimates the speed of the rotor by measuring the induced voltage across the stator windings.

Energy Management in the Programmable Logic Controller

The control and data acquisition during the experiments are performed by a Programmable Logic Controller (PLC), the technical data of which are summarized in Table A.11. The main control loop in the PLC runs at 10 ms, whereas the data logging is configured at 100 ms. The update rate of the stator current and the rotor speed communicated by the power converter of the electric machine is faster than 100 ms. The power converter of the electric machine communicates with the PLC via a Gateway that bridges the protocols Profibus DP and Servolink 4. The power analyser on the grid side has an update rate of 200 ms and communicates with the PLC via the Profibus DP protocol. The communication between the PLC and the BMS is implemented through a Gateway that bridges the protocols Profibus DP and CAN. The update rate of the most significant information provided by the BMS, such as battery voltage and current, is 100 ms.

Limited information on modelling parameters of certain components led to a simplified implementation of the model-based OPS algorithm in the PLC. The measurements performed so far on the flywheel prototype ETA290 exclude the high-speed range, so that its iron resistance could not be identified. Therefore, the iron resistance of the similar prototype SWIVT290 is used. The main technical data of the PMSM integrated into the flywheel prototype ETA290 can be found in Table A.2. The manufacturer specified the series resistance of the lithium-ion cell for a single operating point at 1 kHz (Table A.5). Therefore, a cell equivalent resistance independent of state of charge and temperature is assumed. Furthermore, the characteristic of the open circuit voltage over state of charge is unspecified, thus, a linear U_{oc}-SoC characteristic between the minimum and the maximum operating voltage of the lithium-ion cell is assumed.

At the time of the experimental investigation, the speed of the flywheel prototype was limited to 5500 rpm to ensure a reliable operation of the radial magnetic bearings. As the power of the machine is proportional to its speed, a lower speed limit of 2500 rpm was set to avoid operating the machine at low power. The power converter driving the PMSM does not accept a current reference, but a target speed and acceleration. The acceleration is approximately proportional to the torque exerted on the flywheel, which in turn is roughly proportional to the quadrature current component of the PMSM. Thus, the acceleration has the role of the reference variable instead of the current. Given a flywheel reference power $P_{\mathrm{fw,ref}}$, the acceleration reference approximates

$$\alpha_{\mathrm{ref}} \approx \frac{P_{\mathrm{fw,ref}}}{\Theta \omega_{\mathrm{m}}}$$

where Θ is the inertia and ω_{m} the actual mechanical angular frequency, both with respect to the flywheel's axis of rotation.

Estimation of energy losses and propagation of uncertainty

According to Eq. (3.73), the losses in the combined storage equal the energy supplied to the system reduced by the energy supplied by the system minus the internal energy change

$$E_{\mathrm{cs,L}} = E_{\mathrm{cs,in}} - E_{\mathrm{cs,out}} - \Delta E_{\mathrm{cs,i}}. \tag{5.29}$$

The energy exchange between the grid and the CS or equivalently the energy flow at the grid connection corresponds to E_{cs}=$E_{\mathrm{cs,in}}$-$E_{\mathrm{cs,out}}$. The internal energy change of the CS equals the sum of the flywheel internal energy change and the battery internal energy change

$$\Delta E_{\mathrm{cs,i}} = \Delta E_{\mathrm{fw,i}} + \Delta E_{\mathrm{bs,i}}.$$

The energy exchange of the CS with the power grid is estimated with the aid of the time integral of the power P_{cs} measured on the grid side. Considering a constant sampling time Δt, the energy exchange on the grid side is calculated using the trapezoidal rule

$$E_{\mathrm{cs}} = \Delta t \sum_{i=1}^{N-1} \frac{P_{\mathrm{cs},i} + P_{\mathrm{cs},i+1}}{2}, \tag{5.30}$$

where $P_{\mathrm{cs},i}$ corresponds to the i^{th} power sample and N is the total number of samples.

According to the convention used, the energy $E_{cs,in}$ supplied to the system corresponds to the time integral of positive power $P_{cs}>0$, whereas the energy $E_{cs,out}$ supplied by the system corresponds to the absolute value of the time integral of negative power $P_{cs}<0$. Thus, applying Eq. (3.74) which defines the cycle efficiency of an energy storage, the efficiency of the combined storage system is expressed as

$$\eta_{\mathrm{cs}} = \begin{cases} \dfrac{E_{\mathrm{cs,out}}}{E_{\mathrm{cs,in}} - \Delta E_{\mathrm{cs,i}}}, & \Delta E_{\mathrm{cs}} < 0 \\[2ex] \dfrac{E_{\mathrm{cs,out}} + \Delta E_{\mathrm{cs,i}}}{E_{\mathrm{cs,in}}}, & \Delta E_{\mathrm{cs}} \geq 0 \end{cases} \tag{5.31}$$

The internal energy change of the kinetic storage is estimated with the aid of the measured initial speed ω_{init} and the measured final speed ω_{end} of the flywheel

$$\Delta E_{\mathrm{fw,i}} = \frac{1}{2}\Theta(\omega_{\mathrm{end}}^2 - \omega_{\mathrm{init}}^2). \tag{5.32}$$

The internal energy change in the battery storage is estimated by measuring the initial voltage $U_{bs,init}$, the final voltage $U_{bs,end}$ and the current I_{bs} at the battery terminals. In electrochemical storages diffusion processes take place after current interruption. Therefore, the recording was extended for a sufficient time after current interruption to capture the asymptotic voltage. The energy stored in the battery depends on the characteristic of open circuit voltage over state of charge, which is nonlinear in the general case. However, as the charge capacity of the battery is significantly higher than the net charge exchanged throughout each experiment, a linear characteristic is assumed. Therefore, according to the U_{oc}-Q characteristic presented in Figure 3.6, the internal energy change in the battery can be estimated using the trapezoidal rule. Assuming a coulombic efficiency of unity, the charge stored into the battery storage corresponds to the time integral of the current I_{bs}. Therefore, the internal energy change of the battery system approximates

$$\Delta E_{\mathrm{bs,i}} = \frac{1}{2}(U_{\mathrm{bs,init}} + U_{\mathrm{bs,end}})\Delta t \sum_{i=1}^{N-1} \frac{I_{\mathrm{bs},i}+I_{\mathrm{bs},i+1}}{2}, \tag{5.33}$$

where Δt is a constant sampling time, $I_{bs,i}$ corresponds to the i^{th} current sample and N is the total number of samples.

The power analyser, whose main technical data are summarized in Table A.12, records the power at the grid connection point. Auxiliary devices such as low voltage power supplies, ventilators and pumps are connected to a separate branch. Consequently, the power analyser registers the power flow of the energy storages excluding the auxiliaries. The power analyser registers the total real power that corresponds to the sum of the real power of all three phases. Furthermore, the registered real power includes not only the fundamental component of 50 Hz but also higher harmonic components.

According to the standard IEC 61557-12:2018, power analysers may have different performance classes for different measuring functions, where the performance class corresponds to the nominal intrinsic uncertainty of a measuring function. For real power measured at reference conditions with external current transformers, the relative intrinsic uncertainty should lie below the performance class when the sensed current ranges between $0.05I_N$ and I_{max}, where I_N is the nominal current and I_{max} is the highest current measured by the power analyser.

The power analyser records directly the line voltage, however, it records the secondary current of the three current transformers, the specification of which is summarized in Table A.13. Thus, the accuracy of the current transformers should also be considered in order to estimate the propagation of uncertainty. According to the standard IEC 61869-2:2012, the rated accuracy class of measuring current transformers corresponds to the highest transformation ratio error at nominal primary current. Moreover, IEC 61869-2 defines the permissible transformation ratio error as a function of the primary current; under standard conditions and primary currents that are higher than 20 % of the nominal primary current, the transformation ratio error of the current transformer must lie below its rated accuracy class.

According to IEC 61557-12 and IEC 61869-2, the accuracy class of the measuring instrumentation corresponds to the normalized maximum deviation from reference within a measurement range, in other words, the worst-case relative error. Thus, instead of the standard uncertainty used for random errors, the worst-case error is used in the present investigation, since it can be directly deduced by the accuracy class of the measuring instrumentation. The maximum error Δy of a quantity y that is expressed as a function of n independent quantities x_i that have a certain error Δx_i with considerably lower magnitude than the magnitude of x_i ($|\Delta x_i| < |x_i|$) approximates

$$\Delta y = \sum_{i=1}^{n} \left| \frac{\partial y}{\partial x_i} \Delta x_i \right|, \tag{5.34}$$

(Lerch, 2016). Furthermore, the relative error of the quantity y is defined as $\Delta y/|y|$. The right-hand side of Eq. (5.34) corresponds to the first-order Taylor polynomial of a multivariate function, in other words, to a linear approximation, which is often referred to as propagation of systematic errors or worst-case propagation of uncertainty.

The uncertainty of the real power measured at the grid connection point can be estimated with the aid of the rated accuracy classes of the current transformer and the power analyser. Since the accuracy class of the current transformer is 1 and the accuracy class of the power analyser for the used current transformer and real power measurement is also 1, according to the propagation of uncertainty, the relative uncertainty of the current measured by the power analysers is 2 %. If the current at the grid connection is lower than 20 % of the rated primary current of the current transformer, the relative uncertainty increases to 2.5 %. Furthermore, for currents below 5 % of the rated primary current of the current transformer, the relative uncertainty increases to 4 %. Considering no error in the time recording, according to Eq. (5.30), the propagation of uncertainty in the energy flow at the grid connection approximates

$$G_{\mathrm{E,cs}} = g_{\mathrm{pa}} \overline{|P_{\mathrm{cs}}|} N \Delta t,$$

where N is the number of samples, Δt is the sampling step, g_{pa} is the relative error of the power analyser for current measurement, and $\overline{|P_{\mathrm{cs}}|}$ is the mean absolute power flow at the grid connection during the recording.

In contrast to the power analyser, the accuracy of the devices that measure the quantities required to estimate the internal energy change of the storage units is unknown, as they belong to systems whose manufacturer did not explicitly specify the sensor accuracy. For instance, the uncertainty of voltage and current measured by the BMS is unspecified. However, assuming a reasonable accuracy class for the voltage and current measuring instrumentation, the propagation of uncertainty in the internal energy change of the battery can be estimated through Eq. (5.33). For the voltage and current measuring instrumentation of the BMS an accuracy class of 0.5 is assumed. Furthermore, it is assumed that the accuracy class corresponds to the maximum relative error for the upper 80 % of the measurement range, whereas for the lower 20 % of the measurement range, the maximum relative error increases to 1.5 %. Assuming a measurement range of 0 V to 1000 V for the voltage measuring instrumentation, the voltage of the batteries at operational conditions should always lie within the upper 80 % of the measurement range. Therefore, the lowest relative error is always considered for the voltage measurement of the BMS. Assuming a nominal current of 500 A for the current measuring device of the BMS, results in a relative error of 0.5 % for currents over 100 A and a relative error of 1.5 % for currents under 100 A. According to Eq. (5.33), the propagation of uncertainty in the internal energy change of the battery is

$$G_{\Delta\mathrm{E,bs}} = (g_\mathrm{V} + g_\mathrm{I})\overline{|P_\mathrm{bs}|}N\Delta t,$$

where N is the number of samples, Δt is the sampling step, g_V is the relative error of the voltage measurement, g_I is the relative error of the current measurement and $\overline{|P_\mathrm{bs}|}$ is the mean absolute power flow through the battery during the recording.

The uncertainty of the flywheel speed estimated by the power converter driving the electric machine is also unspecified. In order to estimate the propagation of uncertainty in the internal energy change of the flywheel according to Eq. (5.32), an absolute error of 20 rpm for the flywheel speed within the complete speed range is assumed. Although the inertia of the flywheel is specified in Table A.9, a relative uncertainty of 0.5 % for the rotor inertia is additionally considered as in Schneider (2019). Consequently, the propagation of uncertainty in the internal energy change of the flywheel is

$$G_{\Delta\mathrm{E,fw}} = \Theta\,(\omega_\mathrm{init} + \omega_\mathrm{end})\Delta\omega + \frac{1}{2}(\omega_\mathrm{init}^2 + \omega_\mathrm{end}^2)\Delta\Theta.$$

Compared to the uncertainty of the battery's internal energy change, the uncertainty of the flywheel's internal energy change is independent of time. The uncertainty of the flywheel's internal energy change for a transition from the minimum speed of 2500 rpm to the maximum speed of 5500 rpm is 3.3 Wh. A flywheel cycle that starts at 4000 rpm and returns back to 4000 rpm has an uncertainty of internal energy change of 3.1 Wh.

According to Eq. (5.29), the worst-case propagation of uncertainty in the estimation of the energy losses of the combined storage equals the sum of the derived uncertainties

$$G_\mathrm{E,cs,L} = G_\mathrm{E,cs} + G_{\Delta\mathrm{E,bs}} + G_{\Delta\mathrm{E,fw}}. \tag{5.35}$$

The uncertainty of the cycle efficiency can be estimated according to Eq. (5.31) under the assumption of a symmetrical power flow, which implies an internal energy change approaching zero and an approximately equal duration of negative and positive power flow of similar magnitude. Therefore, the cycle efficiency approximates the ratio of the energy flow out of the system to the energy flow into the system, which are both measured by the same device and therefore have the same relative uncertainty. Thus, the propagation of uncertainty in the cycle efficiency corresponds to a relative error that is double the relative error of the power analyser, hence $2g_\mathrm{pa}$.

Experiments

In a compromise between the available operating range of the flywheel prototype ETA290 at the time of the investigation and the favourable conditions to test the performance of the energy management, a series of experiments were conducted. To investigate the system behaviour at high load a square power refence with a relatively high amplitude was used. The experiments with square power reference aim to approach the maximum load of the combined system that corresponds to the range of low relative error of the measuring instrumentation. Furthermore, high load is advantageous to showcase the performance of the OPS, as the battery losses increase with respect to the no-load losses of the flywheel. The intensity and duration of the square power reference is selected so that the flywheel avoids to operate for long time at its speed limits because such an operation does not showcase its performance. To test the energy management against real applications, a power reference that results from Frequency Containment Reserve (FCR) for a recorded grid frequency profile is applied. For the FCR application, the deadband of ±10 mHz is not used in order to increase the load and therefore the accuracy of the measuring instrumentation. To investigate the performance of the OPS compared to fixed power shares, both OPS and fixed power shares are tested. Furthermore, a varying power level aims to capture the effect of load on the OPS performance. The test matrices for FCR and square power reference are given in Table 5.1 and Table 5.2 respectively.

The initial flywheel speed was adjusted at 4000 rpm and the initial battery voltage at 660 V for FCR power reference, whereas for the square power reference the initial flywheel speed was adjusted at 3000 rpm and the initial battery voltage at 660 V. To clearly record the initial battery voltage and the initial flywheel speed, the data logging was initiated some seconds before the triggering of the power reference. Furthermore, the recording continues for about 60 s after the end of the power reference profile in order to capture the diffusion voltage of the battery. The temperature at the winding overhang of the electric machine and the average temperature of the battery cells were also recorded. During all experiments, the temperature of the winding overhang was in the 30-60 °C range, whereas the average temperature of the lithium-ion cells was in the 21-26 °C range.

Table 5.1 Test matrix of FCR power reference that results from the grid frequency of continental Europe recorded on 01 October 2021 from 08:00 to 08:10 with a sampling time of 1 s for the prequalified power P_{PQ} under OPS as well as under fixed flywheel power shares. The notation x indicates that a test is performed.

		P_{PQ} (kW)	
		120	**140**
OPS		x	x
s_{fw} (%)	**0**	x	x
	2	x	x
	5	x	x

Table 5.2 Test matrix of square power reference with a period of 120 s and the amplitude P_{sqr} under OPS as well as under fixed flywheel power shares, where x denotes that a test is performed.

		P_{sqr} (kW)		
		80	**100**	**120**
OPS		x	x	x
s_{fw} (%)	**0**	x	x	x
	1	x	x	x
	2	x	x	x
	3	x	x	x
	5	x	x	x
	7	x	x	x

Figure 5.9 presents the response of the hsETA prototype to a square power reference with an amplitude of 120 kW and a period of 120 s under a fixed flywheel power share of 10 %. The current I_{bs} and the voltage U_{bs} of the battery storage are shown on the upper two graphs, whereas the lower two graphs show the flywheel current I_{fw} and the flywheel speed n_{fw}. The square power reference is imposed from t_0=10 s to t_e=130 s. The battery voltage resembles the voltage of a resistor-capacitor circuit that is characterized by an increasing voltage for almost constant current when charging and a decreasing voltage for nearly constant current when discharging. Furthermore, a diffusion voltage becomes apparent after the load is removed at t_e=130 s, so that the battery voltage asymptotically converges to the open circuit voltage. At t=52 s and t=114 s the battery load increases, because the flywheel operation is limited either at its lower or its upper speed limit, so that the battery is forced to cover the total load.

The flywheel accelerates from 3000 rpm to the upper speed limit of 5500 rpm in about 42 s, then it rotates about 18 s at the upper speed limit and finally decelerates down to the lower speed limit of 2500 rpm by the time the square reference ends. Since the power of rotating machines is proportional to their angular frequency, the flywheel current decreases with increasing speed in order keep the power constant. An overshoot and a corresponding short oscillation are observed when the reference power of the flywheel changes abruptly. Specifically, oscillations occur at t=10 s when the reference power of 10 % 120 kW=12 kW is first imposed, at t=52 s when the flywheel reaches the upper speed limit and at t=70 s when the reference power steps down to -12 kW. The overshoot and the corresponding oscillations depend on the tuning of the speed and current control implemented in the power converter driving the PMSM. Although overshoot is generally undesired, it has a small effect on the assessment of the high-level energy management. Generally, the speed and current control of the power converter can be tuned to meet the requirements of the application in question.

The energy losses of the combined system are not directly measured but estimated through Eq. (5.29). Figure 5.10 presents the experimentally estimated energy losses of the hsETA for FCR power reference under fixed flywheel shares as well as under OPS. The points that share a common prequalified power are connected to form a curve. It is observed that the lowest losses under FCR correspond to zero fixed flywheel share. Furthermore, the energy losses increase with increasing flywheel share, which can be explained by the fact that the no-load losses of the PMSM mainly depend on its speed and therefore accelerating over the initial speed of 4000 rpm, which is the case when s_{fw}>0, increases the no-load losses. The prequalified power of 140 kW expectedly corresponds to higher losses than that of 120 kW, however only to a small extent, since the step of 20 kW corresponds to a change of only 1.5 kW in the mean absolute power of the FCR power reference.

To estimate the propagation of uncertainty in the CS energy losses, it is assumed that the battery power flow approximates the total CS power flow, as the flywheel power share always lies below 10 %. The mean absolute power of the FCR power reference with P_{PQ}=140 kW corresponds roughly to 12 kW. Considering an increased relative error of 2.5 % for the power measurement at the grid connection due to the low current, an increased relative error of 1.5 % for the battery current measurement and a relative error of 0.5 % for the battery voltage measurement, according to Eq. (5.35), the propagation of uncertainty in the energy losses of the CS is

$$G_{E,cs,L} = 2.5\ \% \cdot 12\ \text{kW} \cdot \frac{10}{60}\ \text{h} + (1.5 + 0.5)\ \% \cdot 12\ \text{kW} \cdot \frac{10}{60}\ \text{h} + 3.3\ \text{Wh} \ \approx 95\ \text{Wh}.$$

The uncertainty of 95 Wh accounts for almost 34 % of the average energy losses presented in Figure 5.10, which implies that the uncertainty in the estimated energy losses of the CS is significant. Although the CS losses under OPS are lower than the losses under fixed flywheel share, the apparent improvement through OPS lies within the uncertainty range of the experimental loss estimation, that is ±95 Wh.

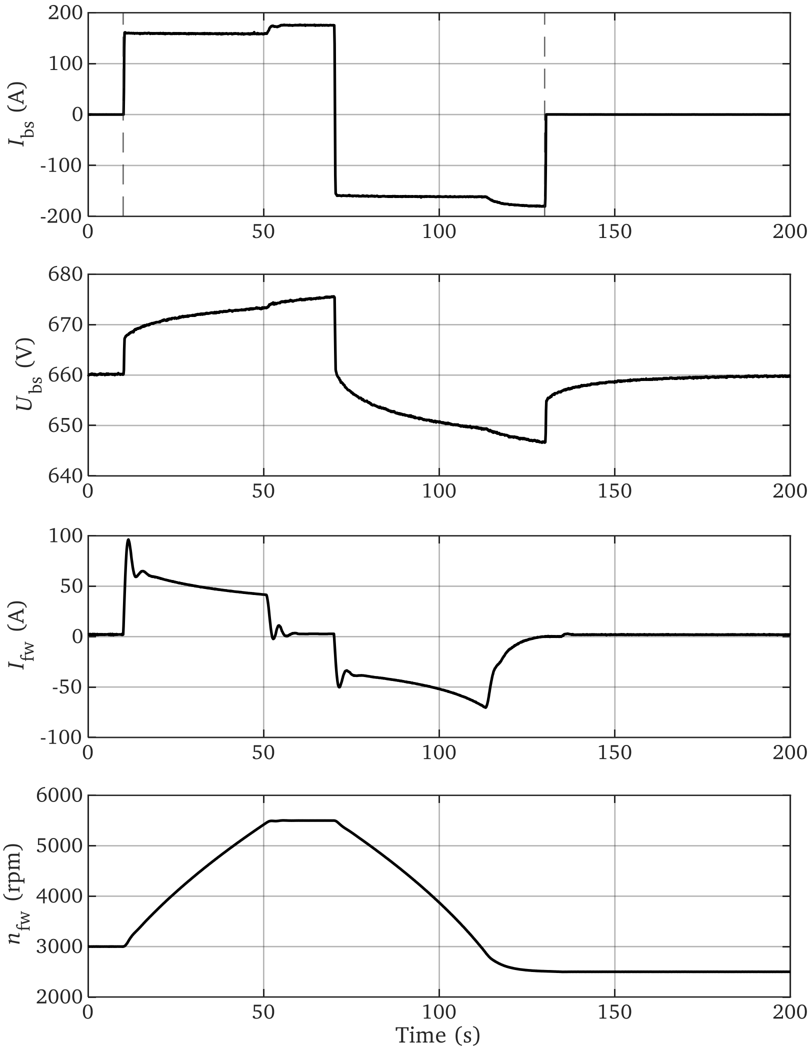

Figure 5.9 Response of the hsETA prototype to a square power reference of 120 kW under a fixed flywheel power share of 10 %. From above; battery current I_{bs}, battery voltage U_{bs}, flywheel current I_{fw} and flywheel speed n_{fw}. The flywheel current corresponds to the quadrature component of the three-phase space vector of the PMSM current times $1/\sqrt{2}$.

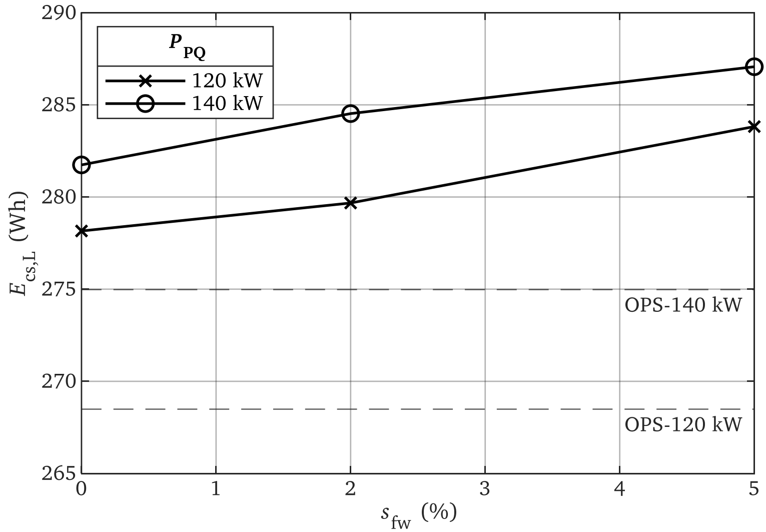

Figure 5.10 Experimentally estimated energy losses of the hsETA prototype under FCR power reference with a prequalified power of 120 kW and 140 kW under fixed flywheel shares as well as under OPS. The CS losses increase with increasing flywheel share.

Figure 5.11 depicts the experimentally estimated losses of the combined storage for square power reference under fixed flywheel shares as well as under OPS. The points of fixed flywheel shares and CS losses that correspond to the same amplitude P_{sqr} are connected to form a curve, whereas the CS losses under OPS for each P_{sqr} are depicted as a level. In contrast to the FCR power reference, several fixed flywheel shares exist that are both higher than zero and lead to lower CS losses than that under zero flywheel share. In particular, the minimum CS losses are observed at s_{fw}=1 % for P_{sqr}=80 kW, at s_{fw}=2 % for P_{sqr}=100 kW and at s_{fw}=3 % for P_{sqr}=120 kW. Therefore, a tendency is observed that the fixed flywheel share that corresponds to the minimum CS losses increases with the amplitude of the square power reference. For each amplitude, the minimum losses are observed for a fixed flywheel share and not for the OPS. Considering that fixed flywheel shares over 10 % that are not depicted in Figure 5.11 further increase the CS losses, the CS losses under OPS lie within the low-loss region, although they are higher than that of some fixed flywheel shares.

The mean absolute power of the square power reference equals its amplitude. For P_{sqr}=100 kW all measuring devices operate at the lowest relative error and therefore the propagation of uncertainty in the CS energy losses is

$$G_{\mathrm{E,cs,L}} = 2\ \% \cdot 100\ \mathrm{kW} \cdot \frac{2}{60}\ \mathrm{h} + (0.5 + 0.5)\ \% \cdot 100\ \mathrm{kW} \cdot \frac{2}{60}\ \mathrm{h} + 3.3\ \mathrm{Wh}\ \approx 100\ \mathrm{Wh},$$

which is significantly high with respect to the estimated losses presented in Figure 5.11. Therefore, the experimentally estimated losses are indicative and serve as qualitative results.

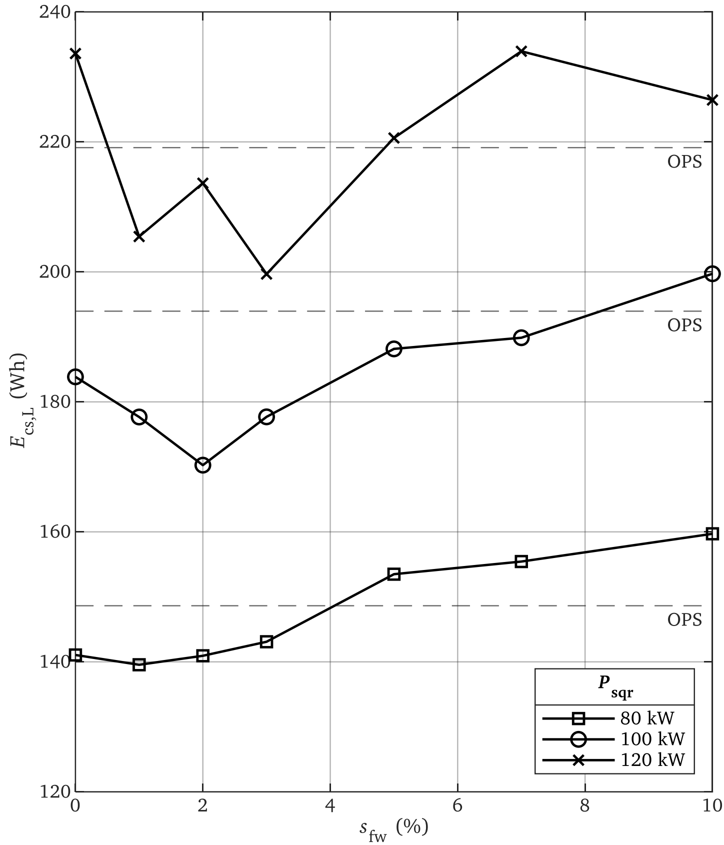

Figure 5.11 Experimentally estimated energy losses of the prototype hsETA for a square power reference with a period of 120 s and varying amplitude under fixed flywheel shares as well as under OPS. The lowest CS energy losses correspond to fixed flywheel shares that are higher than zero.

According to Eq. (5.31), the experimentally estimated cycle efficiency of the CS under FCR power reference ranges between 76 % and 80 %, whereas the CS cycle efficiency under square power reference ranges between 88 % and 90 %. The square reference leads to a higher cycle efficiency than the FCR reference, despite the fact that it involves significantly higher load than the FCR reference. The relatively low efficiency under the FCR reference is mainly the result of significant no-load losses with respect to the total load.

For symmetrical power profiles, the internal energy change in the storages is rather small. Therefore, according to Eq. (5.31), the propagation of uncertainty of the internal energy change in the cycle efficiency of the CS can be neglected. Compared to the estimation of the energy losses according to Eq. (5.29), where the measured quantities are subtracted, the cycle efficiency corresponds to a ratio of measured quantities. Consequently, in contrast to the high uncertainty in the experimental estimation of the energy losses, the uncertainty of the cycle efficiency for the square power refence is substantially lower. The relative uncertainty of the CS cycle efficiency under the square refence is estimated to be twice the relative error of the power measurement at the grid connection, that is 4 %.

Comparison between Experimental and Simulated Results

The combined storage prototype hsETA is modelled, parametrized and simulated, so that simulated and experimental results can be compared. The technical data of the ETA290 flywheel prototype (Table A.2 and Table A.9) are used to parametrize the flywheel model. Due to insufficient measurements on the ETA290 prototype, the iron resistance of the SWIVT290 prototype is used. The assumption of a similar iron resistance is based on the fact that ETA290 and SWIVT290 have similar PMSMs. The batteries and the corresponding lithium-ion cells are modelled according to the available technical data summarized in Table A.5 and Table A.4 respectively. Due to inadequate data to parametrize an elaborate lithium-ion cell model like that presented in Figure 3.7, a constant equivalent resistance and a linear open circuit voltage over state of charge is assumed. The losses of the power converters are modelled according to the technical data listed in Table A.10. Furthermore, the load losses of the grid-side equipment such as the sinus filter are modelled according to the manufacturer specification.

To increase the accuracy of the simulation, the measured no-load consumption of the hsETA prototype is additionally considered, for instance, the iron core of the sinus filter as well as several components of the grid-side power converter consume power already at no-load. The no-load losses are measured when all power converters of hsETA are active, however, without supplying any power. Consequently, the average power consumption of hsETA at no-load is experimentally estimated at 780 W. The low voltage power supplies of the central control unit, the BMS, the AMBs, the vacuum pumps and several sensors belong to a separate circuit, the power consumption of which is not recorded by the power analyser at the grid connection point. Therefore, they are not included in the experimentally estimated losses and also not considered in the simulation.

Speed profiles with a set acceleration and a target speed serve as reference in the control loop of the power converter driving the ETA290 prototype. Since constant acceleration roughly corresponds to constant torque, the control loop of the flywheel prototype is simulated as torque control. The simulation time step corresponds to the sampling time of 100 ms that is used in the real system. The several controllers and communication gateways in the control loop of the real system inevitably cause delays. The delays of the real control loop are not simulated. Consequently, a delay between the simulated and the measured signals in the 300-500 ms range can be observed. Furthermore, the adjustments in the energy management strategy in the real controller are also applied in the simulation, for instance the deadband of ± 10 mHz for FCR is unused.

Figure 5.12 compares the simulated and the measured response of the hsETA prototype for FCR power reference with a prequalified power of 140 kW under OPS. The upper diagram shows the course of the grid frequency of continental Europe on 01 October 2021 from 08:00 to 08:10 imposed between t_0=50 s and t_e=650 s, which serves as reference both for the simulation and the real system. The lower diagram shows the resulting balancing reserve power provided by the combined storage system at the grid connection. The good congruence between experimental and simulated balancing reserve power verifies that the simulation and the real system respond comparably to a common reference. However, although the simulated and the measured curves of the balancing reserve power in Figure 5.12 seem identical, the mean absolute error of the simulated with respect to the measured power on the grid side is 640 W, which reasonably results in discrepancies between experimentally estimated and simulated energy losses.

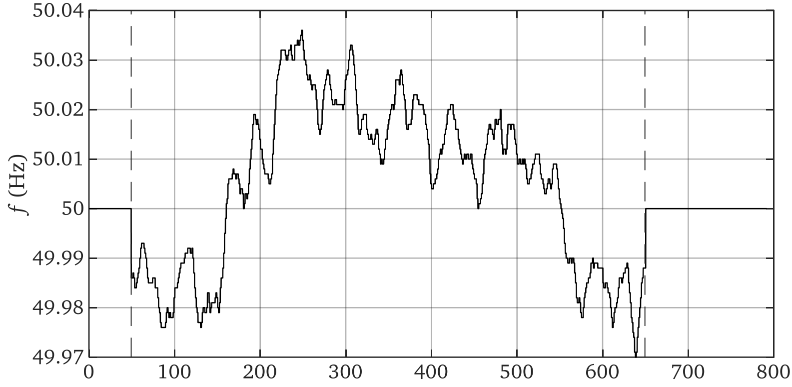

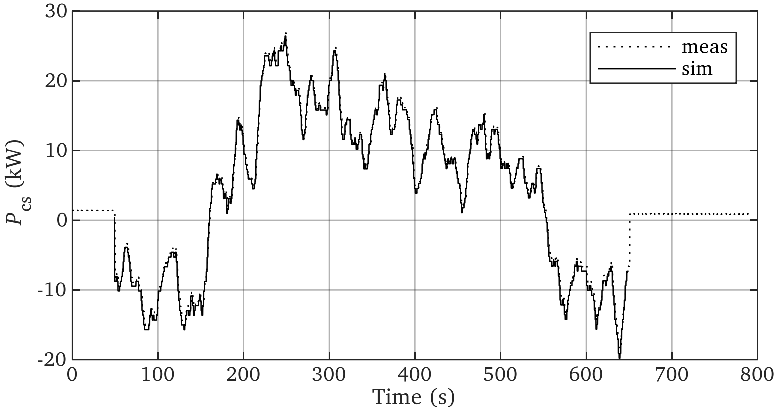

Figure 5.12 Simulated and measured response of the combined storage prototype hsETA for FCR power reference with a prequalified power of 140 kW under OPS. **Up**: grid frequency of continental Europe on 01 October 2021 from 08:00 to 08:10, **bottom**: balancing reserve power on the grid side

Figure 5.13 presents the simulated and the measured response of the flywheel current and the flywheel speed under OPS for the same FCR power reference as that of Figure 5.12. The flywheel current I_{fw} corresponds to the quadrature component of the three-phase space vector of the stator current times $1/\sqrt{2}$. The magnitude of both the measured and the simulated current do not exceed 9 A, which corresponds to approximately 5 % of the nominal current of the PMSM. Whereas discrepancies between measured and simulated current are observed, the simulated and measured speed show good congruence. The mean absolute error of the simulated flywheel current with respect to the measured is 1.1 A, whereas the mean absolute error of the simulated flywheel speed with respect to the measurement is 2 rpm.

The good congruence between simulated and measured speed signifies that an accurate flywheel inertia Θ is used in the model. Although the control runs faster in the simulation than in the real system, there is no observable difference between the measured and the simulated speed response due to the relatively slow dynamics of the FCR reference.

The power converter requires a target speed and a set acceleration in order to internally run a current control loop. The simulated control loop determines the stator current that corresponds to the required torque, subsequently, the stator current is imposed without delay to the model of the electric machine. Therefore, discrepancies in the stator current between the simulation and the real system are reasonable, as the dynamic response of the current is faster in the simulation. The always positive deviation of the measured from the simulated current, which is remarkable at low currents, is the result of higher no-load losses in the real system than in the simulation. In other words, higher current is required in the real system than in the simulation to compensate the braking torque. The discrepancies between the simulated and the measured current also depend on the accuracy of the modelled relationship between current and torque. According to Eq. (3.14) the relationship between current and torque mainly depends on the flux linkage of the stator windings with the permanent magnets, which is denoted as Ψ_{PM}. Therefore, the uncertainties in the modelling of the parameter Ψ_{PM} including its temperature dependence, is one of the main reasons for the discrepancies between measured and simulated current.

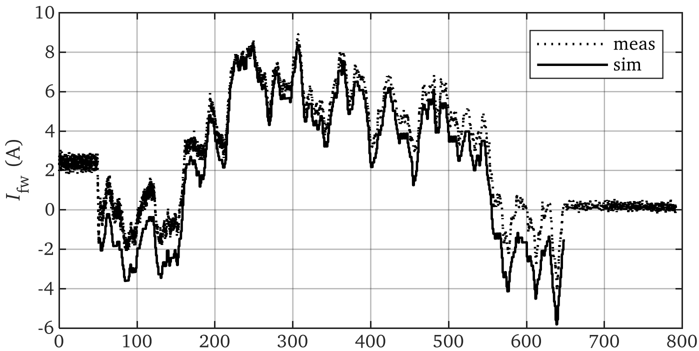

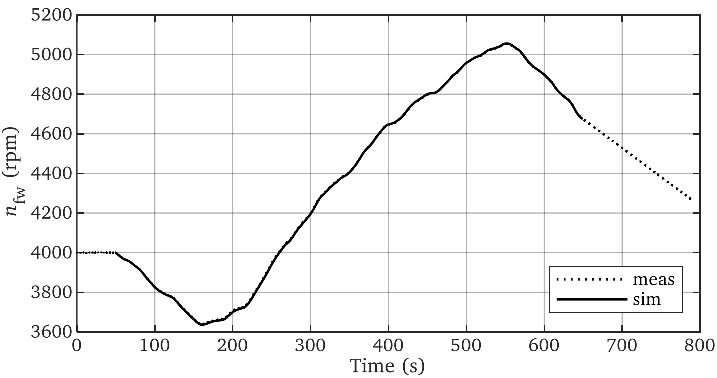

Figure 5.13 Simulated and measured response of current (up) and speed (bottom) of the flywheel prototype ETA290 under FCR power reference. The flywheel current corresponds to the quadrature component of the three-phase space vector of the PMSM current times $1/\sqrt{2}$.

Figure 5.14 presents the simulated energy losses of the hsETA prototype under fixed flywheel shares as well as under OPS for the FCR power reference resulting from the grid frequency of continental Europe on 01 October 2021 from 08:00 to 08:10. The fixed flywheel share that minimizes the energy losses is zero for each prequalified power, which is congruent with the experimental results presented in Figure 5.10. Moreover, a qualitative congruence between experimental and simulated results is observed as the energy losses of the combined system increase with flywheel share and prequalified power. Due to the relatively low load of the FCR power reference, the increase in the energy losses with prequalified power is in the range of a few Wh. Flywheel power shares over 10 % lead to a plateau region, as the flywheel accelerates up to its speed limit and rotates for a significant time at constant speed where its power losses are constant.

The measured energy losses of hsETA under FCR power reference presented in Figure 5.10 are about 80 Wh higher than the corresponding simulated losses presented in Figure 5.14. Besides the uncertainty in the experimental results, the wide discrepancy between measurements and simulation is the result of approximations in the modelling of the no-load losses. The no-load losses of the ETA290 prototype were modelled with the aid of the iron resistance of the SWIVT290 prototype, which is regarded as the main reason for the discrepancies in the energy losses. The difference of 80 Wh in the energy losses corresponds to a difference of 480 W in the no-load power losses, since the duration of the FCR power reference is 10 min.

A direct comparison of the simulated and the experimentally estimated losses under OPS is inexpedient due to the high uncertainties involved in the experimental estimation. Nevertheless, as it can be observed in Figure 5.10 and Figure 5.14, the operation under OPS leads to lower energy losses than several fixed flywheel shares both in the simulation and in the real system, which also signifies a qualitative congruence between simulated and experimental results.

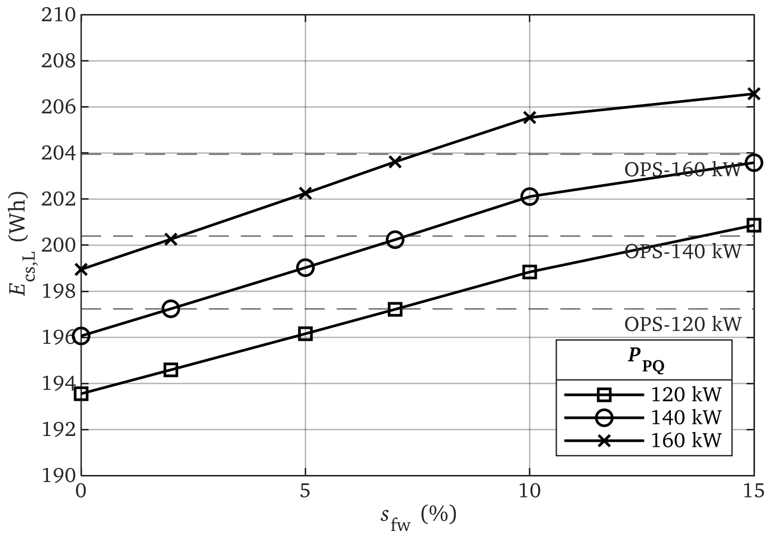

Figure 5.14 Simulated energy losses of the combined storage system hsETA over fixed flywheel power shares as well as over OPS under the FCR power reference resulting from the grid frequency of continental Europe on 01 October 2021 from 08:00 to 08:10 and varying prequalified power.

Figure 5.15 presents the simulated energy losses of the hsETA under square power reference with varying amplitude and a period of 120 s over fixed flywheel shares, where the energy losses under OPS for each amplitude are also annotated as a level. As observed in the experimental results presented in Figure 5.11, the fixed flywheel share that causes the lowest energy losses increases with the amplitude of the square power reference. In contrast to the experimental results, which involve high uncertainties, the simulated results show that the OPS leads to lower losses than the lowest losses observed under fixed flywheel shares. For P_{sqr}=100 kW, the OPS leads to lower losses than each fixed flywheel share. For P_{sqr}=120 kW, a similar behaviour is observed with the exception of s_{fw}<2 %, where the battery power converter peaks at its maximum current, which reduces the energy losses under fixed flywheel shares as the load is not anymore fully covered.

Observing the experimental results of Figure 5.11 and the simulated results of Figure 5.15 becomes apparent that the experimentally estimated energy losses are considerably higher than those simulated with the exception of P_{sqr}=120 kW. Besides the uncertainties involved in the experimentally estimated losses, a systematic discrepancy is apparent, which is linked to the approximations in the modelling of the no-load losses of the flywheel prototype ETA290. The discrepancy is more pronounced for P_{sqr}=80 kW because, at low load, the no-load losses account for a significant part of the total losses.

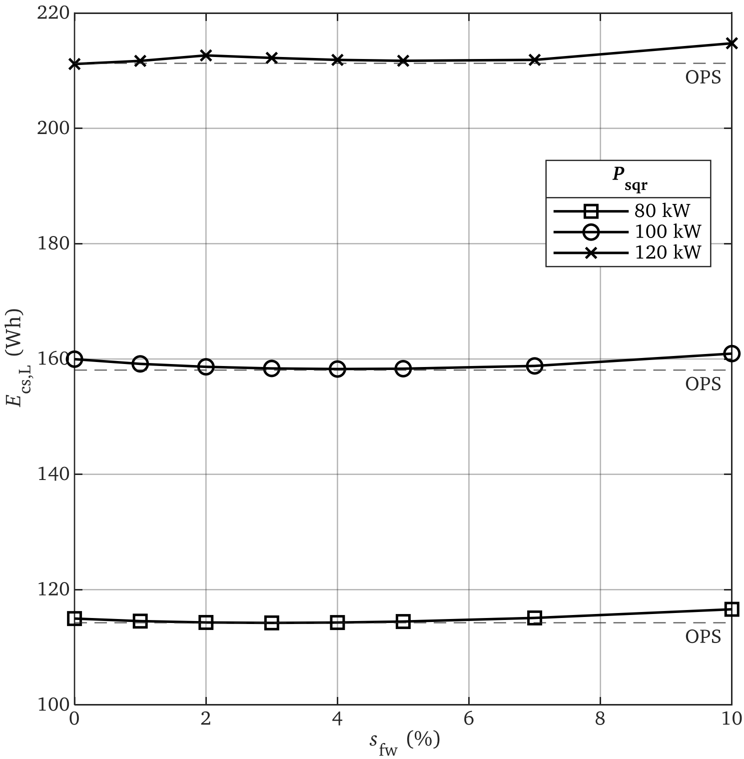

Figure 5.15 Simulated energy losses of hsETA for a square power reference with a period of 120 s and varying amplitude under fixed flywheel power shares as well as under OPS.

The simulated and experimentally estimated cycle efficiencies of the prototype hsETA for FCR and square power reference under OPS are summarized in Table 5.3. The low load of the FCR reference compared to the square reference amplifies the effect of the no-load losses and leads to a relatively low cycle efficiency. A remarkable discrepancy between simulated and experimentally estimated efficiency under FCR is observed, which is a direct consequence of the higher no-load losses in the real system than in the simulation. As the propagation of uncertainty in the cycle efficiency of symmetrical cycles is less significant and the discrepancies in the no-load losses have a less significant effect on short-term power profiles, a good congruence between experimentally estimated and simulated cyclic efficiency under square power reference is observed.

The simulated cycle efficiency of hsETA under square power reference slightly decreases with increasing amplitude. Decreasing efficiency with increasing load is reasonable, since power losses in electrical equipment increase quadratically with current. However, due to the relatively small amplitude increment of 20 kW, a decreasing efficiency with increasing load is not observable in the experimental results. Under FCR power reference, both the simulated and the experimentally estimated efficiency increase with increasing load. Below a certain load, the no-load losses are higher than the load-dependent losses, which results in increasing efficiency with increasing load. Since the FCR reference leads to a substantially lower load than the square reference, an increasing cycle efficiency with increasing load is reasonable.

Table 5.3 Simulated and experimentally estimated cycle efficiency of the combined storage prototype hsETA under OPS for FCR power reference with variable prequalified power P_{PQ} and square power reference with variable amplitude P_{sqr}.

Power Reference Type	P_{PQ} / P_{sqr} (kW)	Simulated cycle efficiency (%)	Experimentally estimated cycle efficiency (%)
FCR	120	85	77
	140	87	80
Square	80	92	89
	100	91	89
	120	90	90

Discussion

Due to the low computational requirements of the energy management algorithm including the OPS, there were no restrictions in the computational resources when compiling and running the application in the PLC. Compared to more elaborate optimization algorithms, the OPS showcases an alternative with low computational requirements, reasonable low-level programming effort and intuitive parameter adjustment.

The operating speed of the flywheel prototype system ranges from 2500 rpm to 5500 rpm. A speed lower than 2500 rpm is less reasonable as it leads to both low energy content and low available power. A speed higher than 5500 rpm was avoided at the time of the investigation due to the limitations of the AMBs. For the specified flywheel inertia of 4.3 kgm^2, the operating speed range corresponds to a usable energy of roughly 160 Wh. The obviously low energy capacity essentially limits the ability of the flywheel to supply or sink power. In other words, high flywheel power shares lead to deceleration or acceleration towards the speed limits, where the flywheel can operate only unidirectionally. Therefore, only flywheel power shares below 10 % were applied.

Due to the significance of the no-load losses at low load, the minimum losses of hsETA under FCR power reference correspond to zero flywheel power share both in the simulated and the experimental results. On the other hand, under square power reference, due to the comparatively high load, there is an observable reduction in the energy losses of hsETA for flywheel shares higher than zero both in the simulated and the experimental results. Although the prequalified power for FCR is about as high as the amplitude of the square power reference, the applied grid frequency profile remains far from the frequency deviation of 200 mHz, which corresponds to a balancing reserve power that equals the prequalified power. The probability distribution of the grid frequency presented in Figure 4.3 illustrates that a frequency deviation of 200 mHz is quite rare. Consequently, considering an FCR reference with a prequalified power that equals the amplitude of a square reference, the load resulting from the FCR reference is considerably lower than that resulting from the square reference.

The experimentally estimated energy losses of the hsETA are significantly higher than the simulated, which is linked to the modelling of the no-load losses of the flywheel prototype ETA290. The discrepancy between simulated and experimentally estimated losses is more pronounced under FCR power reference due to its longer duration. Despite the uncertainties in the parameters used in the objective function of the OPS, the OPS leads to energy losses that approach the minimum energy losses under fixed flywheel shares in the real system. Degradation-dependent parameters such as the internal resistance of the lithium-ion cells change over time and usage. Depending on the available sensors, parameter identification can be applied at regular intervals in order to update the degradation-dependent parameters in the objective function of the OPS and consequently enhance its long-term performance.

The inaccurate estimation of the energy losses is not the result of deficiencies in the measuring instrumentation, but rather the result of the indirect measurement of the energy losses. To estimate the energy losses, quantities of considerably higher magnitude than the magnitude of the energy losses are measured such as the power at the grid connection point. The uncertainties in the measurement of quantities with relatively high magnitude propagates to the estimation of the energy losses that have a relatively low magnitude, which leads to a disproportionally high uncertainty in the estimation of the energy losses.

The propagation of uncertainty in the experimentally estimated energy losses of hsETA does not only depend on the uncertainties of the power measured at the grid connection, but also on the uncertainties involved in the experimental estimation of the internal energy change of the storages. Moreover, it depends on the method used to estimate the internal energy change, for instance, a linear characteristic of the voltage over state of charge is assumed for the battery. Although the uncertainties in the experimental estimation of the energy losses are high, the experimentally estimated losses show qualitative congruence with the simulated losses. The energy losses of hsETA under square power reference minimize for fixed flywheel shares higher than zero in the simulation, which is also observable in the experimental results despite the high uncertainties. Moreover, the experimentally estimated losses under OPS are close to the corresponding minimum losses for fixed flywheel shares, which signifies a positive result concerning the performance of the OPS.

6. Economic Assessment

The economic assessment aims to investigate the conditions under which battery-flywheel storages are cost-efficient compared to battery-only storages. Assuming that combined and battery-only storage systems equivalently fulfil the application requirements, the revenues that can be achieved in a certain application are independent of the composition of the energy storage system. The estimation of revenues for applications like FCR involve higher uncertainties than the estimation of the investment and operating cost. Therefore, the revenues that can be achieved with FCR or other applications are not further investigated. Instead, the investigation focuses on the financial burden of the owner of the energy storage system.

The terms *life cycle cost* and *Total Cost of Ownership* (TCO) are often used interchangeable to describe the cost of an asset throughout its lifetime. The standard IEC 60300-3-3:2017, which relates to the dependability of electrical equipment, defines *Life Cycle Costing* as the process to assess the life cycle cost of an item, which in turn leads to the estimation of the total cost of ownership. Approaches similar to those suggested in IEC 60300-3-3 are applied to estimate the life cycle cost of equipment used in electrical grids (Balzer & Schorn, 2022). The term life cycle cost is perceived as the expenses throughout the lifetime of an asset, whereas the term total cost of ownership is perceived as the part of the expenses connected with the ownership of an asset. For instance, although the life cycle cost includes the disposal cost of an asset such as an electrochemical battery, the owner may not assume such a cost. According to the *Directive 2006/66/EC* of the European Parliament on battery waste, which is realized as the battery act of 2009 in Germany (Batteriegesetz), the manufacturer of the battery, or the distributor in the case of imported batteries, assume responsibility for the disposal. Thus, the battery owner may only deliver the battery to the waste treatment facility. Furthermore, the cost that is linked to the design and the manufacturing of an asset indirectly concerns the asset owner as he assumes only the resulting acquisition cost. It can therefore be claimed that the total cost of ownership results from adding up all the costs incurred by the owner throughout the time he assumes ownership of an asset. Consequently, the term total cost of ownership fits better to the purpose of the present investigation, as the energy storage owner should not always bear the total life cycle cost.

In the present investigation, the ownership cost is categorised into investment cost, operation and maintenance (O&M) cost and disposal cost, which correspond to the three main life cycle stages shown in Figure 6.1: realisation, operation and disposal. The three cost categories are further divided into subcategories that are specific for energy storage systems. Compared to the method suggested in IEC 60300-3-3, the present work uses a simplified approach to estimate the TCO of the investigated energy storage systems because several life cycle stages and cost factors introduced in IEC 60300-3-3 are either irrelevant for the current work or little information is available about them.

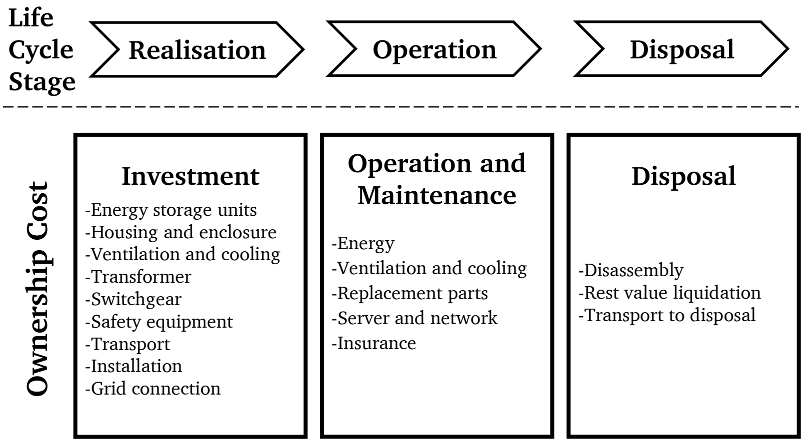

Figure 6.1 Breakdown of ownership cost over the life cycle stages of energy storage systems

6.1 Cost Model

The cost parameters required to estimate the TCO of the investigated energy storage systems are empirically estimated. The economic assessment does not aim to evaluate the cost of a certain storage system but to compare the cost of battery-flywheel storage systems with that of battery-only storage systems. Therefore, detailed information about the equipment cost is unnecessary.

The investment cost mainly depends on the manufacturing cost of the storage units, which may decrease in the future due to economies of scale, improvements in the manufacturing process as well as improvements in the product itself. However, the manufacturing cost can also rapidly increase due to disruptions in the supply chain or shortage of raw materials. The operation and maintenance cost mainly depends on the electricity rate, which in turn is volatile as it depends on the situation of the global energy market. The disposal cost is usually difficult to estimate without detailed information about the recycling process. However, if the storage owner does not assume the cost of the complete recycling process, the part of the disposal cost that the owner has to bear is easier to estimate. To estimate the propagation of uncertainty of the various cost parameters in the TCO, a sensitivity analysis is pursued.

There is no specific need to express the cost in a certain currency, so that the currency independent *cost unit* (cu) is used. Consequently, the investigation shifts away from market prices, in order to focus on the estimation of reasonable relations between the cost parameters.

Investment Cost

The investment cost breaks down into acquisition, transport and installation cost. The acquisition cost corresponds to the cost incurred by the owner in order to purchase the equipment, which means that the product development cost is only indirectly considered. The transport cost corresponds to the shipping expenses, which can be considerable when bulky equipment is involved. The installation cost concerns the expenses to build a functional system from the acquired equipment and put it into operation.

Acquisition Cost

To estimate the acquisition cost of energy storages, a technology-dependent energy capacity cost factor in cu/kWh is used. Lithium-ion cells usually have an energy to power ratio that approximates 1 h, whereas the energy to power ratio of flywheels is more flexible. Thus, a power capacity cost is additionally considered for flywheels. The power capacity cost corresponds to the acquisition cost of the electric machine driving the flywheel, assuming that all other costs related to the flywheel acquisition are included in the energy capacity cost. The cost of the electric machine is estimated with the aid of the power capacity cost factor k_{m} in cu/kW, which depends on the technology of the electric machine. The power converters required for the integration of both storage technologies lead to an additional power capacity cost. Therefore, a power capacity cost factor k_{pc} in cu/kVA for all semiconductor-based power converters used in the configuration is assumed. Since the power rating of converters is usually a bit higher than that of the storage units to which they are connected, different power ratings are used to estimate the cost of the storage units and the cost of the corresponding power converters. Therefore, the acquisition cost of a flywheel storage with power converter is

$$C_{\mathrm{acq,fw}} = k_{\mathrm{fw}} E_{\mathrm{fw,N}} + k_{\mathrm{m}} P_{\mathrm{m,N}} + k_{\mathrm{pc}} S_{\mathrm{fw,pc,N}},$$

where k_{fw} is the energy capacity cost factor for flywheel storages, $E_{\mathrm{fw,N}}$ is the nominal energy capacity of the flywheel, $P_{\mathrm{m,N}}$ is the nominal power of the flywheel's electric machine and $S_{\mathrm{fw,pc,N}}$ is the power rating of the flywheel's power converter. Similarly, the acquisition cost of a battery unit with power converter is

$$C_{\mathrm{acq,b}} = k_{\mathrm{b}} E_{\mathrm{b,N}} + k_{\mathrm{pc}} S_{\mathrm{b,pc,N}},$$

where k_{b} is the energy capacity cost factor for batteries, $E_{\mathrm{b,N}}$ is the nominal energy capacity of the battery and $S_{\mathrm{b,pc,N}}$ is the power rating of the battery's power converter.

Considering that the combined storage system comprises N_{fw} flywheels and N_{b} batteries, the acquisition cost of the storage units including their power converters adds up to

$$C_{\mathrm{acq,b\&fw}} = N_{\mathrm{fw}} C_{\mathrm{acq,fw}} + N_{\mathrm{b}} C_{\mathrm{acq,b}}.$$

If only batteries are considered, the number of flywheels N_{fw} equals zero. The cost of the basic equipment required to build a functional system does not affect the cost difference between combined and battery-only systems, as long as the rated power of the systems remains unchanged. However, as the basic equipment accounts for a significant proportion of the total equipment cost, it affects the ratio of individual to total equipment cost. Therefore, to obtain a realistic breakdown of the equipment cost of the energy storage system, the basic equipment cost is also considered.

The storage owner assumes the cost of the three-phase power transformer required to integrate the energy storage system into the electrical grid instead of the distribution system operator. The cost of the power transformer is estimated through the transformer power capacity cost factor k_{tr} in cu/kVA and the rated power capacity of the installation S_{N}. However, additional equipment is required to realise an energy storage system such as the equipment listed in Figure 6.1 under investment cost. The cost of basic equipment, such as housing, ventilation, switchgear etc., depends on the power rating of the installation and is therefore estimated similar to the power transformer cost with the aid of the power capacity cost factor k_0 in cu/kVA and the rated power capacity of the installation S_{N}. Consequently, the acquisition cost of the basic equipment includes the acquisition cost of the power transformer $C_{\mathrm{acq,tr}}=k_{\mathrm{tr}}S_{\mathrm{N}}$, the acquisition cost of the grid-side power converter $C_{\mathrm{acq,gpc}}=k_{\mathrm{pc}}S_{\mathrm{N}}$ and the acquisition cost of the rest basic equipment $C_{\mathrm{acq,0}} = k_0 S_{\mathrm{N}}$, which leads to the total acquisition cost of the combined storage

$$C_{\mathrm{acq,cs}} = C_{\mathrm{acq,b\&fw}} + C_{\mathrm{acq,tr}} + C_{\mathrm{acq,gpc}} + C_{\mathrm{acq,0}}.$$

The cost factors that are needed to estimate the acquisition cost of the equipment of the energy storage system are summarized in Table 6.1. Unless otherwise specified, the reference value of the cost factors is used in the investigation, whereas the range corresponds to uncertainties in the cost factors which are used in sensitivity analyses.

Table 6.1 Cost factors related to the acquisition cost of the equipment of the combined energy storage

Parameter	Unit	Range	Reference value	Description
k_{pc}	cu/kVA	60…100	80	power converter cost per nominal apparent power
k_{tr}	cu/kVA	30…100	40	power transformer cost per nominal apparent power
k_0	cu/kVA	20..100	50	basic equipment cost per system nominal power
k_{m}	cu/kW	50…100	70	electric machine cost per nominal power
k_{fw}	cu/kWh	2000…20 000	8000	flywheel energy capacity cost factor (excluding electric machine cost)
k_{b}	cu/kWh	100…1000	500	battery energy capacity cost factor

According to the reference values of the cost factors listed in Table 6.1 and the size of the reference combined storage system presented in Table 4.3, the cost for a SWIVT290 flywheel prototype including the power converter is 31 800 cu, whereas the cost of the battery unit including the power converter is 27 740 cu. Furthermore, the acquisition cost of the central power converter is 100 000 cu, the three-phase power transformer costs 50 000 cu, and the basic equipment costs 62 500 cu. Therefore, considering the number of storage units, the acquisition cost of the reference combined storage system adds up to approximately 1.11 Mcu.

Transport Cost

The transport cost of bulky equipment such as energy storage units can account for a significant proportion of the investment cost. The transport cost depends on the volume and weight of the goods to be shipped and the path between warehouse and delivery location. Although batteries have a significantly higher specific energy than flywheels, the specific power of batteries and flywheels is comparable. Therefore, the transport cost factor k_{trs} in cu/kVA, which is listed for clarity in Table 6.2, is used to estimate the transport cost for both storage technologies. The specific power of the power transformers and the semiconductor-based power converters is higher than that of the storage units, so that using the same transport cost factor as for the storage units would lead to an overestimation of their shipping cost. Therefore, the shipping cost of the power transformer and the central power converter are not considered separately but included in the transport cost of the basic equipment which is estimated as the transport cost factor times the rated power of the installation. Consequently, the transport cost of the reference combined storage system results in 5520 cu, which is substantially lower than the corresponding acquisition cost of 1.11 Mcu.

Table 6.2 Cost factor to estimate the transport cost of the equipment required in the combined energy storage system

Parameter	Unit	Range	Reference value	Description
k_{trs}	cu/kVA	1…5	2	cost of transport per equipment rated power

Installation cost

The installation cost comprises the expenses incurred by the owner of the energy storage to combine the various components into a functional system and put it into operation. Thus, the installation cost can be estimated as the cost of the labour and services required to put the system into operation. For instance, the labour cost of the technicians required for the mounting and wiring of the equipment belongs to the installation cost. Moreover, the installation cost includes the labour cost of experts required for the testing and approval both in component and system level. Furthermore, the costs related to the permits required to operate the storage system, which are granted by the responsible authorities, also belong to the installation cost. Consequently, in contrast to the acquisition and the transport cost, a linkage between the power rating of the equipment and the installation cost is less obvious.

At storage unit level, the installation cost concerns the integration and technical approval of each individual flywheel and battery including their corresponding power converter. Similarly, the integration of the power transformer, the grid-side power converter, and the basic equipment is linked to installation cost. The installation cost of flywheel storages is considered significantly higher than that of batteries, due to the relatively high effort involved in the setup and approval of rotating machinery as well as in the setup of the magnetic levitation and the vacuum system. A list of the estimated installation expenses of the combined energy storage system, which is intended for FCR, is provided in Table 6.3. The estimated installation expenses are an application example rather than the result of an extensive investigation, since the required information for a detailed estimation of installation expenses is usually difficult to access. The installation expenses that are not directly connected with the storage units belong to the installation cost of the basic equipment.

Table 6.3 Installation expenses of the combined energy storage system intended for FCR

Type of installation expense	Cost (cu)
Battery with power converter	200
Flywheel with power converter	500
Grid-side power converter	800
Three-phase power transformer	1000
Housing, switchgear, ventilation and cooling, etc.	5000
System integration test and technical approval	3000
Connection to the electrical grid by the distribution system operator	800
Prequalification by the transmission system operator	1000

Breakdown of the investment cost of the reference combined storage system

The investment cost of the reference combined storage system summarized in Table 4.3 (30 batteries and 2 flywheels) results in 1.13 Mcu, whereas the investment cost of the reference battery-only system summarized in Table 4.2 (42 batteries) is 1.38 Mcu, which corresponds to an increase of roughly 22 % compared to the combined storage system. The investment cost of the reference combined storage system breaks down into 98 % for the acquisition, 0.5 % for the transport and 1.5 % for the installation, thus, the acquisition cost is clearly dominant. As illustrated in Figure 6.1, the breakdown of the investment cost into equipment categories results in 75 % for the battery storage including its power converters, 5.5 % for the kinetic storage including its power converters and 19.5 % for the basic equipment.

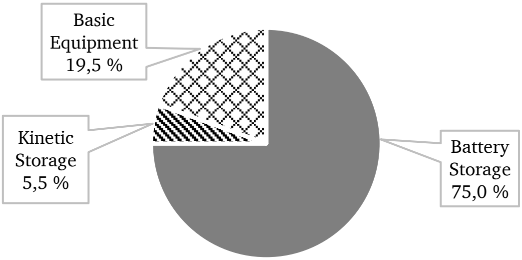

Figure 6.2 Breakdown of the investment cost of the reference combined storage by equipment category

Operation and Maintenance Cost

The operating cost of the combined energy storage system mainly depends on the electricity consumption. Given a symmetrical power flow at the storage terminals, the energy losses in the storage units, the power converters, the power transformer as well as the basic equipment lead to a deficit in the stored energy. If the energy deficit remains uncompensated, the storage would gradually empty out after several repetitions of the symmetrical power profile. Therefore, the energy losses correspond to the energy to be compensated, which in turn corresponds to the electricity consumption. The energy cost is estimated through the electricity rate listed for clarity in Table 6.4, which is the cost per kWh to purchase energy from the power grid.

Table 6.4 Electricity rate for energy purchased from the power grid

Parameter	Unit	Range	Reference value	Description
k_e	cu/kWh	0.05…0.40	0.12	electricity rate

Since the communication requirements of power systems constantly grow, annual costs for access to telecommunication networks and relevant services are considered. Moreover, the cost of an insurance that covers the whole storage system is also considered. The estimated annual operating expenses related to services are summarized in Table 6.5.

Table 6.5 Annual expenses for services related to the operation of the combined storage system

Type of annual expense	Cost (cu)
Insurance	600
Telecommunication network access	200
Data logging at external server	100
Remote monitoring and control	200

The lifespan of equipment under normal conditions is usually given in years. Power transformers, which are required in most electrical installations, have a lifetime that spans over 40 a (Balzer & Schorn, 2022). Contemporary electrochemical storages cannot reach such a long lifetime, even under ideal conditions, due to their pronounced calendrical degradation. Modern lithium-ion batteries, under suitable cycling, for instance one cycle per day, may reach a lifetime of 15 a. The high-speed outer-rotor flywheel storages SWIVT290 and ETA290 constitute a relative new technology, the lifetime of which has not thoroughly been justified through experiments. Recent investigations focus on the lifetime of the fibre reinforced plastic at the circumference of the outer rotor, for instance, Franz, Schneider et al. (2019). Nevertheless, considering that conventional materials, such as steel, copper and aluminium are used, a lifetime over 30 a is estimated for the investigated flywheel prototypes under reasonable operating conditions. It is mentioned that reasonable operating conditions for flywheels involve much more cycles than the typical cycle life of lithium-ion cells.

The lifetime of power converters heavily depends on the application. According to experience gained in photovoltaic systems, an average lifetime of 15 a is expected for central photovoltaic inverters (DNV GL, 2019). However, contemporary manufacturer warranties for central solar inverters cover a period which is often shorter than 15 a (Formica, et al., 2019). Due to the relative low market price of solar inverters, usually no maintenance intervals are scheduled. Nevertheless, some manufacturers recently started to offer repair options for string photovoltaic inverters (DNV GL, 2019). Although the properties of power converters for batteries and flywheels differentiate from that of solar inverters, the power rating of string solar inverters is comparable to that of the power converters used in the combined storage system, hence the assumption of a comparable lifetime. The estimated lifetime of the main equipment of the combined storage system under nominal operating conditions is summarized in Table 6.6.

Table 6.6 Estimated lifetime of the main equipment of the combined energy storage system under nominal operating conditions

Equipment	Estimated lifetime (a)
Three-phase power transformer	40
Flywheel	30
Lithium-ion battery	15
Semiconductor-based power converters	15

According to the estimated lifetime of the equipment listed in Table 6.6, the batteries and the power converters limit the service life of the combined storage. Even if an extended lifetime for the batteries and the power converters could be achieved under ideal operating conditions, the risk of outage increases, which is usually not acceptable in applications that require high reliability such as FCR. Therefore, in order to extend the service life of the system over 15 a, the batteries and the semiconductor-based power converters should be replaced before the flywheels and the transformer. Consequently, two options arise; either limit the target service life of the combined storage to 15 a or replace the power converters and the batteries after 15 a in order to extend the service life to 30 a.

Unlike the equipment that reaches its EoL at the end of a service life of 15 a, the rest value of the flywheels and the power transformer can be deducted from the TCO, as they can potentially be used for other purposes. The option to replace the batteries and the power converters is less practical, since the replacement of major systems 15 a after the initial setup may lead to compatibility issues with several peripheral devices. Moreover, since the battery system is the main cost driver of the combined storage, the decision to replace the batteries is connected with significant expenses, so that it is usually postponed to the future when the conditions are clear enough. It is therefore important for the feasibility of the investment that the estimated payback period of the combined storage is shorter than the battery lifetime.

Pumped-storage power plants, which can be classified as stationary energy storage systems, are designed for a service life that spans over 50 a. Nevertheless, the expectations for the service life of systems in the range of 1…10 MW are not as high as for power plants in the range of 300...1000 MW. Consequently, a service life of 15 a for combined storage systems, which are intended for grid balancing services, is considered adequate.

Unlike conventional rotating machinery, the magnetically suspended and vacuum-operated flywheel storage has low maintenance requirements. Ball bearings which are typically used in electric machines are replaced by magnetic bearings that have a significantly higher lifetime and require no maintenance. However, the vacuum pumps integrated into the flywheel storage have certain maintenance intervals. Furthermore, the ventilation and cooling system needs maintenance, which, however, belongs to the O&M cost of the basic equipment, as the flywheels and the batteries share a common ventilation and cooling system. No specific maintenance requirements are identified for contemporary lithium-ion batteries and thus no maintenance intervals are scheduled for the battery. The maintenance intervals of the combined storage system and the corresponding cost are summarized in Table 6.7.

Table 6.7 Maintenance intervals of the combined storage system and the corresponding cost

Equipment	Maintenance Interval (a)	Cost (cu)
Vacuum pumps of the kinetic storage	5	500
Central ventilation and cooling	2	300

It is considered that the maintenance activities are performed in such a way that the operation of the combined storage is uninterrupted. Independent of the scheduled maintenance intervals, equipment is prone to failures, which result in additional maintenance cost. Equipment failures may lead to power outages, which in turn cause loss of revenues and potential penalties due to service interruption. Because of insufficient information about the failure rates of the equipment, the maintenance cost related to failure rates cannot be estimated. Nevertheless, operating the equipment under normal conditions no longer than its nominal lifetime corresponds to low failure rates. Additionally, the potential loss of revenue due to outages is irrelevant for the estimation of the TCO.

Although the O&M cost belongs to the TCO, energy and maintenance bills are due in the future and not at the time the TCO of the system is estimated. Since the target service life of the system may span several years, the time value of money is considered. For a yearly discount rate r and a yearly inflation rate g the present value C_0 of the expenditure C_n which is due after n years is

$$C_0 = \left(\frac{1+g}{1+r}\right)^n C_n.$$

Unless otherwise specified, the reference values of the discount rate and the inflation rate summarized for clarity in Table 6.8 are used to calculate the present value of future obligations.

Table 6.8 Discount rate and inflation rate used for the estimation of the total cost of ownership

Parameter	Range	Reference value	Description
r	3…10 %	6 %	discount rate
g	1…6 %	2 %	inflation rate

Disposal Cost

According to current legislation, manufacturers or distributors of electrochemical batteries should bear the recycling cost of the products they bring to the market. Similarly, it is assumed that the recycling cost of other equipment, such as flywheels, power converters, transformers etc., burdens directly or indirectly their manufacturer so that the storage owner does not bear any recycling cost. Consequently, the part of the disposal cost that the storage owner should bear includes only the disassembly and the transport of the equipment to a disposal facility or to another owner, if part of the equipment is still useful and therefore acquired by another owner.

Components that reach their EoL rarely have any reasonable use. However, for systems that are made of several components with varying lifetime, the end of system service life does not necessarily correspond to the EoL of each component. Considering a target service life of 15 a for the combined storage due to the limited lifetime of its batteries and its power converters, the lifespan of the flywheels and the power transformer is not fully exploited. Therefore, part of the equipment has still some value at the end of service life, which can be liquidated.

Most equipment is usually both useless and worthless after its EoL because the labour cost to retrieve part of its raw materials is often higher than the value of the raw materials to be retrieved. Nevertheless, equipment such as power transformers include a significant amount of valuable materials such as copper, the value of which may exceed the labour cost for recycling. Therefore, equipment that is made of valuable raw materials has a residual value at the end of its useful life, which is often referred to as salvage value. Considering a linear decreasing equipment value C_{eqm} over time, the equipment value at EoL equals the salvage value of the equipment such that

$$C_{\mathrm{eqm}}(t) = \begin{cases} \left(1 + \dfrac{k_{\mathrm{sal}} - 1}{T_{\mathrm{lf}}} t\right) C_{\mathrm{acq}}, & 0 \leq t < T_{\mathrm{lf}} \\ k_{\mathrm{sal}} C_{\mathrm{acq}}, & T_{\mathrm{lf}} \leq t, \end{cases}$$

where T_{lf} is the lifetime of the equipment, C_{acq} is the acquisition value of the equipment and k_{sal} is the ratio of salvage to acquisition value of the equipment. It is assumed that only the power transformer has a non-negligible salvage value which is estimated as 20 % of its acquisition value, that is $k_{\mathrm{sal,tr}}$=20 %. However, considering a reasonable discount rate and a long lifetime, the present value of the decreasing equipment value $C_{\mathrm{eqm}}(t)$ is significantly reduced. The rest value of the equipment is not a cost but a potential income, if the owner opts to liquidate the equipment.

The estimated labour cost for the disassembly of the storage units and the basic equipment is listed in Table 6.9. The battery is wired up with DC conductors at its power terminals and low-current conductors at the control unit of its BMS. The flywheel wiring is a bit more complicated as it includes three-phase AC conductors for the electric machine and several low-current conductors for the magnetic bearings and the vacuum system. Therefore, a slightly higher disassembly cost for the flywheel is estimated. The disassembly cost of the basic equipment is also estimated and listed together with the disassembly expenses of the storage units in Table 6.9. Moreover, the transport cost of the equipment to the disposal centre is estimated similar to the estimation of the shipping cost, that is, with the aid of the transport cost factor k_{trs}.

Table 6.9 Expenditures for the disassembly of the combined energy storage system

Type of disassembly expense	Cost (cu)
Battery storage unit	50
Flywheel storage unit	60
Grid-side power converter	100
Three-phase power transformer	400
Housing, switchgear, ventilation and cooling, etc.	3000

The present value of both the disassembly and the transport cost of the reference combined storage system after 15 a of operation corresponds roughly to 0.5 % of the investment cost. The present value of the equipment after 15 a of operation corresponds to 2.8 % of the investment cost. In particular, after 15 a, the present value of the power transformer corresponds to 39 % of its acquisition cost and the present value of the flywheel storages, without power converters, corresponds to 28 % of their acquisition cost. Although part of the equipment is still useful at the end of service life, its present value is significantly lower than its acquisition cost. Nevertheless, due to the relatively high salvage value of the power transformer, its liquidation at the end of service life is expedient.

6.2 Battery Degradation

The battery degradation does not directly correspond to cost. However, it affects the operating cost due to the rising energy conversion losses caused by the increasing internal resistance of the lithium-ion cells. Energy losses should be compensated by purchasing energy from the grid, so that the storage does not gradually empty out. Furthermore, it should essentially be checked whether the charge capacity of the battery remains above the threshold considered as EoL throughout the service life of the combined storage. Although the battery degradation under FCR was estimated in order to size the battery storage, a more elaborate estimation that considers the course of the load profile and the actual power share of the battery storage can be achieved through simulations. Given a battery power profile, the battery degradation at the end of the target service life can be estimated using the degradation model of the lithium-ion cells.

The balancing reserve power for FCR sets the load profile for the combined storage. Although the frequency of the electrical grid is a stochastic process, it also includes deterministic processes which result from the dispatch of power plants and the trading intervals. The effect of dispatch and trading on the grid frequency depends on peak and off-peak hours, which, however, repeat daily. Therefore, the balancing reserve power of a single day can be considered as a representative cycle for the FCR application.

According to Eq. (4.10), the mean balancing reserve power for FCR over the course of time tends to zero, as the mean grid frequency tends to 50 Hz. Thus, the power profile of FCR is often described as symmetrical with respect to zero. Because of the voltage drop in the internal resistance of lithium-ion cells, a lower current magnitude is required when charging than when discharging in order to obtain the same power magnitude at cell terminals. Thus, less charge is stored and more charge is retrieved under a symmetrical power profile. Consequently, a symmetrical power profile would lead to a discharged battery after a couple of cycles. In other words, balancing reserve power cannot be provided over several days without correctively charging the battery.

For a reasonably sized battery, a 24-hour balancing reserve power profile usually leads to a small SoC difference between the start and the end of the day, which is unnecessary to be compensated in the same day. However, an unsymmetrical current profile does not represent a cycle that can be repeated several times. Furthermore, an unsymmetrical current profile leads to a less accurate estimation of the cell degradation. For the estimation of the battery degradation, it is important to consider that the charge deficit is compensated, although this may occur at a later time. Therefore, the charge deficit in the lithium-ion cells due to the 24-hour power profile is considered for the estimation of the equivalent charge throughput.

Although the characteristics of lithium-ion cells change with degradation, the average cell voltage mainly depends on control action. Considering that the control action aims to operate the battery towards the middle of its SoC range, the average cell voltage can be assumed constant. Furthermore, considering that the load profile is repeated unchanged, the energy flow and therefore the charge throughput of the cells also remain unchanged over the repetition of the load profile.

The algorithm for the estimation of the battery degradation updates the charge capacity and the internal resistance at the end of each cycle, which corresponds to the 24-hour application of FCR. Therefore, the effects of the rising internal resistance and the charge capacity fade are considered in the next cycle of the estimation of the battery degradation. After each cycle, the charge capacity of the lithium-ion cells decreases. Since the charge throughput remains unchanged over the cycles, the cycle depth of the lithium-ion cells increases with decreasing charge capacity. In other words, the cells tend to operate in a wider voltage range or, equivalently, in a wider SoC range over time. Therefore, the cycle depth is increased after each cycle according to the updated charge capacity of the lithium-ion cells.

The rising internal resistance of the lithium-ion cells leads to increased energy conversion losses and therefore to increased cell temperature. Considering a constant current profile over the cell cycle life, the rms cell current remains unchanged. Therefore, the internal resistance and the power losses of the cells increase proportionally. Assuming unchanged thermal capacity and unchanged heat dissipation conditions for the lithium-ion cells, the cell power losses and the cell temperature difference from ambient also increase proportionally. Consequently, the cell internal resistance and the average cell temperature difference from ambient over a certain current profile increase proportionally.

Figure 6.3 illustrates the algorithm for the estimation of the degradation of the lithium-ion cells with the aid of a flow chart. The battery current profile is estimated using the power profile of the application under the applied energy management strategy. Subsequently, the current profile and the equivalent charge throughput of a single lithium-ion cell are estimated. Thus, the average SoC, the SoC range and the average temperate of the lithium-ion cells are calculated in order to estimate the incremental cell degradation at the end of the current profile. Both the calendrical and the cyclic degradation are estimated and totalled up. The time step for the estimation of the calendrical degradation corresponds to the duration of the current profile. Subsequently, the estimated internal resistance and the estimated charge capacity of the lithium-ion cells are updated and the application of the current profile is repeated until the lithium-ion cells reach EoL or the target service life is reached. If the cells reach EoL before reaching the target service life, the algorithm outputs the achieved service life in years. Otherwise the algorithm outputs the estimated charge capacity and the estimated internal resistance of the lithium-ion cells at the end of the target service life.

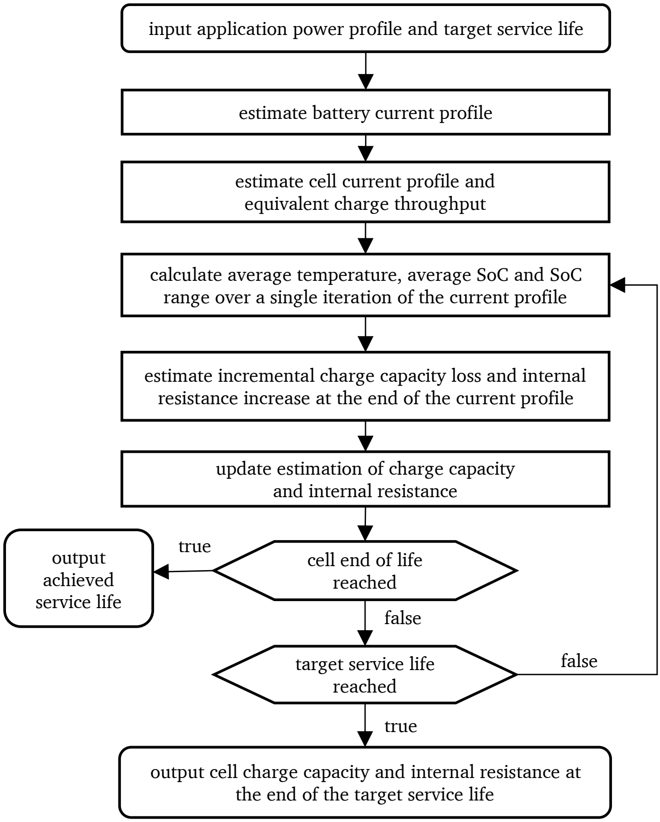

Figure 6.3 Flow chart of the algorithm for the estimation of the degradation of the lithium-ion cells for a given application power profile and a given target service life

6.3 Application of Frequency Containment Reserve

The mean absolute balancing reserve power resulting from the 24-hour grid frequency profile of continental Europe on 01.10.2021 is only 80 kW compared to the prequalified power of 1 MW, for which the reference combined storage is sized. Therefore, the FCR application results in relatively low load compared to the nominal power of the storages. Low load is less appropriate to showcase the reduction in energy losses and the corresponding reduction in operating cost, which can be achieved through the energy management strategy of optimal power share. Consequently, the energy management strategy is configured at maximum kinetic storage share in order to limit the battery degradation.

To evaluate the potential of the combined storage system for FCR, a simulation is developed. The simulation uses the 24-hour grid frequency profile to determine the balancing reserve power, operates the combined storage under maximum kinetic storage share, calculates the energy losses of the electrical equipment and estimates the battery degradation at the end of the service life. The simulation results are used to calculate the O&M cost as well as the TCO at the end of the system service life. The degradation dependent increase in the internal resistance of the lithium-ion cells is considered by increasing the battery losses at the end of each iteration.

The energy losses of the combined storage should be compensated, otherwise the storage units gradually empty out. For instance, the energy loss compensation can be implemented as scheduled power flow which is traded in the energy market. However, for a reasonably sized storage system and a typical grid frequency profile of continental Europe, it is rather uncommon that energy loss compensation is required within a day, provided that the battery lies in the middle of its SoC range at the beginning of the day. Therefore, instead of simulating the compensation of energy losses, the energy losses are considered directly as energy cost.

The target service life of the storage system is set at 15 a. Although a longer service life is often desired by system owners, it is a rather unrealistic option, considering the contemporary calendrical lifetime of lithium-ion cells. Replacement due to calendrical degradation should be done at once for all batteries. Since the acquisition of the battery system is the main cost driver of the combined storage, it can be argued that replacing all batteries corresponds to a new investment rather than a maintenance measure. Instead, the replacement of a single battery due to failure belongs to maintenance cost. Therefore, the replacement of batteries in order to extend the service life of the combined storage is not further investigated as it corresponds to significant replacement costs with respect to the TCO.

Table 6.10 provides an overview of the main input parameters used in the simulation of the combined storage system providing FCR. Although some parameters, such as the size of the combined storage and several cost factors, vary in the context of sensitivity analyses, most of the parameters presented in Table 6.10 remain unchanged throughout the investigation.

Table 6.10 Main input parameters for the simulation of the combined storage system providing FCR

Input parameter	**Configuration**
Simulation step	1 s
Prequalified balancing reserve power	1 MW
Grid frequency profile	grid frequency of continental Europe sampled each second for 24 h on 01.10.2021 by TRANSNET GmbH
Storage system and basic equipment	reference combined storage as summarized in Table 4.3 and Table A.14, and configured as in Figure 4.6
Energy management	maximum kinetic storage share, use of the FCR flexibilities of the ±10 mHz deadband and the 20 % overfulfilment of balancing power, compensation of internal system losses
Flywheel control loop	I_d=0 control
Ambient temperature of lithium-on cells	22 °C
Initial SoC of the batteries	50 %
Initial speed of the flywheels	14 000 rpm
Cost factors	reference cost values according to Table 6.1
Service life	15 a

Effect of Storage Size

In order to investigate the effect of the combined storage size on the trade-off between TCO and battery degradation, the application of FCR is simulated with variable number of flywheels and batteries and the results are shown in Figure 6.4 which depicts the TCO (C_t on the vertical axis) against the battery charge capacity loss (q_L on the horizontal axis) at the end of service life. Each point represents a unique storage system comprising N_{fw} flywheels and N_b batteries. The points that represent combined storages with the same number of flywheels are connected to form a curve. In each curve, the number of batteries is increased one by one starting from the annotated minimum number of batteries to the direction that the arrow annotates. For instance, systems with N_{fw}=0 start from N_b=30 and end up to N_b=42, whereas systems with N_{fw}=4 start from N_b=29 and end up to N_b=36. Obviously, the most cost-efficient system comprises 30 batteries and no flywheels. However, the most cost-efficient system is not always the optimal choice, since nonmonetary criteria may also be worth consideration.

Considering that high uncertainties are involved in the estimation of the battery degradation, it is reasonable to leave a margin for error in the forecast of the charge capacity loss to ensure that a charge capacity loss of 30 %, which usually signifies the EoL of lithium-ion batteries, is not reached. Operating batteries that have already undergone significant charge capacity loss, not only implies a reduced performance but can also lead to high failure rates. Additionally, it should be investigated whether the model used for the estimation of the battery degradation is still valid after significant charge capacity loss (Schuster, et al., 2015). Uncertainties in the estimation of the battery degradation result from both internal factors such as internal cell failures and external factors such as discrepancies between the assumed and actual load applied on the cells. Assessment methods that involve criteria in addition to monetary cost are often referred to as *cost-benefit analyses*. In terms of the combined storage system, a low charge capacity loss of the batteries at the end of the target service life is considered as a benefit to be balanced against monetary cost.

A safety margin of 5 % for the charge capacity forecast at the end of service life with respect to the charge capacity at the EoL of the lithium-ion cells is selected. Considering that a charge capacity loss of 30 % corresponds to the EoL of lithium-ion cells, acceptable combined storages should have a battery charge capacity loss that lies below the threshold of 25 % annotated in Figure 6.4. Consequently, when the safety margin of 25 % for the charge capacity loss is considered, the most cost-efficient combined storage comprises 35 batteries and 2 flywheels, whereas the most cost-efficient battery-only system comprises 41 batteries. Combined storages with three, five or even greater number of flywheels are also simulated, however, they are omitted for clarity from Figure 6.4 as they are less cost-efficient of the optimal system comprising 2 flywheels and 35 batteries.

The optimal combined storage resulting from the simulation has five batteries more than the reference combined storage resulting from the initial sizing shown in Table 4.3, despite the fact that the same maximum charge capacity loss of 25 % after 15 years of operation is required in both cases. The higher number of batteries in the optimal compared to the reference system signifies that the battery load in the simulation is higher than that in the initial sizing, which leads to an increased load per lithium-ion cell and therefore to an increased cyclic degradation. The difference between the optimal and the reference system is reasonable because the control of the storage units, the energy management strategy and the course of the grid frequency are neglected in the initial sizing.

Independent of the criteria used to select an optimum combined storage, Figure 6.4 depicts the trade-off between battery degradation and TCO. Whereas additional storage units increase the TCO, they lead to a decrease in the degradation of the lithium-ion cells. The investment cost increases linearly with the number of storage units. On the other hand, the considered characteristic of the charge capacity loss of lithium-ion cells over time and usage is nonlinear. Increasing the number of storage units affects not only the cyclic but also the calendrical degradation, as additional storage units lead to a decrease in the charge throughput of the lithium-ion cells, which in turn results in a decrease in their operating temperature. Nevertheless, even under ideal temperature conditions the calendrical degradation is considerable, so that the reduction in the charge capacity loss reaches a plateau after a sufficient increase in the storage units. The nonlinear degradation characteristics of lithium-ion cells correspond to the nonlinear trade-off curves in Figure 6.4, where the rate of change of the charge capacity loss decreases with increasing TCO. In other words, an increase in the storage units when the charge capacity loss is relatively low leads to a low benefit to cost ratio.

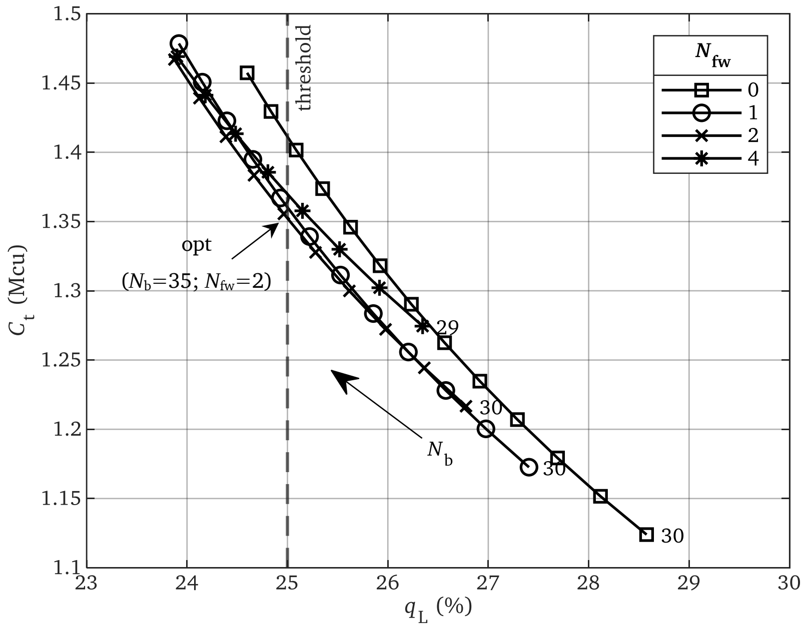

Figure 6.4 Trade-off between battery degradation and TCO under varying combined storage size for a service life of 15 a. The curves correspond to systems with the same number of flywheels. Increasing the number of storage units increases the TCO but also decreases the battery charge capacity loss q_L. The combined system with 35 batteries and 2 flywheels is the most cost-efficient system that preserves the charge capacity loss below 25 %.

Effect of Service Life

The target service life of the combined storage is set at 15 a, which corresponds to the typical calendrical lifetime of lithium-ion cells. However, the degradation model, the load forecast and the operating conditions are subject to uncertainties that affect the actual battery lifetime. Depending on the actual battery degradation, the owner may decide to suspend operation before the system reaches the target service life or to extend operation beyond the target service life. Therefore, it is worth investigating the effect of service life on the main performance indicators.

Figure 6.5 presents the sum of investment and O&M cost as well as the battery charge capacity over the service life of the optimal combined storage with 35 batteries and 2 flywheels, the optimal battery-only storage with 41 batteries and the most cost-efficient storage regardless of additional charge capacity requirements, which has only 30 batteries. The disposal cost is disregarded, as the liquidation of the rest value of equipment leads to a low TCO for a short service life, which hides the investment cost. The investment and O&M cost as well as the battery charge capacity are calculated at one-year intervals. The battery charge capacity decreases fast in the first year of operation due to the nonlinear degradation model. Thus, the charge capacity during the first year is omitted in the plot in order to obtain smooth degradation curves.

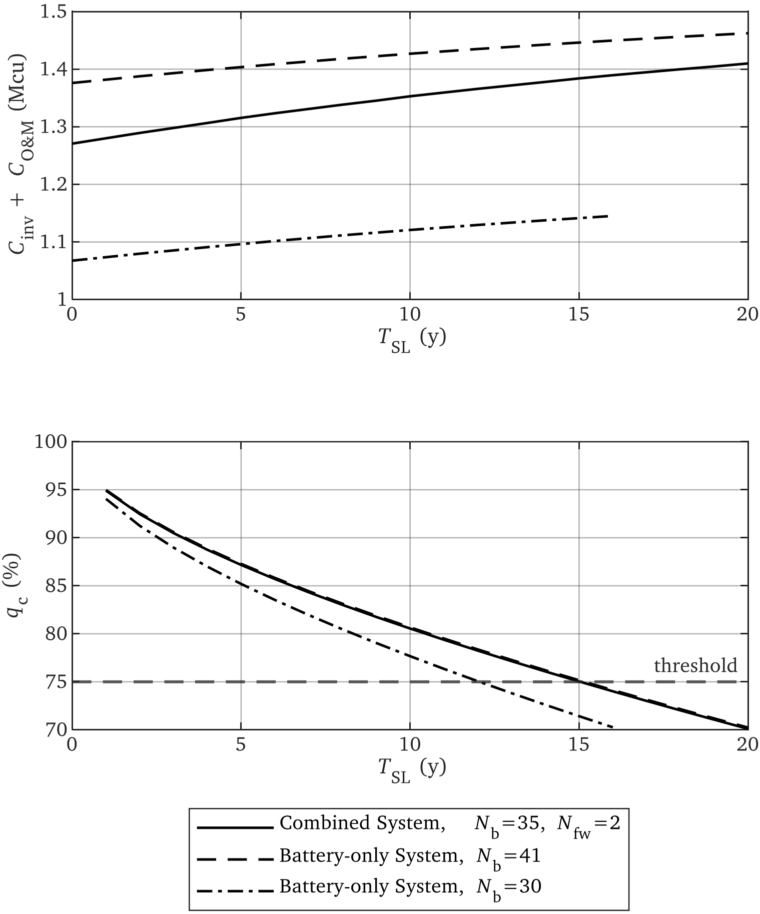

Figure 6.5 Sum of investment and O&M cost (top), and battery charge capacity (bottom) over the service life of the optimal combined system (35 batteries and 2 flywheels), the optimal battery-only system (41 batteries) and the most cost-efficient system independent of additional charge capacity requirements (30 batteries). While the optimal combined and the optimal battery-only systems have a higher investment cost than the system with 30 batteries, they achieve a longer service life.

The charge capacity of the system with 30 batteries falls below 75 % shortly after 12 a and below 70 % shortly after 16 a of operation. In contrast, the optimal systems, which are designed to preserve a charge capacity over 75 % at the end of the target service life of 15 a, not only fulfil their purpose, but also have a charge capacity slightly over 70 % after 20 a of operation. Considering that the battery performance may already be unacceptable with a charge capacity near 75 %, the optimal systems achieve a service life that is 3 to 4 years longer than the service life of the system with 30 batteries.

The optimal systems achieve a longer service life than the system with 30 batteries as a result of additional storage units, which lead to 19 % higher investment cost for the combined system and 29 % higher investment cost for the battery-only system. After 15 a of operation the investment and O&M cost of the combined and battery-only systems are about 21 % and 27 % higher than that of the system with 30 batteries respectively. Thus, a higher O&M cost of the optimal combined system and a lower O&M cost of the optimal battery-only system relative to the system with 30 batteries is observed. The higher O&M cost of the combined system is explained by the no-load losses of the kinetic storage. The lower O&M cost of the optimal battery-only system is due to the reduced battery current and therefore battery losses, since the same load is divided into more batteries (41 batteries compared to 30 batteries).

The comparatively high O&M cost of the combined system leads to a decreasing difference between the cost of the optimal combined system and the cost of the optimal battery-only system over service life. The relative cost difference of the optimal battery-only system with respect to the optimal combined system starts at 8 % (investment cost difference) and declines at 4 % after 20 a of operation. Therefore, for a service life below 20 a, the investment and O&M cost of the combined system lies always below the corresponding cost of the optimal battery-only system. Furthermore, the battery charge capacity over service life of both optimal systems follows a similar characteristic, where the optimal battery-only system has a slightly higher charge capacity.

Effect of Flywheel Technological Improvements

Emerging technologies such as outer-rotor high-speed flywheels often involve significant cost uncertainties. In this respect the analysis of the effect of technological improvements on the TCO facilitates a dedicated flywheel design. Technological improvements not only affect the manufacturing cost but also the O&M cost, for instance, by reducing energy losses and increasing maintenance intervals. To quantify the effect of technological improvements on the O&M cost of outer-rotor high-speed flywheels and consequently on the O&M cost of the combined storage, three scenarios are considered, first the application of field weakening (fdwk), second an enlarged flywheel size (efws) and third an alternative electric machine without permanent magnet excitation (alpm).

Field Weakening

Field weakening decreases the magnetisation losses of PMSMs at the cost of increased resistive losses in the stator windings. Depending on the PMSM, a stator current with negative direct component exists that leads to minimum total losses at a certain operating point. However, it should also be considered that the negative direct current component increases the losses in the power converter that drives the electric machine. Compared to the scenarios of enlarged flywheel size and no permanent magnet excitation, which require modifications in the electric machine design, field weakening can solely be implemented as an additional function in the control loop of the power converter. In addition to PMSMs, field weakening can be implemented in asynchronous machines by increasing the electrical frequency disproportionately to the stator voltage (Binder, 2017, pp. 458-461).

Enlarged Flywheel Size

The prototype SWIVT290 has a nominal power capacity of 50 kW and a nominal energy capacity of 1.8 kWh. The optimal combined system for FCR requires two flywheel storages. The idea is to double both the power and the energy capacity of a single flywheel storage, when the power consumption of its vacuum system and its AMBs remains unchanged. The energy capacity of the flywheel should be increased by increasing the outer diameter and the length of the outer rotor, when its inner diameter remains unchanged. A longer rotor also facilitates an increase in the power capacity, which can be realised by equivalently increasing the length of the permanent magnets in the rotor and the length of the iron stack in the stator of the electric machine. Since the inner diameter remains unchanged, it is reasonable to assume that the power losses in the AMBs also remain unchanged with respect to the initial flywheel. Although the augmented flywheel dimensions correspond to an increased volume to be evacuated, it is reasonable to assume that when the volume is evacuated, the change in the consumption of the vacuum system with respect to the initial flywheel is unnoticeable. Therefore, if a flywheel storage with double the power and double the energy capacity of the SWIVT290 prototype can be manufactured, the total power consumption of the AMBs and the vacuum system is halved compared to the kinetic storage that incorporates two SWIVT290 prototypes.

To simulate the enlarged flywheel, several parameters should be adjusted. In order to double the energy capacity of the flywheel, the inertia of the rotor should double. A twofold increase in the length of the permanent magnets and the length of the stator iron stack leads to a twofold increase in the flux linkage of the stator windings with the permanent magnets. A twofold increase in the flux linkage leads to double the nominal torque and double the nominal power with respect to the initial flywheel, considering that the operating speed range remains unchanged. Despite the twofold increase in the flux linkage, the magnetic flux density in the stator iron stack remains unchanged. Therefore, since the volume of the stator iron stack is double the stack volume of the initial flywheel, the iron losses also double. According to Eq. (3.3) and Eq. (3.12), the iron resistance should be halved in order to obtain double the iron losses of the initial flywheel. Furthermore, a twofold increase in the nominal power of the flywheel requires a twofold increase in the power rating of the converter driving its electric machine.

Alternative to Permanent Magnet Excitation

The no-load losses due to the braking torque exerted by the permanent magnetic field constitute a major drawback of flywheel storages that are driven by PMSMs because the flywheels may often idle. Other electric machine types may lead to reduced no-load losses, which, however, come at the cost of additional conduction losses because an additional stator current should compensate for the absence of permanent excitation. Therefore, it is worthwhile to investigate the effect of electric machines without permanent excitation on the total losses and consequently on the O&M cost of the kinetic storage. For instance, asynchronous machines with squirrel cage rotor and reluctance machines without permanent magnets are feasible with an outer rotor. To approximate the reduction in the no-load losses through an alternative machine, the proportion of the no-load losses caused by the permanent excitation is neglected. Furthermore, to approximate the increase in the conduction losses due to the absence of permanent excitation, the ratio of torque to current is reduced by 20 % and the maximum continuous current is increased by 25 %, so that the alternative electric machine equals the nominal torque of the initial PMSM. The alternative electric machine without permanent magnets aims at estimating the effect of the electric machine design on the TCO of the combined storage. However, in order to accurately estimate the power losses, the alternative electric machine should be elaborately modelled, parametrized and simulated for a given load profile.

Comparison of the effect of technological improvements

Figure 6.6 presents the cost reduction achieved through technological improvements in the flywheel prototype SWIVT290 with respect to the optimal combined storage system comprising 35 batteries and 2 SWIVT290 flywheel protypes for the application of FCR. The cost reduction concerns the TCO of the combined storage, the O&M cost of the combined storage and the O&M cost of the kinetic storage. The alternative electric machine without permanent magnet excitation (alpm) leads to the highest reduction of the O&M cost of the kinetic storage, that is 32.3 %, followed by the enlarged flywheel size (efws) at 23.7 % and the application of field weakening (fdwk) at 8.9 %. However, the reduction in the O&M cost at combined storage level is substantially lower, that is, 12.3 % for alpm, 9.1 % for efws and 3.4 % for fdwk. Nevertheless, the application of field weakening corresponds to the lowest implementation effort, as it only requires an additional control function in the power converter that drives the electric machine, instead of modifications in the flywheel hardware. Although significant improvements are observed in the O&M cost of the kinetic storage, the effect on the O&M cost at combined system level is less pronounced and the effect on the TCO of the combined system is even less obvious. The minor effect of the flywheel technological improvements on the TCO is due to the small number of flywheels with respect to the combined storage size. If the combined storage incorporates more flywheels, the effect on the TCO will be more evident.

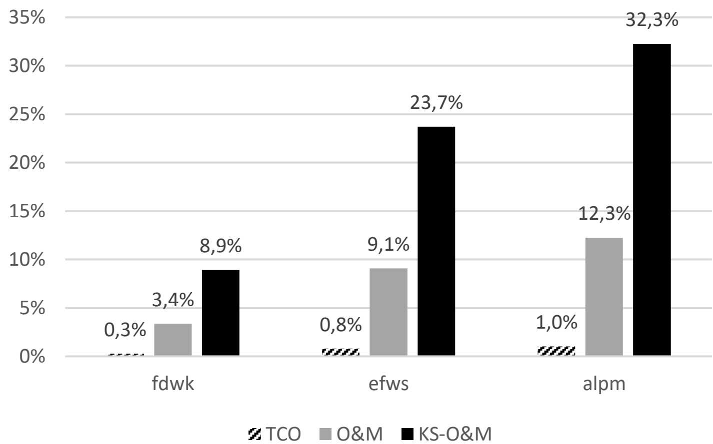

Figure 6.6 Reduction in the TCO, the O&M cost and the kinetic storage O&M cost through technological improvements in the flywheel prototype SWIVT290 with respect to the optimal combined storage system comprising 35 batteries and 2 SWIVT290 flywheel prototypes for the application of FCR. *fdwk* stands for field weakening, *efws* stands for enlarged flywheel size (doubled), *alpm* stands for alternative electric machine without permanent magnet excitation

TCO sensitivity to the acquisition and operating cost of flywheel storages

Apart from the effect of technological improvements on the O&M cost of flywheel storages, it is worthwhile to draw a comparison between the effect of acquisition and operating cost on the TCO. Figure 6.7 shows that the TCO of the combined storage is more sensitive to the kinetic storage energy losses and therefore the operating cost than the flywheel energy capacity cost. The reference energy losses correspond to those of the kinetic storage of the optimal combined system with 35 batteries and 2 flywheels for the application of FCR. To decrease the TCO by 0.5 %, either the kinetic storage losses should be decreased by 17 % or the energy capacity cost of the flywheel should be decreased by 35 %. In other words, the TCO reduction that can be achieved by a reduction of 35 % in the flywheel energy capacity cost, can also be achieved through flywheels that operate under 17 % lower losses for the given load profile.

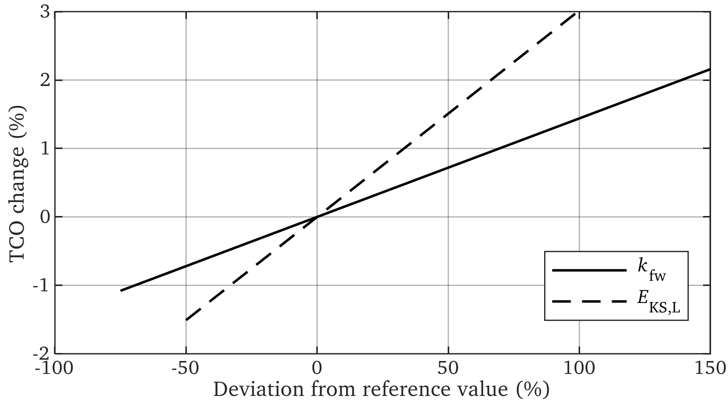

Figure 6.7 TCO sensitivity to the flywheel energy capacity cost k_{fw} and the energy losses of the kinetic storage $E_{ks,L}$ for the optimal combined storage system comprising 35 batteries and 2 flywheels used for FCR. The TCO is more sensitive to the kinetic storage losses than the flywheel energy capacity cost.

TCO sensitivity to the main cost drivers

The investigation of the TCO sensitivity to the main cost drivers is a convenient method to assess different system variants. The cost parameters considered in the present work are not fixed but assume values within a range. Thus, the uncertainties of the cost parameters propagate in the TCO. A sensitivity analysis aims to quantify the influence of the individual cost parameters on the TCO, in order to facilitate decisions concerning potential investments in energy storage systems.

The TCO of the optimal combined storage with 35 batteries and 2 flywheels as well as the TCO of the optimal battery-only system with 41 batteries are investigated through sensitivity analyses. Figure 6.8 presents the TCO sensitivity to the battery energy capacity cost of the optimal combined storage system and the optimal battery-only system. Since the combined system incorporates much more batteries than flywheels, the energy capacity cost of the battery constitutes a significant cost driver. A twofold increase in the battery energy capacity cost from 500 cu/kWh to 1000 cu/kWh corresponds roughly to 60 % increase in the TCO of the combined storage system. It is observed that the battery-only system has a lower TCO than the combined storage system, when the battery energy capacity cost falls below 238 cu/kWh. The difference between the TCO of the combined and the battery-only system rises with increasing battery energy capacity cost and peaks at a reduction of 9 % in the TCO of the combined system relative to the TCO of the battery-only system when the battery energy capacity cost is 1000 cu/kWh.

Figure 6.9 compares the TCO sensitivity to the flywheel energy capacity cost of the optimal combined storage system and the optimal battery-only system. On the one hand, Figure 6.9 constitutes a proof that the TCO of the combined system is lower than that of the battery-only system over the complete range of the flywheel energy capacity cost. On the other hand, the TCO sensitivity to the flywheel energy capacity cost increases with increasing number of flywheels. Therefore, the result is valid only for the particular combined storage with 35 batteries and 2 flywheels.

Figure 6.10 presents the effect of varying electricity rate on the TCO of the optimal combined and the optimal battery-only system. Flywheels have significantly higher no-load losses than batteries, which results in an increased electricity consumption. Therefore, the TCO of the combined system is more sensitive to the electricity cost than that of the battery-only system. If the electricity rate exceeds 0.33 cu/kWh, the TCO of the battery-only system falls below the TCO of the combined system. A twofold increase in the electricity rate from 0.12 cu/kWh to 0.24 cu/kWh results in an increase of approximately 4 % in the TCO of the battery-only system, whereas the TCO of the combined system increases by roughly 7 %. The TCO sensitivity to the electricity rate will further increase, if the combined system incorporates additional flywheels.

Figure 6.11 presents the sensitivity of the TCO of the optimal combined storage to the electricity rate k_e, the battery energy capacity cost k_b and the flywheel energy capacity cost k_fw, relative to their reference values. Evidently, the energy capacity cost of the battery storage is the main cost driver, followed by the electricity rate. A twofold increase in the battery energy capacity cost leads to an increase of 60 % in the TCO, whereas a twofold increase in the electricity rate results in a TCO increase of only 7 %. The energy capacity cost of the flywheel has a less pronounced effect on the TCO because the combined system comprises only two flywheels. A twofold increase in the flywheel energy capacity cost results in a TCO increase of only 1.5 %. The low sensitivity of the TCO to the flywheel energy capacity cost signifies that the uncertainties in the flywheel acquisition cost have a minor effect on the TCO of combined storages that comprise only a few flywheels. Therefore, it can be claimed that if a few flywheels can significantly improve certain performance indicators of combined storage systems such as the battery service life, the acquisition cost of the flywheels can easily be outweighed by the benefits. However, it should be considered that kinetic storages involve relatively high no-load losses, the compensation of which increases the sensitivity of the TCO to the electricity rate.

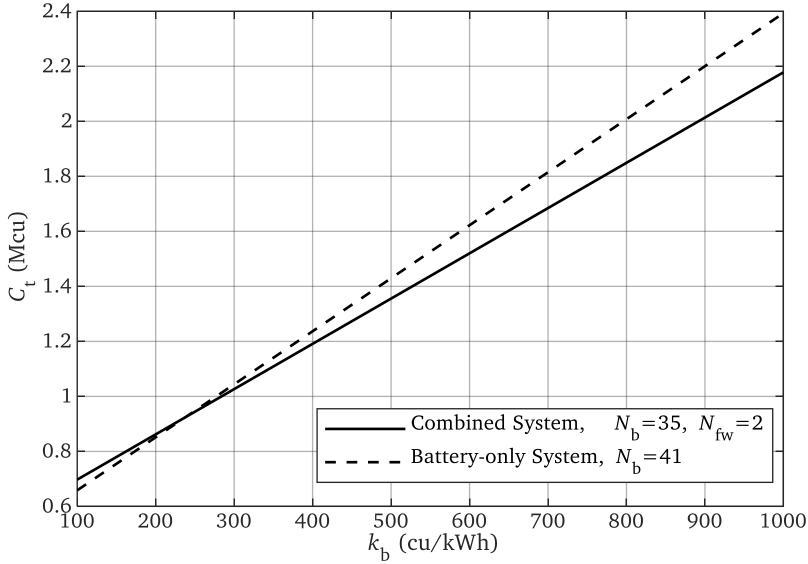

Figure 6.8 TCO sensitivity to the battery energy capacity cost of the optimal combined system and the optimal battery-only system. The combined system has a lower TCO than the battery-only system as long as k_b>238 cu/kWh. The battery energy capacity cost is an important cost driver due to the high number of batteries in both systems.

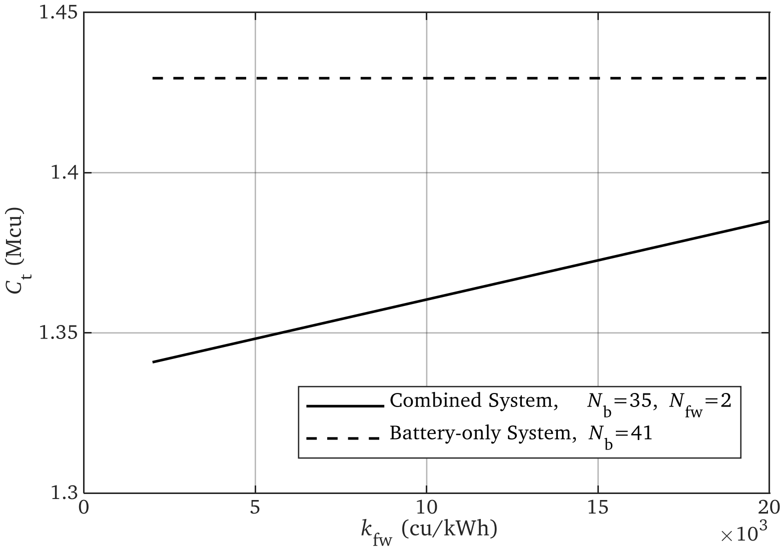

Figure 6.9 TCO sensitivity to the flywheel energy capacity cost of the optimal combined system and the optimal battery-only system. The TCO of the combined system is lower than the TCO of the battery-only system over the complete range of the flywheel energy capacity cost.

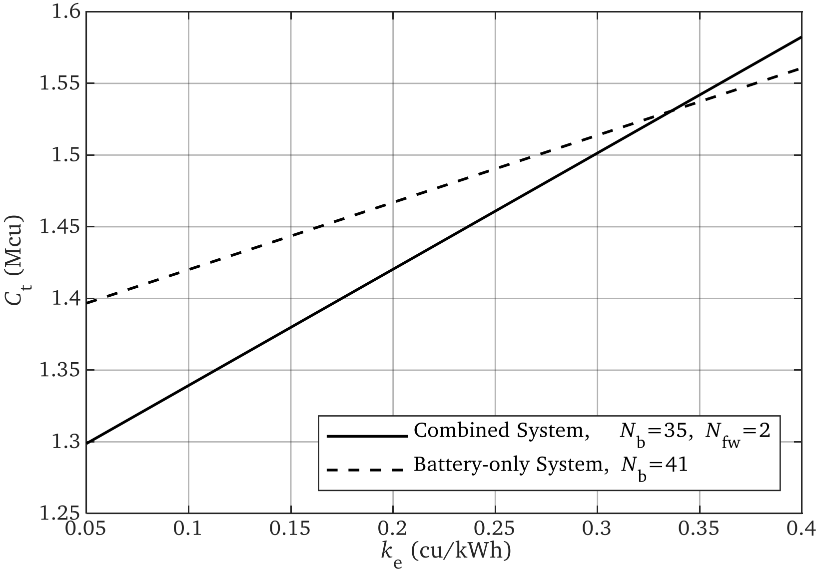

Figure 6.10 TCO sensitivity to the electricity rate of the optimal combined system and the optimal battery-only system. The TCO of the combined system is lower than the TCO of the battery-only system as long as k_e<0.33 cu/kWh.

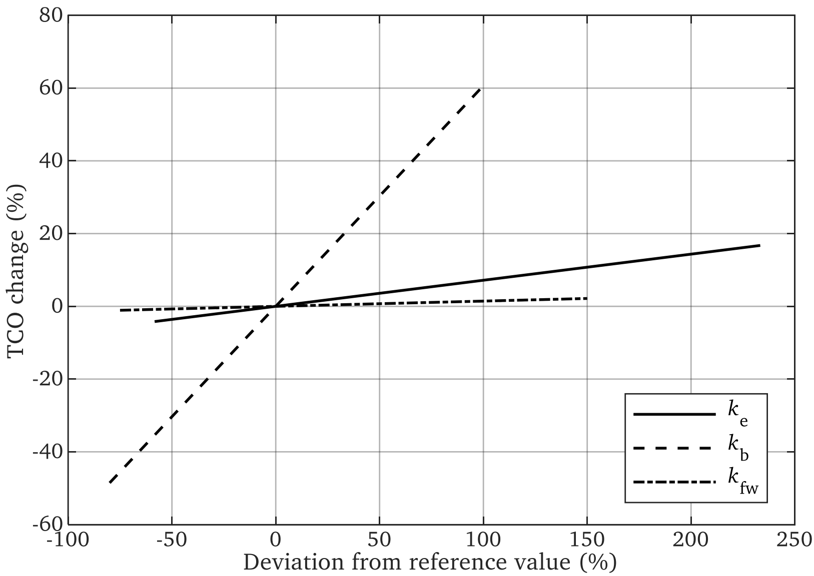

Figure 6.11 Sensitivity of the TCO of the optimal combined storage system to the electricity rate k_e, the battery energy capacity cost k_b and the flywheel energy capacity cost k_{fw}, relative to their reference values. The battery energy capacity cost is the most significant cost driver, followed by the electricity rate.

6.4 Additional Applications

Alternating power with high frequency is the favourable power profile for kinetic storages, where the term alternating signifies that the power flow changes direction like alternating current. The balancing reserve power for FCR constitutes a power profile that alternates 24 hours a day, 7 days a week and 365 days a year, which is obviously advantageous for flywheels. Although energy storages should be sized for maximum FCR balancing reserve power, the maximum power is rarely needed. The requirement for high energy capacity leads to a relatively large battery size in combined storage systems, which in turns leads to a relatively low current in the lithium-ion cells and therefore to low cyclic degradation. A relatively large battery is unfavourable to showcase the advantages of low cyclic degradation through the integration of flywheel storages. Therefore, to showcase the value proposition of the kinetic storage, additional applications that involve short-term and high intensity load are investigated.

Frequency Containment Reserve constitutes a suitable application for energy storages as it sets a basic 24-hour alternating load profile. Therefore, to increase the value proposition of the combined storage, the additional applications should be offered in parallel to FCR. Services offered in addition to FCR are allowed by the TSOs as long as the provided balancing reserve power can be identified by measurements and the energy capacity that is reserved for FCR is bounded by limits (4.7). *Electric Vehicle Fast Charging* (EVFC) and *Wayside Energy Recovery Systems* (WERSs) in railway networks are identified as applications in which the integration of energy storage systems can be beneficial. The fast charging of electric vehicles involves high power, which challenges the distribution networks. Energy storage contributes towards the mitigations of power peaks in distribution networks by locally supplying the charging vehicles. Although modern trams and trains recuperate energy while braking, the recuperated energy is often not used by nearby rail vehicles but dissipated in the railway network. Energy storages can store the braking energy for a short time and feed it back to the same or another rail vehicle that accelerates at a later time.

Electric Vehicle Fast Charging

Recent charging standards for electric vehicles such as the Combined Charging System (CCS) introduced charging rates up to 350 kW (Tu, et al., 2019). Nevertheless, so far, low-end passenger vehicles rarely exceed a charging power of 120 kW. Although some of the batteries integrated into passenger vehicles can be charged at 120 kW, charging at 120 kW is available only for a fraction of the SoC range (Collin, et al., 2019). At normal conditions, fast charging is available in the low SoC range in order to enable vehicle users to quickly charge their vehicle up to a certain SoC. Observing the charging profiles of passenger vehicles in Collin et al. (2019), it can be deduced that if the battery is less than half-charged, there is a high probability that fast charging at a constant power of 120 kW for at least 10 min is permissible. Assuming an efficiency of 98 %, which corresponds to the ratio of the energy stored in the vehicle to the energy supplied by the charging station, charging the vehicle at 120 kW for 10 min corresponds roughly to 19.5 kWh stored in the vehicle. Considering an average power consumption of 0.19 kWh/km, the vehicle extends its range by roughly 100 km through a charging time of 10 min, which constitutes a typical application of opportunity charging.

To facilitate electric vehicle charging, the combined energy storage system should be installed in an accessible location for electric vehicles, for instance, nearby an existing gas station. Furthermore, a connection to the distribution network for the parallel provision of FCR should be ensured. The combination of FCR with EVFC has the advantage that a single grid connection with high power capacity is used for both applications. In other words, the cost of an additional grid connection only for EVFC is saved. The charging of electric vehicles is enabled by a DC-DC power converter, which is connected to the DC bus of the combined storage, as illustrated in Figure 6.12. The DC-DC converter is sized according to the use cases considered. The first use case considers charging of contemporary high-end electric vehicles at 120 kW, whereas the second use case considers the charging of prospective heavy-duty electric vehicles at 350 kW. The additional basic equipment that is required for both use cases is listed in Table A.15.

In contrast to FCR, electric vehicle charging does not constitute a symmetrical power profile. Therefore, the power supplied to electric vehicles should be compensated. A way to compensate for load asymmetries is to purchase appropriate power blocks in the electricity market. Intraday electricity markets often facilitate trading with lead times as low as 5 min, so that charging the storage during the day is possible at short notice. Consequently, electric vehicle charging can be offered several times per day depending on the storage size and the load of FCR. Although energy products can be purchased in intraday markets at short notice, less spontaneous bilateral contracts between energy storage operators and energy trading companies are also possible. The intention is to charge the stationary storage at a lower power than that for EVFC. In this respect stationary energy storage systems for EVFC contribute to a reliable operation of the electrical grid.

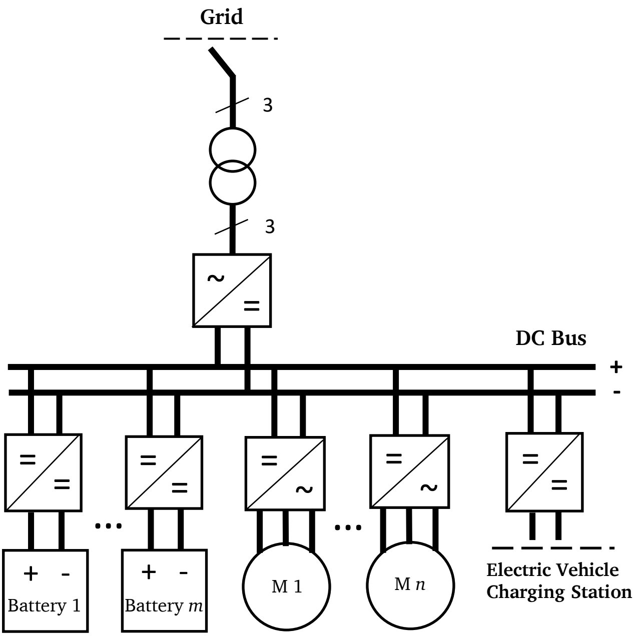

Figure 6.12 Extension of the combined energy storage system with a DC-DC power converter that is intended for the fast charging of electric vehicles.

Several options exist regarding the schedule of charging intervals, for instance, the stationary energy storage can be charged overnight, intermittently during the day or continuously during the day. Although overnight charging corresponds to off-peak electricity pricing, which is usually cost-efficient, it increases the cycle depth of the battery and impedes the energy state regulation of the kinetic storage during the day. Moreover, an almost full storage after overnight charging contradicts the requirements of FCR. Consequently, it is preferred to charge the storage during the day, although it usually involves higher expenses than overnight charging. The expenses for the purchased energy are allocated to the O&M cost of the DC-DC power converter which is placed between the DC bus of the stationary storage system and the charging station because it is the only equipment installed specifically for EVFC.

Considering that electric vehicles are charged repetitively, a power block that spans over the time EVFC is offered should be purchased, so that the power required for the vehicle charging is shared between the stationary storage and the grid. For instance, a vehicle is charged at the power P_{ch} that is equally shared between the stationary storage and the grid. When the vehicle charging is finished or interrupted, the stationary storage shifts to charging mode, while the grid continues to supply the power $P_{ch}/2$ to the stationary storage. The split of the power for the vehicle charging between the grid and the stationary storage has three significant advantages; first the power peaks on the grid side are mitigated, second the required power capacity of the grid connection declines, third the required power rating of the stationary energy storage also declines.

The first EVFC use case considers a single passenger vehicle charging at 120 kW for 10 min, followed by a break of 10 min. The break is relevant only for the charging station and not for the vehicle, which can continue its route after the charging time of 10 min. Disregarding the power flow due to FCR on the grid side, the power at the grid connection and the power at the terminals of the charging station throughout the operating cycle for the charging of the passenger vehicle are shown on the left of Figure 6.13. The difference between the power at the charging station and the grid plus additional energy conversion losses is covered by the stationary storage. The resulting power profile for the stationary storage is symmetrical to zero and thus advantageous for flywheel storages. Specifically, the operating cycle presented on the left of Figure 6.13 corresponds to power peaks of approximately 60 kW for the stationary storage, which are comparable with the power capacity of the SWIT290 prototype, that is 50 kW. However, the energy that should be supplied by the stationary storage is roughly 20 kWh and therefore considerably higher than the energy capacity of the SWIVT290 prototype, that is 1.8 kWh.

The operating cycle presented on the left of Figure 6.13 is repeated between 07:00 and 22:00, which results in 45 operating cycles per day that correspond to a daily energy consumption of 900 kWh at the charging station. Assuming an efficiency of 92 % for the energy supplied to the charging station with respect to the energy supplied by the grid, about 975 kWh should be supplied to the stationary storage system by the grid throughout the day to enable the charging of electric vehicles. Thus, a power block of 65 kW between 07:00 and 22:00 is purchased. A power block of 65 kW cannot be traded in the energy market where a minimum bid of 100 kW applies. However, power blocks below 100 kW can be assumed on the grid side, if the stationary storage participates in a pool.

The second use case concerns the fast charging of heavy-duty electric vehicles that are currently an emerging technology (Arora, et al., 2021). The heavy-duty vehicles are charged for 5 min at 350 kW, followed by a break of 10 min, which is relevant only for the charging station. The power flow at the grid connection and the power flow at the charging station during the operating cycle for the charging of a single heavy-duty vehicle are depicted on the right of Figure 6.13. Charging at 350 kW for 5 min with an efficiency of 98 % regarding the energy stored in the vehicle with respect to the energy supplied by the charging station corresponds roughly to 28.5 kWh stored in the vehicle. Considering heavy-duty vehicles that consume 0.95 kWh/km, the energy stored in the vehicle corresponds to a range extension of 30 km. Although, the range extension is not sufficient for a long trip, it could be enough to bridge the distance to the next logistic centre where long duration charging is offered. Thus, the described use case can be seen as opportunity charging for heavy-duty vehicles that strive to achieve the next delivery goal within the target time rather than scheduled charging.

The operating cycle of 15 min for the fast charging of heavy-duty electric vehicles presented on the right of Figure 6.13 is repeated between 07:00 and 22:00, which corresponds to 60 operating cycles per day. Thus, the total energy supplied to the charging station per day is 1750 kWh. Considering an efficiency of 92 % for the energy supplied to the charging station with respect to the energy supplied by the grid, as in the use case of passenger vehicles, a constant power of 100 kW between 05:00 and 00:00 of the next day, which corresponds to 1900 kWh, is purchased from the grid to compensate for the vehicle charging. The positive effect on the electrical grid is obvious; power peaks of 350 kW shift to constant power flow of 100 kW.

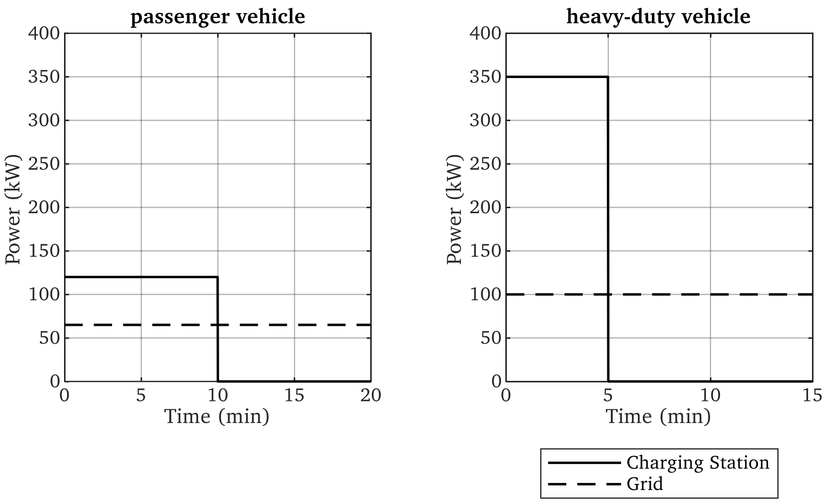

Figure 6.13 Power at the grid connection and the charging station of a stationary storage system throughout an operating cycle for the fast charging of a passenger vehicle (left) and a heavy-duty vehicle (right). The peak power on the grid side is significantly lower than that on the charging station. The difference between the power on the grid side and the charging station plus additional energy conversion losses is covered by the stationary storage. The energy deficit in the stationary storage is compensated by extending the power flow from the grid to the storage when EVFC is not offered.

As in the exclusive FCR application, the optimal combined storage for the parallel application of FCR and EVFC results from a cost-benefit analysis that involves the TCO and the battery degradation. The number of batteries N_b and the number flywheels N_{fw} assume values within a feasible range in order to find the system that results in the lowest TCO when the charge capacity of the battery remains above 75 % at the end of a service life of 15 a. The considered flywheel and battery units correspond to those of the reference combined storage summarized in Table 4.3. Figure 6.14 presents the trade-off between TCO and battery charge capacity loss under varying combined storage size for the parallel application of FCR and EVFC of passenger vehicles from 07:00 to 22:00 after 15 a of operation. The most cost-efficient combined storage that preserves a battery charge capacity over 75 % comprises 34 batteries and 4 flywheels, whereas the most cost-efficient battery-only system that preserves a charge capacity over 75 % comprises 44 batteries. Consequently, the optimal combined system has ten batteries fewer than the optimal battery-only system at the cost of four extra flywheels, which signifies a TCO reduction of roughly 5 % through the combined system.

Figure 6.15 presents the trade-off between battery charge capacity loss and TCO under varying combined storage size for the parallel application of FCR and EVFC of heavy-duty vehicles from 07:00 to 22:00 after 15 years of operation. The most cost-efficient combined storage that preserves a battery charge capacity over 75 % is composed of 48 batteries and 6 flywheels, whereas the most cost-efficient battery-only system that preserves a charge capacity over 75 % consists of 66 batteries. Thus, the optimal combined system leads to 18 fewer batteries than the optimal battery-only system at the cost of 6 flywheels, which corresponds to a TCO reduction of approximately 7 % through the combined system.

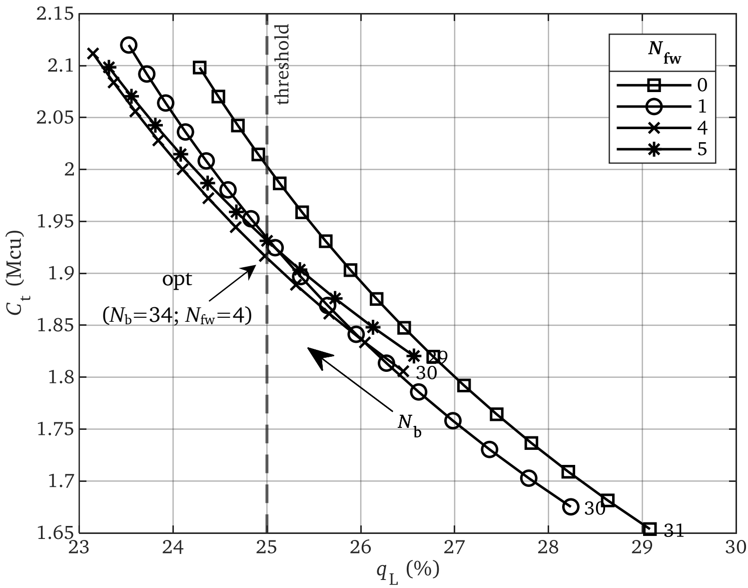

Figure 6.14 TCO over battery charge capacity loss under varying combined storage size for the parallel application of FCR and EVFC of passenger vehicles at 120 kW after 15 a of operation. The combined storage system with 34 batteries and 4 flywheels is the most cost-efficient system that prevents a battery charge capacity loss over 25 %.

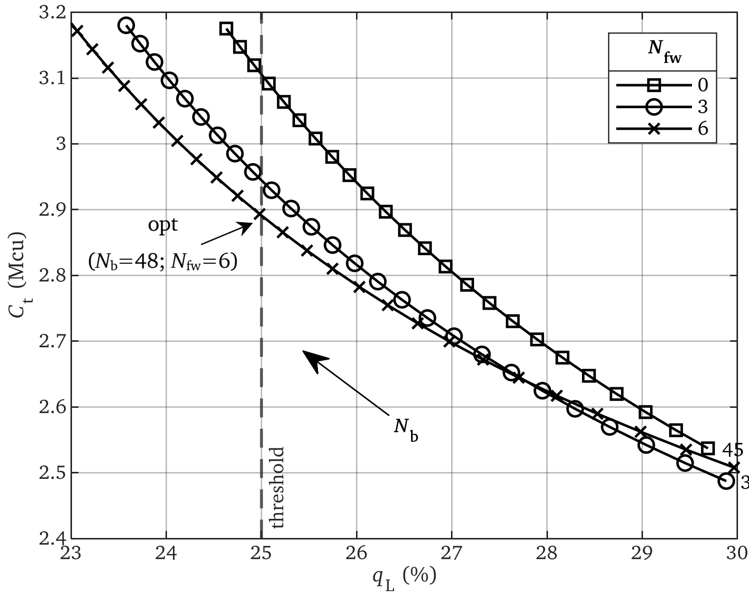

Figure 6.15 Trade-off between TCO and battery charge capacity loss under varying combined storage size for the parallel application of FCR and EVFC of heavy-duty vehicles at 350 kW after 15 a of operation. The combined storage with 48 batteries and 6 flywheels is the most cost-efficient system that prevents a battery charge capacity loss over 25 %.

Wayside Energy Recovery

The term *Wayside Energy Recovery System* (WERS) refers to a configuration that is used for the recuperation of braking energy in electrified railway networks. To distinguish WERS from systems in which the recuperated energy is stored in the braking vehicle or used by nearby vehicles in the same railway network, the term wayside signifies that the recuperated energy flows into a stationary system located nearby the braking vehicle. The braking energy of a decelerating train can therefore be stored in the combined storage and fed back to the same or another train that accelerates in the railway network. To enable a bidirectional power flow between the railway network and the energy storage, the DC bus of the combined storage and the DC line of the railway network should be coupled through a DC-DC power converter. The control of power flow can be implemented by monitoring the voltage on the railway network side (Ciccarelli, et al., 2016). Undervoltage on the railway network side corresponds to an accelerating rail vehicle, so that the energy storage should supply power to the network, whereas overvoltage on the railway network side corresponds to a decelerating vehicle, so that the energy storage should sink the power transmitted from the braking vehicle to the network.

Similar to the charging station for EVFC, the modified configuration of the combined energy storage system that enables wayside energy recovery is presented in Figure 6.16. The DC-DC power converter between the DC bus of the combined storage and the railway network should be sized for the maximum power flow, which is imposed by the traction cycle of the rail vehicle. Furthermore, the DC-DC power converter should be compatible with both the voltage of the railway line and the DC bus.

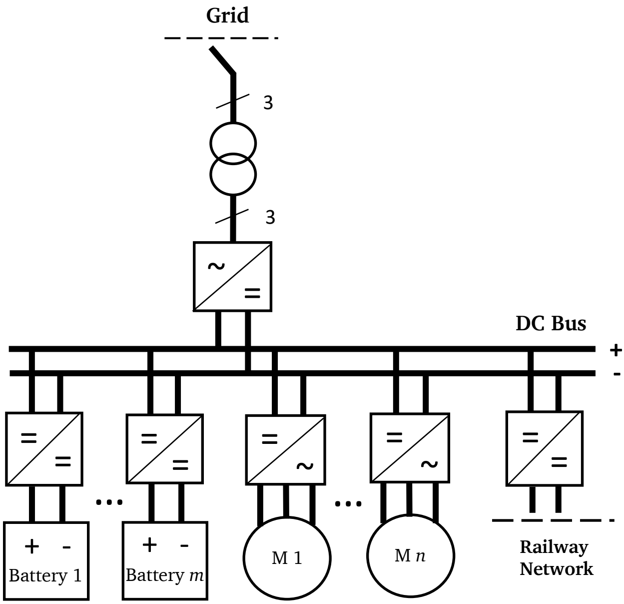

Figure 6.16 Modified configuration of the combined energy storage to facilitate wayside energy recovery in railway networks. The DC-DC power converter that is intended for wayside energy recovery (first from the right) enables the power flow between the railway network and the combined storage by bridging different DC voltage levels.

The main advantage of using WERSs in railway applications is the enhanced efficiency of the railway network because the energy of the braking vehicles is used locally. Using WERS, both power transmission over long distances and power dissipation into resistors in order to contain the line voltage within a permissible range are avoided. Nevertheless, WERSs lead to additional investment cost. Since braking energy can also be used by nearby rail vehicles that operate in the same railway network, the WERS location should be carefully selected. Additional advantages of WERSs include the contribution to the voltage regulation in railway networks, the mitigation of power peaks and eventually the operation as emergency power supplies (Meishner & Sauer, 2019). Generally, the short-term storage of braking energy and the subsequent supply into the railway network constitutes a service that can be offered by the energy storage operator to the operator of the railway network.

To investigate the application of wayside energy recovery through the combined energy storage, a use case should be specified. Since the power capacity of the combined storage, which is sized for FCR, is in the range of a few MW, light railway networks with relatively small rail vehicles such as trams are a reasonable match. The term *headway* refers to the elapsed time between the arrival of two consecutive trams at the same station. Short headways in urban and suburban areas increase the usage of WERSs and therefore constitute favourable use cases. The railway network of Darmstadt is appropriate for the purposes of the investigation, as it operates at an average DC voltage of 600 V, has short headways at peak hours and involves light articulated trams. To estimate the power that can be recovered by regenerative braking, the main technical data of the tram ST14 used in the urban and suburban region of Darmstadt are summarized in Table 6.11.

Table 6.11 Main technical data of the tram ST14 operated by Heag mobilo GmbH in Darmstadt region

Property	**Value**
Manufacturers	Alstom; Vossloh Kiepe; Bombardier
Operator	HEAG mobilo GmbH
Type	ST14
Operating region	Darmstadt
Curb weight	34 000 kg
Length	28 m
Passenger capacity	74 seated and 89 standing
Maximum speed	70 km/h
Supply voltage	750 V DC (-30…+20 %)
Traction machine type	Three-phase asynchronous machine
Number of traction machines	4
Nominal power per machine	95 kW

In the traction cycle considered, the tram ST14 decelerates from 60 km/h to zero speed, spends a dwell time for boarding and deboarding of passengers at the suburban station where the wayside energy recovery system is installed and subsequently accelerates to 60 km/h. Considering a tram loaded with 40 passengers that have an average weight of 75 kg, the gross weight of the tram results in m=37 000 kg, thus, the kinetic energy of the tram travelling at v=60 km/h is

$$E_{\text{kin}} = \frac{1}{2}mv^2 = \frac{1}{2}37000\text{ kg}\left(\frac{60}{3.6}\text{m/s}^2\right)^2 = 5.14\text{ MJ}.$$

It is assumed that the tram decelerates under nominal traction power until the acceleration reaches a=-1 m/s^2, then it decelerates further under the constant acceleration a=-1 m/s^2 to zero speed. Neglecting friction losses, the traction power P_{tr}, the tram speed and the tram acceleration should fulfil the equation $P_{tr}=mav$. For constant acceleration, the speed is a linear function of time such that $v(t)=v_0+at$, where v_0 is the initial speed. Therefore, the traction power is also a linear function of time such that $P_{tr}(t)=mav_0+ma^2t$. Since the tram decelerates under nominal traction power before it shifts to constant acceleration, the traction power at t=0 s, when the tram starts to brake under constant acceleration, corresponds to the nominal traction power $P_{tr}(0)=mav_0=-P_{\text{N}}$. Therefore, the time t_a spent under constant acceleration a=-1 m/s^2 until the tram decelerates to zero speed at zero traction power $P_{tr}(t_a)=0$ should be

$$t_a = \frac{P_{\text{N}}}{ma^2} = \frac{4 \cdot 95\text{ kW}}{37000\text{ kg }(-1\text{ m/s}^2)^2} = 10.27\text{ s}.$$

Integrating over time, the traction energy for the time spent under constant acceleration and linear decreasing traction power is

$$E_a = \frac{1}{2}P_{\text{N}}t_a = \frac{1}{2} \cdot 4 \cdot 95\text{ kW} \cdot 10.27\text{ s} = 1.95\text{ MJ}.$$

The rest energy $E_{\text{b}}=E_{\text{kin}}-E_{\text{a}}$=5.14 MJ-1.95 MJ=3.19 MJ is therefore spent for braking under constant traction power within

$$t_{\text{b}} = \frac{E_{\text{b}}}{P_{\text{N}}} = \frac{3.19\text{ MJ}}{4 \cdot 95\text{ kW}} = 8.39\text{ s}.$$

The energy that can be recovered in the WERS is reduced by powertrain losses, rail losses as well as friction losses. In a similar application, it is estimated that only 70 % of the train's kinetic energy can be recovered (Gelman, 2009). In the present investigation, it is assumed that the efficiency for the energy recovered in the WERS with respect to the kinetic energy of the tram is η_{WERS}=80 % due to superior powertrain efficiency and low rail losses. Moreover, it is assumed that the reverse efficiency, which is the ratio of the kinetic energy of the accelerating tram to the energy supplied by the WERS is also 80 %. Consequently, the energy recovered in the WERS through regenerative braking is $E_{WERS,in}$=0.8·5.14 MJ=4.1 MJ. Furthermore, the peak power at the terminals of WERS when braking is $P_{WERS,in}$=0.8·4·95 kW=304 kW.

After a dwell time of 20 s, the tram accelerates and the energy storage supplies the required traction power until the tram reaches the set speed of 60 km/h. Supplying the tram throughout the complete acceleration profile, reduces the peak power of the railway network, which may lead to a decrease in the number of required substations. It is assumed that the tram accelerates under the constant acceleration a=1 m/s^2 until it reaches its nominal traction power. The acceleration time from zero speed to nominal traction power equals the time already estimated in the deceleration case, which is t_a=10.27 s. Furthermore, since the energy conversion efficiency is η_{WERS}=80 %, the peak power that the energy storage should supply to the tram in order to accelerate under nominal traction power is $P_{WERS,out}$=(380 kW)/0.8=475 kW. When the nominal traction power is reached, the tram accelerates further until the speed of 60 km/h is reached in t_b=8.39 s, as previously calculated for the deceleration case.

Figure 6.17 presents the power flow at the connection between the combined storage, which serves as WERS, and the railway network. Positive sign corresponds to power flow from the railway network to the WERS, whereas negative sign corresponds to power flow from the WERS to the railway network. At t=1.5 s the tram initiates braking by recuperating energy in the railway network. The WERS controller notices the braking tram through the voltage increase in the railway network and commands the energy storage to sink the recuperated energy. During the next 8 s, a constant power of 304 kW flows into the WERS. Between t=10 s and t=20 s, the power decreases linearly, followed by a period of no power flow that corresponds to the dwell time. Shortly after t=40 s, the WERS controller notices a voltage decrease in the railway network due to the accelerating tram and commands the energy storage to feed power into the railway network. The power increases linearly to reach 475 kW shortly after t=50 s and remains constant for the next 8 s. The power supply is interrupted shortly before t=59 s, by the time the tram reaches the set speed of 60 km/h. When the traction cycle is over, no power is exchanged between the WERS and the railway network until the next tram arrives.

The power profile of Figure 6.17 reveals a disadvantage when flywheel storages, which are characterised by low available power at low energy state (low flywheel speed), as shown in Figure 4.1, are used for WERS. The available flywheel power increases as flywheels accelerate in order to sink the power recuperated by a braking rail vehicle, but the traction power decreases as the vehicle decelerates. On the other hand, when flywheels supply power to an accelerating rail vehicle, the traction power increases as the vehicle accelerates, whereas the available flywheel power decreases as flywheels decelerate. On the contrary, it would be advantageous for the flywheel sizing that the traction power of the vehicle increases as it decelerates and decreases as it accelerates.

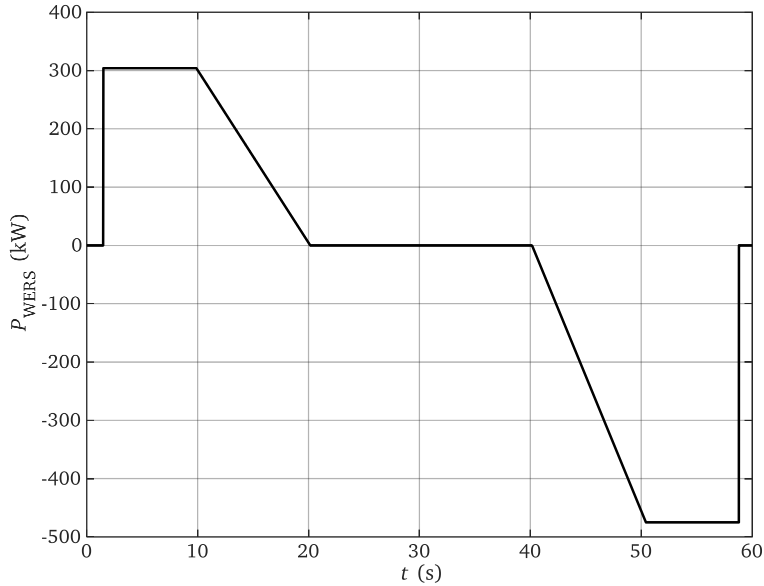

Figure 6.17 Estimated power flow over the time t at the connection between the combined storage system, which serves as WERS, and the railway network for the traction cycle of the tram ST14. The positive power flow between 1 s and 20 s corresponds to a decelerating tram, whereas the negative power flow between 40 s and 59 s corresponds to an accelerating tram.

The estimated maximum power flow between the storage and the railway network is 475 kW. Therefore, the DC-DC power converter between the DC bus of the storage system and the railway network is sized at 500 kVA. Further parameters of the DC-DC power converter are listed in Table A.15.

The efficiency η_{WERS} corresponds to the ratio of the energy recovered at the connection between the stationary storage and the railway network to the kinetic energy of the tram when braking is initiated. However, the power converters and the storage units that are internal to the stationary storage also cause energy conversion losses. Therefore, the efficiency η_{cs}=0.965 % is assumed for the energy stored with respect to the energy recovered at the connection between the stationary storage and the railway network. Furthermore, it is assumed that the efficiency of the reverse process, which is the ratio of the energy supplied at the connection between the stationary storage and the railway network to the energy retrieved from the storage units, is also η_{cs}=0.965 %. Consequently, the energy recovery and the subsequent energy supply for the traction cycle of the tram ST14 results in an energy deficit in the storage units of the combined storage that is

$$E_{\mathrm{def}} = \frac{E_{\mathrm{kin}}}{\eta_{\mathrm{WERS}}\eta_{\mathrm{cs}}} - \eta_{\mathrm{WERS}}\eta_{\mathrm{cs}}E_{\mathrm{kin}} = \frac{5.14\ \mathrm{MJ}}{0.8 \cdot 0.965} - 0.8 \cdot 0.965 \cdot 5.14\ \mathrm{MJ} = 2.69\ \mathrm{MJ}.$$

Although the energy deficit of 2.69 MJ≈0.75 kWh is low relative to the energy capacity of the combined storage system, it is subtracted as often as trams arrive at the station where the WERS is integrated. Therefore, the energy deficit should be compensated by purchasing energy from the grid, so that the stationary storage does not gradually empty out.

The first WERS use case considers a headway of 15 min at peak hours between 06:00 and 20:00, a headway of 30 min at off-peak hours between 20:00 and 24:00 and no operation between 00:00 and 06:00. Thus, the load profile is repeated 64 times per day, which corresponds to an energy deficit of $64 \cdot 0.75\,\mathrm{kWh} = 48\,\mathrm{kWh}$ in the combined storage. Assuming an energy conversion efficiency of 96 % for the energy stored in the storage units with respect to the energy supplied by the grid, to compensate for the energy deficit, a power block of 50 kW between 00:00 and 01:00 is scheduled on the grid side. Power blocks of 50 kW usually lie below the minimum bid of the energy market and should therefore be purchased by participating in a pool. The resulting energy expenses are allocated to the O&M cost of the DC-DC power converter that is placed between the DC bus of the stationary storage system and the railway network, since it is the only additional equipment considered for the application of wayside energy recovery.

Figure 6.18 presents the trade-off between TCO and battery degradation under varying combined storage size for the parallel application of FCR and wayside energy recovery of the traction cycle of tram ST14 with a headway of 15 min at peak hours after 15 a of operation. The most cost-efficient system that preserves a battery charge capacity loss below 25 % comprises 37 batteries and 3 flywheels. Alternatively, a battery-only system that prevents a battery charge capacity loss over 25 % requires 45 batteries. Consequently, the optimal combined system has eight fewer batteries than the optimal battery-only system due to the integration of three flywheels, which corresponds to a TCO reduction of approximately 5 % through the combined system.

The second use case considers a headway of 8 min at peak hours between 06:00 and 20:00, a headway of 15 min at off-peak hours between 20:00 and 24:00 and no operation between 00:00 and 06:00. Consequently, the load profile is repeated 121 times per day, which corresponds to an energy deficit of $121 \cdot 0.75\,\mathrm{kWh} = 90.8\,\mathrm{kWh}$ in the combined storage. The energy deficit is compensated by purchasing 100 kW between 00:00 and 01:00 in the energy market. Considering an energy conversion efficiency of 96 % for the energy stored in the storage units with respect to the energy supplied by the grid, the power block results in a small energy surplus of 5 kWh, which is, however, acceptable in order to reach the minimum bid of the energy market.

Figure 6.19 presents the trade-off between battery degradation and TCO under varying combined storage size for the parallel application of FCR and wayside energy recovery of the traction cycle of tram ST14 with a headway of 8 min at peak hours after 15 a of operation. The most cost-efficient system that preserves a battery charge capacity loss below 25 % at the end of service life comprises 38 batteries and 4 flywheels. Alternatively, a battery-only system with 49 batteries also preserves a battery charge capacity loss below 25 % using eleven batteries more than the combined system and no flywheels. However, the optimal combined system leads to a TCO reduction of roughly 7 % relative to the optimal battery-only system.

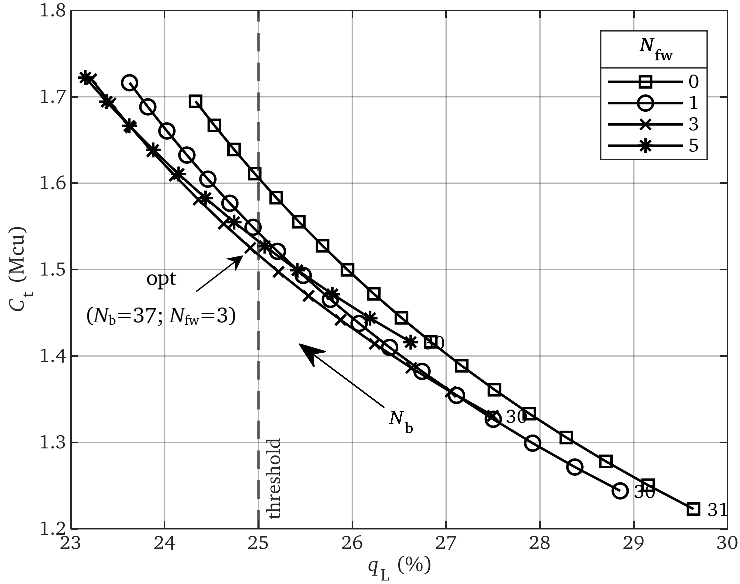

Figure 6.18 TCO over battery charge capacity loss after 15 a of operation under varying number of storage units for the parallel application of FCR and wayside energy recovery of the traction cycle of the tram ST14 with a headway of 15 min at peak hours. The most cost-efficient combined system that leads to a battery charge capacity loss below 25 % comprises 37 batteries and 3 flywheels.

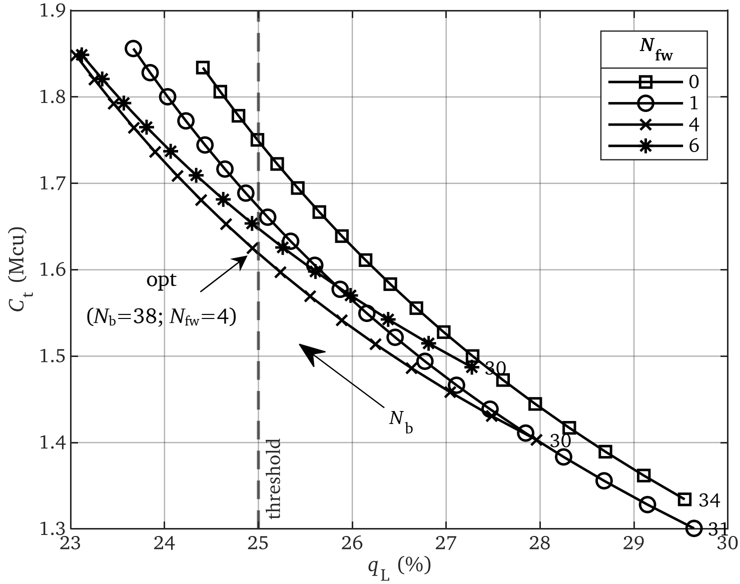

Figure 6.19 Trade-off between TCO and battery charge capacity loss under varying combined storage size for the parallel application of FCR and wayside energy recovery of the traction cycle of the tram ST14 with a headway of 8 min at peak hours after 15 a of operation. The most cost-efficient system that preserves a battery charge capacity loss below 25 % comprises 38 batteries and 4 flywheels.

6.5 Comparison of Applications and Use Cases

The optimal storage size and the corresponding TCO vary with application and use case. It has been observed that applications with an alternating power of high intensity such as EVFC lead to comparatively large storage sizes with relatively high number of flywheels. A comparison of the economic figures of the investigated applications aims to identify use cases in which combined storages perform better than battery-only storages.

Figure 6.20 summarizes the sizes of the most cost-efficient combined storages and the most cost-efficient battery-only storages that preserve a battery charge capacity over 75 % after 15 a of operation for the use case of exclusive FCR, the use cases of FCR in addition to EVFC with a peak power of 120 kW (EVFC-120) and 350 kW (EVFC-350) and the use cases of FCR in addition to WERS with a headway of 8 min (WERS-8) and 15 min (WERS-15) at peak-hours. The highest reduction in battery units of the optimal combined system relative to the optimal battery-only system is observed in use case EVFC-350. The battery units are reduced from 66 to 48, which corresponds to a battery capacity reduction of $18 \cdot 47$ kWh=846 kWh through 6 flywheels of $6 \cdot 1.8$ kWh=10.8 kWh. In other words, 1 kWh of flywheel energy capacity replaces roughly 80 kWh of battery energy capacity or one flywheel replaces three batteries. The lowest reduction in battery units is observed in the exclusive FCR application, where the battery units are reduced from 41 to 35, which signifies a battery energy capacity reduction of $6 \cdot 47=282$ kWh through 2 flywheels of $2 \cdot 1.8$ kWh=3.6 kWh. Although the reduction of battery units in the exclusive FCR use case is significantly lower than that in use case EVFC-350, the ratio of replaced batteries to installed flywheels is the same. A similar behaviour is observed in the other use cases, in which the ratio of replaced batteries to installed flywheels ranges between 2.5 and 3, with the lowest ratio observed in use case EVFC-120.

Depending on the acquisition cost of battery and flywheel storage units, replacing batteries with flywheels can reduce the investment cost. According to the reference cost factors presented in Table 6.1, the investment cost of the optimal battery-only storage and that of the optimal combined storage for the investigated use cases are summarized in Figure 6.21. Obviously, the investment cost exceeds 1.2 Mcu in all use cases. The combined storage in the use case of exclusive FCR has the lowest investment cost as it comprises the lowest number of storage units. The highest investment cost corresponds to the battery-only storage in use case EVFC-350, which has the highest number of battery units, as it can be observed in Figure 6.20. In all use cases the optimal combined storage leads to a lower investment cost than the optimal battery-only storage.

Although the optimal combined storage has a lower investment cost than the optimal battery-only storage in all use cases, the no-load losses of the kinetic storage add to the operating cost which in turn add to the TCO. Figure 6.22 compares the TCO of the optimal combined storage with that of the optimal battery-only storage of each use case for a service life of 15 a. The lowest TCO of 1.35 Mcu corresponds to the combined storage of the exclusive FCR use case, whereas the highest TCO of 3.12 Mcu corresponds to the battery-only storage of use case EVFC-350. The TCO of the storage systems in use case EVFC-350 are significantly higher than that of the systems in the other use cases, which is attributed to the energy cost for electric vehicle charging. Generally, it is observed that when the applications of EVFC and WERS run in parallel with FCR, the load increases, so that the reduction in the TCO achieved through the combined system is less pronounced than the corresponding reduction in the investment cost presented in Figure 6.21. Nevertheless, the comparatively high TCO resulting from applications that run in parallel with FCR should be balanced by corresponding revenues. For the application of EVFC, revenues result from the payments of the users charging their vehicle, whereas for the application of WERS, revenues can be achieved through a subscription of the company which operates the railway network to the company that operates the stationary storage.

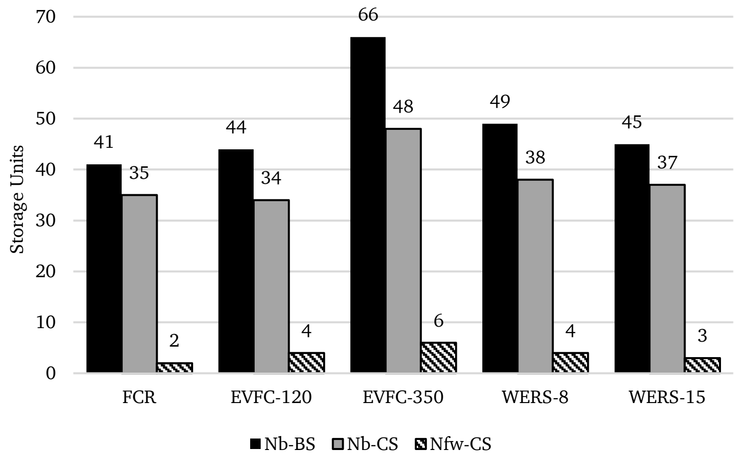

Figure 6.20 Number of storage units of the most cost-efficient battery-only storage and the most cost-efficient combined storage that preserve a battery charge capacity over 75 % after 15 a of operation over the investigated use cases. Nb-BS stands for the number of batteries of the battery-only storage. Nb-CS and Nfw-CS stand for the number of batteries and the number of flywheels of the combined storage respectively. FCR stands for the exclusive application of Frequency Containment Reserve. EVFC-120 and EVFC-350 stand for the parallel application of FCR with electric vehicle fast charging at 120 kW and 350 kW respectively. WERS-8 and WERS-15 stand for the parallel application of FCR with wayside energy recovery in railway networks with a headway of 8 min and 15 min at peak-hours respectively.

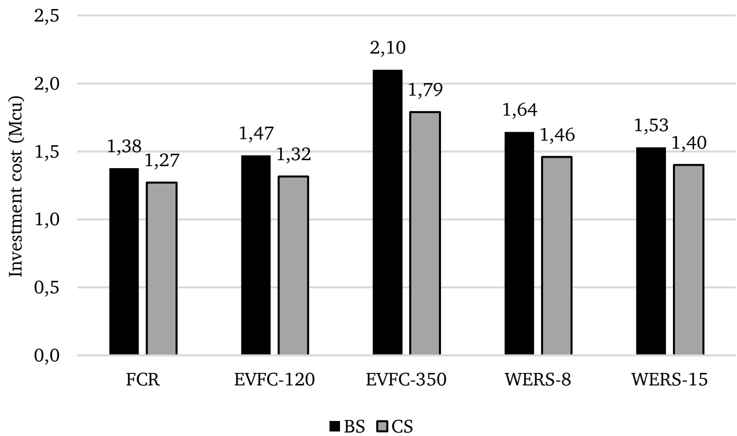

Figure 6.21 Investment cost of the optimal Battery-only Storage (BS) and the optimal Combined Storage (CS) over the investigated use cases. The investment cost exceeds 1.2 Mcu in all use cases. The highest investment cost reduction through a CS is observed in use case EVFC-350.

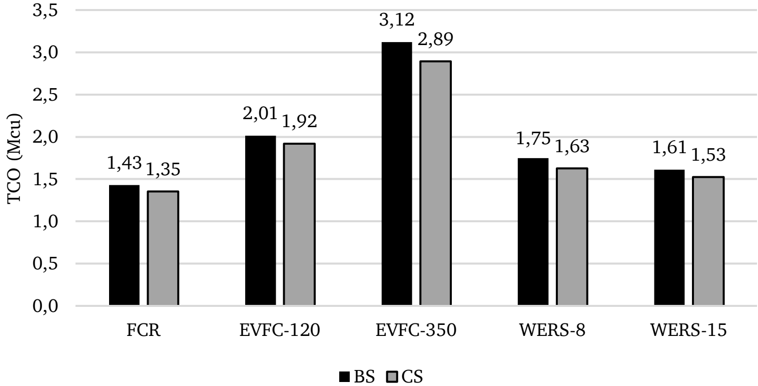

Figure 6.22 TCO of the optimal Battery-only Storage (BS) and the optimal Combined Storage (CS) over the investigated use cases after 15 a of operation. The TCO of the storages in use case EVFC-350 is considerably higher than that of the storages in all other use cases.

Figure 6.23 presents the percentage reduction in the investment cost and the TCO of the optimal combined storage relative to the battery-only storage over the investigated use cases. It is obvious that the TCO reduction is less remarkable than the investment cost reduction in all use cases. The highest investment cost reduction is observed in use case EVFC-350 at 15 %, followed by use case WERS-8 at 11.1 %. Moreover, use case EVFC-350 and use case WERS-8 lead to the highest TCO reduction of 7.3 % and 7.2 % respectively. The remarkable cost reduction achieved through the combined storage in use cases EVFC-350 and WERS-8 is the result of a significant decrease in the number of battery units, as shown in Figure 6.20. Although the difference in the percentage TCO reduction among the use cases is small, the importance of the percentage TCO reduction is the greater, the higher the TCO is. For example, considering the TCO presented in Figure 6.22, a TCO reduction of 1 % in use case EVFC-350 corresponds roughly to double the savings than a TCO reduction of 1 % in the exclusive FCR use case.

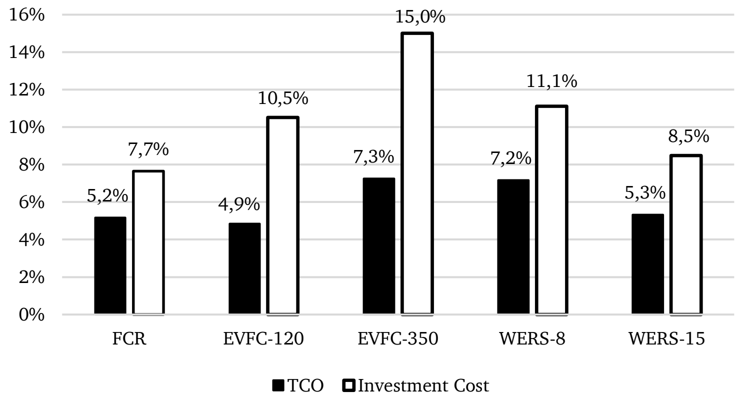

Figure 6.23 Percentage TCO and investment cost reduction of the optimal combined storage relative to the optimal battery-only storage over the investigated use cases. Use case EVFC-350 shows the highest investment cost reduction of 15 %.

It is obvious that some use cases lead to comparatively high O&M cost, thus, it is worth investigating the breakdown of TCO by life cycle stage. Figure 6.24 breaks down the TCO of the optimal combined storage into the life cycle stages of investment, O&M, and disposal over the investigated use cases after 15 a of operation. Obviously, the O&M stage has a significant TCO share in use cases with EVFC, where use case EVFC-350 leads to the highest O&M share of 40 %, followed by use case EVFC-120 that leads to an O&M share of 33 %. The high O&M share in use cases with EVFC is driven by the energy cost to charge the vehicles. The O&M share in use cases with WERS is significantly lower than that in use cases with EVFC, since a substantial amount of the energy provided to the accelerating tram was previously recuperated in the energy storage and only the rest is purchased from the grid. Furthermore, in use cases with WERS the combined storage should supply power only for a few seconds during each operating cycle, whereas, in use cases with EVFC, the storage should supply power for a few minutes in an operating cycle of a comparable duration. The O&M share in use case WERS-8 is 12 % and therefore a bit higher than the O&M share of 10 % in use case WERS-15. The longer the headway is, the less energy is exchanged between the stationary storage and the railway network and therefore less energy should be purchased from the grid to compensate for the energy deficit. No energy is purchased from the grid in the use case of exclusive FCR, since the FCR power profile is almost symmetrical, however, the cost for the compensation of the energy losses of the storage units is considered in the O&M cost.

The exclusive FCR use case leads to the highest TCO share of 94 % in the investment stage, which signifies that in this particular use case the TCO share during the O&M stage is of secondary importance. A similar conclusion can be drawn for use cases with WERS, in which the TCO share in the investment stage ranges between 90 % and 92 %. Although the TCO share in O&M stage is small in some use cases, it can be critical when deciding between system variants. It is worth mentioning that the combined storages are optimized in all use cases, among others things, for low TCO, which indirectly leads to low O&M cost. The TCO share in the disposal stage is -2 % in all use cases due to the liquidation of the rest value of the flywheels and the power transformer at the end of service life. Evidently, the rest value of the transformer and the flywheels after 15 a of operation are secondary to the investment and O&M cost.

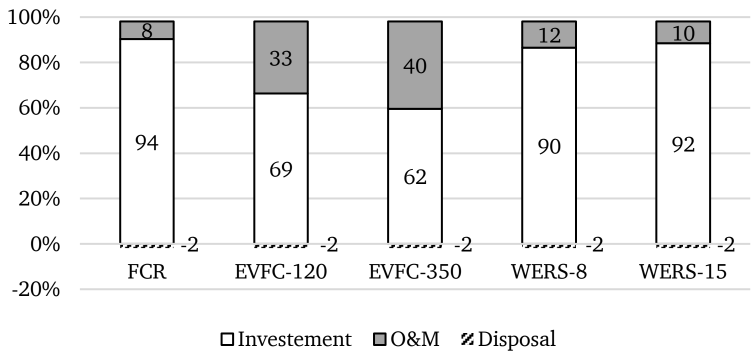

Figure 6.24 Breakdown of the TCO of the optimal combined storage by life cycle stage over the investigated use cases after 15 a of operation. The O&M share in use cases with EVFC is considerably higher than in the other use cases due to the energy cost for vehicle charging. The negative TCO share in the disposal stage is due to the rest value of equipment that is liquidated at the end of service life.

The breakdown of the TCO into life cycle stages provides an insight into the cost over the course of time, whereas the breakdown of the TCO into equipment categories facilitates the identification of cost drivers among the equipment. The equipment is classified into four categories, the battery storage which comprises the battery units with their power converters, the kinetic storage which comprises the flywheel storages with their power converters, the basic equipment, such as the central power converter and the power transformer, and the additional equipment that comprises the extra power converters required for the applications of EVFC and WERS. The energy cost to compensate for the energy deficit resulting from the applications of EVFC and WERS is allocated to the additional equipment because the power flow through the additional DC-DC power converters is the cause of the additional cost.

Figure 6.25 breaks down the TCO of the optimal combined storage into equipment categories over the investigated use cases for a service life of 15 a. Obviously, the TCO share of the battery storage is dominant in all use cases and peaks at 73 % in the exclusive FCR use case. The TCO share of the kinetic storage varies slightly between 7 % and 11 % over the use cases. The basic equipment has a remarkable TCO share that ranges between 9 % and 20 %, where the lowest share is observed in use case EVFC-350 and the highest in the use case of exclusive FCR. The additional equipment has a significant TCO share in use cases with EVFC, which ranges between 26 % and 34 %, primarily due to the high O&M cost for the charging of electric vehicles and only secondarily due to the investment cost of the power converters. In contrast, the TCO share of additional equipment in use cases with WERS ranges between 4 % and 6 %. Although the power converters in use cases with WERS are larger than that in use cases with EVFC, the energy purchased from the grid in use cases with WERS is substantially lower than that in use cases with EVFC, which leads to a significant lower TCO share of additional equipment in use cases with WERS.

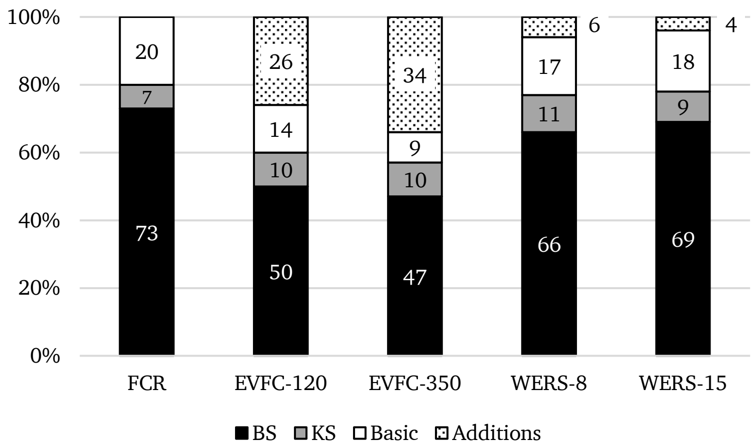

Figure 6.25 Breakdown of the TCO of the optimal combined storage by equipment category over the investigated use cases after 15 a of operation. Battery Storage (BS) stands for the battery units with their power converters, Kinetic Storage (KS) stands for the flywheel units with their power converters, Basic stands for the basic equipment, such as the central power converter and the power transformer, and Additions stands for the extra equipment required for the applications of EVFC and WERS.

As observed in Figure 6.24, the O&M cost is less significant than the investment cost with the exception of use cases with EVFC. However, even small variations in the O&M cost could be important when evaluating system variants. Furthermore, although the investment cost can be estimated with relatively low uncertainties during project planning, the estimation of the present value of O&M cost that spans the complete service life involves high uncertainties. Therefore, in order to identify potential cost drivers, the O&M cost of the optimal combined storage after 15 a of operation is broken down by equipment category over the investigated use cases in Figure 6.26. It is observed that the O&M cost share of additional equipment dominates in use cases with EVFC, specifically, it is 76 % in use case EVFC-120 and 82 % in use case EVFC-350. Plainly, the energy conversion losses in the power converters is no the main reason that accounts for the high O&M cost share of additional equipment but the energy purchased from the grid to charge the electric vehicles. In contrast, the O&M cost share of additional equipment in use cases with WERS lies below 25 %, since significantly less energy is purchased from the grid.

The O&M cost of the battery storage corresponds to the electricity consumption to compensate for the power losses in its lithium-ion cells and its power converters. The O&M cost share of the battery storage lies below 8 % in all use cases. Since the energy conversion efficiency of lithium-ion batteries is relatively high, the losses in the battery storage are comparatively low and therefore its O&M cost share is low compared to that in the other equipment categories. Although the kinetic storage has a significantly lower power capacity than the battery storage in all use cases, the O&M cost share of the kinetic storage is remarkably higher than that of the battery storage in every use case. The comparatively high O&M cost of the kinetic storage is primarily due to the no load-losses of the flywheels and secondarily due to the maintenance intervals of the vacuum system. The O&M cost share of basic equipment is higher than that of the kinetic storage in the use case of exclusive FCR because the power losses in the central power converter, the power transformer and the auxiliary systems are significant. However, in use cases with EVFC and WERS, the O&M cost share of the kinetic storage exceeds (or equals) that of the basic equipment because more flywheels than in the exclusive FCR use case are installed, whereas the basic equipment remains unchanged.

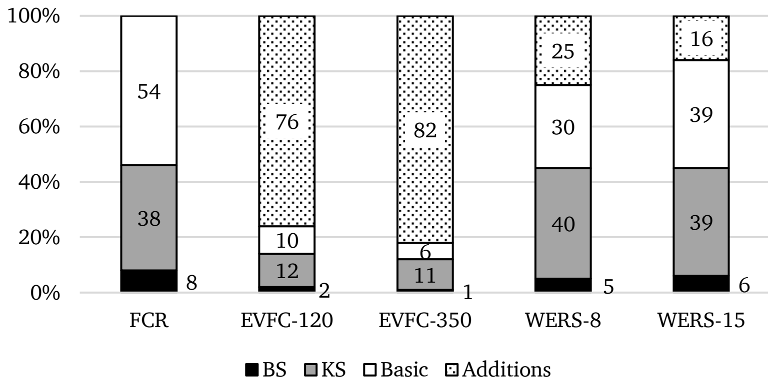

Figure 6.26 Breakdown of the O&M cost of the optimal combined storage by equipment category over the investigated use cases after 15 a of operation. The cost share of the battery storage is remarkably low in all use cases. The cost share of additional equipment in use cases with EVFC dominates the O&M cost.

7. Conclusion

The work focused on the cost-efficiency of combined storage systems that comprise lithium-ion batteries and high-speed flywheels intended for balancing services in electrical grids. For the considered load profiles and cost parameters, optimally sized combined storage systems led to a lower Total Cost of Ownership (TCO) than optimally sized battery-only systems. The storage systems were sized so that their TCO is minimized, on condition that the degradation of the battery storage lies below a certain threshold at the end of service life.

Although uncertainties in the cost parameters affect the economic assessment, according to the sensitivity analyses for the use case of exclusive Frequency Containment Reserve (FCR), the TCO of the optimal combined storage is lower than that of the optimal battery-only storage for a wide variation of the main cost drivers. Flywheels have a remarkably higher operating cost than batteries because their idle losses should be compensated to keep rotating. Although the idle losses of flywheel storages are comparatively high, in the exclusive FCR use case, the TCO of the optimal combined storage was lower than that of the optimal battery-only storage, even for a twofold increase in the electricity rate. Nevertheless, the energy cost of the kinetic storage is a significant cost driver. Although the optimal combined storage led to a lower investment cost than the optimal battery-only storage in all use cases considered, the reduction in the TCO was less pronounced due to the O&M cost of the flywheels. For example, for the use case of FCR along with the fast charging of passenger vehicles at 120 kW, the investment cost of the optimal combined storage was reduced by 10.5 % compared to that of the optimal battery-only storage, however, the corresponding TCO was reduced by only 4.9 %.

Regarding the use case of exclusive FCR, the study demonstrated that the TCO is more sensitive to the energy losses in the flywheel than the energy capacity cost for the acquisition of the flywheel. The study investigated the effect of technological improvements on the operating cost of the flywheel prototype SWIVT290. An alternative electric machine without permanent excitation demonstrated the highest potential to reduce the operating cost. An enlarged flywheel size, which can be achieved through a twofold increase in the rotor inertia and the power rating of the electric machine without changing the magnetic suspension and the vacuum system, also led to a significant reduction in the operating cost. Operating the electric machine in field weakening in order to reduce its iron losses showed the lowest potential to decrease the operating cost, however, without requiring any modification in the flywheel hardware.

The study investigated the effect of service life on the battery degradation for the application of FCR. For the implemented battery degradation model, the optimal combined storage and the optimal battery-only storage not only exceeded a service life of 15 a but could ideally reach a service life of 20 a. In this respect the investment cost of the battery-only storage was about 8 % higher than that of the combined storage. Moreover, after 20 a of operation the investment and O&M cost of the battery-only storage was still higher than that of the combined storage. It can therefore be claimed that for the given FCR load profile, replacing part of the batteries with flywheels constitutes a way to extend the battery service life at low cost.

For all use cases investigated in this work, the application of FCR was running in the background. The application of wayside energy recovery in railway networks along with FCR demonstrated that a reduction in the headway from 15 min to 8 min, which corresponds to more frequent stops of the tram and therefore to a more dynamic load profile for the storage, expands the reduction in the TCO of the optimal combined storage relative to that of the optimal battery-only storage. Similarly, the load profile for the fast charging of heavy-duty electric vehicles at 350 kW has both higher frequency and higher intensity than that for the fast charging of passenger vehicles at 120 kW. Therefore, as expected, the use case of heavy-duty vehicle fast charging along with FCR demonstrated a higher decrease in the TCO of the combined storage relative to that of the battery-only storage than the corresponding use case of passenger vehicle fast charging. The highest reduction in battery units among all use cases was also observed in the use case of heavy-duty vehicle fast charging along with FCR, where 18 batteries in the battery-only storage were replaced by 6 flywheels in the combined storage reducing the TCO by 7.3 %. It can therefore be claimed that for the use case of heavy-duty vehicle fast charging along with FCR, 1 kWh of flywheel energy capacity can roughly replace 80 kWh of lithium-ion battery energy capacity.

Generally, the integration of flywheels in a battery storage system reduces the load share of batteries and therefore their cyclic degradation. On the other hand, a similar effect can be achieved by increasing the number of battery units. Apart from the acquisition cost of storage technologies, whether the integration of additional battery or flywheel units lead to a lower TCO at the end of service life depends on the load profile. Load profiles of relatively low intensity are favourable for batteries, whereas flywheels are usually advantageous for high intensity alternating load profiles. In this respect alternating means that the load profile changes direction like alternating current.

A storage system that comprises only batteries should be usually oversized in order to withstand a relatively intense load profile over a service life of 15 years. On the other hand, a flywheel-only storage intended for applications that require relatively high energy capacity substantially raises the cost. It can therefore be claimed that battery-flywheel storage systems are favourable for applications that not only require a considerable amount of energy capacity such as the application of FCR, but also impose an alternating load profile of high intensity such as that resulting from the applications of electric vehicle fast charging and wayside energy recovery.

In applications that require high energy capacity and impose an intense alternating load profile, the battery storage should be able to operate unidirectionally for a relatively long time, when needed, whereas the flywheel should cover the alternating load protecting the battery from intense cycling. To effectively exploit the kinetic storage, the alternating part of the load should oscillate with a period and an amplitude that correspond to the power and energy capacity of the kinetic storage. In other words, the kinetic storage should be sized according to the alternating part of the load profile. High-frequency but rarely alternating load profiles are less advantageous for kinetic storages because the flywheels tend to operate unidirectionally and thus reach relatively fast their energy capacity limits. In this respect the split of the load in a low dynamic part for the batteries and a high dynamic part for the flywheels through a low pass filter, which is suggested in some articles in the literature, has low practical importance because it leads to a mutual energy exchange between the flywheels and the batteries, which causes energy conversion losses without contributing to cover the load.

To assess the economic performance of battery-flywheel storages, the strategy of maximum kinetic storage power share is applied, so that the cyclic degradation of the battery is minimized. However, when the battery degradation is of secondary importance, alternative power split strategies can be applied. To minimize the instantaneous energy conversion losses of the combined storage, the energy management strategy of Optimal Power Share (OPS) is developed. The OPS is a computational-efficient strategy suitable for applications in which the load is unpredictable such as FCR. An energy management algorithm that includes the OPS strategy was successfully implemented in a real controller at a fixed cycle time of 10 ms and tested on the combined storage prototype hsETA located at the Technical University of Darmstadt. Despite the high uncertainties involved in the experimental estimation of the energy losses, a qualitative congruence between the simulated and the experimental results under OPS was observed.

In order to model the power losses of the flywheel prototype SWIVT290, which are needed in the OPS algorithm as well as in the economic assessment, advances in the modelling of high-speed flywheels with Permanent Magnet Synchronous Machines (PMSMs) were made, which have implications for future research. Two aspects of the loss model are highlighted for future investigations; first, the inclusion of the iron losses in the equivalent circuit of the electric machine in order to estimate the operating cost, second, the cost savings that can be achieved through the operation of flywheel storages that are based on PMSMs in field weakening. The identification of the iron resistance of the electric machine through measurements on flywheel prototypes facilitates the development of an equivalent circuit, which can be used to estimate the total power losses of the electric machine. With the aid of the equivalent circuit, the power losses at any operating point of the electric machine can be estimated and used to evaluate the thermal behaviour of the flywheel storage. The analytical expressions that are derived in this work for the braking torque and the current required to keep flywheels with PMSMs rotating at constant speed can be used to estimate the self-deceleration and the idle power consumption respectively.

Iron losses are significant in high-speed flywheels due to the relatively high electrical frequency, especially when electric machines with several pole pairs are used. In electric machines with permanent excitation, iron losses occur as long as the machine rotates. Therefore, an optimization-based strategy that minimizes the power losses of flywheel storages by operating their PMSM in field weakening is developed. Using field-oriented control, the magnetic field generated by the current in the stator windings can be oriented so that it counters the rotating magnetic field of the permanent magnets, hence reducing the magnetisation losses in the stator iron. The simulation of the optimization-based field weakening strategy for the use case of FCR demonstrated a reduction of almost 9 % in the operating cost of the flywheel storage including its power converter compared to that of the conventional operating strategy. However, the optimization-based field weakening strategy was not verified through experimental results because the control units of the power converters of the available flywheel prototypes restrict the modification of the current control loop.

The results of this work have also practical implications, for instance, it was shown that the energy management strategy of OPS can be implemented in real controllers. Since the OPS strategy requires parametrized loss models of the storage units, this work suggests loss models for batteries and flywheels, the parameters of which are often available in the manufacturer specification such as, the internal resistance of lithium-ion cells, the phase resistance of electric machines and the nominal losses of power converters. The OPS strategy should be preferred when the battery degradation is of secondary importance in order to minimize the operating cost of the combined storage. If the battery degradation should be limited instead, the strategy of maximum kinetic storage power share can be applied. Monitoring the lithium-ion cells and therefore estimating their actual degradation, which is usually implemented in real systems, facilitates the decision to switch between the OPS strategy and the strategy of maximum kinetic storage share.

The estimation of the cyclic degradation of the battery storage is based on an empirical model for cells with lithium Nickel Manganese Cobalt oxides (NMC) in the cathode. However, the empirical model is modified in order to be parametrized according to the manufacturer specification regarding the degradation of the lithium-ion cells used in the investigation. The method to parametrize the empirical cyclic degradation model for NMC lithium-ion cells that is described in this work can also be applied in other investigations as long as the manufacturer provides typical data for the cyclic degradation of the cells.

Project planning of energy storage systems is not anymore state-of-the-art if only a single storage technology is considered. It was shown that the combination of flywheels and batteries for grid balancing services reduces the total cost of ownership compared to single-technology systems for a wide variation of the main cost drivers. In this respect the total cost of ownership is not the only indicator that facilitates the decision among system variants. The study suggests a cost-benefit analysis which in addition to the total cost of ownership considers the forecast for the battery degradation at the end of service life. Engineers can apply the cost-benefit analysis suggested in this work to evaluate variants of energy storage systems in the conceptual phase of projects that are intended for grid balancing services.

The cost-benefit analysis can also be applied in order to assess combined storage systems under varying load profiles that result from different applications and use cases. It was demonstrated that the application of frequency containment reserve along with the fast charging of electric vehicles is advantageous for battery-flywheel storage systems. Additionally, it was shown that the advantages are more pronounced when fast charging of heavy-duty electric vehicles is involved. The power peaks for the fast charging of heavy-duty electric vehicles, which are considered in this work, can be effectively and cost-efficiently mitigated by battery-flywheel combined storage systems that simultaneously offer the service of frequency containment reserve to the power gird.

References

Abele, E., Bauerdick, C. J., Strobel, N. & Panten, N., 2016. ETA Learning Factory: A Holistic Concept for Teaching Energy Efficiency in Production. *Procedia CIRP,* Volume 54, pp. 83-88.

Amiryar, M. E. & Pullen, K. R., 2017. A Review of Flywheel Energy Storage System Technologies and Their Applications. *applied sciences,* Volume 7.

Arora, S., Abkenar, A. T., Jayasinghe, S. G. & Tammi, K., 2021. *Heavy-Duty Electric Vehicles - From Concept to Reality.* Oxford: Butterworth-Heinemann.

Ayodele, T. R., Ogunjuyigbe, A. S. O. & Oyelowo, N. O., 2020. Hybridisation of battery/flywheel energy storage system to improve ageing of lead-acid batteries in PV-powered applications. *International Journal of Sustainable Engineering,* 13(5), pp. 337-359.

Balzer, G. & Schorn, C., 2022. *Asset management for infrastructure systems.* 2 ed. Cham: Springer Nature Switzerland.

Barelli, L., Bidini, G., Ciupageanu, D. & Pelosi, D., 2021. Integrating Hybrid Energy Storage System on a Wind Generator to enhance grid safety and stability: A Levelized Cost of Electricity analysis. *Journal of Energy Storage,* Volume 34.

Binder, A., 2017. *Elektrische Maschinen und Antriebe - Grundlagen, Betriebsverhalten.* 2 Hrsg. Berlin: Springer Vieweg.

Bocklisch, T., 2016. Hybrid energy storage approach for renewable energy applications. *Journal of Energy Storage,* Volume 8, pp. 311-319.

Böhm, R. et al., 2019. Control of a Hybrid Energy Storage System for a Hybrid Compensation System. *Chemical Engineering Technology,* 42(9), pp. 1879-1885.

Briat, O. et al., 2007. Principle, design and experimental validation of a flywheel-battery hybrid source for heavy-duty electric vehicles. *IET Electric Power Applications,* 1(5), pp. 665-674.

Ciccarelli, F., Iannuzzi, D., Kondo, K. & Fratelli, L., 2016. Line-Voltage Control Based on Wayside Energy Storage Systems for Tramway Networks. *IEEE Transactions on Power Electronics,* 31(1), pp. 884-899.

Colby, R. S. & Novotny, D. W., 1987. Efficient Operation of Surface-Mounted PM Synchronous Motors. *IEEE Transactions on Industry Applications,* IA-23(6), pp. 1048 - 1054.

Collin, R. et al., 2019. Advanced Electric Vehicle Fast-Charging Technologies. *Energies,* Volume 12.

Conci, M. & Schneider, J., 2017. A District Approach to Building Renovation for the Integral Energy Redevelopment of Existing Residential Areas. *sustainability,* Volume 9.

Dambone Sessa, S., Tortella, A., Andriollo, M. & Benato, R., 2018. Li-Ion Battery-Flywheel Hybrid Storage System: Countering Battery Aging During a Grid Frequency Regulation Service. *Applied Sciences,* Volume 8.

Dhand, A. & Pullen, K., 2015. Optimal energy management for a flywheel-assisted battery electric vehicle. *Journal of Automobile Engineering,* 229(12), pp. 1672-1682.

Ding, K., Li, F. & Zhang, X., 2019. *Power Smoothing Control of DC Microgrid Hybrid Energy Storage System Based on Fuzzy Control.* Guangzhou, China, Chinese Control Conference (CCC).

DNV GL, 2019. *PV Inverter Useful Life Considerations,* Oakland, CA, USA: DNV GL - Energy.

Dorn, R., Schwartz, R. & Steurich, B., 2018. Battery Management System. In: R. Korthauer, ed. *Lithium-Ion Batteries: Basics and Applications.* Berlin: Springer, pp. 165-175.

Ecker, M. et al., 2014. Calendar and cycle life study of Li(NiMnCo)O2-based 18650 lithium-ion batteries. *Journal of Power Sources,* Volume 248, pp. 839-851.

Emde, A., Kratzer, B. & Sauer, A., 2020. *Auslegung von hybriden Energiespeichern.* Graz, Austria, Symposium Energieinnovation.

Fernández-Bernal, F., García-Cerrada, A. & Faure, R., 2001. Determination of Parameters in Interior Permanent-Magnet Synchronous Motors With Iron Losses Without Torque Measurement. *IEEE Transactions on Industry Applications,* 37(5), pp. 1265-1271.

Figgener, J. et al., 2022. The development of battery storage systems in Germany – A market review (status 2022). *10.48550/arXiv.2203.06762.*

Formica, T. J., Khan, H. A. & Michael G. Pecht, 2019. The Effect of Inverter Failures on the Return on Investment of Solar Photovoltaic Systems. *IEEE Access,* Volume 5, pp. 21336-21343.

Franz, D., Richter, M., Schneider, M. & Rinderknecht, S., 2019. *Homopolar Active Magnetic Bearing Design for Outer Rotor Kinetic Energy Storages.* San Diego, CA, USA, IEEE International Electric Machines & Drives Conference (IEMDC).

Franz, D., Schneider, M., Richter, M. & Rinderknecht, S., 2019. Thermal Behavior of a Magnetically Levitated Spindle for Fatigue Testing of Fiber Reinforced Plastic. *Actuators,* 8(2).

Gelman, V., 2009. Braking Energy Recuperation. *IEEE Vehicular Technology Magazine,* 4(3), pp. 82-89.

Hou, J., Song, Z., Hofmann, H. F. & Sun, J., 2021. Control Strategy for Battery/Flywheel Hybrid Energy Storage in Electric Shipboard Microgrids. *IEEE Transactions on Industrial Informatics,* 17(2), pp. 1089-1099.

Huria, T., Ceraolo, M., Gazzarri, J. & Jackey, R., 2012. *High fidelity electrical model with thermal dependence for characterization and simulation of high power lithium battery cells.* Greenville, SC, USA, IEEE International Electric Vehicle Conference.

IRENA, 2017. *Electricity Storage and Renewables: Costs and Markets to 2030,* Abu Dhabi: International Renewable Energy Agency.

Jaafar, A. et al., 2009. Sizing and Energy Management of a Hybrid Locomotive Based on Flywheel and Accumulators. *IEEE Transactions on Vehicular Technonology,* 58(8), pp. 3947-3958.

Karrari, S., 2021. *Integration of Flywheel Energy Storage Systems in Low Voltage Distribution Grids.* Karlsruhe: Karlsruhe Institute of Technology.

Kundur, P., 1994. *Power Systems Stability and Control.* Toronto: McGraw-HIll.

Leon, J. I. et al., 2021. Hybrid Energy Storage Systems: Concepts, Advantages, and Applications. *IEEE Industrial Electronics Magazine,* 15(1), pp. 74 - 88.

Lerch, R., 2016. *Elektrische Messtechnik.* 7 Hrsg. Heidelberg: Springer Vieweg.

Mademlis, C., Kioskeridis, I. & Margaris, N., 2004. Optimal Efficiency Control Strategy for Interior Permanent-Magnet Synchronous Motor Drives. *IEEE Transactions on Energy Conversion,* 19(4), pp. 715-723.

Mademlis, C., Xypteras, J. & Margaris, N., 2000. Loss Minimization in Surface Permanent-Magnet Synchronous Motor Drives. *IEEE Transactions on Industrial Electronics,* 47(1), pp. 115-122.

Meishner, F. & Sauer, D. U., 2019. Wayside Energy Recovery Systems in DC Urban Railway Grids. *eTransportation,* Volume 1.

Meng, L. et al., 2020. Fast Frequency Response From Energy Storage—A Review of Grid Standards Projects and Technical Issues. *IEEE Transactions on Smart Grid,* 11(2), pp. 1566-1581.

Meschede, D., Hrsg., 2015. *Gerthsen Physik.* 25 Hrsg. Berlin: Springer.

Michel, M., 2011. *Leistungselektronik - Einführung in Schaltungen und deren Verhalten.* 5 Hrsg. Berlin: Springer.

Mongird, K. et al., 2020. An Evaluation of Energy Storage Cost and Performance Characteristics. *energies,* Volume 13.

Morimoto, S., Tong, Y., Takeda, Y. & Hirasa, T., 1994. Loss Minimization Control of Permanent Magnet Synchronous Motor Drives. *IEEE Transactions on Industrial Electronics,* 41(5), pp. 511-517.

Mouratidis, P., Schneider, M., Genov, I. V. & Rinderknecht, S., 2019. *Hybrid Energy Storage test bench using a combined kinetic and electrochemical storage.* Paderborn, Germany, Fachtagung VDI Mechatronik.

Mouratidis, P., Schüßler, B. & Rinderknecht, S., 2019. *Hybrid Energy Storage System consisting of a Flywheel and a Lithium-ion Battery for the Provision of Primary Control Reserve.* Brasov, Romania, International Conference on Renewable Energy Research and Applications (ICRERA).

Oudalov, A., Chartouni, D. & Ohler, C., 2007. Optimizing a Battery Energy Storage System for Primary Frequency Control. *IEEE Transactions on Power Systems,* 22(3), pp. 1259-1266.

Perez-Diaz, J. I., Lafoz, M. & Burke, F., 2020. Integration of fast acting energy storage systems in existing pumped-storage power plants to enhance the system's frequency control. *WIREs Energy and Environment,* Volume 9.

Plett, G. L., 2015. *Battery Management Systems, Volume I: Battery Modeling.* Norwood, MA, USA: Artech House.

Plößer, T., Niersbach, B., Hanson, J. & Roloff, N., 2017. *PHI-Factory: Provision of Network Services by a Flexible Factory.* Bonn, Germany, International Energietechnische Gesellschaft (ETG) Congress.

Prodromidis, G. N. & Coutelieris, F. A., 2012. Simulations of economical and technical feasibility of battery and flywheel hybrid. *Renewable Energy,* Volume 39, pp. 149-153.

Quurck, L. et al., 2017. Design and practical Realization of an innovative Flywheel Concept for industrial Applications. *Techinsche Mechanik,* 37(2-5), pp. 151-160.

Rahmoun, A. & Biechl, H., 2012. Modelling of Li-ion batteries using equivalent circuit diagrams. *Przegląd Elektrotechniczny (Electrical Review),* 88(7b), pp. 152-156.

Ramli, M. A., Hiendro, A. & Twaha, S., 2015. Economic analysis of PV/diesel hybrid system with flywheel energy storage. *Renewable Energy,* Volume 78, pp. 398-405.

Rigo-Mariani, R. et al., 2016. Power flow optimization in a microgrid with two kinds of energy storage. *COMPEL: The International Journal for Computation and Mathematics in Electrical and Electronic Engineering,* 35(3), pp. 860-870.

Sarasketa-Zabala, E., I. Gandiaga, E. M.-L., Rodriguez-Martinez, L. & Villarreal, I., 2015. Cycle ageing analysis of a LiFePO4/graphite cell with dynamic model validations: Towards realistic lifetime predictions. *Journal of Power Sources,* Volume 275, pp. 573-587.

Schaede, H., 2015. *Dezentrale elektrische Energiespeicherung mittels kinetischer Energiespeicher in Außenläufer Bauform.* Aachen: Shaker Verlag.

Schäfer, B. et al., 2018. Non-Gaussian power grid frequency fluctuations characterized by Lévy-stable laws and superstatistics. *Nature Energy,* Volume 3, pp. 119-126.

Schimpe, M. et al., 2018. Energy efficiency evaluation of grid connection scenarios for stationary battery storage systems. *Energy Procedia,* Volume 155, pp. 77-101.

Schmalstieg, J., Käbitz, S., Ecker, M. & Sauer, D. U., 2014. A holistic aging model for Li(NiMnCo)O2 based 18650 lithium-ion batteries. *Journal of Power Sources,* Volume 257, pp. 325-334.

Schneider, M., 2019. *Ganzheitlicher modellbasierter Entwurf von kinetischen Energiespeichern in Außenläuferbauform.* Düren: Shaker Verlag.

Schneider, M. & Rinderknecht, S., 2019. *System Loss Measurement of a Novel Outer Rotor Flywheel Energy Storage System.* San Diego, CA, USA, IEEE International Electric Machines and Drives Conference (IEMDC).

Schneider, M., Rinderknecht, S. & Schaab, D., 2017. *Loss Models of a PMSM in an Outer Rotor Flywheel Concept.* Miami, FL, USA, IEEE International Electric Machines and Drives Conference (IEMDC).

Schröder, D. & Kennel, R., 2021. *Elektrische Antriebe - Grundlagen.* 7 Hrsg. München: Springer Vieweg.

Schuster, S. F. et al., 2015. Nonlinear aging characteristics of lithium-ion cells under different operational conditions. *Journal of Energy Storage,* Volume 1, pp. 44-53.

Schwungrad Energie, 2017. *Rhode System Service Facility - EirGrid Demonstration Project: Flywheel-Battery Hybrid Project Report,* Tullamore, Offaly, Ireland: Schwungrad Energie.

Smith, K. et al., 2021. Lithium-Ion Battery Life Model with Electrode Cracking and Early-Life Break-in Processes. *Journal of The Electrochemical Society,* Volume 168.

Tu, H., Feng, H., Srdic, S. & Lukic, S., 2019. Extreme Fast Charging of Electric Vehicles: A Technology Overview. *IEEE Transactions on Transportation Electrification,* 5(4), pp. 861-878.

Urasaki, N., Senjyu, T. & Uezato, K., 2003. A Novel Calculation Method for Iron Loss Resistance Suitable in Modeling Permanent-Magnet Synchronous Motors. *IEEE Transactions on Energy Conversion,* 18(1), pp. 41-47.

Wandelt, F., Gamrad, D., Deis, W. & Myrzik, J., 2015. *Comparison of flywheels and batteries in combination with industrial plants for the provision of Primary Control Reserve.* Eindhoven, IEEE PowerTech.

Weitzel, T. & Glock, C. H., 2018. Energy management for stationary electric energy storage systems: A systematic literature review. *European Journal of Operational Research,* 264(2), pp. 582-606.

Weitzel, T. et al., 2018. *Sizing and Operating a Hybrid Electric Energy Storage System using Meta Heuristics.* Venice, International Conference & Workshop REMOO Energy.

Weitzel, T. et al., 2018. Operating a storage-augmented hybrid microgrid considering battery aging costs. *Journal of Cleaner Production,* Volume 188, pp. 638-654.

Zakeri, B. & Syri, S., 2015. Electrical energy storage systems: A comparative life cycle cost analysis. *Renewable and Sustainable Energy Reviews,* Volume 42, pp. 569-596.

Zeh, A. et al., 2016. Fundamentals of Using Battery Energy Storage Systems to Provide Primary Control Reserves in Germany. *Batteries,* 2(3).

Zhao, P., Wang, J. & Dai, Y., 2015. Capacity allocation of a hybrid energy storage system for power. *Renewable Energy,* Volume 75, pp. 541-549.

Zhao, Z., Xiao, H. & Yang, Y., 2018. Improved coordinated control strategy of hybrid energy storages in PV Power Smoothing. *Energy Procedia,* Volume 145, pp. 151-156.

Standards

IEC 60300-3-3:2017. *Dependability management - Part 3-3: Application guide - Life cycle costing.* Geneve: International Electrotechnical Commission.

IEC 61557-12:2018. *Electrical safety in low voltage distribution systems up to 1000 V AC and 1500 V DC - Equipment for testing, measuring or monitoring of protective measures - Part 12: Power metering and monitoring devices (PMD).* Geneve: International Electrotechnical Commission.

IEC 61869-2:2012. *Instrument transformers - Part 2: Additional requirements for current transformers).* Geneve: International Electrotechnical Commission.

Regulations and Acts

Bundestag, 2009. *Gesetz über das Inverkehrbringen, die Rücknahme und die umweltverträgliche Entsorgung von Batterien und Akkumulatoren (Batteriegesetz, BattG).* Bonn: Bundesgesetzblatt.

European Commission, 2017. *Regulation 2017/1485 - Establishing a guideline on electricity transmission system operation*. Brussels: Journal of the European Union.

European Parliament, 2016. *Directive 2006/66/EC of the European Parliament and of the Council of 6 September 2006 on batteries and accumulators and waste batteries and accumulators and repealing Directive 91/157/EEC*. Brussels: Journal of the European Union.

50Hertz Transmission GmbH, Amprion GmbH, TenneT TSO GmbH, TransnetBW GmbH, 2020. *Prequalification Process for Balancing Service Providers (FCR, aFRR, mFRR) in Germany*. Berlin.

Publication List

P. Mouratidis, H. Gockel, D. Franz, S. Rinderknecht, "Loss and thermal model for an outer rotor flywheel storage," in Fachtagung VDI Mechatronik, Darmstadt, Germany, March 2022, pp. 170-175. https://doi.org/10.26083/tuprints-00020963

P. Mouratidis, M. Knipper, N. Ó Brolcháin, A. De Shryver, G. Kinget, P. Eckerle, I. Ellerington, F. Vanden Hautte, S. Azizighalehsari, "State of the Art Report on Storage Technologies, Opportunities and Trends", European Union, Interreg NWE, Lille, France, May 2021. https://www.nweurope.eu/media/14318/state-of-the-art-report-steps.pdf

P. Glücker, K. Kivekäs, J. Vepsäläinen, P. Mouratidis, M. Schneider, S. Rinderknecht, K. Tammi, "Prolongation of Battery Lifetime for Electric Buses through Flywheel Integration", Energies, 2021, 14(4):899. https://doi.org/10.3390/en14040899

P. Mouratidis, M. Schneider, S. Rinderknecht, "Hybrid Energy Storage System for Peak Shaving Application in Industries," in 16. Symposium Energieinnovation, Graz, Austria, February 2020.
https://www.tugraz.at/events/eninnov2020/nachlese/download-beitraege/stream-h/

P. Mouratidis, B. Schüßler, S. Rinderknecht, "Hybrid Energy Storage System consisting of a Flywheel and a Lithium-ion Battery for the Provision of Primary Control Reserve," in 8th International Conference on Renewable Energy Research and Applications (ICRERA), Brasov, Romania, November 2019, pp. 94–99.
https://doi.org/10.1109/ICRERA47325.2019.8996553

P. Mouratidis, M. Schneider, I. V. Genov, S. Rinderknecht, "Hybrid Energy Storage test bench using a combined kinetic and electrochemical storage," in Fachtagung VDI Mechatronik, Paderborn, Germany, March 2019, pp. 61-66.

A. Appendix

Table A.1 Technical data of the Permanent Magnet Synchronous Machine integrated into the flywheel prototype SWIVT290 (Schneider & Rinderknecht, 2019)

Parameter	**Value**
Maximum electric power	100 kW
Maximum continuous phase current	119 A
Number of pole pairs	5
Phase self-inductance	145 µH
Phase DC resistance	6.5 mΩ
Counter EMF constant	0.0273 V/rpm

Table A.2 Technical data of the Permanent Magnet Synchronous Machine integrated into the flywheel prototype ETA290 (Schneider, et al., 2017)

Parameter	**Value**
Maximum electric power	120 kW
Maximum continuous phase current	182 A
Number of pole pairs	4
Phase self-inductance	81 µH
Phase DC resistance	6 mΩ
Counter EMF constant	0.0285 V/rpm

Table A.3 Technical data of the lithium-ion cell with the mode name SLPB120216216 manufactured by KOKAM Co., Ltd.

<table>
<tr><th>Property</th><th>Value</th><th>Notes</th></tr>
<tr><td>Manufacturer</td><td>KOKAM Co., Ltd.</td><td></td></tr>
<tr><td>Model</td><td>SLPB120216216</td><td></td></tr>
<tr><td>Nominal Capacity</td><td>53 Ah</td><td>at 0.2C, 25±3 °C</td></tr>
<tr><td>Nominal Energy</td><td>196.1 Wh</td><td></td></tr>
<tr><td>Internal Resistance</td><td>0.9 mΩ</td><td>at 1kHz, SoC 30±5 %</td></tr>
<tr><td>Weight</td><td>1095 g</td><td></td></tr>
<tr><td>Width</td><td>228 mm</td><td></td></tr>
<tr><td>Length</td><td>227 mm</td><td></td></tr>
<tr><td>Thickness</td><td>12 mm</td><td>at SoC 30±5 %</td></tr>
<tr><td>Max Voltage</td><td>4.2 V</td><td></td></tr>
<tr><td>Min Voltage</td><td>2.7 V</td><td></td></tr>
<tr><td>Average Voltage</td><td>3.7 V</td><td></td></tr>
<tr><td>Cycle Life</td><td>6000 cycles</td><td>at 25±3 °C,
90 % DoD,
70 % remaining capacity</td></tr>
<tr><td>Maximum Continuous Charge Current</td><td>106 A (2C)</td><td>at 25±3 °C</td></tr>
<tr><td>Maximum Continuous Discharge Current</td><td>265 A (5C)</td><td>at 25±3 °C</td></tr>
<tr><td rowspan="3">Permissible temperature range when charging</td><td>0…10 °C</td><td>up to 0.2C</td></tr>
<tr><td>10…35 °C</td><td>up to 2.0C</td></tr>
<tr><td>35…45 °C</td><td>up to 1.0C</td></tr>
<tr><td>Permissible temperature range when discharging</td><td>-20…55 °C</td><td></td></tr>
</table>

Table A.4 Technical data of the lithium-ion cell with the model name SLPB120216216HR2 manufactured by KOKAM Co., Ltd. used in the combined storage prototypes hsSWIVT and hsETA

Property	Value	Notes
Manufacturer	KOKAM Co., Ltd.	
Model name	SLPB120216216HR2	
Nominal Capacity	46 Ah	at 0.2C, 25±3 °C
Nominal Energy	170.2 Wh	
Internal Resistance	0.5 mΩ	at 1kHz, SoC 30±5 %
Weight	1145 g	
Width	226 mm	
Length	227 mm	
Thickness	12.2 mm	at SoC 30±5 %
Max Voltage	4.2 V	
Min Voltage	2.7 V	
Average Voltage	3.7 V	
Cycle Life	10000 cycles	at 25±3 °C, 90 % DoD, 70 % remaining capacity
Maximum Continuous Charge Current	138 A (3C)	at 25±3 °C
Maximum Continuous Discharge Current	368 A (8C)	at 25±3 °C
Permissible temperature range when charging	0…10 °C	up to 0.3C
	10…35 °C	up to 3.0C
	35…45 °C	up to 1.0C
Permissible temperature range when discharging	-20…55 °C	

Table A.5 Technical data of the battery system named AKASYSTEM 15 AKM 46 NANO NMC manufactured by AKASOL AG integrated into the combined storage prototype hsETA

Property	Value
Manufacturer	AKASOL AG
Model name	AKASYSTEM 15 AKM 46 NANO NMC
Number of modules	15
Cell connection in module	12s1p
Nominal charge capacity	46 Ah
Nominal energy capacity	30.6 kWh
Nominal voltage	666 V
Maximum voltage	756 V
Minimum voltage	486 V
Permissible temperature range when discharging	-15…55 °C
Permissible temperature range when charging	0…45 °C
Weight	372 kg
Length	1546 mm
Width	570 mm
Height	216 mm

Table A.6 Identified equivalent circuit parameters of the KOKAM 53 Ah SLPB120216216 lithium-ion cell under charging at an SoC of 50 % and a temperature of 25 °C (Rahmoun & Biechl, 2012)

Parameter	Value	Description
R_0	3.5 mΩ	series resistance
R_1	1.5 mΩ	Resistance of 1st RC-loop
C_1	4.4e5 F	Capacitance of 1st RC-loop
R_2	1.4 mΩ	Resistance of 2nd RC-loop
C_2	0.5e5 F	Capacitance of 2nd RC-loop

Table A.7 Parameters of the cyclic and calendrical degradation model of the lithium-ion cells

Parameter	Value	Unit	Description
$a_{\mathrm{cyc,q}}$	0.5	-	exponent
$a_{\mathrm{cyc,r}}$	1	-	exponent
$a_{\mathrm{cal,q}}$	0.75	-	exponent
$a_{\mathrm{cal,r}}$	0.75	-	exponent
$k_{\mathrm{cal,q1}}$	7.543e6	day*	related to time
$k_{\mathrm{cal,r1}}$	5.27e5	day*	related to time
$k_{\mathrm{cal,q2}}$	0.05	-	SoC offset
$k_{\mathrm{cal,r2}}$	0.1	-	SoC offset
$k_{\mathrm{cal,q3}}$	6976	Kelvin	related to temperature ratio
$k_{\mathrm{cal,r3}}$	5986	Kelvin	related to temperature ratio
$k_{\mathrm{cyc,q1}}$	2.635e-3	-	related to max EFC
$k_{\mathrm{cyc,r1}}$	7.716e-5	-	related to max EFC
$k_{\mathrm{cyc,q2}}$	2.143e-3	-	related to nominal cycle depth
$k_{\mathrm{cyc,r2}}$	1.715e-4	-	related to nominal cycle depth
$k_{\mathrm{EFC,max}}$	3	-	ratio of max to nominal EFC
$r_{\mathrm{c,EoL}}$	2	-	normalized resistance at EoL

Table A.8 Technical data of the flywheel prototype SWIVT290 (Schneider & Rinderknecht, 2019)

Property	Value
Nominal power	50 kW
Nominal energy capacity	1.8 kWh
Maximum power	100 kW
Maximum speed	17 500 rpm
Minimum operating speed	9 000 rpm
Rotor length	850 mm
Outer rotor diameter	430 mm
Inner rotor diameter	290 mm
Rotor weight	170.6 kg
Rotor Inertia	5.1 kgm^2

Table A.9 Technical data of the flywheel prototype ETA290 (Schneider, et al., 2017)

Property	Value
Nominal power	60 kW
Nominal energy capacity	1.4 kWh
Maximum power	120 kW
Maximum speed	15 000 rpm
Minimum operating speed	7 500 rpm
Rotor length	600 mm
Outer rotor diameter	430 mm
Inner rotor diameter	290 mm
Rotor weight	153 kg

Table A.10 Technical data of the power converters installed in the prototypes hsSWIVT and hsETA. The nominal current of the DC-3xAC converters is the maximum continuous rms phase current. The power converters operate at constant switching frequency. The maximum power losses are for nominal current.

Power Converter Type	Manufacturer	Model	Nominal Current (A)	Nominal Power	Nominal switching frequency (kHz)	Maximum power losses (W)	Integrated into
DC-3xAC	Bosch Rexroth	HMS01-1N-W0350	250	140 kVA	12	2750	hsSWIT
DC-3xAC	Sieb& Meyer	SD2M-03622 82AF	212	145 kVA	16	4800	hsETA
DC-DC	Siemens	Sinamics DCP 30	200	120 kW	15	2800	hsSWIT
DC-DC	Siemens	Sinamics DCP 120	50	30 kW	20	800	hsETA

Table A.11 Selected technical data of the Programmable Logic Controller Bosch Rexroth XM21

Property	Value
Manufacturer	Bosch Rexroth
Model	XM2100.01-01-01-31-31-301-NN-100N1NN
Processor	Intel E620T 600 Mhz
Dynamic Random-Access Memory	512 Mbyte
Number of Digital Inputs	16
Number of Digital Outputs	16
Number of Analog Inputs	8
Number of Analog Inputs for thermocouples	8
Selection of supported communication protocols	Sercos III, Profibus DP, TCP/IP, OPC UA

Table A.12 Selected technical data of the power analyser Janitza UMG 605 according to IEC 61557-12

Measuring function	Accuracy class	Measurement range	Notes
Real power (total)	0.5	0…15.3 kW	The accuracy class degrades one level if the rated secondary current of the current transformer is 1 A instead of 5 A.
Line-to-line voltage (U_{LL})	0.2	18…1000 Vrms	
Phase current	0.25	0.001…8.5 Arms	
Power factor	0.5	0.00…1.00	

Table A.13 Technical data of the current transformer Janitza KUW2/40 according to IEC 61869-2

Property	Value
Transformation ratio	400/1 A
Nominal burden	0.2 VA
Accuracy class	1

Table A.14 Parameters of the basic equipment of the reference combined storage system

Equipment	Property	Value
Three-phase power transformer	Rated power	1250 kVA
	Nominal line-to-line low voltage	690 V
	Nominal line-to-line high voltage	20 kV
	Equivalent resistance	0.01 pu
	No-load losses	0.0015 pu
Central DC-3xAC power converter	Nominal DC voltage	1000 V
	Nominal line-to-line AC voltage	690 V
	Equivalent resistance	0.02 pu
Ventilation and cooling	Nominal power consumption	1.5 kW
Control and sensors	Nominal power consumption	0.4 kW

Table A.15 Parameters of the additional equipment intended for the applications of EVFC and WERS

Equipment	Property	Value
DC-DC power converter for wayside energy recovery in railway networks	Rated power	500 kVA
	Nominal voltage stationary storage side (DC bus)	1000 V
	Nominal voltage railway network side	600 V
	Equivalent resistance	0.02 pu
DC-DC power converter for the fast charging of passenger vehicles	Rated power	120 kVA
	Nominal voltage stationary storage side (DC bus)	1000 V
	Nominal voltage charging station side (vehicle side)	800 V
	Equivalent resistance	0.025 pu
DC-DC power converter for the fast charging of heavy-duty vehicles	Rated power	350 kVA
	Nominal voltage stationary storage side (DC bus)	1000 V
	Nominal voltage charging station side (vehicle side)	1200 V
	Equivalent resistance	0.022 pu